The Pennsylvania State University

The Graduate School

Department of Physics

GRAVITATIONAL WAVES AND THE DEFORMATION OF COMPACT OBJECTS: TOPICS IN RELATIVISTIC ASTROPHYSICS

A Dissertation in

Physics

by

Nathan Kieran Johnson-McDaniel

Submitted in Partial Fulfillment
of the Requirements
for the Degree of

Doctor of Philosophy

August 2011

The dissertation of Nathan Kieran Johnson-McDaniel was reviewed and approved[1] by the following:

Benjamin J. Owen
Associate Professor of Physics
Dissertation Adviser
Chair of Committee

Martin Bojowald
Associate Professor of Physics

Irina Mocioiu
Associate Professor of Physics

Steinn Sigurðsson
Associate Professor of Astronomy and Astrophysics

Nitin Samarth
Professor of Physics
Associate Head of the Department of Physics

[1]Signatures on file in the Graduate School.

Abstract

In this dissertation, we present various theoretical investigations of sources of gravitational waves, relevant to interpreting the data from current and planned gravitational wave detectors; an *idée fixe* is the deformation of compact objects.

We begin in the strong field, vacuum regime, with a construction of initial data for the numerical simulation of black hole binaries (specializing to the case of nonspinning holes in a quasicircular orbit). The data we construct contain more of the binary's expected physics than any other current data set. In particular, they contain both the binary's outgoing radiation and the expected tidal deformations of the holes. Such improved initial data will likely be necessary for simulations to achieve the accuracy required to supply advanced gravitational wave detectors with templates for parameter estimation.

We end in the weak field, hydrodynamic regime with a calculation of the expected accuracy with which one can combine standard electromagnetic and gravitational wave observations of white dwarf binaries to measure the masses of the binary's components. In particular, we show that this measurement will not be contaminated by finite size effects for realistic sources observed by LISA, though such effects could be important for exceptional sources and/or advanced mHz gravitational wave detectors.

In the middle, we make a detour into the messy and poorly constrained realm of the physics of neutron star interiors, calculating the shear modulus of hadron–quark mixed phase in hybrid stars. Here we include a rough treatment of charge screening, dimensional continuation of the lattice, and the contributions from changing the cell volume when shearing lower-dimensional lattices. We find that the last of these contributions is necessary to stabilize the lattice for those dimensions, where it makes a considerable contribution to the shear modulus.

We then move back to sounder theoretical footing in making a general relativistic calculation of the maximum elastic quadrupole deformation that could be sustained by a star with a known shear modulus and breaking strain (provided by, e.g., the hadron–quark mixed phase in the core, or the more standard lattice of nuclei in the crust). We find that the standard Newtonian calculation considerably overestimates the quadrupole, particularly for massive, compact stars.

We also present the dimensionally continued Poisson summation formula we discovered while performing the shear modulus calculation, and thought interesting enough to prove rigorously. Our method of proof also provides a new way of proving other (Voronoi) summation formulae obtained from functions satisfying modular transformations, and allows one to relax certain of the standard hypotheses.

Table of Contents

List of Tables

List of Figures

Preface

Portions of the work presented in this dissertation were completed in collaboration with other researchers. However, in all cases, I am responsible for the vast majority of the work presented here (including proposing portions of the investigations, writing up the work, creating the figures, and performing analytic and numerical computations).

In particular, Chapter 2 is based on a paper published in *Physical Review D*, coauthored with Nicolás Yunes, Wolfgang Tichy, and Benjamin J. Owen. I was primarily responsible for writing and editing the manuscript, though my coauthors also participated in the editing process, and made certain contributions to the text (all of which I edited, quite often heavily). W. Tichy carried out all the computations involving BAM, and N. Yunes did much of the coding in MAPLE, though I assisted in almost all aspects of the MAPLE work, and performed careful checks of the resulting scripts. Additionally, N. Yunes carried out certain analytic computations, most notably the computation of the far zone metric detailed in Sec. 2.6; I made a parallel, independent computation.

Chapters 3 and 4 made use of Benjamin J. Owen's MATHEMATICA notebooks for computing hybrid star equations of state and solving the Oppenheimer-Volkov equations, which I then modified to perform the specific computations detailed in those chapters.

Chapter 6 is based on work done in collaboration with Michael J. Koop, Amanda R. Lundberg, Hampton Scott Langdon, and Lee Samuel Finn. I am responsible for almost all the content presented here. The only significant contributions to the text are from M. J. Koop, who wrote the original draft of portions of Secs. 6.4 and 6.5, which I then edited quite heavily. M. J. Koop, A. R. Lundberg, and H. S. Langdon also performed checks of certain of my codes and calculations.

Acknowledgments

I first must thank my research advisor, Ben Owen, for suggesting excellent research topics while still giving me plenty of room to explore things on my own. In addition, Ben provided a window into the fascinating world of LIGO. Sam Finn and his group provided a welcoming environment for me while Ben was on sabbatical; I owe particular thanks to Sam for introducing me to the realm of gravitational wave data analysis and LISA.

Wolfgang Tichy provided invaluable numerical expertise for the initial data project, and indulged all my parameter investigations, while Nico Yunes was my guide to some of the more arcane facets of Maple and GRTensorII, and has been an inspiration in the speedy completion of projects.

In more mundane matters, I must acknowledge the work of all the support staff and administrators who made sure that everything ran smoothly, and that the necessary paperwork was completed and filed. In particular, in the Institute for Gravitation and the Cosmos and the Center for Gravitational Wave Physics, Randi Neshteruk and Kathy Smith aided with paperwork and other logistical matters, while Cindy Titsler provided ever-prompt computer support, even at odd hours of the night. In the physics main office, Megan Meinecke, Aimée Grugan-Long, Carol Deering, and Anne Stover made sure that all the bureaucratic requirements were fulfilled.

I must also thank Abhay Ashtekar for pointed questions about the initial data project during a seminar, and for his leadership of the Institute. My other colleagues in the Institute provided many stimulating discussions—I must single out Xihao Deng, Artur Tšobanjan, and Hannah Williams, in particular.

Many other musically inclined people helped me keep those parts of my interests well-satisfied, to balance out all the scientific work. In particular, in the Penn State School of Music, Tim Deighton let me participate in two memorable semesters of viola ensemble, and Max Zorin coached two chamber music ensembles in which I participated. I also played music with other amateurs, most notably John Collins, who joined me in working on various interesting repertoire (including trios with Michael Wenger), and giving two holiday party performances (in addition to conveying some of his deep intuition for quantum field theory). And finally, the members of the Nittany Valley Symphony were highly supportive. I owe special thanks to the viola section (particularly Avis Jones and Carol Motta, who helped transport me to many rehearsals), and also to the orchestra's conductor, Michael Jinbo, and concertmaster, Joanne Feldman.

In scientific computing matters, some of the computations reported here were performed on the Penn State Linux cluster, and much use was made of NASA's Astrophysics Data System in tracking down all the appropriate references. I must also thank all the participants in the local farmers' markets for providing me with the wide range of comestibles that fueled much of the work presented here.

Additionally, I owe special appreciation to the people who aided me during the two major crises that occurred during the work presented here: First, the skillful surgeon and physical therapists, Paul Sherbondy, Susan Fix, and Sally Bondurant who helped me successfully recover from a broken elbow suffered in a cycling accident, as well as the rest of the staff at Penn State Orthopædics. And second, the people who helped me find a new viola after mine was stolen, particularly John Collins, Mary Brown, Joanne Feldman, and Melissa Deines.

Finally, I must thank my family for their unwavering support throughout my studies. In particular, my mother, Barbara Johnson, and sister, Darrah Johnson-McDaniel, were always ready to provide amusing anecdotes and a sympathetic ear, when necessary.

To my first viola (2002–2010):

In memory of our many performances together.

Chapter 1

Introduction

"...mid visionless wilds of space ... in the full-fugued song of the universe unending." —Thomas Hardy [1]

It is an exciting time for gravitational wave (astro)physics. The Laser Interferometric Gravitational-Wave Detector (LIGO) [2] has just finished its "enhanced" science run, and is currently being upgraded to a sensitivity at which detections are expected. The companion Virgo detector [3] is just now nearing the end of its enhanced run, after which it will also be upgraded to a similar sensitivity. (These detectors have already placed some interesting upper limits at their current sensitivities—see [4] for a review.) Additionally, the upgraded, advanced detectors may be joined by other detectors to form a worldwide network, allowing for better science results, in particular better sky localization of detected signals (see, e.g., [5, 6]).

There are also complementary methods of gravitational wave detection currently being pursued. In particular, radio observers have already used pulsar timing to exclude a model for a galaxy's electromagnetic emission involving a supermassive black hole binary by a nondetection of the gravitational waves it would have been emitting [7], and there is an active effort to exploit multiple pulsars—in pulsar timing arrays—to detect the very low-frequency gravitational waves expected to be generated by supermassive black hole binaries [8].

Finally, there are plans for future, even more advanced interferometric gravitational wave detectors, both on the ground (the Einstein Telescope [9]), and in space (LISA [10], and even further in the future, ASTROD [11] and DECIGO [12]). Such space-based detectors are particularly interesting, as they will probe the rich mHz region of the gravitational wave spectrum. (Ground-based detectors operate in roughly the audio band, and pulsar timing is applicable to nHz gravitational waves.)

While the direct detection of gravitational waves will be a milestone in physics, particularly in the tests of general relativity gravitational wave observations will provide, gravitational wave detectors are fundamentally *observatories*, and their largest contribution will almost surely be to astronomy and astrophysics. In particular, gravitational wave astronomy will provide us with a direct window onto previously unavailable portions of the universe (most notably those involving black holes in the strong-field regime), as well as give us completely new views of more standard astrophysical objects, such as neutron stars and close binaries, complementing the standard electromagnetic observations of such objects.

In order to detect gravitational waves, and then to utilize them to learn about interesting physics and astronomy, one needs not only exacting experimental work, but also considerable theoretical modeling of possible sources: The vast majority of gravitational wave signals will be buried in the instrument's noise, and having a good template for the expected signal, when possible, allows one to use the method of matched filtering to optimally detect such weak signals.

Such theoretical templates also allow one to measure the parameters of any signals one does detect. More generally, theoretical predictions let one motivate searches and interpret upper limits (and possible detections).

This dissertation presents such theoretical investigations of three sources of gravitational radiation, along with the proof of a mathematical result that was discovered in the course of one of the investigations. We start in the strong-field regime in Chap. 2, constructing initial data for numerical simulations of binary black holes using a method that includes more of the system's expected physics than any other extant data. We then move into the somewhat weaker field regime of neutron stars. We first consider the condensed matter problem of calculating the shear modulus of the hadron–quark mixed phase in hybrid stars in Chap. 3. Then, in Chap. 4, we return to general relativity, making a relativistic calculation of the maximum elastic quadrupole that can be sustained by relativistic stars with a known shear modulus. (We apply this calculation to the mixed phase shear modulus from Chap. 3, as well as to the more standard case of the crustal shear modulus.) In Chap. 5, we also present a proof of the dimensionally continued Poisson summation formula we discovered in the process of calculating the shear modulus of the mixed phase. We end in the (relatively) weak field regime of white dwarf binaries in Chap. 6, where we concern ourselves with observational matters, calculating the accuracy with which one could combine together standard electromagnetic measurements with gravitational wave measurements to measure the individual masses. (We also consider the contribution from finite size effects.) We give various ancillary results in appendices.

These chapters present the technical papers (either published, submitted, or to be submitted) prepared for specialists in the appropriate fields. In the remainder of this introduction, we motivate our particular investigations for nonspecialists. We thus first give a general overview of the aspects of gravitational wave theory and observation used in this dissertation, and then provide relevant background concerning each of the gravitational wave sources we consider. We also provide further physical and mathematical background about regularizing divergent series that is relevant to the Poisson summation formula chapter.

1.1 Gravitational waves in theory and experiment

Gravitational waves were suggested by Einstein as a consequence of his general theory of relativity very soon after its development [13]. But even though it is intuitively reasonable that any causal theory of gravity will support wave-like excitations (by analogy with electromagnetism, if nothing else), the gauge invariance of general relativity under diffeomorphisms (i.e., smooth coordinate transformations) greatly complicates the theoretical analysis. Gravitational waves have thus had a long and rather tortuous journey (documented by Kennefick [14]) to their current status as a staple of astrophysics, and the subject of vast international collaborations, working with multimillion dollar instruments.

And while the theoretical framework for gravitational waves is now very well developed, a good portion of gravitational waves' current very mainstream status comes from the observational evidence provided by binary relativistic pulsars. Here one observes the effects of gravitational wave emission on the binary's orbit through radio observations of the pulsar, as first done by Hulse and Taylor. (See [15] for a review.) In fact, gravitational waves are now a frequently invoked ingredient in scenarios involving the evolution of close binaries containing

any sort of compact object (see, e.g., [16]). Finally, not only are there many projects for the direct detection of gravitational radiation currently planned or underway (as discussed above), but there is also great interest in detecting the effects of gravitational waves on the cosmic microwave background, either with the existing satellite Planck, or future missions (see, e.g., [17]).

While gravitational waves were first obtained from general relativity in the linearized approximation, the most rigorous—and in many senses most satisfactory—theoretical view of gravitational waves comes from studies of the asymptotic properties of spacetime for isolated systems, which are applicable to the full nonlinear case. In such *asymptotically flat* cases, one is able to rigorously define what is meant by a gravitational wave by looking at the energy such a wave carries off to infinity. These asymptotic approaches are reviewed in [18].

However, almost all of the practical work on gravitational waves uses far less geometrical approximate results with poorly controlled remainders; such treatments are necessary to deal with the problem of gravitational wave generation from all the various sources of interest. In particular, the predictions that have been verified by radio observations of pulsars are all obtained using the post-Newtonian approximation. As discussed in Blanchet [19], this approximation is formally an expansion in G, Newton's gravitational constant (known as the post-Minkowskian iteration), and $1/c$, where c is the speed of light (the post-Newtonian expansion proper, though the combination of expansions usually goes by that name). It is thus valid for slow motion and weak field situations (though the effects of strong internal gravity are "effaced," in the terminology of Damour, up to a considerably higher order than most current calculations). The canonical application is to the motion of compact binaries in the so-called inspiral phase, where they are well separated and being driven together by the emission of gravitational radiation. There are impressively high-order post-Newtonian results for such compact binaries: For instance, [19, 20] give the highest-order results for the standard post-Newtonian approximation for comparable-mass, nonspinning binaries; [21] presents very high-order post-Newtonian results for extreme mass-ratio systems, where one expands in the binary's mass ratio about a black hole background, in addition to $1/c$. These extensive computations have been motivated by the demands of gravitational wave observatories, first articulated in [22].

The lowest-order post-Newtonian (PN) prediction for gravitational wave emission is just the famous Einstein quadrupole formula (first given in [23]), which itself is simply the spin-2 analogue of the (spin-1) formula for electric dipole radiation in Maxwell theory. This formula also tells us that gravitational waves are generated by bulk motion of matter (and curvature, in a more careful treatment). It also implies that the only potential sources of detectable gravitational radiation involve large masses moving rapidly: Compared with the (strong) electromagnetic dipole radiation, we have to contend both with the overall weakness of the gravitational force (i.e., the fact that spacetime is stiff—a small amplitude gravitational wave carries a large amount of energy) and with extra factors of the emitter's velocity (since momentum conservation prohibits dipole radiation) in considering gravitational waves. Realistic sources of gravitational waves thus all involve compact objects (excluding early universe sources, or speculative physics, such as cosmic strings). These compact objects are most often considered in binaries, though they could also be isolated and deformed. But despite the weakness of gravitational waves from realistic sources, it is still thought to be likely that proposed gravitational wave observatories will be able to measure the higher harmonics (suppressed by successive factors of v/c) for certain sources, in addition to various high-order post-Newtonian contributions. These higher

harmonics come in both mass and current varieties, the analogues of electric and magnetic multipole radiation, and are described in, e.g., [19, 24]. The next few higher-order PN corrections are also discussed in [19]; perhaps the most fascinating of these are the hereditary contributions that depend on the source's history, including the so-called tail contributions from backscattering of radiation off of the background spacetime.

The other prominent analytic approach to the generation of gravitational waves is the perturbation of nonflat exact solutions (primarily the Schwarzschild and Kerr solutions for black holes, and the Oppenheimer-Volkov solution for static relativistic stars). Here one works almost exclusively to first order, though there are a few second-order results in the literature (e.g., [25]). Notable results include the computation of the quasinormal modes of these objects (see [26] for a review), applicable, in particular, to the description of a deformed compact object immediately following the merger of a binary. Perturbation theory also gives the proofs of linear stability of the spacetimes being perturbed (see [27] for a review and recent results in the black hole case, and [28] in the case of relativistic stars), and allows one to compute the gravitational waves from so-called extreme mass-ratio inspirals, where a small compact object spirals into a supermassive black hole (so the mass ratio is $\lesssim 10^{-4}$), as reviewed in [29].

While these analytic methods can be quite powerful, and have provided almost all the intuition one applies to gravitational wave generation, they are not capable of dealing with the most relativistic, dynamical processes that will be the strongest emitters of gravitational waves (e.g., mergers of compact objects, supernovae) with the requisite accuracy. They do not even appear to be sufficiently accurate to describe the late portions of the inspiral of two compact objects with the accuracy required to fully exploit the capabilities of gravitational wave detectors to measure the system's parameters (see, e.g., [30]). In such situations, one has to use nonperturbative, fully numerical methods to solve the full nonlinear Einstein equations. Due to the complexity of these equations (in particular, their nonlinearity, and the large gauge group of all diffeomorphisms, with its associated constraint equations), placing them in a form well-suited to numerical evolution has been a nontrivial task, and the first successful simulations of an inspiralling black hole binary through to merger—that paradigmatic numerical relativity calculation—only finally took place over 40 years since the very first study by Hahn and Lindquist [31], after significant technical and conceptual developments.

The basic idea of all numerical relativity approaches is to convert the Einstein equations on 4-dimensional spacetime into an evolution system for some 3-dimensional hypersurface (most commonly a spatial hypersurface, in the Cauchy approach, though null hypersurfaces have been considered, in the characteristic approach), where the specific variables evolved depend upon the particular formulation. It is not our purpose here to review the extensive literature on these formulations, merely to note that there are some which have been found to be amenable to stable numerical evolutions. More to our point is to note that one has to specify the system one wishes to evolve in the initial data for the simulation. This is not at all straightforward, since such initial data have to satisfy the Einstein constraint equations, and posing completely accurate initial data for a nonlinear continuum dynamical system is likely just as hard as evolving the system. We discuss binary black hole initial data further in Sec. 1.2 and Chap. 2.

In this dissertation, we touch upon all of the methods discussed above: Chap. 2 makes heavy use of both post-Newtonian and black hole perturbation results, while being geared towards providing analytic input to numerical relativity simulations in the form of initial data. We

make similar extensive use of the post-Newtonian approximation in Chap. 6, including computing finite size contributions to the standard point-mass binary waveform in Appendix F. And in Chap. 4, we perform a computation in relativistic stellar perturbation theory.

We also need to consider the detectors whose existence motivates all this theoretical work. All modern gravitational wave detectors rely on some method of measuring the phase changes in an electromagnetic wave traveling between two masses (the first detectors used a resonant bar); these are sensitive to gravitational waves through the geodesic deviation equation (see [32] for a derivation of the response of an interferometer to gravitational waves). In the case of pulsar timing, the two masses are the pulsar and the Earth, and the electromagnetic wave is emitted by the pulsar. The laser interferometers measure the distance between carefully designed test masses.

The current primary interferometric detectors are LIGO and Virgo, which are ground-based and sensitive to gravitational waves in the audio band (10s of Hz to a few kHz). The standard figure of merit for their sensitivity is the distance to which they are sensitive to an optimally-oriented binary neutron star in the last few orbits of inspiral; this is now around 10–20 Mpc. The upgraded, advanced detectors are expected to be able to detect such binary neutron star inspirals at distances of $\sim$ 200 Mpc. There are also a few smaller detectors, mostly used for technology development; the current status of interferometric gravitational wave detection is reviewed in [33].

The low-frequency cutoff for ground-based detectors is set by seismic noise, so to gain access to the lower frequency portions of the gravitational wave spectrum, one has to go into space (or use the entire Earth as your test mass, as in pulsar timing). And these lower-frequency waves are well worth the trouble: The mHz band accessible by space-based detectors is where the signals from supermassive black hole coalescences, extreme mass-ratio inspirals, and an entire zoo of galactic compact binaries will reside. The LISA mission [10] has been the premier proposed low-frequency gravitational wave detector for many years now (its basic design goes back to 1985), with a stable design and a strong science case. Very recently, the funding agencies have instigated a major redesign, and it remains to be seen what the capabilities of the revised instrument will be. Looking further in the future, there are various proposed follow-ups to LISA, from the incremental (ASTROD [11]) to the highly optimistic (DECIGO [12]).

Of course, there are a multitude of other effects that will also lead to phase changes in these detectors, and the gravitational wave signals one expects will not be particularly strong, particularly for ground-based detectors, so one has to have some way of extracting potential gravitational wave signals from the noise. For signals with a known form—which are almost all we consider in this dissertation—this is provided by the method of matched filtering, which can be shown to be optimal in such cases. Here one integrates waveforms from a template bank against the detector's output: The value of this integral is maximized if the data contain the template waveform. This method also allows one to extract the parameters that characterize the signal by looking at the parameters of the template waveform with the largest overlap. The most complicated waveforms for which we can make good theoretical predictions are those from compact binaries, and the construction of such template banks of compact binary coalescence waveforms is an important task for analytical and numerical relativity.

1.2 Initial data for numerical relativity simulations of black hole binaries

While there is no direct evidence for the existence of binary black holes (unlike white dwarf and neutron star binaries), there is such a clear theoretical path for their formation that they are considered a standard gravitational wave source: We have observational evidence for black holes, both isolated (e.g., our galaxy's central black hole), and in binaries with stars (e.g., Cygnus X-1). We thus expect the universe to contain binaries consisting of two black holes, even though it is difficult to observe such binaries electromagnetically.

Stellar-mass binary black holes are thought to be formed most often "*in situ*" from a binary of suitably massive stars. The binary has to survive the two supernovae that form the black holes, but there is evidence that this will occur reasonably frequently (see, e.g., [34]). In this case, one simply has to wait for gravitational radiation to slowly drive the binary to coalescence. (There are also scenarios involving capture which we will not discuss further here.) Supermassive black hole binaries are expected to form during galaxy collisions, and observers have recently detected evidence for dual black holes (i.e., ones that are not yet bound systems on their own) in the remnants of galaxy mergers [35, 36]. These holes have to migrate together through complicated N-body processes before their gravitational radiation will be strong enough for them to merge within a Hubble time. However, there dynamical friction provides a well-established theoretical process for this migration up to the "final parsec," and recent developments claim to solve this so-called "final parsec problem" (see, e.g., [37, 38]). (As discussed in [37], the observed X-shaped radio sources are interpreted as evidence that mergers of supermassive black holes do occur.)

In both cases, one expects the holes to have a lengthy inspiral where their evolve is dominated by gravitational radiation before they merge. The orbit will rapidly circularize (see, e.g., [39, 19]), so much of this inspiral will take place in the quasicircular regime (at least for stellar-mass holes; supermassive black holes binaries may not have enough time in the gravitational radiation-dominated regime to shed all of the very appreciable eccentricity with which they are expected to enter that regime). As discussed above, much of the inspiral can be treated using the post-Newtonian approximation, while the final portions of the inspiral and merger require a full numerical treatment.

Such a full numerical treatment was a long-standing problem for many years, but in 2005, numerical relativists achieved the first successful evolutions of a black hole binary through merger [40, 41, 42], and the field has taken off since—see [43, 44] for recent reviews. While not all the corners of parameter space have been fully explored to date—in particular, even the highest-spin evolution to date has dimensionless spins of only 0.95 [45] (where a maximally-spinning Kerr hole has a spin of unity)—it has been sampled reasonably well. In particular, people have discovered large recoil velocities after merger ("kicks") for certain spin configurations in quasicircular inspiral [46], and even larger ones for hyperbolic encounters [47]. There has also been work in improving the numerical accuracy and speed of the simulations: Numerical relativists can now evolve black hole binaries for as many as 64 cycles (Abdul Mroué using the SpEC code [48], reported in [44]), and have started to implement advanced, faster time-stepping schemes [49]. Numerical relativists have also worked on improving the physical accuracy of their simulations. In particular, they have recently developed codes that extract the waveform at future null infinity (see [50, 51, 52]), removing any ambiguities present in previous work that extracted the waves at a finite radius (and possibly extrapolated to an infinite extraction radius).

While the two-body problem in general relativity holds considerable theoretical appeal on its own, the extensive studies alluded to above have been motivated by the need to supply gravitational wave detectors with templates for detection and parameter estimation. In particular, binary black holes offer an otherwise unprecedented opportunity for probing (both theoretically and observationally) the nonlinear dynamics of spacetime predicted by Einstein's equations in a very clean situation. This makes them ideal for high-precision tests of general relativity, particularly because the black holes' large masses are expected to lead to gravitational detections with very high signal to noise ratios. But even the much less precise measurements of masses, spins, and sky location that are interesting for astrophysics (in particular, testing models for binary evolution) still require quite accurate templates. There has thus been considerable work recently on generating numerical templates for gravitational wave detectors (by stitching together PN and numerical relativity results), and considering the length and accuracy of the simulations required to produce such templates (e.g., [30, 53, 54, 55, 56, 57, 58]).

However, none of these simulations start with initial data that describe a timeslice of an astrophysical binary black hole: They are missing the binary's outgoing radiation from its long inspiral, and instead have a burst of so-called spurious (or "junk") radiation of a much higher frequency at the start of the simulation. Due to curved spacetime effects, such deficiencies in the initial data will affect (in principle all of) the binary's subsequent evolution, even after the initial burst has left the computational grid. In particular, one knows from post-Newtonian results that the binary's evolution depends upon its entire past history due to the tail effects caused by backscattering of the binary's outgoing radiation off of the curved spacetime. (In addition, the high frequency of the junk radiation causes numerical difficulties for SpEC that also persist after the junk has left the grid [59, 60].) I have started to estimate the magnitude of these backscattering effects on the binary's evolution, using lowest-order post-Newtonian results, as part of a general program to determine how accurate initial data need to be to supply current and planned gravitational wave detectors with templates for parameter estimation that allow the observers to fully exploit the instruments' abilities for strong signals. (One would want this full accuracy to, e.g., make high-precision tests of general relativity and search for subtle astrophysical effects.)

In principle, the solution to these initial data problems is straightforward: Simply start evolving the binary from the Newtonian regime where one can give initial data with the appropriate accuracy simply using a superposition of black hole metrics. (The holes will be far enough apart that the errors from the nonlinearity of the Einstein equations will be negligible.) However, this is impossible, in practice: Even with the increases in speed and accuracy of numerical codes, it is only possible to evolve these binaries for tens of orbits, not the $> 10^{11}$ orbits it would take for this to be feasible. [The second number comes from Eq. (235) in [19], taking the initial separation (in geometrized units) to be $\sim 10^5$ times the system's mass, so the first post-Newtonian corrections are $\sim 10^{-5}$.] One thus has to evolve the binary using an approximate scheme during the early portion of its evolution. The easiest way to do this is to use analytic post-Newtonian results (supplemented with perturbed black hole metrics near the holes), which is what we do in Chap. 2, though in the ideal case, one would likely evolve completely numerically, using an appropriate approximation to the Einstein equations at each stage of the binary's evolution. (The 4PN truncation obtained by Brizuela and Schäfer [61] may be a first step towards such approximations.)

The initial data construction described in Chap. 2 combines together the post-Newtonian approximation and black hole perturbation theory results to generate approximate initial data that contain more of the binary's expected physics than any other set. (The post-Newtonian approximation is an obvious choice to use to include known physical effects, since it has been iterated to a high order, though it is a weak-field approximation and thus has to be supplemented with perturbed black hole metrics.) This paper is the latest in a line of papers that have developed this construction, starting with the original, flawed version by Kashif Alvi [62], and moving through two versions by Nico Yunes and collaborators [63, 64]. The present version iterates the construction to a high enough order that it has the possibility of improving on standard initial data. In particular, standard initial data assume conformal flatness (i.e., that the spatial metric is the just the flat space metric times a scalar), for technical convenience, while the post-Newtonian metric is known not to be conformally flat past a certain order. This version of the construction iterates to that order, thus including the first conformally curved pieces one expects in the metric. In addition, it also makes various improvements to the construction, both formal (e.g., a more careful and algorithmic treatment of the matching, allowing us to obtain the perturbations on the holes in the process of matching), and practical (e.g., using coordinates for the perturbed black holes that have no singularity at the holes' horizons from the outset, and implementing the data in freely available MAPLE scripts and C code).

There are still many ways in which the construction could be improved (even neglecting the issues of generalizing the data to include spin and eccentricity, or even iterating to higher order), some of which are discussed in Chap. 2. In particular, the transition functions we use to stitch together the different spacetimes numerically doubtless will require a fair amount of fine-tuning. Nevertheless, the data we have constructed are currently being evolved in two different implementations: George Reifenberger and Wolfgang Tichy (at Florida Atlantic University) are evolving the data we constructed as is, *à la* Kelly *et al.* [65, 66]—i.e., not solving the constraints and evolving using the BAM code [67, 68]. Tony Chu (at Caltech) is evolving just the perturbed black hole metrics, superposed as in Lovelace [69] (i.e., with Gaussian attenuation functions, and flat space everywhere except close to the holes) using the SPEC code [48] and first running the data through a constraint solver. Here the idea is to see how much including the tidal deformations on the holes reduces the high-frequency component of the junk radiation.

Since the paper on which Chap. 2 is based was published, there have been various developments in numerical relativity, data analysis, and, in particular, studies and construction of initial data that deserve comment, which we will make here. (We have made some tacit updates to Chap. 2, particularly in updating references, but have reserved the majority of the discussion to here.)

Concerning the waveform accuracy requirements, Lindblom, Baker, and Owen [54] formulated time-domain versions of the accuracy standards given in Lindblom, Owen, and Browm [53] which can be applied more readily to the output of numerical simulations (and are not overly restrictive). The original standards have been applied in, e.g., [30, 56, 70].

The characteristic wave extraction approaches mentioned above [that extract the waveform at future null infinity by evolving the output of a standard (Cauchy, $3+1$) numerical evolution code along null hypersurfaces] have recently progressed to the point of studying the effects of initial data: Bishop, Pollney, and Reisswig [71] find long-lasting transients in the waveform that they attribute to incoming radiation in both the Cauchy and (standard) characteristic data.

(They also generate characteristic initial data that only contain outgoing radiation, to linear order.)

There has also been progress with other conformally curved initial data constructions. The initial steps in evolving and fine-tuning the other mature PN-based construction (that of Kelly *et al.* [72]) have taken place, with evolutions first reported in [65], and some fine-tuning carried out in [66]. (Reifenberger and Tichy are also currently evolving these data.) And the conformally curved initial data with spin constructed by Lovelace *et al.* [73] has now been evolved through merger and ringdown [45] for two holes with dimensionless spins of 0.95, above the limit of ~ 0.93 imposed by standard (conformally flat) Bowen-York data.

1.3 Elastic deformations of neutron stars

None of the known neutron star binaries are anywhere close to the separations at which their orbital gravitational radiation would be able to be detected by ground-based detectors (though the neutron star binary PSR J0737-3039 is a marginal source for LISA). However, there are scenarios that lead to potentially detectable gravitational waves from isolated neutron stars (or even a single star in a binary—e.g., Sco X-1). These sources are particularly convenient from a data analysis standpoint, since we know exactly where they are on the sky, and even how fast they are spinning (including spindown, glitches, etc.) with very high accuracy, if they are observed as pulsars, or when they experience large perturbations, if they are observed to emit electromagnetic flares. Knowing these quantities helps enormously with reducing the very high computational burden of the search over unknown quantities (e.g., when searching for continuous, periodic emission, the star's inclination angle, the gravitational wave polarization angle, and—in the cases where no pulses are observed—the star's phase evolution), enabling one to search the gravitational wave data more deeply. The LIGO/Virgo searches for continuous periodic emission from known neutron stars are reported in [74, 75, 76, 77, 78], those from unknown stars in [79, 80], and the searches for bursts from magnetars are given in [81, 82, 83].

The scenarios that can generate such gravitational waves all necessarily involve deforming the neutron star in some manner: If one has a non-axisymmetric deformation of a rotating neutron star, one will generate a continuous signal; if the deformation suddenly relaxes, it will emit a burst of gravitational waves. These deformations can be supported either using magnetic fields or elastic stresses—we consider the latter here.

The consideration of such elastic deformations of neutron stars dates back to soon after pulsars were discovered, with Ruderman's suggestion [84] that the glitches (sudden changes in period) observed in many pulsars were due to starquakes in a solid crust. It was quickly realized that the energetics did not allow this mechanism to explain all of the glitches [85], but starquakes are still regarded as a possible mechanism for some glitches, along with the standard model of superfluid vortex unpinning. (These models are reviewed in Sec. 12.4 of [86].) Much of the work on elastic deformations has considered the case of stresses in the crust, generated by the shear modulus of the lattice of ions. However, the resulting maximum quadrupoles and elastic energies are not large enough to be detected by current gravitational wave detectors.

Such large maximum quadrupoles and elastic energy can, however, be generated by a solid phase in the cores of neutron stars. While there is great uncertainty about the properties of

matter at such extreme densities, there are speculative—though theoretically well-motivated—models that predict a substantial shear modulus. This was first appreciated by Owen [87], and has since been explored by several other authors [88, 89, 90].

The hadron–quark hybrid stars first proposed by Glendenning [91, 92] are a particularly attractive possibility. One expects to obtain deconfined quark matter at sufficiently high densities, due to asymptotic freedom, and these densities may be low enough to be attained in stable stars. As realized by Glendenning, there can be a substantial region of coexistence between the hadron and quark phases, the so-called *hadron–quark mixed phase*. Due to the competition between the surface tension and Coulomb force, one expects this mixed phase to form a lattice, which will have a nonzero shear modulus. (This lattice will have the same density-dependent structure seen in the pasta phases of nuclei in the inner crust. We treat this using a continuous dimension parameter, as was first suggested by Ravenhall, Pethick, and Wilson [93].)

This shear modulus was estimated very roughly by Owen [87], with some improvements made by Nayyar [94]. We make a significantly more careful calculation of this shear modulus in Chap. 3. In particular, we include the effects of charge screening (in the Debye model) and the varying dimensionality of the lattice (including the averaging to obtain an effective isotropic shear modulus from the lattice's anisotropic elastic modulus tensor). These were the additions that I had originally intended to include, based upon suggestions from Ben Owen. However, I found that it was also necessary to include the contributions from the change in the volume of the unit cell when shearing lower-dimensional lattices, since these contributions are responsible for stabilizing the lattice for those dimensions (where they also make a significant contribution to the shear modulus). We then calculate this shear modulus for a small selection of equations of state that all lead to a maximum mass compatible with the recent Demorest *et al.* [95] measurement of a $1.97 \pm 0.04\,\mathrm{M}_\odot$ neutron star. (The method we develop for calculating dimensionally continued lattice sums could also be applied to calculations involving the nuclear pasta in the crust, and possibly other, more standard, terrestrial colloidal condensed matter systems. The application to the crustal pasta seems particularly pertinent, due to two very recent papers that discuss possible observable effects, but use very rough models for the shear modulus [96, 97].)

One then wants to translate this shear modulus (or the one in the crust) into a maximum quadrupole deformation or elastic energy for a given star. The standard expression for obtaining such a maximum quadrupole is due to Ushomirsky, Cutler, and Bildsten (UCB) [98], who obtained it in an investigation of the possibility of gravitational wave emission due to an elastically-supported quadrupole limiting the spin period of weakly magnetized neutron stars. UCB derived their expression using a Newtonian first-order perturbation calculation and the Cowling approximation (i.e., neglecting the self-gravity of the perturbation). Except for two works by Haskell *et al.* [88, 99] which drop the Cowling approximation (but are still Newtonian), all calculations of maximum elastic quadrupoles in the literature use the UCB expression for the maximum quadrupole.

In Chap. 4, we develop a Newtonian no Cowling approximation expression that directly generalizes the UCB integral, as opposed to the more involved Haskell *et al.* calculation. In particular, we are able to directly generalize the UCB proof that a uniform maximal strain gives the maximum quadrupole. We find that the UCB estimates of the effect of dropping the Cowling approximation (a $\sim$ 200% increase in the maximum quadrupole moment) are accurate for the hybrid star quadrupoles coming from stresses in the core, but that the Cowling approximation

slightly *overestimates* the quadrupole generated by crustal stresses, in agreement with the result of Haskell, Jones, and Andersson [99].

We then further generalize to the full relativistic case. (The calculation is still first-order perturbative, but that should be a good approximation—the shear modulus is always a small fraction of the star's pressure.) Ben Owen had noticed that using a relativistic local gravity term reduced the maximum quadrupole by about a factor of 2 when using the UCB integral, so I thought that it would be worthwhile to attempt a full relativistic calculation at some point. Upon reading Tanja Hinderer's calculation of relativistic tidal quadrupoles [100], I then realized that the relativistic maximum quadrupole calculation would be a reasonably straightforward generalization of the work I had already done. After performing the calculation, I found that the relativistic maximum quadrupoles can be significantly suppressed, compared with those calculated using the Newtonian expressions, particularly for massive, compact stars. This should be expected: These suppressions have been seen in calculations of tidal and magnetic perturbations of relativistic stars, and come from a combination of an increased effective gravitational field and—primarily—"no-hair" type suppressions due to matching onto the vacuum exterior. (As the exterior spacetime approaches that of a Schwarzschild black hole, it becomes more and more difficult to sustain a static, nonspherical perturbation.)

One of the reasons that people might have avoided performing a relativistic calculation—besides thinking that it might not make a large effect on the result—is concerns about having to deal with the complicated relativistic theory of elasticity. This turns out not to be a problem here. Since we are only concerned with maximum quadrupoles, we can simply use the obvious covariant version of the expressions used by UCB. In fact, we barely use a theory of elasticity at all: The UCB treatment amounts to adding on a generic tracefree contribution to the stress-energy tensor, constrained in magnitude by the material's shear modulus and von Mises breaking strain (which gives the maximum energy density the sheared material can store).

We have not yet made the same careful, relativistic calculations of the maximum elastic energy, only giving rather naïve Newtonian and relativistic calculations here. It would seem that a proper treatment would be straightforward using results for the Hamiltonian of relativistic perturbed stars given in the literature. However, even in the Newtonian case, one cannot apply the standard results directly, due to the distributional nature of the density and pressure perturbations. Attempting to obtain an expression for the energy that does not suffer from these problems will be the subject of future work. In the future, we will also use a more detailed model for the crust's shear modulus.

Of course, we only consider the maximum values of these quantities here. The problem of determining the perturbations expected for the isolated neutron stars in the galaxy is a difficult problem, which we will not address at all here (except to note that neutron stars are expected to be born deformed, due to the violent supernovae that form them). In fact, it seems likely that this will be addressed observationally before it is addressed theoretically.

1.4 Lattice sums, summation formulae, and the regularization of divergent series

Divergent (or conditionally convergent) series arise quite often in physics and mathematics, and require some form of regularization in order to make sense. In particular, the paradigmatic condensed matter lattice sum—the Madelung constant, which gives the electrostatic energy of NaCl—is only conditionally convergent, and many others are actually divergent. (One

can sum the series one obtains for the Madelung constant given by Coulomb's law by "brute force" if one sums on expanding cubes, though the sum on expanding spheres *diverges* in three dimensions, as first shown by Emersleben [101]; see [102] for a more modern discussion. Physically, the sum on expanding cubes is preferable, as discussed in Campbell [103], since NaCl crystals grow in this manner. This dependence on summation method is interpreted as implying that surface effects are important, since the electrostatic force is long range.)

Likely the most famous divergent series in theoretical physics is associated with toy treatments of the Casimir force (a 1-dimensional scalar field model), viz.,

$$1 + 2 + 3 + 4 + \cdots = -\frac{1}{12}. \tag{1.1}$$

(See, e.g., Sec. 6.6 in [104]; this is also used in a simple, nonrigorous calculation of the critical dimension in string theory—see Sec. 2.5 in [105].) These sorts of seemingly absurd equalities involving divergent series were often obtained by virtuoso formal manipulations in the early days of the calculus. In fact, the above summation of the integers is sometimes attributed to Euler in the literature, though I can find no evidence that Euler ever wrote down an expression for this series in particular. However, he did write down results for very closely related series, and obtained the basic result one uses to justify the above evaluation. (Euler's work on divergent series is discussed in Hardy [106].) However, a fully rigorous justification of this result had to wait until Riemann's analytic continuation of the zeta function. Here, one defines

$$\zeta(s) := \sum_{n=1}^{\infty} \frac{1}{n^s}, \quad \mathrm{Re}\, s > 1, \tag{1.2}$$

and then extends to the entire complex plane, except for a pole at $s = 1$, by analytic continuation (using, e.g., Riemann's integral-splitting method, discussed below). One obtains the given expression by noting that $\zeta(-1) = -1/12$. (We shall see another version of this, for a related zeta function, in Appendix E.) This sort of zeta function regularization is a common tool in theoretical physics, and is even applicable to calculations in curved spacetime (see [107]).

In our computation of the lattice sums in Chap. 3, we use a different method of regularization, more well-suited to the numerical computation of such sums, namely that due to Ewald. However, the methods are intimately related. In particular, the method used by Riemann to analytically continue the zeta function uses the imaginary transformation of theta functions (as is discussed, e.g., in Sec. 24 of Bellman [108]). As I (re)discovered, this also underlies the Poisson summation formula used in the Ewald method. [Recall that the Poisson summation formula says that the sum of well-behaved function over a lattice is equal to the sum of the function's Fourier transform over the dual lattice, times a factor associated with the lattice.] In Chap. 5, I give a new proof of this result which allows us to generalize it in various ways; the most important generalization is to the dimensionally continued case. Looking a bit more deeply, these relations are all tied up with the Mellin transform, and how it transforms theta function symmetries to zeta function symmetries. (But note that the proof we give does not use the Mellin transform, unlike most other proofs.) N.B.: In order to regularize series, one uses the Poisson summation formula outside its formal domain of validity; I concentrated on proving the summation formula for nicely behaved functions and have not attempted to make these regularizations rigorous at present.

I discovered the dimensionally continued Poisson summation formula presented in Chap. 5 while dimensionally continuing the Ewald method. The least straightforward portion of this generalization is the dimensional continuation of the lattice sums, but upon consulting Conway and Sloane's book on lattices [109], I realized that the theta series of common lattices were already written in dimensionally continued form. [These theta series are the generating functions for the number of points in the intersection of a lattice (or lattice-like object, e.g., a shifted lattice) and a sphere centered at the origin; i.e., the coefficient of the αth power in the theta series gives the number of points in the intersection of the lattice with a sphere of radius $\sqrt{\alpha}$.] I was then gratified to find that the obvious dimensionally continued Poisson summation formula one obtained using these theta series, the already dimensionally continued Jacobi transformation formula (which converts the theta series of the direct lattice to the theta series of the dual lattice), and the obvious dimensionally continued Fourier transform, was supported by numerical experiments. In fact, there appeared to be a fairly wide variety of theta series-like functions for which the formula was true, not all of which were obviously associated with a lattice, even in integer dimensions.

I wanted to understand this, and could not find anything even tangentially related in the literature at the time, so I played around with the expressions, and eventually realized that the formula was almost trivially true for a Gaussian centered at the origin: In essence, this is because the dimensionally continued Fourier transform still maps Gaussians to Gaussians, and, in the integer dimensional cases, that fact provides the simplest way of obtaining the Jacobi transformation formula from the standard Poisson summation formula. This realization then suggested that I could prove the formula for more general functions using a density argument. Unfortunately, such an argument requires a reasonably strong topology in order to control both direct and dual sums, and I ended up working in the Schwartz topology. This topology [which is the topology of the Schwartz space of rapidly decreasing, smooth (i.e., C^∞) functions] is given by an infinite family of seminorms, instead of a single norm, which leads to some technical difficulties: While using the Schwartz topology made the density argument simple, it was more difficult to characterize the final space of functions for which the proof held (as something other than a closure in the Schwartz topology). It seemed intuitively obvious that this closure was all the even Schwartz functions, and I finally realized that I could prove this using an elegant representation of the Schwartz space as a sequence space, due to Barry Simon [110].

When writing up the result for publication, I finally came across its antecedents, finding that similar results have already been obtained by analytic number theorists. The Poisson summation formula is a standard tool in analytic number theory, and various generalizations have been proposed over the years. A paradigmatic number theory application is due to Voronoi, who realized that one could use the standard (multidimensional) Poisson summation formula to obtain a better bound on the growth of the number of lattice points within a disk with the disk's radius (see [111] for a modern exposition). Voronoi also asked about what sort of other similar summation formulae were true, so his name is often assigned to Poisson summation formula analogues. Modern research relates these analogues to group theory and modular forms, noting that the Jacobi transformation formula is a modular-type transformation. (See [111] for some recent results involving L-functions.) However, while some of these results are similar to ours, none of them are dimensionally continued, and all of them use a different method of proof than our density argument. (While some of the other results are presented in what appears to be a dimensionally continued form, their proof only holds for integer dimensions.)

1.5 Close white dwarf binaries as sources of gravitational and electromagnetic radiation

White dwarfs are by far the least relativistic of all the standard gravitational wave sources: They have compactnesses on the order of 10^{-3} (where a star's compactness is defined as its Schwarzschild radius over its true areal radius, so a Schwarzschild black hole has a compactness of unity). However, they are highly important in their contributions to the low-frequency gravitational wave spectrum. In particular, white dwarf binaries are the only guaranteed sources for any current or proposed gravitational wave detector: There are a handful of white dwarf binaries—the so-called *verification binaries*—whose parameters are sufficiently well-characterized that they are guaranteed sources for LISA [112, 113]. Additionally, a few percent of the $\sim 10^8$ white dwarf binaries estimated to be present in our galaxy will generate a confusion background for low-frequency gravitational detectors, such as LISA: There are expected to be enough binaries with closely-spaced periods (and thus gravitational-wave frequencies) and large enough gravitational wave amplitudes in certain frequency ranges that it will be impossible to resolve all of them (see [114] for an analysis algorithm that can resolve some of these signals).

Estimating this confusion background has been the subject of a fair amount of work using the same binary population synthesis methods used to obtain the figure of $\sim 10^8$ white dwarf binaries (see, e.g., [115, 116, 117] for some recent work). In these methods, one uses some models for the formation of binaries in the galaxy, and evolves them forward in time (with appropriate approximate treatments of all the astrophysics involved in binary evolution, including stellar evolution, mass loss due to winds, accretion, and finally gravitational radiation, when the stars are close enough for it to be important). These models are calibrated using the observed (small—only 52) number of double white dwarfs (plus other binaries containing compact objects).

While there are electromagnetic programs designed to discover more white dwarf binaries, a large survey of such object will likely have to wait for low-frequency gravitational wave detectors, such as LISA, which (at least prior to its redesign) was expected to observe $\sim 10^4$ such binaries. In addition to discovering many white dwarf binaries, LISA will be able to characterize these systems in various ways. In Chap. 6, we consider combining low-frequency gravitational wave measurements of these systems from LISA with standard electromagnetic measurements (of parallax and/or mass function) to obtain the systems' individual masses. (The electromagnetic measurements of the system's position and frequency evolution also improve the accuracy of the gravitational wave data analysis.) Here the geometric parallax (i.e., the shift in a star's apparent position on the sky due to Earth's motion around the Sun) gives a direct measurement of the system's distance with no significant systematics; the astrometry mission GAIA is expected to measure the parallax of many white dwarf binaries. The mass function is obtained spectroscopically and gives a combination of the system's masses and inclination angle (using Kepler's third law). This is not nearly as clean a measurement as the parallax—not only does the system need to have an easy-to-track spectral feature, but for close binaries one has to worry about which portion of the binary emits this spectral feature (e.g., does it come from uniform emission across one of the stars, or a hot spot, disk, or some other nonuniform feature), which can lead to so-called K-corrections of 20% or greater to the mass function. These can be modeled, though doing so introduces further uncertainties.

The gravitational wave (GW) measurements supply the system's inclination angle (from the ratio of the amplitudes of the polarization states) and a different combination of its masses than the mass function provides (scaled by the system's distance) from the overall amplitude of the signal. In addition, the GW measurements also supply another combination of the masses from the amplitudes of one of the next two harmonics. (A small but significant fraction of the signals from the galaxy's population of white dwarf binaries will be strong enough to make measuring the higher harmonics a possibility.) One can thus combine together the GW observations with higher harmonics plus one of the two electromagnetic observations to measure the binary's individual masses. (In practice, the parallax measurement is the only one that gives reasonable accuracies.) Alternatively, one can just use the lowest-order ("quadrupole formula") GW signal combined with both electromagnetic measurements. This method is applicable to many more systems, though a successful measurement relies on getting good control over the statistical and systematic errors associated with the mass function.

We use standard statistical methods (along with models—of varying degrees of accuracy—for the distribution of the binary parameters and the instruments' measurement accuracy) to estimate the accuracy with which one can perform such measurements with LISA and GAIA. We made these calculations before the funding agencies instigated LISA's redesign, and will redo the calculations after the new design is finalized, seeing how much the new design impacts this science. We shall also take this opportunity to revisit and improve some of our models and computational practices. In particular, we shall smooth out the period distribution in our population model, and possibly make other improvements. We might also compare with other models. We shall also revisit our code for computing LISA's high-frequency response and inverting the Fisher matrix, making it more accurate and robust—and possibly also more efficient—by returning to an explicit preconditioning and numerical inversion. Finally, we will likely further investigate the correlations between the parameters. (We had investigated these in the past, noting that the two mass measurements are almost perfectly anticorrelated, but did not find a sufficiently uncorrelated set of parameters when using realistic GAIA errors.)

Our method of measurement is applicable to both of the basic types of white dwarf binaries, viz., ones that are detached (i.e., each star is within its own Roche lobe,[1] so its matter does not interact directly with its companion), and ones that are accreting (AM CVn systems, where one star has overflowed its Roche lobe and its matter accretes onto its companion). This ability to study AM CVn systems is a distinguishing feature of our method: For detached systems, one can contemplate using the dependence of the gravitational wave phase on the system's so-called chirp mass to determine its distance as in the "standard sirens" proposed for use in cosmology [118]; this chirp mass is the same combination of masses that enters into the lowest-order GW amplitude. (An accreting system's frequency evolution will be driven by the effects of mass transfer, not point mass gravitational wave emission.) However, even neglecting the difficulties of determining whether a system is really detached (e.g., the white dwarf binary HM Cnc exhibits a decreasing period even though it is thought to be an AM CVn system, and thus undergoing accretion [119]), this measurement is only applicable to the short-period systems for

[1]The Roche lobes are given by the binary's zero equipotential surface (often calculated in the point mass approximation). Once a star overflows its Roche lobe, its matter is no longer bound to it and can either flow onto its companion or leave the system.

which the system's frequency evolution is large enough to be observed during the mission lifetime of a low-frequency gravitational wave detector (which is nominally typically a few years). And for relatively (optically) bright, nearby systems, the parallactic distance will be far more accurate than the distance obtained from measuring the GW "chirp."

Since we are interested in applying our measurement to AM CVn systems (and, generically, because white dwarfs are not compact), one might be concerned that the standard, point particle GW waveforms will not be applicable. (Here we are only considering the amplitude of the waveform; one knows that the binary's phase evolution will be strongly affected by finite size effects.) We thus estimated finite size effects using the expressions obtained in Appendix F and found that they will not affect this measurement for realistic systems. (We have not yet considered accretion disks—doing so will be a subject for future work, though we naïvely expect that they will not contain enough mass to be worth worrying about.) On the other hand, for very strong signals, and/or more advanced low-frequency detectors, one will be able to make direct measurements of the internal structure of the white dwarfs in a binary. (It is also possible to make this sort of measurement slightly less directly by observing the phase evolution of an eccentric white dwarf binary, where one can measure the apsidal shift induced by the tidal deformations—see [120, 121].)

Chapter 2

Conformally curved binary black hole initial data including tidal deformations and outgoing radiation

"And I suppose that in ten years he [Chandra] will be doing the tenth post-Newtonian." —a senior colleague to one of S. Chandrasekhar's students, quoted in K. S. Thorne's introduction to [122].

By asymptotically matching a post-Newtonian (PN) metric to two perturbed Schwarzschild metrics, we generate approximate initial data (in the form of an approximate 4-metric) for a nonspinning black hole binary in a circular orbit. We carry out this matching through $O(v^4)$ in the binary's orbital velocity v, and thus the resulting data, like the $O(v^4)$ PN metric, are conformally curved. The matching procedure also fixes the quadrupole and octupole tidal deformations of the holes, including the 1PN corrections to the quadrupole fields. Far from the holes, we use the appropriate PN metric that accounts for retardation, which we construct using the highest-order PN expressions available to compute the binary's past history. The data set's uncontrolled remainders are thus $O(v^5)$ throughout the timeslice; we also generate an extension to the data set that has uncontrolled remainders of $O(v^6)$ in the purely PN portion of the timeslice (i.e., not too close to the holes). This extension also includes various other readily available higher-order terms. The addition of these terms decreases the constraint violations in certain regions, even though it does not increase the data's formal accuracy. The resulting data are smooth, since we join all the metrics together by smoothly interpolating between them. We perform this interpolation using transition functions constructed to avoid introducing excessive additional constraint violations. Due to their inclusion of tidal deformations and outgoing radiation, these data should substantially reduce both the high- and low-frequency components of the initial spurious ("junk") radiation observed in current simulations that use conformally flat initial data. Such reductions in the nonphysical components of the initial data will be necessary for simulations to achieve the accuracy required to supply Advanced LIGO and LISA with the templates necessary for parameter estimation.

2.1 Introduction

2.1.1 Motivation and overview of results

At present, several years after the initial breakthroughs in the evolution of binary black hole spacetimes [40, 41, 42], numerical relativity has matured to the point where successful

This chapter is based on N. K. Johnson-McDaniel, N. Yunes, W. Tichy, and B. J. Owen, Phys. Rev. D **80**, 124039 (2009).

binary black hole simulations are now commonplace (see, e.g., [123] for a review). Recent progress in the nonspinning case includes simulations of systems with mass ratios of up to ten to one [124, 125, 126] and longer, more accurate simulations of equal-mass systems [60, 127].

It is now time to consider what improvements need to be made to these simulations so that they are accurate enough to provide gravitational wave detectors such as LIGO [2] with the model waveforms they need to detect and study binary black holes. The accuracy required of such waveforms has been studied by Lindblom, Owen, and Brown (LOB) [53]. Their results imply that current simulations are sufficiently accurate to supply the waveforms necessary for detection with either LIGO or LISA [10]. This conclusion is supported by the Samurai [128] and NINJA [129] projects, which indicate that currently used data analysis pipelines (including some not based on matched filtering) can detect a wide variety of numerical relativity waveforms at comparable levels in stationary Gaussian noise. The Samurai project also performs a more detailed comparison of a subset of waveforms for parameter estimation, and finds that—modulo possible systematic errors in sky position and arrival time—they are all indistinguishable if used for estimation of intrinsic parameters (i.e., not sky position or arrival time) at a signal-to-noise ratio (SNR) of less than 14 (25 if one eliminates the code that disagrees the most with the others).

However, Advanced LIGO may detect binary black hole signals with SNRs of order 100 [53]. According to LOB [53], if a waveform's phase error (suitably averaged in the frequency domain) is less than 0.007 radians, then it is suitable for use in parameter estimation with Advanced LIGO with such an SNR. But even the Caltech/Cornell group's simulations (which are arguably the most accurate yet) have maximum phase errors (in the time domain) of order 0.01 radians or more (see [59, 60] for some discussion of their error budget). Converting such error measures to the criteria of LOB is more subtle than it looks and we do not attempt it here. (See [55] for a discussion of some possible pitfalls, along with suggestions for successful applications of the standards from LOB.) Nevertheless, it seems likely that even the Caltech/Cornell group's simulations may not satisfy the LOB conditions for parameter estimation, at least for binaries whose masses place the worst phase error in the detector's most sensitive frequency band.

All current binary black hole simulations incur some error from the initial data used. These data sets' lack of astrophysical realism is clearly announced by the burst of spurious (or "junk") radiation present at the beginning of these simulations. This junk radiation is also responsible for various deleterious effects on simulations. First, one wastes the computer time required for the spurious radiation to propagate off the computational grid. Second, the system that remains after that time has been perturbed by the spurious radiation. This radiation's most prominent effect is to increase the binary's eccentricity,[1] though it also slightly increases the masses of the holes—see [133]. Additionally, in the unequal-mass or spinning cases, the initial junk radiation is emitted anisotropically, giving the system a small "kick" (see, e.g., [134, 135]). The high-frequency component of the spurious radiation is a particular problem for spectral codes. For instance, the Caltech/Cornell group finds that the high-frequency component of the initial pulse of spurious radiation generates secondary spurious waves that propagate throughout the computational domain for two light-crossing times after the initial junk radiation has exited [59, 60]. (These effects can be reduced—though by no means eliminated—by appropriate choices for the constraint damping parameters [136].)

[1] In practice, the eccentricity can be reduced by various means [130, 131, 132].

Currently employed initial data's omission of significant features of the spacetime can also be seen analytically. Except for occasional tests of initial data (discussed in Sec. 2.1.2), all current simulations use initial data sets that assume *conformal flatness* (i.e., that the spatial metric is a scalar multiple of the flat 3-metric). The assumption of conformal flatness is convenient, since it allows one to get simple, mostly analytic expressions for initial data that exactly solve the constraint equations and include orbiting black holes (see, e.g., [137, 138] for reviews).

In general, these sets are geared either towards the puncture or excision approaches. The majority of the community uses punctures, with initial data stemming from [139]. These data are very flexible, as they contain parameters with which one can directly set the momentum and spin of each hole. For instance, for evolutions with spinning holes, one can simply set these parameters using post-Newtonian (PN) results as in [140, 141, 142, 143]. For nonspinning configurations in a circular orbit, parameter choices based on the assumption of a helical Killing vector [144, 145] are possible as well. The Caltech/Cornell and Princeton groups use excision [146, 147], with initial data constructed using the conformal thin-sandwich method (see, e.g., [148]). These data are slightly harder to construct than puncture data are, since one has to solve a larger number of elliptic equations. However, excision data have the advantage of a direct connection to the isolated horizon formalism [149], which allows one to construct holes with well-defined masses and spins. Additionally, the excision approach is applicable to a wider array of initial data construction methods: It is used in all of the extant evolutions of superposed black hole data sets except for one specifically tailored to the puncture approach. (See Sec. 2.1.2 for a discussion of these evolutions.) The data we present here also require evolutions using excision or the turducken approach [150].

Conformally flat initial data cannot accurately represent some features of a binary black hole spacetime, since the PN metric for a binary system stops being spatially conformally flat at $O(v^4)$, where v is the binary's orbital velocity in units of c, the speed of light (see Sec. 2.4.1 for discussion). The order at which this fundamental disagreement with PN predictions first occurs gives a rough indication of the error committed in using conformally flat initial data. At present, the simulation for which this error is the smallest is the longest of the Caltech/Cornell runs (in [60]), for which $v_{\rm initial} \simeq 0.24$, where $v_{\rm initial}$ is the binary's initial orbital velocity. We expect the initial data's conformal flatness to only affect the waveform at $O(v^4_{\rm initial})$, which for this run is comparable to the phase error allowed for a waveform to be used for parameter estimation with Advanced LIGO. It is thus possible (though perhaps not likely) that conformally flat initial data would be suitable for use in the simulations that will generate such waveforms.

It is unlikely that conformally flat initial data can be used to generate the waveforms required for parameter estimation with LISA. Here the required (appropriately averaged frequency domain) phase accuracy is 2×10^{-4} radians [53], ~ 21 times smaller than $v^4_{\rm initial}$ for the longest of Caltech/Cornell's simulations. One can reduce the error in the initial data by starting the simulation with a larger separation. However, $v^4_{\rm initial} \simeq 2 \times 10^{-4}$ implies an initial (PN coordinate) separation of ~ 71 times the binary's mass, and thus a merger time that is over 400 times as long as the Caltech/Cornell group's longest simulations to date, which start from a (PN coordinate) separation of ~ 15.3 times the binary's mass. It is thus necessary to improve the accuracy of the initial data. Evolutions of more accurate initial data will also give a direct measure of the errors introduced in using current, conformally flat initial data.

This paper provides initial data that include more of the physics present in the binary's spacetime than any previous constructions. (For technical simplicity, we specialize to a non-spinning binary in a circular orbit. However, the construction generalizes straightforwardly to include either eccentricity or spin, though the algebraic complexity increases substantially, and not all the pieces are available in the spinning case to carry out the construction to the same order we have done here—see the discussion in Sec. 2.9.2.) In particular, our data's accurate description of certain properties of the spacetime should substantially reduce *both* components of the aforementioned spurious radiation. These two components are thought to come from different physical effects. The long-wavelength component is thought to correspond to the initial data's lack of outgoing gravitational radiation, whose wavelength would be somewhat longer than the orbital separation. Of course, one expects the junk to be generated predominantly in the strong-field region near the holes, where the binary's gravitational radiation cannot be disentangled from the rest of its gravitational field. However, one also expects the pieces that one wants in the strong-field region to appear at $O(v^4)$, just as the true gravitational waves do in the radiation (or far) zone (defined in Sec. 2.2)—see Sec. 2.4.2 for some discussion. Our data include all the $O(v^4)$ terms in the strong and weak field regions. The short-wavelength component is thought to come from the holes' quasinormal modes ringing down, emitting gravitational radiation with wavelengths on the order of their masses, as they relax from their initial, close to spherical state to their desired tidally deformed state (see, e.g., [59]). Our data include the Newtonian quadrupole and octupole tidal deformations each hole induces on the other, as well as the 1PN corrections to the quadrupole deformations.

The tidal deformations are contained in perturbed Schwarzschild metrics, given (in the horizon-penetrating coordinate system we use) in Eqs. (2.2) and (2.3). The tidal fields are fixed by asymptotically matching these Schwarzschild metrics to an $O(v^4)$ PN metric, given in Eqs. (2.4); expressions for the tidal fields around hole 1 are given in Eqs. (B.1). One also needs to introduce a coordinate transformation in order to put the black hole metrics in the same coordinate system as the PN metric. This transformation is also determined (perturbatively) by the matching; instructions for putting it together around hole 1 are given in Sec. 2.5.7. Instructions for converting all of these results to the region around hole 2 are given at the beginning of Sec. 2.5.1.

The PN metric mentioned above treats retardation perturbatively and thus becomes inaccurate far from the binary. In that region, we thus use a version of the PN metric that includes retardation explicitly (but also uses a multipolar decomposition, so it does not provide the desired accuracy closer to the holes). This metric is given in Eqs. (2.48). Due to retardation, one needs to know the binary's past history accurately in order to obtain the far zone metric accurately far from the binary. This past history is computed in Sec. 2.6.1 to the highest PN order possible with current results. The contributions of these terms are of equal or higher order than some of our uncontrolled remainders, but their inclusion is necessary if one wishes to obtain, e.g., accurate phasing for the outgoing radiation.

We have also added other formally higher-order terms to the metrics, including all the readily available PN results, along with a resummation of the black hole backgrounds in the PN metric. We found that certain of these terms improved the constraint violations in various regions; other of these additional terms are expected to improve evolutions of the data. The resummation is given in Sec. 2.8.1; all the remaining higher-order terms are discussed in Sec. 2.7.

The transition functions that we use to stitch the metrics together smoothly are given in Sec. 2.8.2. These functions satisfy the hypotheses of the two so-called Frankenstein theorems [151]; this guarantees that the resulting initial data will have constraint violations whose formal order is no larger than that of the constraint violations of the initial data obtained from the constituent metrics. In particular, the first theorem guarantees that the merged metric satisfies the Einstein equations to the same formal order as its constituent metrics, provided that the derivatives of the transition functions satisfy certain sufficient conditions (given in Sec. 2.8.2). The second theorem shows that the same conditions are sufficient to guarantee that the differences between an initial data set obtained from the merged 4-metric and one constructed by merging the initial data sets obtained from the constituent 4-metrics are contained in the uncontrolled remainders. (We followed the latter approach in obtaining the initial data used to generate the plots, but it is also possible to use the former approach and obtain initial data from our merged 4-metric directly. We also carried out the requisite differentiation numerically: The expressions for the relevant metrics are too complicated to make analytic expressions for the initial data practicable.) See Appendix D for the technical details of how we compute the metrics.

We have generated MAPLE scripts and C code (available at [152]) that produce initial data for a nonspinning binary in a quasicircular orbit. This binary can, in principle, have any mass ratio and initial separation, though the data will decrease in accuracy as the initial separation decreases, and will also likely lose accuracy as the mass ratio increases. (We expect the latter to occur since there is evidence that the PN approximation converges more slowly for extreme mass ratios than for equal mass ratios—see, e.g., [19, 153]. Additionally, the transition functions we give do not behave quite as well as might be desired for unequal mass systems.) We suggest using initial separations of less than about $10m$ (m is the binary's mass) with caution, and strongly recommend using larger initial separations if at all possible: The data's constraint violations decrease dramatically with increasing initial separation, as illustrated in Figs. 2.12, 2.13, and 2.14; we expect a concomitant increase in the data's physical accuracy. (See Sec. 2.8.3 for further discussion of the constraint violations' scaling with initial separation.)

The constraint violations give a measure of how much more accurate this paper's data are compared with those constructed in previous papers (viz., [63] and [64], which we refer to as Papers I and II). We plot the constraint violations of the three sets of data in Fig. 2.1. [See, e.g., Eqs. (14)–(15) in [137] for expressions for the constraint equations.] N.B.: While the Hamiltonian constraint violations of this paper's data are larger close to the hole than those of either of the previous papers' data, this is due to our inclusion of the full time dependence of the tidal fields, as discussed in Appendix D.1; the motivation for doing this, even at the cost of larger constraint violations, is given in Sec. 2.7. If one does not include these higher-order terms, then the new data's constraint violations are smaller close to the hole than those of either of the previous papers' data. See Fig. 2.17 for a comparison of the constraint violations of the inner zone metric with and without full time dependence in the tidal fields.

For a simple, quantitative comparison of the overall constraint violations, we can consider their L^2 and sup norms. These are presented for all three sets of data in Table 2.1 and show, as expected, that the new data have smaller overall constraint violations than either of the previous papers' data. Of course, the L^2 norm of the new data's Hamiltonian constraint violations is only very slightly less than that of the data from Paper II, but this is probably to be expected: See Sec. 2.8.3 for some discussion of this, as well as further details about the comparison plot and table.

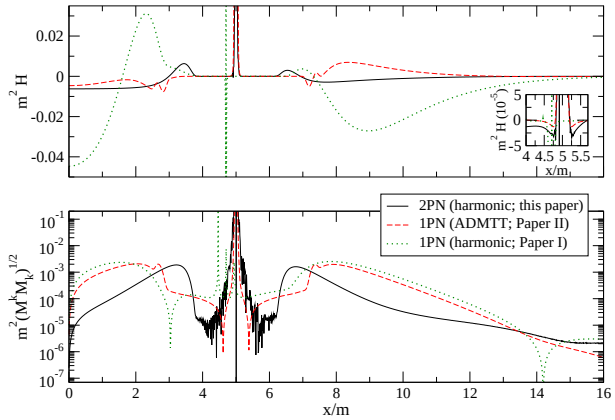

Fig. 2.1. The Hamiltonian constraint and norm of the momentum constraint along the *x*-axis around hole 1 for this paper's data along with the data from Papers I and II. (In the norm of the momentum constraint, the index is raised using the metric in question.) All of these were computed for an equal-mass binary with a coordinate separation of 10 times its total mass, *m*. In the inset, we zoom in to show how the Hamiltonian constraint violations behave close to the horizon. Note that the data from Paper II are in a different coordinate system throughout, and that the black hole background in Paper I's data is in a different (and not horizon penetrating) coordinate system.

2.1.2 Conformally curved initial data

The problems with conformally flat data have inspired a variety of constructions of conformally curved binary black hole data, for which there are two general approaches. One approach—the one we have taken—is primarily motivated by a desire for astrophysical realism, seeing the spurious radiation as an indicator of the failure of conformally flat initial data to model the desired spacetime accurately enough. These constructions so far have restricted their attention to nonspinning binaries and used the PN approximation to include the binary's physics. (Of course, true astrophysical binaries are expected to have significant spins, so the consideration of nonspinning binaries is merely a technical convenience appropriate for initial attempts at constructing astrophysically realistic data.) The other approach is primarily concerned with reducing the junk radiation in practice with relatively simple choices for initial data (viz., a superposition of boosted black holes). This approach is often geared primarily towards spinning black holes, since the amount of spurious radiation increases with the spin of the holes. (This is due to the nonexistence of a conformally flat slicing even of an isolated Kerr black hole with nonzero spin—see [154, 155].)

Besides our present work, other constructions in the first category are this work's antecedents ([62, 63, 64], discussed in the next subsection), along with the approaches of Nissanke [156] and Kelly *et al.* [72]. (The latter two only use the PN approximation in their construction, so the resulting data cannot accurately describe the spacetime near the holes.) Nissanke, building on the work of Blanchet [157] (who constructed initial data for a head-on

	$m^{3/2}\|\|H\|\|_2$ (10^{-2})	$m^2\|\|H\|\|_\infty$ (10^{-2})	$m^{3/2}\|\|\vec{M}\|\|_2$ (10^{-3})	$m^2\|\|\vec{M}\|\|_\infty$ (10^{-3})
This paper	1.565	0.631	2.973	1.879
Paper II	1.566	0.758	4.627	2.065
Paper I	9.149	4.466	5.837	2.531

Table 2.1. The L^2 and sup norms (denoted by $\|\cdot\|_2$ and $\|\cdot\|_\infty$, respectively) of the Hamiltonian and momentum constraints (H and $\vec{M}$) for an equal-mass binary with a coordinate separation of 10 times its total mass, m. (The norms of the momentum constraint include the L^2 3-vector norm $\sqrt{M^k M_k}$, where the index is raised using the metric under consideration.) These are computed along the x-axis outside the unperturbed horizons of the holes but inside the interval $[-16.4m, 16.4m]$.

collision of initially stationary holes), obtains explicit analytic expressions for the 3-metric and extrinsic curvature from the 2PN metric. (N.B.: These constructions only use the version of the PN metric that treats retardation perturbatively, so the resulting data rapidly lose accuracy away from the binary.) Kelly *et al.* [72] extend the work of Tichy *et al.* [158] to give initial data from the 2.5PN ADMTT metric that are valid through $O(v^4)$ wherever the PN approximation is and thus contain the binary's outgoing radiation in the far zone. (See Sec. 2.4.2 for a discussion of why gravitational radiation is present at that order.) In order to obtain these data, they have to evaluate an integral numerically, so their data are not completely analytic.

The most recent progress in the second category for nonspinning black holes is Lovelace's [69] construction and evolution of superposed Schwarzschild data for an orbiting binary. (There is a companion construction and evolution of superposed spinning black hole data for an orbiting binary in Lovelace *et al.* [73]. Additionally, two versions of the spinning data are evolved in head-on collisions in [135].) Lovelace uses the superposed black hole data as free data for a constraint solver and finds that the resulting data produce less spurious radiation than conformally flat data. There are also older constructions in a similar vein [159, 160, 161], though their data have only been evolved in head-on collisions without first solving the constraints [162] and did not reduce the spurious radiation. Hannam *et al.*'s Kerr puncture data [163] have been evolved, and found to reduce the spurious radiation, but they are only applicable to head-on collisions. Neither of the other conformally curved spinning data constructions [164, 165] have been evolved, to our knowledge.

While several of the superposed data sets have been evolved, the only evolution of PN initial data of which we are aware is that of Kelly *et al.* [65]. They evolved the data they obtained in [72] (as well as the original version without waves from [158]) and found that the junk radiation was indeed reduced, compared to standard puncture data. However, as expected, the spurious radiation appears to be unchanged when the waves are added: We expect the junk to be generated primarily near the holes, and both data sets have the same accuracy in the strong field

region. In addition, Kelly *et al.* only find a reduction in the low-frequency component of the spurious radiation. This is again as expected, since their data do not include the tidal deformations on the holes.

As mentioned in the previous subsection, the data set we construct here should help reduce *both* components of the junk radiation, since it includes an accurate description of the spacetime near the holes (including the quadrupole and octupole tidal deformations), matched to the PN metric through $O(v^4)$. We also offer an extension to these data that are accurate through $O(v^5)$ in the PN portions of the timeslice (i.e., not too close to the holes), allowing our data to be compared more directly with Kelly *et al.*'s.

2.1.3 Specifics of our approach and its relation to other work

With currently available technology, if one wishes to generate initial data that include the holes' tidal deformations or the binary's outgoing radiation, it is necessary to allow the initial data (as first constructed) to be merely an approximate solution of the constraint equations. (One can always use these approximate data as free data for a constraint solver and thus obtain an exact solution of the constraints, to numerical precision.) Since the post-Newtonian approximation has been developed to a very high order, it is an obvious choice for the description of the binary's spacetime. Indeed, an explicit expression for the metric to 2.5PN order (with a perturbative treatment of retardation) is given by Blanchet, Faye, and Ponsot (BFP) [166].

However, one cannot obtain accurate initial data throughout a timeslice of the binary's spacetime using just the PN metric, since the PN approximation breaks down near the holes: The PN approximation is a weak-field approximation (due to the post-Minkowskian iteration in powers of G, Newton's gravitational constant), in addition to being a slow-motion approximation (the post-Newtonian expansion proper, which formally proceeds as an expansion in $1/c$, where c is the speed of light). Moreover, the standard PN approximation (as presented, e.g., in BFP) treats retardation perturbatively. It thus becomes inaccurate quite rapidly as one enters the radiation zone (i.e., when one is further than about a reduced gravitational wavelength away from the binary's center of mass).

The resolution of both of these problems is to realize that there is an appropriate approximate description of the spacetime in each of the regions where the standard PN metric breaks down: Near each of the holes, in the regions known as the *inner zones*, spacetime is well described by a perturbed black hole metric. (These zones, as well as the others we mention here, are defined more precisely in Sec. 2.2.) In the radiation zone (or *far zone*) there is another version of the PN metric that incorporates retardation nonperturbatively. These are all readily available in the literature to the order we need them—see Sec. 2.1.3.1 for the details.

One then has to stitch all these spacetimes—the far zone, inner zones, and the *near zone* where the standard PN metric is valid—together into one global approximate metric. (Of course, this metric will be global in space, but not in time—i.e., it will only be accurate in a temporal neighborhood of a timeslice of the binary's spacetime.) This stitching-together proceeds in two steps: First, one uses the technique of matched asymptotic expansions to match the metrics at a formal level. This puts all the metrics in the same coordinate system (up to uncontrolled remainders) and fixes any previously undetermined parameters (e.g., the holes' tidal perturbations) so that the metrics are asymptotic to each other in their regions of mutual validity (the *buffer zones*). The final, numerical merging of the metrics is then effected by *transition functions* that

smoothly interpolate between the metrics in their mutual buffer zones. The resulting merged metric is guaranteed to satisfy the Einstein equations to the same order as its constituent metrics if the transition functions are constructed to satisfy the hypotheses of the so-called Frankenstein theorems [151]. (We check that our transition functions satisfy these hypotheses in Sec. 2.8.3.)

Once one has obtained such approximate initial data, it is, of course, possible to use them as the input to a numerical constraint solver, and thus obtain an exact solution, to numerical precision. In fact, it is probably desirable to do so. The idea when doing this is that if the input to the constraint solver satisfies the constraints and describes the desired physics to some reasonably good tolerance, the "exact" solution one obtains after solving the constraints will not differ too much from the input in its physical content. This is probably true regardless of how one chooses to produce the "exact" solution to the constraints, as long as the procedure modifies the initial guess in a reasonable way. One commonly used procedure is the York-Lichnerowicz decomposition [137]. Both Tichy *et al*. [158] and Pfeiffer *et al*. [167] have implemented this numerically without the assumption of conformal flatness. However, it is unclear exactly how the output from the York-Lichnerowicz procedure (or similar decompositions) relates to its input in physical content. It may thus be preferable to project the approximate initial data onto the closest "point" on the constraint hypersurface (as measured by some appropriate norm), possibly using the results of [168].

If one chooses to evolve without solving the constraints (as did Kelly *et al.* [65]), then one will not have a true vacuum evolution: The constraint violations will act as matter (which may not satisfy any of the standard energy conditions). For instance, Bode *et al.* [169] investigated the evolution of initial data that only approximately satisfied the Hamiltonian constraint (though the momentum constraint was satisfied exactly). They found that the holes accreted the negative Hamiltonian constraint violations that surrounded them, decreasing their masses.

2.1.3.1 Comparisons with similar constructions

All three of the previous constructions of matched initial data restricted their attention to the simplest case of nonspinning holes in a (quasi)circular orbit, as we do here: Alvi [62] made the first attempt, though his data were found to be unsuitable for numerical evolutions [170]. Yunes *et al*. [63] (Paper I) then revisited the problem, correcting various deficiencies in Alvi's method. Yunes and Tichy [64] (Paper II) then obtained a better numerical match (in the sense of smaller constraint violations) by using ADMTT PN coordinates (as opposed to the harmonic coordinates of all the other constructions) and some resummation. They also constructed horizon-penetrating coordinates to provide the first usable initial data constructed using this method. However, in all these cases the initial data are only valid through $O(v^2)$ and the tidal fields are still just the lowest-order quadrupole ones Alvi had obtained.

The present calculation builds on all these previous constructions, computing data that are fully matched through $O(v^4)$, so as to include the pieces of the PN metric that break conformal flatness (and contain gravitational radiation), and reading off the tidal fields from the matching. In addition, we include the radiation zone portion of the metric. This was done explicitly by Alvi and implicitly in Paper II, due to its use of the ADMTT PN metric, though neither of them included the effects of radiation reaction on the binary's past evolution in their far zone metric, as we do. We also employ background resummation (discussed in Sec. 2.8.1) in the

near zone metric, inspired by similar resummations in Paper II. Additionally, we stay in inertial coordinates, while all the previous versions use a corotating coordinate system.

While we only obtain fully matched initial data through $O(v^4)$, we actually have to carry out the matching of the 4-metric through $O(v^5)$ in order to do so: We need to match the $O(v^5)$ pieces of the spatiotemporal components of the 4-metrics in order to obtain the extrinsic curvature consistently [see the discussion after Eq. (2) in Paper I], and one needs to carry out the matching of all the components in order to obtain the $O(v^5)$ piece of the coordinate transformation.

Additionally, while our goal was simply to keep terms of quadrupole order overall in the multipole expansion, as was done previously, we found that it was necessary to match the lowest-order octupole pieces in order to match the 1PN corrections to the quadrupole pieces consistently. This is discussed in Sec. 2.5.1. In fact, we have carried out the matching of quadrupole pieces to the highest possible order to which it can be done consistently without the inclusion of the hexadecapole tidal fields. (These hexadecapole pieces can be included with input from nonlinear black hole perturbation theory, since carried out by Poisson and Vlasov [171].) We also obtained the 1PN correction to the electric octupole and the associated piece of the coordinate transformation as a further application of our matching procedure. However, we could not obtain the other $O(v^4)$ octupole pieces in the initial data (since they include the hexadecapole tidal fields), so our knowledge of these corrections does not allow us to increase the formal order to which our data are valid.

Building on the work done in Paper II, we have used horizon-penetrating coordinates for the black holes from the outset. This requirement of horizon penetration is necessary for numerical purposes. The coordinates need to be regular and the lapse positive in a neighborhood of the horizon: Even though the spacetime near the singularity will be excised or filled with matter, one needs to be able to evolve at least a small portion of the spacetime inside the horizon.

At the same time, we want the coordinates for the black hole and PN metric to agree as closely as possible before the matching has been performed: Close agreement makes for simple matching algebraically and improves the numerical agreement of the resulting matched metrics, as was seen in Paper II. Ideally, the coordinates would agree exactly for an unperturbed black hole, though this is not compatible with the requirement of horizon penetration unless one transforms the PN metric's coordinates: Standard PN coordinates (harmonic or ADMTT) are not horizon penetrating. We decided to avoid the complications such a transformation would entail and thus attempted instead to obtain agreement between the two coordinate systems to as high a PN order as possible.

These desiderata are satisfied if we use the fully harmonic version of Cook-Scheel coordinates [172] for the black hole and standard (PN) harmonic coordinates for the PN metric:[2] Cook-Scheel coordinates are horizon-penetrating, and in their fully harmonic version only differ from PN harmonic coordinates for an unperturbed Schwarzschild black hole at $O(v^4)$. See

[2]We use the term *harmonic coordinates* to refer to *any* coordinates x^α that satisfy $\nabla_\alpha \nabla^\alpha x^\beta = 0$, not just PN harmonic coordinates. (Here ∇_α is the covariant derivative associated with the metric under consideration and indices are raised using that metric.) For an unperturbed Schwarzschild black hole of mass M, PN harmonic coordinates are obtained by transforming the Schwarzschild radial coordinate $\mathcal{P}$ to $R_{\rm PN} = \mathcal{P} - M$ and thus retain the coordinate singularity at the horizon present in Schwarzschild coordinates.

Appendix A for an explicit comparison. This agreement was the best of any of the horizon-penetrating coordinate systems present in the literature we consulted (even if we also consider ADMTT coordinates for the PN metric). Of course, we then adjust this coordinate system perturbatively so that it agrees with the near zone coordinate system to the order we have matched. However, we have checked that this adjustment does not affect the coordinates' horizon penetration.

The other choices for our ingredients were made for computational ease. We selected Detweiler's perturbed black hole metric [173] instead of Poisson's [174] because Detweiler expresses the tidal fields in the Thorne-Hartle-Zhang (THZ) harmonic specialization of locally inertial coordinates [175, 176]. This gauge choice agrees better with the PN metric in harmonic coordinates than does Poisson's light-cone gauge. For the far zone, the results from the direct integration of the relaxed Einstein equations (DIRE) approach were the obvious choice: Pati and Will [177, 178] give an explicit recipe for computing the far zone metric to the order we need it (which, in the extension, is higher than the order to which Alvi [62] gives it), along with all the necessary ingredients (except for a few that can be obtained from Will and Wiseman [179]). Even more conveniently, their expression is in the same (harmonic) coordinate system as BFP's PN metric, so we do not have to determine a coordinate transformation for the matching between the near and far zones. [We have checked explicitly that the near and far zone metrics match through $O(v^5)$ in all components.] One also needs to know the binary's past history in order to obtain the far zone metric accurately, due to retardation: We calculate this in the PN approximation using Blanchet's results [19].

2.1.3.2 Comparison with Taylor and Poisson's determination of the tidal fields

Our method for determining the tidal fields can be compared and contrasted with that employed in the recent calculation by Taylor and Poisson [180]. Most importantly, Taylor and Poisson's aims are more general: Their calculation matches a single nonrotating black hole to an arbitrary 1PN metric (expressed in terms of potentials). Our results extend to higher orders (particularly in the spatial components of the coordinate transformation), but are restricted to the case of a (post-Newtonian) binary in a (quasi)circular orbit. However, the pieces that we both computed agree exactly. See Appendix B.1 for a comparison, including explicit expressions for the tidal fields we obtained.

The details of the calculations share some similarities (e.g., both use THZ coordinates for the perturbation), though the primary methods of determining the tidal fields differ substantially: Most importantly, Taylor and Poisson specialize the coordinate transformation and perform a decomposition of the potentials before matching. Our approach is more "brute force," requiring no such specialization or decomposition, but relying heavily on the computer algebra system MAPLE and the associated tensor manipulation package GRTENSORII [181]. See Sec. 2.5.1 for a detailed presentation of our algorithm.

2.1.4 Structure of the paper

We begin by giving an overview of asymptotic matching in Sec. 2.2 and then present the inner and near zone metrics to be matched in Secs. 2.3 and 2.4, respectively. In Sec. 2.4, we also consider two relevant aspects of the PN metric, viz., conformal flatness breaking and gravitational radiation effects. Next we discuss the specifics of our matching procedure and

read off the matching parameters and coordinate transformation order-by-order in Sec. 2.5. We compute the far zone metric in Sec. 2.6, where we also discuss the PN results we use to obtain the effects of radiation reaction on the binary's evolution. In Sec. 2.7 we give an overview of the construction of an extension of this data set that is valid through $O(v^5)$ in the near and far zones, in addition to including various other higher-order terms. Then we stitch the metrics together numerically in Sec. 2.8, first resumming the near zone metric to improve its strong field behavior (and thus the numerical agreement of the metrics), then constructing transition functions to stitch all the metrics together smoothly, and finally considering the constraint violations of the resulting merged metric. Lastly, we conclude and summarize in Sec. 2.9.

We present various ancillary results and technical details in the appendices: Appendix A compares Cook-Scheel and PN harmonic coordinates. We provide explicit expressions for the tidal fields and some related discussion in Appendix B, along with the calculation of the fourth order pieces of the octupole tidal fields and the polynomial part of the associated coordinate transformation. In Appendix C, we give the details of our calculation of the far zone metric used in the higher-order extension to the data, and in Appendix D the precise details of how the metrics are implemented numerically.

2.1.5 Notation and conventions

Units: We use geometrized units with $G = c = 1$ almost exclusively. (G is Newton's constant and c is the speed of light.) The only exception to this comes when we are describing certain post-Newtonian expansions. Here, in keeping with the standard formal approach to the post-Newtonian approximation (see, e.g., [19]), we shall use G and $1/c$ as convenient bookkeeping parameters. For instance, we may refer to some term as being $O(c^{-n})$, or describe an expansion as proceeding in powers of G, though we shall not display these constants in any other context.

Binary parameters: The binary's orbital velocity is v, its orbital angular velocity is ω, and its coordinate separation is b. The masses of the holes are m_1 and m_2; their total mass is $m := m_1 + m_2$.

Indices: We use the standard convention that Greek letters denote spacetime indices, while lowercase Roman letters denote spatial indices. The uppercase indices A and B label the holes, as well as (by extension) the zones into which we divide the data's timeslice. We use Q to denote a multi-index [see, e.g., the discussion following Eq. (2.14) in Pati and Will [177] for a definition].

Index operations: Except where otherwise noted (e.g., in Secs. 2.4.1, 2.6, and 2.8), spacetime indices are raised and lowered using the Minkowski metric $\eta_{\alpha\beta}$, so spatial indices are raised and lowered using the Kronecker delta δ_{kl}. We may even freely raise and lower spatial indices within expressions for notational convenience, particularly in Sec. 2.4. The summation convention is always in force, and may even be applied to spatial indices that are at the same level, particularly in Sec. 2.6. Parentheses, square brackets, and angle brackets on indices denote symmetrization, antisymmetrization, and the symmetric trace-free projection, respectively. (See, e.g., [24] for explicit expressions for the last of these.) We use vertical bars to exclude indices from these operations. The notation "$+\,(1 \leftrightarrow 2)$" denotes that the preceding expression is to be added to itself with the labels 1 and 2 switched.

Arrays: In addition to the ordinary 3-dimensional Kronecker delta, we also define a "lowered 4-dimensional Kronecker delta," $\Delta_{\alpha\beta} := \mathrm{diag}(1,1,1,1)$. Our conventions for the three- and four-dimensional Levi-Civita symbols ϵ_{klp} and $\epsilon_{\alpha\beta\gamma\delta}$ are that $\epsilon_{123} = \epsilon_{0123} = 1$.

Metrics: As is usual, $\eta_{\alpha\beta}$ denotes the Minkowski metric; our signature is $(-,+,+,+)$. In Secs. 2.4 and 2.5 (and Appendix B) $g_{\alpha\beta}$ denotes the near zone (PN) metric and $h_{\alpha\beta}$ denotes the inner zone (perturbed black hole) metric. In Sec. 2.8.1 and Appendix A, $g_{\alpha\beta}$ (sometimes with decorations) is also used for the unperturbed Schwarzschild metric. In Sec. 2.6 (and the associated Appendix C), $g_{\alpha\beta}$ denotes the far zone metric, and $h_{\alpha\beta}$ its associated metric perturbation.

Coordinates: Cook-Scheel coordinates (used in the inner zone) are $X^\alpha = (T, X^k) = (T, X, Y, Z)$, with $R := \sqrt{X_k X^k}$. PN harmonic coordinates (used in the near and far zones) are $x^\alpha = (t, x^k) = (t, x, y, z)$, with $r := \sqrt{x_k x^k}$; r^α denotes just the spatial coordinates [i.e., $r^\alpha = (0, x^k)$]. Unit vectors are denoted by "hats." For instance, $\hat{t}^\alpha, \hat{x}^\alpha, \hat{y}^\alpha$, and $\hat{z}^\alpha$ are the Cartesian PN coordinate basis vectors corresponding to indices 0, 1, 2, and 3, respectively. We also define "tilded" coordinates $\tilde{x}^\alpha := x^\alpha - (m_2/m) b \hat{x}^\alpha$, $\tilde{x} := x - (m_2/m)b$, $\tilde{r} := \sqrt{\tilde{x}_k \tilde{x}^k}$, and $\tilde{r}^\alpha := r^\alpha - (m_2/m) b \hat{x}^\alpha$. Spatial vectors (or the spatial parts of spacetime vectors) will be denoted either with an arrow or a spatial index.

Norms: The Euclidean norm for spatial vectors is denoted by $\|\cdot\|$ (so, e.g., we could write the definition of R above as $R := \|\vec{X}\|$).

Derivatives: All partial derivatives are taken with respect to harmonic PN coordinates, so $\partial_\alpha := \partial/\partial x^\alpha$. Overdots on the tidal fields denote differentiation with respect to Cook-Scheel time T, but all other overdots denote differentiation with respect to PN harmonic time t. We use the shorthand $\partial_{\alpha\beta} := \partial_\alpha \partial_\beta$.

Order notation: We use $(\cdot)_j$ to denote the coefficient of $(m_2/b)^{j/2}$ in the (asymptotic) power series expansion of its argument. As discussed in Sec. 2.5.1, this includes multipoles through octupole order for $j \in \{2,3\}$ but only through quadrupole order for $j \in \{4,5\}$. (In principle, we include all the multipoles for $j \in \{0,1\}$, since there are only monopole contributions.) Similarly, $(\cdot)_{j,n}$ and $(\cdot)_{j,\le n}$ denote the 2^nth multipole-order and multipoles-up-to-2^n-order pieces of $(\cdot)_j$, respectively.

Polynomial and nonpolynomial parts: The superscripts P and NP denote the polynomial (in $\tilde{x}^\alpha$) and nonpolynomial parts of the object to which they are attached. See Sec. 2.5.1 for a more precise definition of the nonpolynomial part.

References: [63] and [64] will be referred to as Papers I and II, respectively.

2.2 Asymptotic matching

The technique of asymptotic matching is a standard one in the analysis of multiscale and singular perturbation problems, allowing one to relate and combine approximate solutions that are valid on different scales [182]. It has been used in general relativity to obtain, e.g., PN equations of motion—[180] contains the most recent of these calculations—and the radiation zone metric of a binary system [183]. (See Paper I and [180] for further discussion and references.) Here we specialize our discussion to the case of a black hole binary.

A timeslice of a binary black hole spacetime divides naturally into four primary zones and three secondary *buffer zones*: See Fig. 2.2 for an illustration. In practical work, the boundaries of all of these zones are necessarily only given approximately, since we do not currently possess sharp estimates for the error bars of the approximations used to describe this spacetime.

There are two *inner zones* around the black holes, given by $r_A \ll b$, where r_A is the distance from (the point particle associated with) hole A and b is the initial (PN coordinate) separation of the binary: In each of these, the spacetime is well described by a perturbed black hole. Surrounding (and partially overlapping) the inner zones is the *near zone*, where the standard (harmonic coordinate) PN metric is valid—i.e., not too close to the holes, yet not so far away that retardation cannot be treated perturbatively. This is given by $r_A \gg m_A$ and $r \lesssim \lambda\!\!\!^{-}$, where m_A is the mass of hole A, r is the distance from the system's center-of-mass, and $\lambda\!\!\!^{-} = b/2v$ is the reduced characteristic wavelength of the binary's gravitational radiation. Finally, the remainder of the timeslice (including a small amount of the outer portion of the near zone) comprises the *far zone*, given by $r \gtrsim \lambda\!\!\!^{-}$, where retardation can no longer be treated perturbatively, and spacetime is described by a separate PN metric that accounts for this. (N.B.: Different relations were given for the outer edge of the near zone and inner edge of the far zone in Papers I and II, but the ones used here are more accurate.) See Table 2.3 (in Sec. 2.8.2) for numerical values for the boundaries of the zones for a particular equal-mass binary.

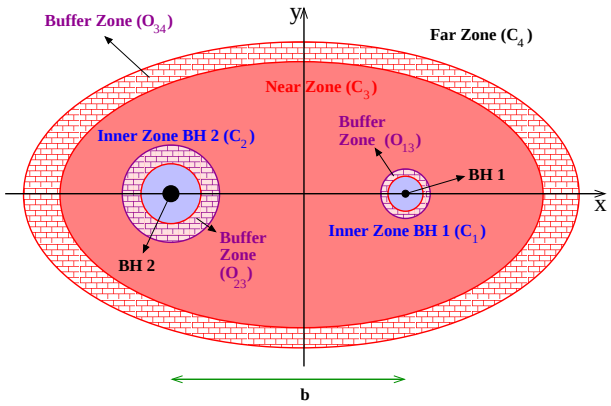

Fig. 2.2. A diagram of the zones into which we divide the binary black hole timeslice. The two black holes (BH 1 and BH 2, denoted by filled-in circles) lie on the x-axis, surrounded by their respective inner zones (C_1 and C_2) and inner-to-near buffer zones (O_{13} and O_{23}). (In actuality, the black holes should be tidally distorted, along with their associated inner and buffer zones. We neglect this distortion in the above diagram for simplicity.) The near zone, C_3, covers the orbit of the binary and is surrounded by the far zone, C_4, and the near-to-far buffer zone, O_{34}.

The three buffer zones are the portions of the timeslice where the preceding four regions overlap. (Due to the "fuzziness" inherent in $\lesssim$ and $\gtrsim$, the near and far zone can have a substantial overlap, despite formal appearances.) We restrict our attention to cases in which the specified zones overlap in the manner we shall describe, but in no other fashion (e.g., we do not want the two inner zones to overlap). There are two buffer zones where the two inner zones overlap the near zone, and are given by $m_A \ll r_A \ll b$. The third buffer zone is given by the intersection of the near and far zones. It is thus very roughly a shell whose radius and thickness are both

of order λ. (The order of the thickness of the shell is our choice—see Sec. 2.8.2: All that is required formally is that it increase as ν decreases, corresponding to a larger realm of validity of the near zone metric's perturbative treatment of retardation. Additionally, as is indicated in the figure, this buffer zone would not be spherical in a more nuanced description.) These buffer zones are where we perform the formal matching that determines the coordinate transformation and relations between parameters as well as where we stitch the metrics together numerically.

This matching and stitching relies on the observation that if the metrics that are valid in the various zones are all to be different approximations to the same (unknown) global exact metric, then, considered as abstract tensors, they should agree with each other in their realms of mutual validity. More specifically, assume that there exists a buffer zone in which two approximate metrics $\mathbf{g}^{(1)}$ and $\mathbf{g}^{(2)}$ are both valid. (We write these metrics without indices to emphasize that they are currently being considered as abstract tensors.) Take their associated small parameters to be ϵ_1 and ϵ_2, respectively. (The buffer zone is then defined to be the region in which these parameters are indeed small.) Then make a bivariate expansion of the metrics in both small parameters. That is, take $\mathbf{g}^{(1)}$, which is already an expansion in ϵ_1, and expand it in ϵ_2 as well; similarly expand $\mathbf{g}^{(2)}$ in ϵ_1. The coefficients of both bivariate expansions, considered as abstract tensors, should then be equal if the metrics describe the same spacetime. The resulting equations relate the parameters of the two metrics.

While the statement of this result in terms of abstract metrics is simple, in practice one works with the metrics' coordinate components. In general, the coordinate systems in which the metrics' components are known will not agree, so one first chooses the coordinate system in which one of the metrics is expressed to be the primary coordinate system. (For us, this will be the near zone's PN harmonic coordinate system.) One then applies an arbitrary coordinate transformation to the other metric in order to put it in the same coordinate system as the first (to the order one matches). Equating coefficients of the bivariate expansions of the components of the metrics (including the coordinate transformation) is then equivalent to equating the coefficients of the expansions of the abstract tensors. In this case, the resulting equations will determine not only the relations between the metrics' parameters, but also the arbitrary coordinate transformation (though there may be some freedom at each order).

2.3 Inner zone metric

In Detweiler's perturbed black hole metric [173], the tidal perturbations are encoded by symmetric trace-free electric and magnetic tidal fields $\mathcal{E}_{kl}$ (electric quadrupole), $\mathcal{E}_{klp}$ (electric octupole), $\mathcal{B}_{kl}$ (magnetic quadrupole), and $\mathcal{B}_{klp}$ (magnetic octupole). These come from the Thorne-Hartle-Zhang (THZ) harmonic specialization of locally inertial coordinates (from [175, 176]), which Detweiler uses to express the perturbation of Minkowski space that his metric approaches in the buffer zone. [N.B.: Detweiler made a tacit gauge transformation away from the pure THZ gauge to obtain the compact expressions for the metric perturbation he gives [184]. This only affects the portion of the perturbation involving the time derivatives of the tidal fields, as can be seen by comparing his Eq. (53) to his Eqs. (56)–(57).]

Detweiler derives his metric under the slow-motion and weak-curvature assumptions of Thorne and Hartle [175]. With these assumptions, the time derivative of a quadrupole field is of octupole order. Since one is only able to include quadrupole and octupole perturbations in linear

black hole perturbation theory, the time dependence of the tidal fields in the metric is restricted to the quadrupole fields, and even there it is only linear.

Detweiler [173] presents the metric perturbation in Schwarzschild coordinates, which we denote by $\mathcal{X}^\alpha = (\mathcal{T}, \mathcal{X}^k)$, with a radial coordinate of $\mathcal{P} := \sqrt{\mathcal{X}_k \mathcal{X}^k}$. He gives the portion involving the quadrupole fields, including their time derivatives (which are actually of octupole order), in his Eqs. (G.6)–(G.11), and the portion with the octupole fields in his Eq. (58). The quadrupole tidal fields depend (linearly) on the null ingoing Eddington-Finkelstein coordinate $V := \mathcal{T} + \mathcal{P} + 2M \log(\mathcal{P}/2M - 1)$. (The octupole fields are treated as constants, since their time derivatives are of hexadecapole order.) We have converted his metric to the quasi-Cartesian form of Cook-Scheel harmonic coordinates (from [172]), which we denote by $X^\alpha = (T, X^k)$, with $R := \sqrt{X_k X^k}$. The transformation is given by

$$\mathcal{T} = T - 2M \log\left|\frac{R-M}{R+M}\right|, \qquad \mathcal{X}^k = \left[1 + \frac{M}{R}\right] X^k, \tag{2.1}$$

so $\mathcal{P} = R + M$. Here M is the mass of the hole. This comes from Cook and Scheel's Eqs. (20), (41), and (43) upon noting that Boyer-Lindquist coordinates reduce to Schwarzschild coordinates for a Schwarzschild hole. (This transformation is for an unperturbed black hole, so the resulting metric will not be in harmonic coordinates, in general, even though the perturbation is in asymptotically harmonic coordinates.) The resulting line element (including the unperturbed Schwarzschild metric) is

$$\begin{aligned} h_{\alpha\beta} dX^\alpha dX^\beta = {} & -H_{T^2} dT^2 + H_{RT} dR dT + \frac{16}{3}\frac{M^2}{R}\left\{1 + \frac{M}{R} - \frac{2}{3}\frac{M^2}{R^2}\left[1 - \frac{M}{R+M}\right]\right\} \dot{C}_{klp} X^l X^p dX^k dT \\ & + H_k^{[1]} dX^k \left[\left(1 - \frac{M^2}{R^2}\right) dT - 4\frac{M^2}{R^2} dR\right] + H_k^{[2]} dX^k dR + H_{R^2} dR^2 + H_{\mathrm{trc}} dX_s dX^s \\ & + O(R^4/\mathcal{R}^4), \end{aligned} \tag{2.2}$$

where

$$H_{T^2} := \frac{R-M}{R+M} + \left[1 - \frac{M}{R}\right]^2 \left[(\mathcal{E}_{kl} + T\dot{\mathcal{E}}_{kl}) X^k X^l + \frac{1}{3}\mathcal{E}_{klp} X^k X^l X^p\right] + \frac{4M^2}{(R+M)^2}\left[R - \frac{5}{3}\frac{M^2}{R}\right]\dot{\mathcal{E}}_{kl} X^k X^l, \tag{2.3a}$$

$$\begin{aligned} H_{RT} := {} & \frac{8M^2}{(R+M)^2} + 8\frac{M^2}{R^2}\frac{R-M}{R+M}\left[(\mathcal{E}_{kl} + T\dot{\mathcal{E}}_{kl}) X^k X^l + \frac{1}{3}\mathcal{E}_{klp} X^k X^l X^p\right] - \left[\frac{4}{3}R + \frac{14}{3}M + \frac{8}{3}\frac{M^2}{R}\right. \\ & \left. - 2\frac{M^3}{R^2} - \frac{104}{3}\frac{M^4}{R^2(R+M)} + \frac{80}{3}\frac{M^5}{R^2(R+M)^2} + \frac{32}{3}\frac{M^6}{R^2(R+M)^3}\right]\dot{\mathcal{E}}_{kl} X^k X^l, \end{aligned} \tag{2.3b}$$

$$H_k^{[1]} := \frac{2}{3}\left[1 + \frac{M}{R}\right]\left[2(C_{klp} + T\dot{C}_{klp}) X^l X^p + \left(1 - \frac{1}{3}\frac{M}{R}\right) C_{klps} X^l X^p X^s\right], \tag{2.3c}$$

$$H_k^{[2]} := \left[\frac{R}{3} + 2M + \frac{16}{3}\frac{M^2}{R} + \frac{26}{3}\frac{M^3}{R^2} - 11\frac{M^4}{R^3} - \frac{32}{3}\frac{M^5}{R^3(R+M)} - \frac{64}{9}\frac{M^6}{R^3(R+M)^2}\right]\dot{C}_{klp} X^l X^p, \tag{2.3d}$$

$$H_{R^2} := \sum_{n=1}^{3}\left(\frac{2M}{R+M}\right)^n - \frac{2M}{R} - \frac{M^2}{R^2} + \left[2\frac{M}{R} + 3\frac{M^2}{R^2} - \frac{M^4}{R^4} - \frac{16M^4}{R^2(R+M)^2}\right](\mathcal{E}_{kl} + T\dot{\mathcal{E}}_{kl})X^kX^l$$
$$+ \left[\frac{1}{3}\frac{M}{R} + \frac{1}{3}\frac{M^2}{R^2} - \frac{2}{5}\frac{M^3}{R^3} - \frac{7}{15}\frac{M^4}{R^4} - \frac{1}{15}\frac{M^5}{R^5} - \frac{16}{3}\frac{M^4}{R^2(R+M)^2}\right]\mathcal{E}_{klp}X^kX^lX^p + \left[\frac{16}{3}\frac{M^2}{R}\right.$$
$$+ \frac{80}{3}\frac{M^3}{R^2} + 28\frac{M^4}{R^3} + \frac{40}{3}\frac{M^5}{R^4} - \frac{176}{3}\frac{M^6}{R^4(R+M)} + \frac{72M^7}{R^4(R+M)^2} - \frac{32}{3}\frac{M^8}{R^4(R+M)^3}$$
$$\left. - \frac{32}{3}\frac{M^9}{R^4(R+M)^4}\right]\dot{\mathcal{E}}_{kl}X^kX^l, \tag{2.3e}$$

$$H_{\rm trc} := \left[1+\frac{M}{R}\right]^2\left[1 - \left(1 + 2\frac{M}{R} - \frac{M^2}{R^2}\right)(\mathcal{E}_{kl} + T\dot{\mathcal{E}}_{kl})X^kX^l - \frac{1}{3}\left(1 + \frac{M}{R} - \frac{M^2}{R^2} - \frac{1}{5}\frac{M^3}{R^3}\right)\right.$$
$$\left. \times\, \mathcal{E}_{klp}X^kX^lX^p - 4\frac{M^2}{R^2}\left(R + 2M - \frac{2}{3}\frac{M^2}{R+M}\right)\dot{\mathcal{E}}_{kl}X^kX^l\right], \tag{2.3f}$$

and $\mathcal{R}$ is a length scale characterizing the strength of the perturbation (see Thorne and Hartle [175] for further discussion). We have defined $C_{klp} := \epsilon_{kls}\mathcal{B}^s{}_p$ and $C_{klps} := \epsilon_{klu}\mathcal{B}^u{}_{ps}$, for convenience, as the magnetic tidal fields only appear in the perturbation in these dual forms. Here ϵ_{klp} is the 3-dimensional Levi-Civita symbol, with $\epsilon_{123} = 1$.

We include the $\dot{\mathcal{B}}_{kl}$ contributions here, even though they do not increase the formal accuracy of our initial data: We fix the lowest-order piece of $\dot{\mathcal{B}}_{kl}$ when we read off the 1PN correction to the electric octupole (in Appendix B.2) as an application of our matching procedure. Additionally, we have used the fact that $\mathcal{E}_{kl}$ and C_{klp} only depend linearly on V (to the multipolar order we are considering) to express their T-dependence explicitly (where the logarithm in the definition of V cancels one appearing in the Schwarzschild coordinate expression for the metric): An overdot denotes a derivative with respect to T, and all the symbols for the tidal fields denote constants, so, e.g., $\mathcal{E}_{kl}$ and $\dot{\mathcal{E}}_{kl}$ are treated formally as independent tidal fields, despite the notation. That is, $\mathcal{E}_{kl}$ just denotes the constant part of $\mathcal{E}_{kl}(T) = \mathcal{E}_{kl} + T\dot{\mathcal{E}}_{kl}$. Finally, despite appearances, this expression for the metric is in fact in a quasi-Cartesian form: dR should just be considered a shorthand for $X_k dX^k/R$.

2.4 Near zone metric

We take the harmonic coordinate metric from Eqs. (7.2) in Blanchet, Faye, and Ponsot (BFP) [166] and specialize it to a circular orbit, obtaining

$$g_{00} + 1 = \frac{2m_1}{r_1} + \frac{m_1}{r_1}[4v_1^2 - (\hat{n}_1\cdot\vec{v}_1)^2] - 2\frac{m_1^2}{r_1^2} - m_1m_2\left[\frac{2}{r_1r_2} + \frac{r_1}{2b^3} - \frac{r_1^2}{2r_2b^3} + \frac{5}{2r_2b}\right] + (1\leftrightarrow 2) + O(v^6), \tag{2.4a}$$

$$g_{0k} = -\frac{4m_1}{r_1}v_1^k - \left\{\frac{m_1^2}{r_1^2}(\hat{n}_1\cdot\vec{v}_1) + 4\frac{m_1m_2}{S^2}[4(\hat{n}_2\cdot\vec{v}_1) - 3(\hat{n}_2\cdot\vec{v}_2)]\right\}n_1^k - 4m_1m_2\left\{\frac{\hat{n}_1\cdot\vec{v}_1}{b^2} - 3\frac{\hat{n}_1\cdot\vec{v}_1}{S^2}\right\}$$
$$\times n_{12}^k + \left\{2\frac{m_1}{r_1}[(\hat{n}_1\cdot\vec{v}_1)^2 - 2v_1^2] + \frac{m_1^2}{r_1^2} + \frac{m_1m_2}{b^3}[3r_1 - 2r_2] - \frac{m_1m_2}{b}\left[\frac{r_2^2}{r_1b^2} + \frac{3}{r_1} - \frac{8}{r_2} + \frac{4}{S}\right]\right\}$$
$$\times v_1^k + (1\leftrightarrow 2) + O(v^6), \tag{2.4b}$$

$$g_{kl} - \delta_{kl} = \left\{2\frac{m_1}{r_1} - \frac{m_1}{r_1}(\hat{n}_1\cdot\vec{v}_1)^2 + \frac{m_1^2}{r_1^2} + m_1m_2\left[\frac{2}{r_1r_2} - \frac{r_1}{2b^3} + \frac{r_1^2}{2r_2b^3} - \frac{5}{2r_1b} + \frac{4}{bS}\right]\right\}\delta_{kl}$$
$$+ 4\frac{m_1}{r_1}v_1^kv_1^l + \frac{m_1^2}{r_1^2}n_1^kn_1^l - m_1m_2\left[\frac{4}{S^2} + \frac{4}{bS}\right]n_{12}^kn_{12}^l + 4\frac{m_1m_2}{S^2}\left[n_1^{(k}n_2^{l)} + 2n_1^{(k}n_{12}^{l)}\right] \tag{2.4c}$$
$$+ 8\frac{m_1m_2}{b^2}n_{12}^{(k}v_{12}^{l)} + (1\leftrightarrow 2) + O(v^6).$$

(N.B.: We use more of the metric than we give here in the `05` and `all` data sets, discussed in Sec. 2.7. In fact, the `all` data set includes the full metric that BFP present. We have chosen to only present the portion of the metric that we use in the matching, doing so for reference and to fix notation.) Here $\vec{x}_A(t)$, $A\in\{1,2\}$ denotes the position of (the point particle associated with) hole A.[3] Thus $\vec{r}_A := \vec{x} - \vec{x}_A(t)$ gives the displacement from hole A, with $r_A := \|\vec{r}_A\|$ giving the distance from hole A and $\hat{n}_A := \vec{r}_A/r_A$ the associated unit vector. Similarly, $\vec{v}_A := \dot{\vec{x}}_A$ denotes the velocity of hole A. The displacement vector from hole B to hole A is given by $\vec{r}_{AB} := \vec{r}_A - \vec{r}_B$, with an associated unit vector of $\hat{n}_{AB} := \vec{r}_{AB}/\|\vec{r}_{AB}\|$. Thus, specializing to a (quasi)circular orbit, $\|\vec{r}_{12}\| = b$, where b is the separation of the holes and is therefore constant up to orbital shrinkage (which we can neglect when performing the matching, given the order to which we are calculating, though we include it when implementing the metrics numerically—see Sec. 2.6.1). Additionally, we shall usually use the shorthand $\vec{b} := \vec{r}_{12}$. (We do not use it in the above expression for the metric since $\vec{r}_{12}$ changes sign under $1\leftrightarrow 2$, while $\vec{b}$ does not.) Similarly, $\vec{v}_{AB} := \vec{v}_A - \vec{v}_B$; we also have $S := r_1 + r_2 + b$. Finally, the notation "$+(1\leftrightarrow 2)$" denotes that the preceding expression is to be added to itself with the labels 1 and 2 switched.

For a circular orbit, we have $\ddot{\vec{b}} = -\omega^2\vec{b}$, by definition, where

$$\omega = \sqrt{\frac{m}{b^3}}\left[1 + \frac{m}{2b}(\eta - 3) + O\left(\frac{m^2}{b^2}\right)\right] \tag{2.5}$$

is the (harmonic coordinate) angular velocity [obtained from Eq. (8.6) in [166]], and $\eta := m_1m_2/m^2$ is the symmetric mass ratio. Since we assume a (quasi)circular orbit, the separation vector of the point particles is orthogonal to their velocities up to $O(v^5)$ radiation reaction effects. We have thus taken $\hat{n}_{12}\cdot\hat{v}_1 = \hat{n}_{12}\cdot\hat{v}_2 = \hat{n}_{12}\cdot\hat{v}_{12} = O(v^5)$ in obtaining the expression for the metric given in Eqs. (2.4). We take the explicit expression for the orbit to be $\vec{b} = b(\hat{x}\cos\omega t + \hat{y}\sin\omega t)$. From the definition of the center-of-mass coordinates used in the PN metric, the positions of (the

[3] We shall henceforth refrain from belaboring the distinction between the PN point particles and true black holes, except where we feel that it is important to emphasize this point.

point particles associated with) the holes are given, to the order we need them, by

$$\vec{x}_1 = \frac{m_2}{m}\vec{b}, \qquad \vec{x}_2 = -\frac{m_1}{m}\vec{b}. \tag{2.6}$$

[For a circular orbit, the first PN corrections to these are $O(v^4)$ and are thus not needed here.] The expressions for the holes' velocities are obtained by taking a time derivative.

2.4.1 The PN metric and conformal flatness

At $O(v^4)$, the spatial PN metric is no longer conformally flat: That is, there does not exist a coordinate system in which the 3-metric can be written as $g_{kl} = \Psi\delta_{kl}$. This can be guessed from a cursory inspection of the PN metric, as nondiagonal spatial components first appear at $O(v^4)$, but was established more firmly in [185], and then further studied in [186]. In both cases, this result was an offshoot of a comparison of the predictions of a post-Newtonian analysis of the Isenberg-Mathews-Wilson (IMW) approximation [187, 188] with those of the full PN approximation: They were found to differ starting at $O(v^4)$. Such a comparison gives the desired result because the IMW approximation assumes spatial conformal flatness (along with maximal slicing—i.e., a vanishing trace of the extrinsic curvature) in an attempt to remove the dynamical degrees of freedom from the gravitational field.

It is also possible to demonstrate this lack of spatial conformal flatness directly, and we shall do so here. In four or more dimensions, the Weyl tensor settles questions of conformal flatness: It vanishes if and only if a space is conformally flat [189]. However, in three dimensions the Weyl tensor vanishes identically, and its analogue for settling questions of conformal flatness is the Bach or Cotton-York tensor, C_{kl}. This is defined (with indices raised by the 3-metric) by

$$C_{kl} := 2\epsilon_k{}^{ps}\nabla_s R_{lp} - \frac{1}{2}\epsilon_{kl}{}^{p}\nabla_p R. \tag{2.7}$$

Here ∇_k, R_{kl}, and R are, respectively, the (three-dimensional) covariant derivative, Ricci tensor, and Ricci scalar associated with g_{kl}. In fact, the nonvanishing of the Cotton-York tensor is a necessary and sufficient condition to render its associated 3-metric non-conformally flat [189, 154] (for a proof, see Chap. VI, §5 in [190]).

We have computed the $O(v^4)$ pieces of this tensor symbolically (using MAPLE and GRTENSORII) for the PN spatial metric, and verified that certain components are nonvanishing at various points of the timeslice. As an illustration, we have plotted the lowest-order piece of the norm of the Cotton-York tensor, $\sqrt{\delta^{kp}\delta^{ls}C_{kl}C_{ps}}$ along the axis passing through the holes in Fig. 2.3 for the standard equal-mass test system of $m_1 = m_2 = m/2$, $b = 10m$. As expected, the values are largest in the region around the holes, showing that this is the region in which the largest perturbation would be required to make the 2PN metric conformally flat.

There is, however, a more intuitive way of understanding the breaking of spatial conformal flatness of the PN metric (here returning to the ADMTT slicing). This approach relates explicitly to the failure of the PN metric to be manifestly conformally flat at $O(v^4)$ and comes

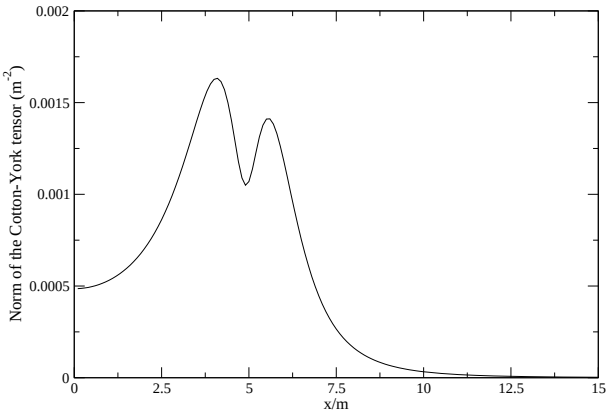

Fig. 2.3. The norm of the Cotton-York tensor for the test system $m_1 = m_2 = m/2$, $b = 10m$ along the x-axis (i.e., the axis passing through both holes). (We only show it around hole 1 because it is symmetric about $x = 0$.)

from the work of Nissanke [156].[4] From the study of PN theory in the canonical ADM formalism [192], one knows that the PN metric can be rewritten as

$$g_{kl} = \Psi\delta_{kl} + h_{kl}, \tag{2.8}$$

where Ψ is some conformal factor, while h_{kl} is not proportional to the flat metric. In fact, h_{kl} must be symmetric and trace-free and contains a piece that is proportional to

$$\frac{\partial^2}{\partial x_1^{\langle k}\partial x_2^{l\rangle}} \log S, \tag{2.9}$$

where S was defined in the above discussion of the metric, and the angle brackets stand for the symmetric trace-free projection. [See, e.g., Eq. (3.1) in [156]; we have left off pieces of the form $v_1^{<k}v_1^{l>}$.] This is clearly not a manifestly conformally flat contribution to the metric, so we can use it to connect with the heuristic that "the 2PN metric is not spatially conformally flat because it contains various pieces that are not manifestly conformally flat."

To do so, we shall demonstrate how the presence in h_{kl} of the term given in Eq. (2.9) prevents the obvious sort of coordinate transformation from rendering g_{kl} conformally flat. For the purposes of illustration, we take our coordinate transformation to be of the form $x^k \to x'^k = x^k + \xi^k$, where $\xi^k = O(v^4)$, and ask that it remove the h_{kl} piece from the 3-metric. (Of course, in general the coordinate transformation would just need to turn h_{kl} into a scalar multiple of δ_{kl}, and would not have to be of the form above, but our assumptions suffice for a heuristic argument.) Thus, ξ^k should satisfy

$$\partial_{(k}\xi_{l)} = -\frac{1}{2}h_{kl}, \tag{2.10}$$

[4] This argument was suggested to one of us by Luc Blanchet [191].

but this equation has no solution when the right-hand side is given by Eq. (2.9). To show that this is the case, it is sufficient [by the gauge invariance of the linearized Riemann tensor—see the discussion surrounding Eq. (2.15)] to show that the (three-dimensional) flat space linearized Riemann tensor associated with h_{kl} does not vanish. We have computed this tensor [with h_{kl} given by Eq. (2.9)] and verified that several components are indeed generically nonzero.

2.4.2 Gravitational radiation in the PN metric

The order at which the effects of gravitational radiation appear in the PN metric is different for different effects, which can easily lead to confusion. We thus offer a brief discussion of these orders here. To avoid even further confusion, since we shall discuss some pieces that are not dimensionless, we shall describe all orders in terms of the formal slow motion expansion in $1/c$, as do Blanchet, Faye, and Ponsot (BFP) [166]. [Since the metric is dimensionless, an $O(c^{-n})$ contribution to it can be unambiguously identified as being $O(v^n)$.] It is well known that the effects of gravitational radiation reaction first enter the equations of motion at $O(c^{-5})$ for a circular orbit. [See, e.g., Eq. (189) in Blanchet [19].] This is also the leading order of the binary's gravitational wave luminosity. [See, e.g., Eq. (171) in Blanchet [19].] However, the lowest-order "quadrupole formula" piece of the gravitational waveform appears in the PN far zone metric at one order lower, viz., $O(c^{-4})$. This can be seen in Blanchet's Eq. (238) [19]; his x variable (not to be confused with our x-coordinate) is $O(c^{-2})$. The explanation for the factor-of-c discrepancy is given by Blanchet in [193].

Our initial data will thus contain at least the lowest-order piece of the binary's outgoing gravitational radiation (whether one uses the extension that adds on various higher-order terms or not), since we have included all the $O(v^4)$ pieces in the spatial metric, along with the matching $O(v^5)$ pieces in the extrinsic curvature. In fact, one can see the lowest-order piece of the waveform explicitly in our expression for the far zone spatial metric in Eq. (2.48c): The relevant terms are the final two in the curly brackets. [These terms are presented in Eqs. (6.10) and (6.11a) of [179] in a form that allows for a more direct comparison with our expression, though without the explicit factors of c^{-1} that Blanchet provides.]

2.5 The matching calculation

2.5.1 The setup

By symmetry, we can concentrate on performing the matching around hole 1: The transformed metric around hole 2 can be obtained from that around hole 1 by taking $m_1 \leftrightarrow m_2$ and making the coordinate transformation $(t, x, y, z) \to (t, -x, -y, z)$ (i.e., rotating by π radians about the z-axis).

Since our matching calculation will determine the coordinate transformation, the relations between the metrics' mass parameters, and the inner zone metric's tidal fields, we need to posit expansions for all of these. For the coordinate transformation, we make nearly the same ansatz as in Papers I and II, viz.,

$$X^\alpha(x^\beta) = \sum_{j=0}^{5} \left(\frac{m_2}{b}\right)^{j/2} (X^\alpha)_j (x^\beta) + O(v^6). \tag{2.11}$$

(This is slightly more general than the ansatz used in the previous papers because we do not fix the zeroth order coordinate transformation from the outset.) We choose $\sqrt{m_2/b}$ as our expansion parameter because it makes for slightly simpler notation than either $v = \sqrt{m/b}$ or $\sqrt{m_1/b}$ when expanding in the buffer zone around hole 1, as we are doing here. We can make this choice without loss of generality: The resulting coordinate transformation will be the same regardless of which of these three possibilities we choose to use as our expansion parameter, though the coefficients of the expansion parameter will differ by ratios of the masses. As in the previous papers, we implicitly assume that $(X_\alpha)_j$ is a power series in $\tilde{r}/b$, including negative powers—i.e., a Laurent series—so we can write, e.g., $m_2/\tilde{r} = (m_2/b)(b/\tilde{r})$. However, $(X_\alpha)_j$ should not depend on m_2/b, by definition.

We also need to worry about the multipole expansion of each $(X_\alpha)_j$. This would seem to be straightforward, since we only want to keep terms through quadrupole order overall. However, the structure of the inner zone metric creates some complications: In order to obtain data that include all the quadrupole $[O([\tilde{r}/b]^2)]$ pieces at fourth and fifth orders,[5] one needs to obtain the octupole $[O([\tilde{r}/b]^3)]$ pieces of the coordinate transformation when matching at second and third orders. This is due to the appearance of $b/\tilde{r}$ terms in $(h_{\alpha\beta})_j$ for $j \geq 2$. These enter the fourth and fifth order coordinate transformation equations, where they multiply the second and third order pieces of the coordinate transformation and thus produce quadrupole contributions from octupole pieces of the coordinate transformation. The octupole fields themselves also enter, as they are multiplied by $b/\tilde{r}$ in the fourth and fifth order pieces of the inner zone metric.

This increase in the number of multipoles that have to be kept as one proceeds to higher and higher orders in v is a general feature of the matching of these two metrics. It is thus a source of significant technical difficulty: One would need to include the hexadecapole pieces in the matching calculation if one wanted to include all of the quadrupole pieces at sixth and higher orders. This follows since at sixth order the hexadecapole pieces start to be multiplied by $b^2/\tilde{r}^2$, making them of quadrupole order. (It would still be possible to, e.g., obtain all the dipole-and-lower pieces at sixth order if one had an expression for the near zone metric through sixth order, but one would not be able to include any new higher-order corrections to the tidal fields this way.)

We posit the same expansion in $\sqrt{m_2/b}$ for the mass parameter of the inner zone metric, M_1, as we did for the coordinate transformation, so

$$M_1 = \sum_{j=0}^{3} \left(\frac{m_2}{b}\right)^{j/2} (M_1)_j + O(v^4). \tag{2.12}$$

However, it will turn out that we did not need to allow this freedom, as we shall find that the mass parameters of the two metrics agree to the highest order to which our matching fixes them—i.e.,

[5] We count orders using our primary expansion in v (or, equivalently, $\sqrt{m_2/b}$).

$M_1 = m_1 + O(v^4)$. Similarly, we asymptotically expand the tidal fields in $\sqrt{m_2/b}$, so

$$\mathcal{E}_{kl} = \frac{m_2}{b^3}\sum_{j=0}^{3}\left(\frac{m_2}{b}\right)^{j/2}(\bar{\mathcal{E}}_{kl})_j + O(v^6), \qquad \mathcal{B}_{kl} = \left(\frac{m_2}{b}\right)^{3/2}\frac{1}{b^2}\sum_{j=0}^{2}\left(\frac{m_2}{b}\right)^{j/2}(\bar{\mathcal{B}}_{kl})_j + O(v^6),$$

$$\dot{\mathcal{E}}_{kl} = \frac{m_2}{b^3}\sum_{j=1}^{2}\left(\frac{m_2}{b}\right)^{j/2}(\dot{\bar{\mathcal{E}}}_{kl})_j + O(v^5), \qquad \dot{\mathcal{B}}_{kl} = \left(\frac{m_2}{b}\right)^{2}\frac{1}{b^2}(\dot{\bar{\mathcal{B}}}_{kl})_1 + O(v^5),$$

$$\mathcal{E}_{klp} = \frac{m_2}{b^4}\sum_{j=0}^{2}\left(\frac{m_2}{b}\right)^{j/2}(\bar{\mathcal{E}}_{klp})_j + O(v^5), \qquad \mathcal{B}_{klp} = \left(\frac{m_2}{b}\right)^{3/2}\frac{1}{b^3}\sum_{j=0}^{1}\left(\frac{m_2}{b}\right)^{j/2}(\bar{\mathcal{B}}_{klp})_j + O(v^5). \tag{2.13}$$

[The expansions of the duals of the magnetic fields—e.g., C_{klp}—are defined analogously. Additionally, the tidal fields and their time derivatives—e.g., $\mathcal{E}_{kl}$ and $\dot{\mathcal{E}}_{kl}$—are treated as formally independent.] The overbars on the tidal fields appearing in the right-hand sides of these expressions indicate that we have taken out the fields' overall scaling, as given in, e.g., Eqs. (2.1) and (2.2) in [180] (though we take the time derivatives of the tidal fields to scale the same way as the fields themselves when doing this, for clarity). We do not include the $O(v^5)$ pieces of the octupole tidal fields here because we did not fix them in the matching: We only had to match the octupole fields through $O(v^3)$ to obtain initial data with formal uncontrolled remainders of $O(v^5)$ and $O([\tilde{r}/b]^3)$ (i.e., octupole order). We also chose to read off the $O(v^4)$ pieces of the octupole fields separately (in Appendix B.2), but did not do so for the $O(v^5)$ parts.

In order to read off the matching parameters (and any undetermined pieces of the lower-order coordinate transformations) as efficiently as possible, we note that all of our equations for the coordinate transformation at orders beyond the zeroth will be of the form

$$\partial_{(\alpha}X_{\beta)} = S_{\alpha\beta} \equiv S_{(\alpha\beta)}. \tag{2.14}$$

Here $\partial_\alpha := \partial/\partial x^\alpha$ (i.e., all partial derivatives are taken with respect to PN harmonic coordinates), X^α is a function of x^α, and $S_{\alpha\beta}$, the equation's source, is some (symmetric) matrix function of x^α (either explicitly, or implicitly through X^α) which is C^2 in the buffer zone. The integrability condition for this equation is that the flat-space linearized Riemann tensor associated with $S_{\alpha\beta}$ vanish, i.e., that we have

$$\mathcal{I}_{\alpha\beta\gamma\delta} := \partial_{\alpha\beta}S_{\gamma\delta} + \partial_{\gamma\delta}S_{\alpha\beta} - \partial_{\alpha\delta}S_{\gamma\beta} - \partial_{\gamma\beta}S_{\alpha\delta} = 0. \tag{2.15}$$

[N.B.: For convenience, we have defined $\mathcal{I}_{\alpha\beta\gamma\delta}$ with a slightly different index ordering than the linearized Riemann tensor—given for flat space in, e.g., Eq. (5.44) of [194]—and without the factor of 1/2.] This follows from the gauge invariance of the linearized Riemann tensor. (See, e.g., §4.1 in Straumann [195] for a proof and discussion of that result. In [196], Blanchet and Damour use this gauge invariance for the same purpose we do.)

For future use, we note that the homogeneous equation, $\partial_{(\alpha}X_{\beta)} = 0$, is the flat space Killing equation, and its most general solution is given by

$$X_\alpha = F_{\beta\alpha}x^\beta + C_\alpha, \tag{2.16}$$

where $F_{\alpha\beta} \equiv F_{[\alpha\beta]}$ and C_α are arbitrary constant matrices. See, e.g., §13.1 in Weinberg [197] for a proof. (Our X_α, $F_{\alpha\beta}$, and C_α correspond to Weinberg's ξ_α, $b_{\beta\alpha} = -b_{\alpha\beta}$, and a_α, respectively.) We shall primarily employ this result tacitly at each order beyond the zeroth to ensure that we have the most general expression for that order's contribution to the coordinate transformation.

Our general approach to the nontrivial matching that occurs at second order and beyond will be as follows: We first use the above integrability condition to read off the matching parameters, exploiting the linear independence of various terms to simplify the process and justify our claims of uniqueness. We start with the nonpolynomial terms, which determine many of the previously undetermined parts of the coordinate transformation from two orders lower, as well as the inner zone mass parameter; the polynomial part then determines the tidal fields.[6] [The nonpolynomial part consists of all the terms that are not polynomials in $\tilde{x}^\alpha := x^\alpha - (m_2/m)b\hat{x}^\alpha$. For this calculation, these are all of the form of a polynomial in $\tilde{x}^\alpha$ multiplied by $\tilde{r}^n$, where $n \in \mathbb{Z} \setminus \{0, 2, 4, 6, \cdots\}$.] After we have fixed all the parameters that can be fixed at a given order, we then solve for that order's contribution to the coordinate transformation (and the polynomial part can be solved for separately from the nonpolynomial part that first appears at fourth order). In all of this, Maple and GRTensorII proved very helpful: They work extremely well for all aspects of the polynomial part, while requiring more care when applied to the nonpolynomial part.

2.5.2 Zeroth order [$O([m_2/b]^0)$]

At lowest (zeroth) order in $(m_2/b)^{1/2}$, we find that the coordinate transformation is a (general) Poincaré transformation—i.e., not necessarily one continuously connected to the identity—since the lowest-order piece of either metric is the Minkowski metric. For simplicity, we shall take this lowest-order piece to be the expected translation due to the position of m_1 at $t = 0$, viz.,

$$(X_\alpha)_0 = \tilde{x}_\alpha := x_\alpha - (m_2/m)b\hat{x}_\alpha. \tag{2.17}$$

In fact, one can show that matching through third order requires that the spatial part of the translation be as given above (though the temporal part can still be freely specified). Similarly, that matching requires the Lorentz transformation portion of the Poincaré transformation to differ from the identity only by a possible rotation about the y-axis, along with possible spatial and temporal reflections. These are combined with a rotation that takes $+y$ to $-y$ if we have an odd number of reflections. We thus conjecture that matching at higher orders will further constrain this lowest-order coordinate transformation to be as given above. At the very least, the matching at fourth and fifth orders is independent of the remaining freedom.

[6] It is intuitively reasonable that the polynomial and nonpolynomial parts should determine the parameters that they do: If one neglects all gauge subtleties and the like, the nonpolynomial terms can be thought of as being those associated with hole 1, and the polynomial terms with (the tidal fields of) hole 2. We discuss this more fully in Sec. 2.5.7.

2.5.3 First order [$O([m_2/b]^{1/2})$]

Since $(g_{\alpha\beta})_1 = (h_{\alpha\beta})_1 = 0$, our equation is just the homogeneous one whose solution is given in Eq. (2.16). We thus have

$$(X_\alpha)_1 = (F_{\beta\alpha})_1 \tilde{x}^\beta + (C_\alpha)_1 \,, \tag{2.18}$$

where we have written this in terms of $\tilde{x}^\alpha := x^\alpha - (m_2/m) b \hat{x}^\alpha$ because $\tilde{r}/b := \sqrt{\tilde{x}_k \tilde{x}^k}/b$ is one of our small parameters. We can do this without loss of generality, as it simply entails a different value for C_α.

This result differs from that given in Eqs. (21) of Paper I; the latter suffers from some sign errors introduced during transcription. However, this does not affect that paper's final coordinate transformation, as the relevant constants were all taken to be zero. This is appropriate for Papers I and II, since they were using a corotating coordinate system: The boost encoded in our $\left(F_{\alpha\beta}\right)_1$ [seen in Eqs. (2.30)] would thus not be expected to appear in the coordinate transformation.

2.5.4 Second order [$O(m_2/b)$]

Proceeding to the next order, we have, recalling that $(\bar{\mathcal{E}}_{kl})_0 = 0$,

$$(h_{\alpha\beta})_2 = \left[\frac{2\,(M_1)_0}{m_2} \frac{b}{(R)_0} - \frac{(\bar{\mathcal{E}}_{kl})_0}{b^2} (X^k)_0 (X^l)_0 - \frac{(\bar{\mathcal{E}}_{klp})_0}{3b^3} (X^k)_0 (X^l)_0 (X^p)_0 \right] \Delta_{\alpha\beta}. \tag{2.19}$$

Similarly, noting that $(\dot{b}_k)_0 = 0$,

$$\begin{aligned} (g_{\alpha\beta})_2 = \Bigg[& \frac{2m_1}{m_2} \frac{b}{(r_1)_0} + 2 - \frac{2}{b} \{ (\vec{r}_1)_0 \cdot (\hat{b})_0 \} + \frac{1}{b^2} \{ 3[(\vec{r}_1)_0 \cdot (\hat{b})_0]^2 - [(r_1)_0]^2 \} \\ & + \frac{1}{b^3} \Big\{ 3[(r_1)_0]^2 [(\vec{r}_1)_0 \cdot (\hat{b})_0] - 5[(\vec{r}_1)_0 \cdot (\hat{b})_0]^3 \Big\} \Bigg] \Delta_{\alpha\beta}. \end{aligned} \tag{2.20}$$

Here $\Delta_{\alpha\beta} := \mathrm{diag}(1,1,1,1)$ is the "lowered 4-dimensional Kronecker delta." Also, we have $(\hat{b}_k)_0 = \hat{x}_k$ and $(r_1^k)_0 = \tilde{r}^k$. Thus, at this order, the source of the differential equation [cf. Eq. (2.14)] is given by

$$2(S_{\alpha\beta})_2 = 2(A_{(\alpha\beta)})_2 = (g_{\alpha\beta})_2 - (h_{\alpha\beta})_2 - (F_\alpha{}^\gamma)_1 (F_{\beta\gamma})_1, \tag{2.21}$$

where $A_{\alpha\beta} := \partial_\alpha X_\beta$. We now apply the integrability condition from Eq. (2.15) and focus on the nonpolynomial piece of $(S_{\alpha\beta})_2$; here this is the one that diverges [as $(R)_0 = (r_1)_0 = \tilde{r} \to 0$]. It must satisfy the integrability condition independently of the other pieces, by linear independence, and [considering, e.g., $(\mathcal{I}_{kl00})_2$] gives $(M_1)_0 = m_1$, as expected. The polynomial piece of the integrability conditions tells us that

$$(\bar{\mathcal{E}}_{kl})_0 = -3\hat{x}_{\langle k}\hat{x}_{l\rangle}, \qquad\qquad (\bar{\mathcal{E}}_{klp})_0 = 15\hat{x}_{\langle k}\hat{x}_l\hat{x}_{p\rangle}, \tag{2.22}$$

using linear independence to read off the quadrupole and octupole tidal fields separately. Solving for the coordinate transformation, we obtain

$$(X_\alpha)_2 = \left[1 - \frac{\tilde{x}}{b}\right]\Delta_{\alpha\beta}\tilde{x}^\beta + \frac{\Delta_{\beta\gamma}\tilde{x}^\beta\tilde{x}^\gamma}{2b}\hat{x}_\alpha - \frac{1}{2}\,(F_\alpha{}^\gamma)_1\,(F_{\beta\gamma})_1\tilde{x}^\beta + (F_{\beta\alpha})_2\tilde{x}^\beta + (C_\alpha)_2\,. \tag{2.23}$$

2.5.5 Third order [$O([m_2/b]^{3/2})$]

At this order, the inner zone metric is

$$\begin{aligned}(h_{00})_3 = {}& \frac{2\,(M_1)_0}{m_2}b\left(\frac{1}{R}\right)_1 + \frac{2\,(M_1)_1}{m_2}\frac{b}{(R)_0} - 2\frac{(\bar{\mathcal{E}}_{kl})_0}{b^2}(X^k)_0(X^l)_1 - \frac{(\bar{\mathcal{E}}_{kl})_1}{b^2}(X^k)_0(X^l)_0 \\ & - \frac{(\bar{\mathcal{E}}_{kl})_1}{b^2}\,(T)_0\,(X^k)_0(X^l)_0 - \frac{(\bar{\mathcal{E}}_{klp})_0}{b^3}(X^k)_0(X^l)_0(X^p)_1 - \frac{(\bar{\mathcal{E}}_{klp})_1}{3b^3}(X^k)_0(X^l)_0(X^p)_0,\end{aligned} \tag{2.24a}$$

$$(h_{0k})_3 = \frac{2}{3}\frac{(\bar{C}_{klp})_0}{b^2}(X^l)_0\,(X^p)_0 + \frac{1}{3}\frac{(\bar{C}_{klps})_0}{b^3}(X^l)_0\,(X^p)_0\,(X^s)_0 - \frac{2}{3}\frac{(\bar{\mathcal{E}}_{lp})_1}{b^2}(X^l)_0\,(X^p)_0\,(X_k)_0\,, \tag{2.24b}$$

$$(h_{kl})_3 = (h_{00})_3\,\delta_{kl}, \tag{2.24c}$$

and the near zone metric is

$$\begin{aligned}(g_{00})_3 = {}& \frac{2m_1}{m_2}b\left(\frac{1}{r_1}\right)_1 - \frac{2}{b}[(\vec{r}_1)_0\cdot(\hat{b})_1] + \frac{2}{b^2}\{3[(\vec{r}_1)_0\cdot(\hat{b})_1][(\vec{r}_1)_0\cdot(\hat{b})_0] - (\vec{r}_1)_1\cdot(\vec{r}_1)_0\} \\ & + \frac{6}{b^3}[(\vec{r}_1)_0\cdot(\vec{r}_1)_1][(\vec{r}_1)_0\cdot(\hat{b})_0],\end{aligned} \tag{2.25a}$$

$$\begin{aligned}(g_{0k})_3 = {}& 4\frac{m_1}{m}\Big\{1 - \frac{b}{(r_1)_0} - \frac{1}{b}[(\vec{r}_1)_0\cdot(\hat{b})_0] + \frac{1}{2b^2}[3\{(\vec{r}_1)_0\cdot(\hat{b})_0\}^2 - \{(r_1)_0\}^2] \\ & + \frac{1}{2b^3}[3\{(r_1)_0\}^2\{(\vec{r}_1)_0\cdot(\hat{b})_0\} - 5\{(\vec{r}_1)_0\cdot(\hat{b})_0\}^3]\Big\}(\dot{b}_k)_1,\end{aligned} \tag{2.25b}$$

$$(g_{kl})_3 = (g_{00})_3\,\delta_{kl}. \tag{2.25c}$$

Here we have $(\vec{b})_1 = \sqrt{m/m_2}\,t\hat{y}$, so $(\vec{r}_1)_1 = -(m_2/m)(\vec{b})_1 = -\sqrt{m_2/m}\,t\hat{y}$, and thus $(\vec{r}_1)_1\cdot(\hat{b})_0 = 0$. Additionally, $(\hat{b})_1 = \sqrt{m/m_2}(t/b)\hat{y}$ and $(\dot{b}_k)_1 = \sqrt{m/m_2}\hat{y}_k$. We also have

$$\left(\frac{1}{R}\right)_1 = -\frac{1}{(R)_0}\frac{(X_k)_0\,(X^k)_1}{[(R)_0]^2} = -\frac{\tilde{r}^k[(F_{\alpha k})_1\,\tilde{x}^\alpha + (C_k)_1]}{\tilde{r}^3}, \tag{2.26}$$

and

$$\left(\frac{1}{r_1}\right)_1 = -\frac{1}{(r_1)_0}\frac{(\vec{r}_1)_0\cdot(\vec{r}_1)_1}{[(r_1)_0]^2} = \sqrt{\frac{m_2}{m}}\frac{yt}{\tilde{r}^3}, \tag{2.27}$$

where $\tilde{r}^\alpha := r^\alpha - (m_2/m)b\hat{x}^\alpha$.

At this order, the equations for the coordinate transformation are

$$2(S_{\alpha\beta})_3 = 2(A_{(\alpha\beta)})_3 = (g_{\alpha\beta})_3 - (h_{\alpha\beta})_3 - 2(h_{(\alpha|\gamma)})_2(F_{|\beta)}{}^\gamma)_1 - 2\,(F_{(\alpha|}{}^\gamma)_1\,(A_{|\beta)\gamma})_2, \tag{2.28}$$

recalling that $(h_{\alpha\beta})_1 = 0$ and utilizing our lower-order results. To obtain $(F_{\alpha\beta})_1$, we look at the $\tilde{r}^{-7}$ piece of $(\mathcal{I}_{kl00})_3$. Such a piece can only come from two spatial derivatives both acting on $\tilde{r}^{-3}$ in the $\tilde{r}^{-3}$ pieces of $(S_{00})_3$; those pieces, in turn, only come from $(1/R)_1$ and $(1/r_1)_1$. Therefore, using Eqs. (2.26) and (2.27), the integrability conditions require that we have

$$\tilde{r}^k[(F_{\alpha k})_1\,\tilde{x}^\alpha + (C_k)_1] = -\sqrt{\frac{m_2}{m}}yt, \tag{2.29}$$

from which we immediately see that

$$(C_k)_1 = 0, \qquad (F_{\alpha\beta})_1 = 2\sqrt{\frac{m_2}{m}}\hat{t}_{[\alpha}\hat{y}_{\beta]}, \tag{2.30}$$

using the antisymmetry of $F_{\alpha\beta}$. (Recall that $\hat{t}_0 = -1$.) By similar logic, the $\tilde{r}^{-5}$ piece of $(\mathcal{I}_{kl00})_3$ only comes from the $(M_1)_1$ piece of $(h_{00})_3$ and gives us $(M_1)_1 = 0$. The remaining nonpolynomial pieces cancel, so we have extracted all the information we can from the nonpolynomial part of the integrability condition.

From the polynomial part of the integrability conditions, we first read off the octupole parts of the tidal fields, which are

$$(\bar{\mathcal{E}}_{kl})_1 = -\frac{6}{b}\sqrt{\frac{m}{m_2}}\hat{x}_{(k}\hat{y}_{l)}, \qquad (\bar{\mathcal{E}}_{klp})_1 = 0, \qquad (\bar{\mathcal{B}}_{klp})_0 = \frac{45}{2}\sqrt{\frac{m}{m_2}}\hat{x}_{\langle k}\hat{x}_l\hat{z}_{p\rangle}, \tag{2.31}$$

and then the quadrupole parts, which are

$$(\bar{\mathcal{E}}_{kl})_1 = 0, \qquad (\bar{\mathcal{B}}_{kl})_0 = -6\sqrt{\frac{m}{m_2}}\hat{x}_{(k}\hat{z}_{l)}. \tag{2.32}$$

The third order coordinate transformation is thus

$$\begin{aligned}(X_\alpha)_3 = \sqrt{\frac{m}{m_2}}\Bigg\{&-\frac{yt}{b^2}\Delta_{\alpha\beta}\tilde{x}^\beta + \left[\frac{\tilde{x}_\mu\tilde{x}^\mu - 4\tilde{x}^2}{2b^2} + \left(2 - \frac{m_2}{m}\right)\frac{\tilde{x}}{b} + \left(2 + \frac{1}{2}\frac{m_2}{m}\right)\frac{m_2}{m}\right]y\hat{t}_\alpha + 2\left[1 - \frac{m_2}{m}\right]\frac{yt}{b}\hat{x}_\alpha \\ &+ \left[\frac{3\tilde{r}^2 + t^2}{6b^2} + \left(\frac{m_2}{m} - 2\right)\frac{\tilde{x}}{b} + \frac{1}{2}\left(\frac{m_2}{m}\right)^2 + 4\right]t\hat{y}_\alpha\Bigg\} + \Bigg\{\sqrt{\frac{m_2}{m}}\left[\hat{y}_{(\alpha}(F_{\beta)0})_2 - \hat{t}_{(\alpha}(F_{\beta)2})_2\right] \\ &+ (F_{\beta\alpha})_3\Bigg\}\tilde{x}^\beta + (C_\alpha)_3 + \frac{1}{2b^3}\sqrt{\frac{m}{m_2}}\tilde{x}y(4\tilde{x}^2 - y^2 - z^2)\hat{t}_\alpha,\end{aligned} \tag{2.33}$$

where the octupole part is the final term.

2.5.6 Fourth and fifth orders [$O([m_2/b]^2)$ and $O([m_2/b]^{5/2})$]

The matching at fourth and fifth orders proceeds in the same way as it did at lower orders, though the algebraic complexity increases substantially. We shall thus give far fewer details of the calculations than we did before, and mostly concern ourselves with pointing out the new features of the calculation that arise at these orders. The most prominent new feature, and the one responsible for much of the algebraic complexity, is the presence of a nonpolynomial part in

the coordinate transformation. We know to expect this at fourth order because the transformation between Cook-Scheel and PN harmonic coordinates is nonpolynomial, and its lowest-order piece is $O(v^4)$—see Sec. 2.5.7. However, there are various other nonpolynomial pieces present in the coordinate transformation at fourth and fifth orders. We have to solve for these nonpolynomial parts of the coordinate transformation by inspection (though we can still use MAPLE to obtain the polynomial part). It is reasonably easy to do so if one first breaks the source into pieces by multipolar order.

The other subtleties involve the multipole expansion and are best illustrated by giving two examples: $(h_{00})_4$ contains the terms $-2(\bar{\mathcal{E}}_{kl})_0(X^k)_0(X^l)_{2,0}/b^2$ and $(2/3)[(M_1)_0/m_2] \times (\bar{\mathcal{E}}_{klp})_0(X^k)_0(X^l)_0(X^p)_0/b^2(R)_0$. The first of these reflects the necessity of avoiding "hidden octupole" pieces (i.e., pieces of octupole order that arise when multiplying together pieces of lower multipolar order) when looking at corrections to lower-order terms: The dipole piece of $(X^k)_2$ would give an octupole contribution to $(\bar{\mathcal{E}}_{kl})_0(X^k)_0(X^l)_2/b^2$, so we only include the monopole piece, denoted by $(X^k)_{2,0}$. Contrariwise, as illustrated by the second term, we do not want to leave out any terms of quadrupole order, even if they arise from, e.g., octupole tidal fields.

These subtleties arise in a slightly different form in the equation for the fifth order piece of the coordinate transformation. Here we have to avoid "hidden octupole" terms in many of the contractions: For instance, we only want the quadrupole-and-lower pieces of $(A_{(\alpha|\gamma)})_2(A_{|\beta)}{}^{\gamma})_3$, which are given by $(A_{(\alpha|\gamma)})_2(A_{|\beta)}{}^{\gamma})_{3,\le 1} + (A_{(\alpha|\gamma)})_{2,0}(A_{|\beta)}{}^{\gamma})_{3,2}$. However, it is also necessary to split up the inner zone metric's contributions into polynomial and nonpolynomial parts to keep from excluding quadrupole pieces as well [since the nonpolynomial parts of the second and third order pieces of the inner zone metric are all $O(b/R)$]. In fact, this behavior means that we need to include the octupole part of the third order piece of coordinate transformation [in $(h^{\rm NP}_{(\alpha|\gamma)})_2(A_{|\beta)}{}^{\gamma})_{3,\le 3}$]. (One would also need to include the octupole part of the second order piece of the coordinate transformation, but it vanishes.)

The rest of the calculation proceeds as before, with the same general results: We obtain the next two orders' contributions to the matching parameters, with the nonpolynomial pieces giving $(F_{\alpha\beta})_2 = 0$ and

$$(F_{\alpha\beta})_3 = \left[\left(\frac{m_2}{m}\right)^{3/2} + 3\sqrt{\frac{m_2}{m}} + 5\sqrt{\frac{m}{m_2}}\right]\hat{t}_{[\alpha}\hat{y}_{\beta]}, \tag{2.34}$$

along with $(C_k)_j = 0$ and $(M_1)_j = 0$ for $j \in \{2,3\}$. Similarly, the polynomial pieces give

$$(\bar{\mathcal{E}}_{kl})_2 = \frac{3}{2}\left[\hat{x}_{\langle k}\hat{x}_{l\rangle} + \frac{m}{m_2}(\hat{x}_{\langle k}\hat{x}_{l\rangle} - 2\hat{y}_{\langle k}\hat{y}_{l\rangle})\right], \qquad (\bar{\mathcal{B}}_{kl})_2 = \left[5\left(\frac{m}{m_2}\right)^{3/2} + 7\sqrt{\frac{m}{m_2}} - 3\sqrt{\frac{m_2}{m}}\right]\hat{x}_{(k}\hat{z}_{l)}, \tag{2.35}$$

along with $(\bar{\mathcal{B}}_{kl})_1 = (\bar{\mathcal{E}}_{kl})_3 = 0$. The fourth order piece of the coordinate transformation is

$$\begin{aligned}(X_\alpha)_4 = &-(\mathcal{A}_t)_4\hat{t}_\alpha + \frac{1}{2}\frac{m_1}{m_2}\frac{\tilde{x}}{b}\left[5\frac{\tilde{x}^2}{b\tilde{r}} - 6\frac{\tilde{x}}{\tilde{r}} - \frac{\tilde{r}}{b}\right]\tilde{r}_\alpha + (\mathcal{A}_x)_4\hat{x}_\alpha + (\mathcal{A}_y)_4\hat{y}_\alpha + (\mathcal{A}_z)_4\hat{z}_\alpha \\ &+ \left\{\sqrt{\frac{m_2}{m}}\left[\hat{y}_{(\alpha}(F_{\beta)0})_3 - \hat{t}_{(\alpha}(F_{\beta)2})_3\right] + (F_{\beta\alpha})_4\right\}\tilde{x}^\beta + (C_\alpha)_4,\end{aligned} \tag{2.36}$$

where

$$
\begin{aligned}
(\mathcal{A}_t)_4 &:= 4\frac{m_1^2}{m_2^2}\frac{b^2}{\tilde{r}} + t\left[\frac{t^2}{6b^2} + \frac{5(y^2-\tilde{x}^2)+z^2}{2b^2} + 2\frac{m}{m_2}\frac{\tilde{x}^2-y^2}{b^2} - \left(\frac{1}{2}\frac{m_2}{m} + \frac{m}{m_2} - 2\right)\frac{\tilde{x}}{b}\right.\\
&\quad \left. + 1 + \frac{m}{2m_2} + \frac{3}{2}\frac{m_2}{m} + \frac{5}{8}\left(\frac{m_2}{m}\right)^2\right],\\
(\mathcal{A}_x)_4 &:= \frac{1}{2}\frac{m_1}{m_2}\left[\frac{\tilde{r}^2}{b^2} - 5\frac{\tilde{x}^2}{b^2} + 6\frac{\tilde{x}}{b} + 4\right]\tilde{r} + \left[\left(\frac{t^2-z^2}{b^2} + \frac{m}{m_2}\frac{z^2-y^2}{b^2} + 4 - \frac{7}{2}\frac{m}{m_2}\right)\tilde{x} + \left(\frac{m}{2m_2} - 1\right)\frac{\tilde{x}^2}{b}\right.\\
&\quad \left. + \left(\frac{m_2}{m} - \frac{m}{2m_2}\right)\frac{y^2}{b} - \left(1 + \frac{3}{2}\frac{m}{m_2} - \frac{m_2}{m}\right)\frac{t^2}{b} + \left(2 - \frac{3}{2}\frac{m}{m_2}\right)\frac{z^2}{b}\right],\\
(\mathcal{A}_y)_4 &:= y\left[\frac{m_1}{m_2}\frac{3\tilde{x}^2-y^2}{b^2} - \left(\frac{1}{2}\frac{m_2}{m} + 2\frac{m}{m_2} - 2\right)\frac{\tilde{x}}{b} + \frac{5}{2}\frac{m}{m_2} - \frac{9}{2} - \frac{m_2}{2m} - \frac{5}{8}\left(\frac{m_2}{m}\right)^2\right],\\
(\mathcal{A}_z)_4 &:= z\left[\frac{t^2+z^2+3y^2-5\tilde{x}^2}{2b^2} + \frac{m}{m_2}\frac{\tilde{x}^2-y^2}{b^2} + \frac{m}{2m_2} - \frac{1}{2}\right].
\end{aligned}
\tag{2.37}
$$

The fifth order piece is

$$
\begin{aligned}
(X_\alpha)_5 &= (\mathcal{A}_t)_5\hat{t}_\alpha - \left\{\mathcal{M}_0\left(6,\frac{1}{2}\right)\frac{\tilde{x}yt}{b^2\tilde{r}} + \mathcal{K}\left[3 - \frac{5}{2}\frac{\tilde{x}}{b}\right]\frac{\tilde{x}^2yt}{b\tilde{r}^3}\right\}\tilde{r}_\alpha + \frac{5}{2}\mathcal{K}\frac{\tilde{x}^2t}{b^2\tilde{r}}\epsilon_{0\alpha k3}\tilde{r}^k + (\mathcal{A}_x)_5\hat{x}_\alpha\\
&\quad + (\mathcal{A}_y)_5\hat{y}_\alpha + \frac{yzt}{2b^2}\mathcal{M}(3,3,-5)\hat{z}_\alpha + \left\{\sqrt{\frac{m_2}{m}}\left[\hat{y}_{(\alpha}(F_{\beta)0})_4 - \hat{t}_{(\alpha}(F_{\beta)2})_4\right] + (F_{\beta\alpha})_5\right\}\tilde{x}^\beta\\
&\quad + (C_\alpha)_5,
\end{aligned}
\tag{2.38}
$$

where $\epsilon_{\alpha\beta\gamma\delta}$ is the 4-dimensional Levi-Civita symbol, with $\epsilon_{0123} = 1$. We have also defined

$$
\begin{aligned}
(\mathcal{A}_t)_5 &:= \mathcal{M}_0(1,0)\left[1 + \frac{14}{3}\frac{\tilde{x}}{b}\right]\frac{y}{b}\tilde{r} - 4\mathcal{M}_0(1,1)\frac{ytb^2}{\tilde{r}^3} - \frac{y}{4}\left[\mathcal{M}(1,11,-10)\frac{t^2}{b^2} + \mathcal{M}\left(\frac{35}{3},-\frac{35}{3},10\right)\frac{\tilde{x}^2}{b^2}\right.\\
&\quad \left. - \mathcal{M}\left(3,-\frac{17}{3},6\right)\frac{y^2}{b^2} - \mathcal{M}\left(\frac{5}{3},\frac{7}{3},2\right)\frac{z^2}{b^2} - \mathcal{M}(4,-6,6)\frac{\tilde{x}}{b} - \mathcal{M}\left(4,\frac{17}{3},-\frac{17}{3},10\right)\frac{m_2}{m}\right],\\
(\mathcal{A}_x)_5 &:= \mathcal{M}_0\left(3,\frac{3}{2}\right)\frac{yt}{b^2}\tilde{r} - \mathcal{K}\left[2 + 3\frac{\tilde{x}}{b}\right]\frac{yt}{\tilde{r}} - \frac{yt}{b}\left[\frac{1}{2}\mathcal{M}(-11,9,1)\frac{\tilde{x}}{b} + \mathcal{M}(8,-11,2,1)\right],\\
(\mathcal{A}_y)_5 &:= \left[\mathcal{M}_0(2,0) + \mathcal{M}_0\left(3,-\frac{1}{2}\right)\frac{\tilde{x}}{b}\right]\frac{t}{b}\tilde{r} + 3\mathcal{K}\frac{\tilde{x}^2t}{b\tilde{r}} - \frac{t}{4}\left[\mathcal{M}\left(3,\frac{7}{3},-\frac{4}{3}\right)\frac{t^2}{b^2} - \mathcal{M}_0(7,12)\frac{\tilde{x}^2}{b^2}\right.\\
&\quad \left. + \mathcal{M}_0(7,8)\frac{y^2}{b^2} + \mathcal{M}(9,-5,0)\frac{z^2}{b^2} + \mathcal{M}_0(16,6)\frac{\tilde{x}}{b} - \mathcal{M}\left(0,\frac{47}{3},-\frac{17}{3},10\right)\frac{m_2}{m}\right] - \mathcal{M}_0(8,0)\tilde{x},
\end{aligned}
\tag{2.39}
$$

and

$$\begin{aligned}
\mathcal{M}(A,B,C,D) &:= A\left(\frac{m}{m_2}\right)^{3/2} + B\sqrt{\frac{m}{m_2}} + C\sqrt{\frac{m_2}{m}} + D\left(\frac{m_2}{m}\right)^{3/2},\\
\mathcal{M}(A,B,C) &:= A\left(\frac{m}{m_2}\right)^{3/2} + B\sqrt{\frac{m}{m_2}} + C\sqrt{\frac{m_2}{m}},\\
\mathcal{M}_0(A,B) &:= \mathcal{M}(A,-A-B,B) = A\left(\frac{m}{m_2}\right)^{3/2} - (A+B)\sqrt{\frac{m}{m_2}} + B\sqrt{\frac{m_2}{m}},\\
\mathcal{K} &:= \mathcal{M}_0(0,-1) = \sqrt{\frac{m}{m_2}} - \sqrt{\frac{m_2}{m}},
\end{aligned} \tag{2.40}$$

where $\mathcal{M}_0(A,B)$ and $\mathcal{K}$ vanish in the limit $m_1 \to 0$ ($\Rightarrow m \to m_2$).

2.5.7 Summary of matching results

The final output of the matching is a set of expressions for the tidal fields, which are given explicitly in Eqs. (B.1); a relation between the mass parameters M and m_1, which we found to be equal [up to uncontrolled remainders of $O(v^4)$]; and the coordinate transformation necessary to place the inner zone metric in the same coordinate system as the near zone metric to the order we matched, which we shall discuss further here. To obtain the full coordinate transformation, we start from Eq. (2.11) and insert the various pieces we have read off or chosen. We shall take anything we were unable to fix by matching to be zero—here this will be C_0 (to all orders), along with $(F_{\alpha\beta})_j$ and $(C_k)_j$ for $j \in \{4,5\}$. With the results of our matching, this means that we have $C_\alpha = 0$ (to all orders). We took the zeroth-order piece of the coordinate transformation to simply be the expected translation of the origin from the binary's center-of-mass to hole 1, so

$$(X_\alpha)_0 = \tilde{x}_\alpha := x_\alpha - (m_2/m)b\hat{x}_\alpha. \tag{2.41}$$

With $(C_\alpha)_1 = 0$, we also have

$$(X_\alpha)_1 = (F_{\beta\alpha})_1 \tilde{x}^\beta, \tag{2.42}$$

where

$$(F_{\alpha\beta})_1 = 2\sqrt{\frac{m_2}{m}}\hat{t}_{[\alpha}\hat{y}_{\beta]}. \tag{2.43}$$

Continuing onward, $(X_\alpha)_2$ is given by Eq. (2.23), where $(F_{\alpha\beta})_2 = 0$ and $(C_\alpha)_2 = 0$; $(X_\alpha)_3$ comes from Eq. (2.33), where

$$(F_{\alpha\beta})_3 = \mathcal{M}(0,5,3,1)\hat{t}_{[\alpha}\hat{y}_{\beta]}, \tag{2.44}$$

and $(C_\alpha)_3 = 0$. [$\mathcal{M}(A,B,C,D)$ is defined in Eqs. (2.40).] Similarly, $(X_\alpha)_4$ can be obtained from Eq. (2.36), and we take $(F_{\alpha\beta})_4 = 0$ and $(C_\alpha)_4 = 0$. Finally, $(X_\alpha)_5$ is given in Eq. (2.38); again, we set $(F_{\alpha\beta})_5 = 0$ and $(C_\alpha)_5 = 0$.

Looking back over this coordinate transformation, it is possible to gain some physical intuition about what it is accomplishing: The expected Lorentz boost due to the holes' orbital motion is present (through third order, which is the highest order at which we have fixed all the coordinate transformation, up to a possible temporal shift). We also have the lowest-order piece of the transformation between Cook-Scheel and harmonic PN coordinates for an unperturbed

Schwarzschild black hole. [This is given by the first term in $(\mathcal{A}_t)_4$ in Eqs. (2.37).] The remainder of the coordinate transformation is probably mostly concerned with effecting the transformation from locally inertial coordinates centered on the black hole to PN barycentric coordinates. In addition, as we noted previously, the polynomial and nonpolynomial parts of the full coordinate transformation are related to the individual holes in the expected manner: The nonpolynomial parts are associated with hole 1 and vanish in the limit $m_1 \to 0$. The polynomial pieces are associated with hole 2—indeed, everything except for the piece of the background Cook-Scheel-to-PN-harmonic transformation vanishes in the limit $m_2 \to 0$.

2.6 Far zone metric

The direct integration of the relaxed Einstein equations (DIRE) approach can be used to compute the full 4-metric $g_{\alpha\beta}$ (in harmonic coordinates) in the far zone. The resulting far zone metric is expressed in terms of derivatives of source multipole moments obtained by integrating the "effective" stress-energy pseudotensor over the near zone. One also obtains nonlinear contributions from integrating over the far zone (known as the *outer integral* in the DIRE approach), though only two of the resulting terms appear in the metric perturbation $h^{\alpha\beta}$ [defined in Eq. (2.2) of [177]] to the order we are considering.

In this formalism, the metric perturbation in the far zone is given in terms of the source multipoles $\mathcal{I}^Q$ and $\mathcal{J}^Q$ (Q is a multi-index[7]) via [Eqs. (5.12) in [177]][8]

$$h^{00} = 4\frac{\mathcal{I}}{r} + 2\partial_{kl}\left[\frac{\mathcal{I}^{kl}(u)}{r}\right] - \frac{2}{3}\partial_{klm}\left[\frac{\mathcal{I}^{klm}(u)}{r}\right] + 7\frac{\mathcal{I}^2}{r^2} + O(v^6), \tag{2.45a}$$

$$h^{0k} = -2\partial_l\left[\frac{\dot{\mathcal{I}}^{kl}(u)}{r}\right] + 2\epsilon^{lkp}\frac{n^l\mathcal{J}^p}{r^2} + \frac{2}{3}\partial_{lp}\left[\frac{\dot{\mathcal{I}}^{klp}(u)}{r}\right] + \frac{4}{3}\epsilon^{lkp}\partial_{ls}\left[\frac{\mathcal{J}^{ps}(u)}{r}\right] + O(v^6), \tag{2.45b}$$

$$h^{kl} = 2\frac{\ddot{\mathcal{I}}^{kl}(u)}{r} - \frac{2}{3}\partial_p\left[\frac{\ddot{\mathcal{I}}^{klp}(u)}{r}\right] - \frac{8}{3}\epsilon^{ps(k|}\partial_s\left[\frac{\dot{\mathcal{J}}^{p|l)}(u)}{r}\right] + \frac{\mathcal{I}^2}{r^2}\hat{n}^k\hat{n}^l + O(v^6). \tag{2.45c}$$

Here $r := \|\vec{x}\|$ is the distance from the binary's center-of-mass to the field point and $\hat{n}^k := x^k/r$ is its associated unit vector. The $(\mathcal{I}/r)^2$ terms are the two contributions from the outer integrals mentioned previously. We have included all the terms Pati and Will give, even though some of the ones in the purely temporal and spatial components only contribute terms that are of a higher order than we need here. We do this for completeness and also because we shall need these higher-order terms when we construct the higher-order extension to the data set (the computation of the higher-order far zone metric is sketched in Appendix C).

The source multipoles $\mathcal{I}^Q$ and $\mathcal{J}^Q$ are defined in Eqs. (4.5) of [177]. With these definitions, the mass monopole $\mathcal{I}$ is simply (a PN corrected version of) the total mass of the system, the dipole moment $\mathcal{I}^k$ is the center of mass vector (so it vanishes in our coordinate system), and the current dipole $\mathcal{J}^k$ is the total angular momentum. One can show that these three quantities are conserved up to radiative losses.

[7] See, e.g., the discussion following Eq. (2.14) in Pati and Will [177] for the definition of a multi-index.

[8] We have corrected a sign error in Pati and Will's expression for h^{kl}: They give coefficients of $+2/3$ and $+8/3$ for the second and third terms. The correct signs can be obtained from Pati and Will's Eqs. (2.13) and (4.7b) in [177].

The source multipoles can be expanded in the PN approximation to find

$$\mathcal{I} = m_1\left(1 + \frac{1}{2}v_1^2 - \frac{m_2}{2b}\right) + (1 \leftrightarrow 2) + O(bv^4), \tag{2.46a}$$

$$\mathcal{J}^k = \epsilon^{klp} m_1 x_1^l v_1^p + (1 \leftrightarrow 2) + O(b^2v^3), \tag{2.46b}$$

$$\mathcal{I}^{kl} = m_1 x_1^{kl}\left(1 + \frac{1}{2}v_1^2 - \frac{m_2}{2b}\right) + \frac{7}{4}m_1 m_2 b\delta^{kl} + (1 \leftrightarrow 2) + O(b^3v^4), \tag{2.46c}$$

$$\mathcal{J}^{kl} = \epsilon^{kps} m_1 v_1^s x_1^{pl} + (1 \leftrightarrow 2) + O(b^3v^3), \tag{2.46d}$$

$$\mathcal{I}^{klp} = m_1 x_1^{klp} + (1 \leftrightarrow 2) + O(b^4v^2). \tag{2.46e}$$

The first two come from Will and Wiseman's Eqs. (4.16) [179], and the remainder from Pati and Will's Eqs. (D1) [178]. (Even though we only need the lowest-order piece of $\mathcal{I}^{kl}$ here, we include the 1PN corrections that Pati and Will give since we need them in our construction of the higher-order extension in Appendix C.) Here the notation is mostly the same as for the near zone metric and was defined in Sec. 2.4. The only new definition is $x_1^{kl} := x_1^k x_1^l$ (with similar definitions holding for different vectors, as well as larger collections of indices).

When calculating the metric, we follow the far zone order counting given in Sec. IV C of Pati and Will [177], where each *additional* power of r^{-1} in an expression is treated as $O(v)$. [This is equivalent to the order counting used by Alvi [62].] In obtaining the far zone metric for the $O(v^4)$ data, we modify this prescription slightly to treat factors of r^{-1} that come with factors of G in the far zone's post-Minkowskian expansion as not being "additional," so, e.g., $(\mathcal{I}/r)^2 = O(v^4)$, not $O(v^5)$. The only effect this has is to imply that we keep the outer integral terms in the $O(v^4)$ version of the data instead of dropping them. (We revert back to the pure Pati-Will order counting in the higher-order extensions to the data, as discussed in Appendix C.)

With this order counting, we have $h^{00} = O(v^2)$, $h^{0k} = O(v^4)$, and $h^{kl} = O(v^4)$, so the full 4-metric in the far zone is given by [Eqs. (4.2) in [177]]

$$g_{00} = -\left[1 - \frac{1}{2}h^{00} + \frac{3}{8}(h^{00})^2\right] + \frac{1}{2}h^{kk}, \tag{2.47a}$$

$$g_{0k} = -\left[1 - \frac{1}{2}h^{00}\right]h^{0k}, \tag{2.47b}$$

$$g_{kl} = \left[1 + \frac{1}{2}h^{00} - \frac{1}{8}(h^{00})^2 - \frac{1}{2}h^{pp}\right]\delta^{kl} + h^{kl}, \tag{2.47c}$$

with remainders of $O(v^6)$. Here we have kept the $-(1/2)h^{00}$ term in the expression for g_{0k} for formal consistency (and because we shall need it when we construct the higher-order extension in Appendix. C). This term gives a contribution of $O(v^6)$ with our order counting (which we neglect here), but would give terms of $O(v^5)$ if we had used the standard near zone order counting, where $h^{0k} = O(v^3)$. This is the only $O(v^6)$ term in the expression for g_{0k}, so the uncontrolled remainder in that expression is thus actually $O(v^7)$.

We can now easily compute the full metric by taking all the derivatives in the expression for the metric perturbation, Eqs. (2.45). In doing this, it is important to realize that the multipoles depend on retarded time, which must be carefully accounted for when differentiating. Eqs. (2.47) then give the full metric. In performing this calculation, we assume a (quasi)circular orbit, so

we can make the same sorts of simplifications as we did in obtaining the expression for the near zone metric in Sec. 2.4. After much algebra, we finally obtain the full metric in the far zone:

$$g_{00}+1 = \frac{2m_1}{r}+\frac{m_1}{r}\Big\{v_1^2-\frac{m_2}{b}+2\left(\vec{v}_1\cdot\hat{n}\right)^2-\frac{2m}{r}+6\frac{\left(\vec{x}_1\cdot\hat{n}\right)}{r}\left(\vec{v}_1\cdot\hat{n}\right)-\frac{x_1^2}{r^2} + \frac{\left(\vec{x}_1\cdot\hat{n}\right)^2}{r^2}\left(3-2r^2\omega^2\right)\Big\}+(1\leftrightarrow 2)+O(v^5), \tag{2.48a}$$

$$g_{0k} = -\frac{m_1}{r}\Big\{4(\vec{v}_1\cdot\hat{n})+4(\vec{v}_1\cdot\hat{n})^2-6(\vec{x}_1\cdot\hat{n})^2\,\omega^2+4\frac{(\vec{x}_1\cdot\hat{n})}{r}+12\frac{(\vec{x}_1\cdot\hat{n})}{r}(\vec{v}_1\cdot\hat{n})-2\frac{x_1^2}{r^2} + 6\frac{\left(\vec{x}_1\cdot\hat{n}\right)^2}{r^2}\Big\}v_1^k+\frac{m_1}{r}\Big\{4\left(\vec{x}_1\cdot\hat{n}\right)+8(\vec{x}_1\cdot\hat{n})(\vec{v}_1\cdot\hat{n})-2\frac{x_1^2}{r}+6\frac{\left(\vec{x}_1\cdot\hat{n}\right)^2}{r}\Big\}\omega^2x_1^k+(1\leftrightarrow 2) + O(v^6), \tag{2.48b}$$

$$g_{kl}-\delta_{kl} = \frac{2m_1}{r}\delta_{kl}+\frac{m_1}{r}\Big\{\Big[v_1^2-\frac{m_2}{b}+2\left(\vec{v}_1\cdot\hat{n}\right)^2+\frac{m}{r}+6\frac{\left(\vec{x}_1\cdot\hat{n}\right)}{r}\left(\vec{v}_1\cdot\hat{n}\right)-\frac{x_1^2}{r^2} + \frac{\left(\vec{x}_1\cdot\hat{n}\right)^2}{r^2}\left(3-2\omega^2r^2\right)\Big]\delta_{kl}+\frac{m}{r}\hat{n}^{kl}+4v_1^{kl}-4\omega^2x_1^{kl}\Big\}+(1\leftrightarrow 2)+O(v^5), \tag{2.48c}$$

where everything is evaluated at the retarded time $u := t - r$. [This expression agrees with Alvi's result, given in his Eqs. (2.17) [62], though he also includes the $O(v^5)$ terms in the purely temporal and spatial components. We include these pieces—as well as even higher-order ones—when we construct the extension to the data in Sec. 2.7 and have checked that we agree with Alvi about all the $O(v^5)$ terms.]

2.6.1 Evolution of the binary's phase and separation

Even though the effects of radiation reaction on the binary's orbital separation and phase are formally small, only beginning at $O(v^5)$, they produce large corrections to the far zone metric in practice when one is far away from the binary, since the retarded time at which one is evaluating the binary's parameters becomes large. For instance, even as close as $r = 50m$, which is inside the outermost extraction radius (usually well inside) for all the simulations used in the Samurai project [128], the phase difference between a circular orbit [using the 3PN expression for ω given in Eq. (190) of [19]] and 3.5PN inspiral (the computation of which is detailed below) is ~ 0.015 radians for an equal-mass binary with an instantaneous separation of $10m$. (This phase difference should be compared with the averaged frequency domain phase accuracy required for parameter estimation with Advanced LIGO, viz., 0.007 radians, from [53]. While such a comparison is not really warranted—see [55] for some discussion—it gives a rough idea of the required accuracy.) See Sec. IV A in Kelly *et al.* [72] for further discussion of the necessity of using formally higher-order PN results in obtaining the far zone metric.

We thus use the most accurate (3.5PN) expression for the inspiral, as given by Blanchet [19], who obtains it from an energy balance argument. The phase itself is given by Blanchet's Eq. (234) [19], where it is expressed in terms of the dimensionless time variable Θ, defined in his Eq. (232) [19]. Since we are evaluating everything at the retarded time u, we have

$\Theta = (\eta/5m)(t_c - u)$. Here the "coalescence time" t_c is defined as the time at which the binary's frequency goes to infinity (or, equivalently, its separation goes to zero). One can calculate this in the PN approximation by using the energy balance relation $dE/dt = -\mathcal{L}$, where E and $\mathcal{L}$ are the binary's energy and gravitational wave luminosity, respectively. These are given in terms of $\gamma := m/b$ though 3.5PN in Blanchet's Eqs. (191) and (230) [19], respectively. We can then compute t_c by integrating $dt/db = -(dE/db)/\mathcal{L}$ from $b = 0$ to $b = b_0$ (where b_0 is the binary's separation at $t = 0$). Here we expand the quotient as a power series (to 3.5PN) rather than using a Padé approximant (or performing any resummation of the energy or luminosity), as is sometimes done in the literature (see, e.g., [198]).

With the 3.5PN expression for t_c in hand, we can simply substitute it (via Θ) into Eq. (234) in Blanchet [19] to obtain the phase as a function of u, making sure to expand to 3.5PN order after substituting. We add a constant to the phase so that it is zero when $t = 0$, to be consistent with our choice of initial phase in the matching (i.e., so the holes initially lie on the x-axis, with our expression for the orbit). We also take the freely specifiable gauge constant r'_0 and constant of integration Θ_0 to be m and 1, respectively. The dependence of ω on u is then obtained by differentiating the phase with respect to time.

To obtain the retarded time dependence of b, we use $b = m/\gamma$, along with the expressions for γ in terms of Blanchet's frequency-related parameter $x := (m\omega)^{2/3}$ [Blanchet's Eq. (193) [19]] and x in terms of Θ [Blanchet's Eq. (233) [19]], expanding the quotient consistently to 3.5PN. (Here Blanchet's x should not be confused with our x-coordinate. Also, we take the appearance of b in a logarithm in the expression for γ to consist only of b's lowest-order dependence on Θ, viz., $4m\Theta^{1/4}$.)

We do not display the resulting expressions, as they are quite lengthy, and best handled entirely within a computer algebra system. (We have carried out the calculations in Maple and our scripts are available at [152].) Our results can be seen graphically in Fig. 2.4, where we plot the past history of an equal-mass binary's separation (starting from $b_0 = 10m$) along with the fractional deviations of its phase from $\omega_0 u$. N.B.: The final expansions of the expressions for ϕ and b are important. If they are not performed, then one does not recover the expected values for b and ω at $u = 0$ [viz., b_0 and ω_0, respectively—here ω_0 is the binary's 3PN angular velocity for $b = b_0$ obtained from Blanchet's Eq. (190) [19]].

Using these high-order phasing relations means that we are effectively using high-order equations of motion. We would have thus liked to include higher-order terms in the relative-to-center-of-mass (relative-to-COM) variable relation as well, for consistency, rather than merely the lowest-order Newtonian relation [given in Eqs. (2.6)], which is all that is needed formally in the far zone, even in our extended data. However, the resulting expressions for the far zone metric components are algebraically too complex for Maple to handle, so we had to forego including any additional terms. Fortunately, unlike the secular radiation reaction effects in the binary's phase and separation considered above, the neglected PN corrections to the relative-to-COM relation are numerically small in addition to being formally small: They first enter the metric at $O(v^8)$ (in the purely temporal component), and produce corrections of $\sim 5 \times 10^{-7}$ to terms whose uncorrected value is $\sim 10^{-4}$.

We *were* able to include these additional terms in the relative-to-center-of-mass relation in the near zone metric: For consistency, we include the same higher-order terms in the phasing and separation in the near zone metric as in the far zone metric, so it makes sense to attempt to include the higher-order relative-to-COM relation there, even though we were unable to do

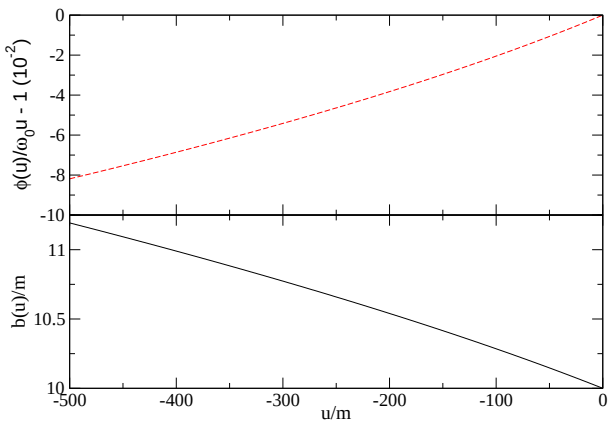

Fig. 2.4. The 3.5PN results for the past history of an equal-mass binary's separation, starting from $10m$ at $u = 0$, along with the fractional deviations of its phase from $\omega_0 u$.

so in the far zone metric. In fact, these corrections contribute to the near zone metric at one order lower than to the far zone metric [viz., $O(v^7)$ in the spatiotemporal components] and are numerically quite a bit larger: They give corrections of $\sim 2 \times 10^{-3}$ to terms whose uncorrected value is ~ 0.2.

Blanchet and Iyer give these corrections through 3PN in Eqs. (3.11)–(3.14) of [199]. We have specialized their result to a circular orbit by using the 2PN expression for ω to express v in terms of m, b, and η. Blanchet gives this relation specialized to a circular orbit through 2.5PN in Eq. (187) of [19], so we shall just quote the 3PN contribution to $\vec{x}_A$ (which has no A-dependence):

$$\vec{x}_A^{\,3\mathrm{PN}} = -\eta \frac{(m_1 - m_2)m^2}{b^3}\left[\frac{7211}{1260} + \eta - \frac{22}{3}\log\left(\frac{b}{r_0''}\right)\right]\vec{b}. \tag{2.49}$$

In this expression, r_0'' is another freely specifiable gauge constant which, though *a priori* different from r_0', we shall take to have the same value, viz., m. [This is equivalent to taking the related gauge constants r_1' and r_2' to both be m—see Eqs. (3.15) and (3.19) in [199].] The expression for the binary's separation vector that we substitute into the resulting relative-to-center-of-mass relation to obtain the trajectories of the point particles is $\vec{b} = b(\hat{x}\cos\phi + \hat{y}\sin\phi)$, where b and ϕ are functions of t (in the near zone) or u (in the far zone).

2.7 Including higher-order terms

Here we construct an extension to our data using various readily available higher-order terms. This extension includes all the $O(v^5)$ terms in the near and far zones, but also includes even higher-order terms that do not improve the data's formal accuracy. The general philosophy is that adding higher-order terms can often improve the quality of the data in practice, even if it does not improve their formal accuracy. As we have seen in the previous section, this is

Zone	Attribute	Versions			
		`04_NoOct`	`04`	`05`	`all`
Inner	Time dependence	Perturbative	Perturbative	Full	Full
Inner	Fourth order octupoles	No	Yes	Yes	Yes
Near, Far	Metric order	$O(v^4)$	$O(v^4)$	$O(v^5)$	Full extended

Table 2.2. An overview of the contents of the various data sets we considered.

particularly true in the far zone, where the binary's phase evolution depends sensitively on the inclusion of quite high-order radiation reaction terms.

There are also more specific reasons for including certain of these terms: We would like for a putative evolution of our data to be able to be compared directly with Kelly *et al.*'s evolution of their data [65]. (Such a comparison will give an indication of how much of the junk radiation is due to the failure of the initial data to include the correct tidal deformations.) Kelly *et al.* include the $O(v^5)$ pieces of the spatial metric in the near zone [though not the matching $O(v^6)$ pieces of the extrinsic curvature]. The extension we have constructed includes these terms, as well. It also includes (as noted above) the $O(v^5)$ terms in the far zone, along with the $O(v^6)$ terms in the extrinsic curvature in the near and far zones, so the extended data are valid through $O(v^5)$ in those zones. However, we have coded our data in such a way that one can easily produce a data set that only includes the pieces that Kelly *et al.* have, or some other subset of the pieces in the extension.

We would have liked to have included the $O(v^5)$ terms in the inner zone as well, for completeness, but it is not possible to obtain initial data in that zone that is formally $O(v^5)$ while still including the quadrupole pieces with the inner zone metric we have: We would need the $O(v^6)$ pieces of (the spatiotemporal components of) the inner zone metric. The quadrupole parts of these include hexadecapole tidal fields, and knowledge of how those fields enter the inner zone metric requires nonlinear black hole perturbation theory (this has since been carried out by Poisson and Vlasov [171]). However, we *are* able to calculate the polynomial parts of the fourth and fifth order octupole pieces, and actually carried out the calculation for the fourth order pieces. We present the results in Appendix B.2 and include these additional contributions in the extension. (These pieces include the 1PN correction to the electric octupole tidal field.)

Moreover, we are also able to include the full time dependence of the tidal fields (up to radiation reaction effects): See Appendix B.1. It seems desirable to include these terms, since some of them are necessary for obtaining the pieces of the extrinsic curvature that describe how the tidal fields evolve. We already have the necessary, linear-in-t pieces for the lowest-order quadrupole fields, but not for their 1PN corrections, the explicit appearance of their time derivatives, or any of the octupole fields. We discuss the specifics of how we include this time dependence, and what exactly we are neglecting in its inclusion in Appendix D. We have *not* attempted to obtain the full time dependence of the coordinate transformation, since this is a rather more involved task than obtaining that of the tidal fields. Moreover, our rationale for including the tidal fields' full time dependence was to improve the evolution of the tidal perturbations: Including the full time dependence of the coordinate transformation would only improve the agreement of the inner and near zone metrics in the buffer zone, while the largest effect of the

tidal perturbations (e.g., in reducing the high-frequency junk radiation) presumably comes from closer to the horizons.

The other higher-order pieces we have added are all in the purely temporal components of the near and far zone metrics. We have included these since Blanchet, Faye, and Ponsot [166] give an explicit expression for the purely temporal component of the near zone metric through $O(v^7)$ and it is easy enough to calculate the matching terms in the far zone. The specifics of where we obtained all the extra terms are given in Appendix C, along with the accompanying caveats and new order counting in the far zone. We refer to these "state-of-the-art" versions of the near and far zone metrics as the full extended versions.

We have considered the effects of these additional terms on how well the metrics stitch together by putting together four versions of the data, shown in Table 2.2. While the versions in the table are given the labels we use for the corresponding MAPLE scripts and C code (available at [152]), we shall usually refer to them by the order of their near and far zone metrics [i.e., as $O(v^4)$, $O(v^5)$, and full extended]. This will not cause confusion, since we will almost always consider just the right-most three. While the `04_NoOct` version is important, since it contains only the pieces that can be included consistently in the matching (except for the higher-order terms necessary to obtain the phasing in the far zone accurately and the analogous terms in the near zone), we only consider it in Fig. 2.18. Thus, when we refer to the $O(v^4)$ version without any qualifiers, we mean `04`, the version including the fourth order octupole pieces. See Appendix D for the specific details of how all these metrics are calculated. (N.B.: The near zone metrics in all of these versions contain the background resummation detailed in Sec. 2.8.1.)

As we shall see in the next section (particularly in Figs. 2.15, 2.16, 2.17, and 2.18), including the additional terms reduces the resulting data's constraint violations, or at least does not affect them adversely .The only exception to this is the addition of the full time dependence in the inner zone, which increases the constraint violations in the inner zone. However, it does not increase them by much, and they were originally quite small: Our philosophy is thus to include these terms, which we think will improve the data's evolution, even at the cost of slightly higher constraint violations. (Kelly *et al.* [65] have also seen that including more physics—from the TT piece of the metric—increases the constraint violations.)

2.8 Numerical considerations

To gain some feel for how well the matching is working numerically, along with the differences between the various versions of the initial data, we plot the volume elements of the various 4-metrics in the vicinity of their buffer zones. The volume element is, of course, coordinate-dependent, but is nevertheless a very convenient quantity to use, particularly when comparing the matching of different versions of the data. We display the differences between the volume elements of various versions of the constituent metrics in the inner-to-near transition in Fig. 2.5, and the volume elements themselves in the near-to-far transition in Fig. 2.6, along with the volume element of the merged metric. Of course, we first transform the inner zone metric using the coordinate transformation obtained from the algebraic matching above.

To obtain a simple, easily interpreted plot, we choose the test system $b = 10m$, $m_1 = m_2$ (the mass is in arbitrary units) and restrict our attention to the $t = 0$ timeslice and the x-axis (i.e., we consider the spatial slice along the separation between the holes), concentrating on the portion near hole 1. We expect this slice to provide the most stringent test of the matching,

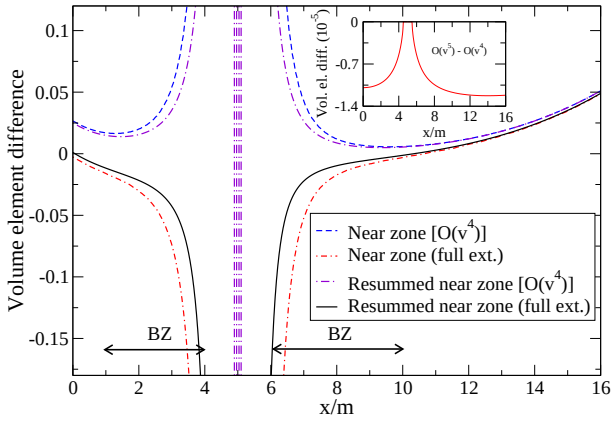

Fig. 2.5. The differences between the volume elements of various near zone metrics and the volume element of the full extended inner zone metric. We have indicated the rough locations of the intersection of the x-axis with hole 1's inner-to-near buffer zone (BZ) using double-headed arrows. We have also displayed the differences between the volume elements of the $O(v^4)$ and $O(v^5)$ resummed metrics in the inset.

since it contains the portions of the buffer zones where the field is strongest and changes most rapidly. Additionally, an initial separation of $10m$ is large enough that it is reasonable to expect that the ingredients making up the construction are valid. But it is also small enough to test the ingredients near the edge of their region of validity, and to be comparable to the initial separations used in most current numerical relativity simulations. We shall thus use this setup (or slight modifications thereof) for all of our later examples. In all these plots, we use the full extended version of the data discussed in the previous section, unless otherwise noted.

The inner zone metric we display here contains the fourth-order octupole pieces discussed in Appendix B.2. To avoid clutter, we did not plot the "plain" version without these additional pieces: It agrees very closely with the version we have plotted near and inside the horizon, but bends away from the near zone metric further away from the hole. The differences between the versions of the inner zone with full and perturbative time dependence would not appear in this plot, since we are looking at the $t = 0$ timeslice. We display the differences between the $O(v^4)$, $O(v^5)$, and full extended far zone metrics in Fig. 2.7, considering a binary with mass ratio $3 : 1$ so that these differences are more pronounced. (In this plot, we have concentrated on the portion of the x-axis to the right of the more massive hole, for clarity: The relations between the various metrics are qualitatively the same to the left of the less massive hole, except for differences in relative amplitude.)

In the near zone metric, the extension adds certain terms that become large when evaluated close to the holes (e.g., $4m_1^2 m_2/r_1^3$ in g_{00}, which equals $1/2$ at $r_1 = m$ for our test system) and others that grow rapidly as one moves away from the holes (e.g., $-m_1^2 m_2 r_1^3/4b^6$, also in g_{00}, which is about -0.03 at $r_1 = 100m$ for our test system). The terms that become large near the holes cause the $t = 0$ timeslice of the near zone metric to no longer be spacelike in a region that

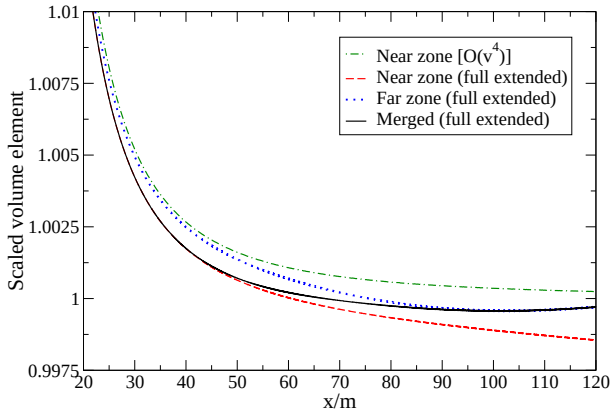

Fig. 2.6. The scaled volume elements of the (resummed) near zone [both $O(v^4)$ and extended], far zone, and merged metrics. These are calculated for our equal-mass test system and plotted along the x-axis in the portion of the near-to-far transition region that lies to the right of hole 1. To obtain a less crowded plot, we have scaled these by the contribution to the volume element of the lowest-order nontrivial pieces of the far zone metric, viz., $(1 + 2m/r)\sqrt{1 - 4m^2/r^2}$. The buffer zone is roughly the region in which we transition, which, in turn, is roughly the region plotted.

extends outside the horizon. However, for this separation, the timeslice is still spacelike in the buffer zone, so its bad behavior closer to the holes does not cause any problems in the merged metric.

N.B.: The unperturbed horizon is $m_1[1 - m_2/b + O(m_2^2/b^2)]$ away from the point particle associated with hole 1 in the new coordinates. For the test system, the correction is small, so hole 1's unperturbed horizon intersects the x-axis at $\sim 4.5m$ and $\sim 5.5m$ in the new coordinates. There are also corrections due to the tidal distortion, but for the test system these are even smaller than those due to the new coordinates: See Sec. VIII in Taylor and Poisson [180] for a study of the effects of the lowest-order quadrupole tidal distortion on the horizon.

The Newman-Penrose scalar ψ_4 provides a coordinate-independent (though still tetrad-dependent) measure of the success of the matching. (It also provides a measure of the data's gravitational wave content in the far zone.) Compared to the volume element, ψ_4 is also more sensitive to the specifics of the transition functions, since it contains first and second derivatives of the metric. We plot ψ_4 for the merged and constituent full extended metrics in the inner-to-near and near-to-far transitions in Fig. 2.8 and 2.9, respectively. (We computed ψ_4 using BAM [67, 68]; its built-in tetrad is discussed in Sec. III A of [68]. Additionally, we only plot the real part of ψ_4 because the imaginary part is several orders of magnitude smaller.)

In the inner-to-near transition, the volume elements and ψ_4 generally behave in the expected manner: They differ when considered either too near or too far from the hole and approach each other in the buffer zone. Things look a bit more unusual in the near-to-far transition, since the two volume elements agree better in the region between $20m$ to $30m$ than they do further

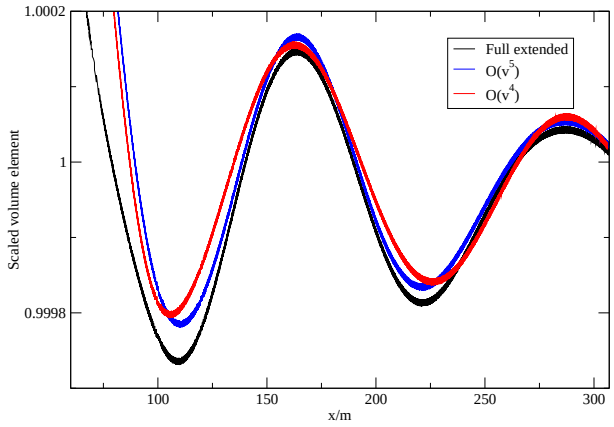

Fig. 2.7. The scaled volume element of the far zone metric for a binary with a separation of $10m$ and a mass ratio of $3:1$ along the x-axis to the right of hole 1 (the more massive hole). We display this for the extended data (the darkest curve in greyscale) as well as the $O(v^5)$ and $O(v^4)$ versions of the data (the medium and lightest curves in greyscale, respectively) to illustrate their differences. (We considered an unequal mass binary to make these differences more pronounced.) As before, we have scaled these volume elements by the contribution from the lowest-order nontrivial piece of the metric, viz., $(1 + 2m/r)\sqrt{1 - 4m^2/r^2}$.

away from the holes, and ψ_4 actually agrees (somewhat) better even further in. However, this should not be surprising: The reduced wavelength of the gravitational radiation is $\sim 16m$ for the equal-mass test system, and the difference between the near zone metric's perturbative treatment of retardation and the far zone metric's full treatment should become quite apparent beyond that radial distance. In fact, the oscillations we see in the far zone metric's volume element and ψ_4 (in Figs. 2.7 and 2.9, respectively) are due to the far zone metric's dependence on retarded time. (Even though the metric contains gravitational radiation, this is not the only source of the oscillations of the volume element. However, it does contribute to them, as expected. The oscillations in ψ_4 can likely be identified with gravitational radiation, though we are probably not quite far enough from the binary to do so completely unambiguously.) The former plot also illustrates the phase differences between the various versions of data.

2.8.1 Background resummation

In the inner-to-near transition (as shown in Fig. 2.5), the volume elements of the original (unresummed) metrics do not agree as closely as we might like. In fact, the agreement is *worse* near the hole with the higher-order extended version of the near zone metric than it is with the original $O(v^4)$ version (though the agreement further away from the hole and outside the orbit is slightly better). However, even the agreement with the original version is not much better than

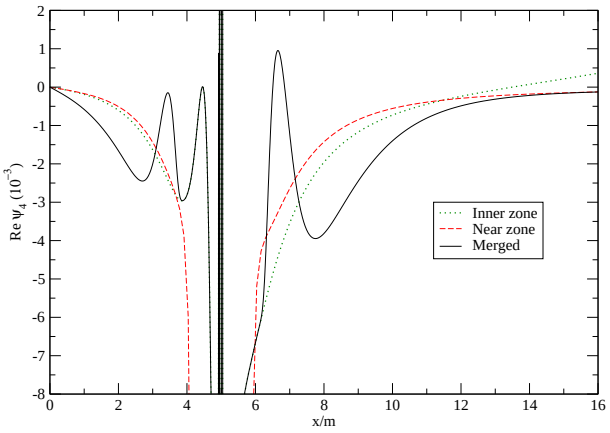

Fig. 2.8. The real part of the Newman-Penrose scalar ψ_4 of the inner, near, and merged metrics computed for our equal-mass test system and displayed in the vicinity of the inner-to-near transition.

that found in Paper II (see its Fig. 2), even though we have matched to higher order.[9] Part of the resolution of this apparent problem is that we have not yet used one of the "tricks" from Paper II, namely background resummation.

The idea of background resummation is to add higher-order terms to the near zone metric in order to improve its strong field behavior. If one considers the limit $m_2 \to 0$ ($\Rightarrow v_1 \to 0$) of the near zone metric, then one finds that it reduces to the far field asymptotic expansion of the unboosted Schwarzschild metric (with mass parameter m_1) in PN harmonic coordinates. This expansion, however, lacks the causal structure of the Schwarzschild metric—it has no horizon.

One method to restore this causal structure is to resum the PN metric. This resummation consists of adding an infinite number of higher-order terms, such that the metric reduces identically to the *full* unboosted Schwarzschild metric in PN harmonic coordinates in the limit $m_2 \to 0$. *A priori*, there is no reason to suspect that adding such higher-order terms would increase the accuracy of the PN metric. *A posteriori*, however, it is usually the case that such resummed metrics are indeed closer to the exact solution, as was seen in Paper II. Moreover, we should stress that these higher-order terms are not arbitrary, but guided by the physical requirement of restoring the apparent horizons. Such physically informed resummations have met with great success in general relativity, notably in the effective one-body formalism (see, e.g., [200]).

It would also be possible to resum the far zone metric: One can calculate its Newtonian part without making a multipole decomposition by proceeding in the same manner as in the calculation of the Liénard-Wiechert 4-potential in electrodynamics (as given in, e.g., §14.1 in Jackson [201]). However, we have not pursued this line of investigation further. Simone *et*

[9]The figures are not directly comparable, since the one in Paper II plots the *xx* components of the metrics, not their volume elements. However, the plot of just the *xx* components of this paper's inner and near zone metrics displays the same behavior as that of the volume elements, including roughly the same numerical values for the difference between the metrics.

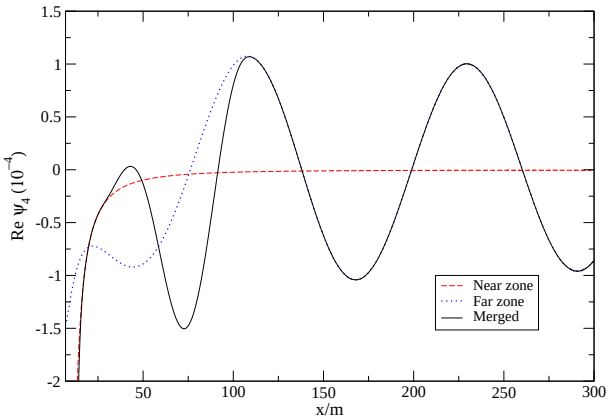

Fig. 2.9. The real part of the Newman-Penrose scalar ψ_4 of the near, far, and merged metrics computed for our equal-mass test system and displayed in the vicinity of the near-to-far transition, as well as the far zone proper, and even some of the inner-to-near transition (included to show how the near and far zone metrics compare close to the binary).

al. [153] performed a related resummation of the Newtonian pieces of the luminosity of an extreme mass-ratio binary, though they did this by first calculating the multipole expansion and then resumming directly, while the resummation of the metric we are suggesting here would involve computing the integral directly, with no multipole expansion of the Newtonian part. This resummation amounts to using the metric of two point particles in the first post-Minkowskian approximation. The resulting Liénard-Wiechert solution has been considered by, e.g., Kopeikin and Schäfer [202] [see their Eq. (10)], and second-order corrections have been computed by Thorne and Kovács [203].

With these points in mind, let us now describe the near zone resummation in detail, exemplifying it using the purely temporal component of the metric. In PN harmonic coordinates, this component of the Schwarzschild metric takes the form $-(R-M)/(R+M)$. Here R is the harmonic radial coordinate and M is the hole's mass. (As our use of "R" indicates, this is the same radial coordinate as in Cook-Scheel harmonic coordinates—see Appendix A for a comparison of the two coordinate systems.) We expect to have $m_1 \to M$ and $r_1 \to R$ as $m_2 \to 0$, which suggests that the purely temporal component of the PN metric should approach $-(r_1 - m_1)/(r_1 + m_1)$ as $m_2 \to 0$. The far field asymptotic expansion of this metric component (i.e., for $r_1 \gg m_1$) is given by

$$-1 + \frac{2m_1}{r_1} - \frac{2m_1^2}{r_1^2} + O\left(\left[\frac{m_1}{r_1}\right]^3\right). \tag{2.50}$$

This identically reproduces all the terms in the PN near zone metric in the limit $m_2 \to 0$. We then resum the PN near zone g_{00} by taking

$$g_{00} - g_{00}^{\rm old} = -\frac{r_1 - m_1}{r_1 + m_1} - \left(-1 + \frac{2m_1}{r_1} - \frac{2m_1^2}{r_1^2}\right) + (1 \leftrightarrow 2), \tag{2.51}$$

where $g_{00}^{\rm old}$ is the version of this component without resummation, given in Eq. (2.4a).

A similar procedure can be applied to the spatial sector of the metric. Carrying this out, we obtain

$$g_{kl} - g_{kl}^{\rm old} = \frac{r_1 + m_1}{r_1 - m_1} n_{kl}^{(1)} + \left(1 + \frac{m_1}{r_1}\right)^2 \left[\delta_{kl} - n_{kl}^{(1)}\right] - \left[\left(1 + \frac{2m_1}{r_1} + \frac{m_1^2}{r_1^2}\right)\delta_{kl} + \frac{m_1^2}{r_1^2} n_{kl}^{(1)}\right] + (1 \leftrightarrow 2). \tag{2.52}$$

where $n_{kl}^{(1)} := x_1^k x_1^l / r_1^2$ and $g_{kl}^{\rm old}$ is given by Eq. (2.4c). One can check that g_{kl} reduces to $g_{kl}^{\rm old}$ identically as $m_2 \to 0$.

We have used the unboosted Schwarzschild metric in PN harmonic coordinates to resum the PN metric here, since it is this background that the PN metric approaches in the $m_2 \to 0$ limit. We thus cannot resum the spatiotemporal components of the metric, since they already match the background in this limit. If we had first transformed the PN metric to Cook-Scheel coordinates, then we would have been able to resum the background so that it exactly matched that of the inner zone metric. This would have guaranteed a better agreement, and would have probably also given a merged metric with smaller constraint violations, since there would be no coordinate singularity at the horizons in the resummed near zone metric. Additionally, we could have introduced the expected Lorentz boost due to the hole's orbital motion, which might also have improved the matching, and would probably improve the data's properties when evolved (since all the pieces we add in the resummation would have the appropriate evolution, at least to lowest order).

However, if we had chosen this route, we would have had to pick some region surrounding the buffer zone for each hole in which to perform this transformation. This would have introduced further complications that we thought it best to avoid in this implementation, even at the possible cost of somewhat poorer matching. Moreover, the background resummation procedure that we have implemented has indeed improved the matching, as can be seen in Fig. 2.5: The improvement is particularly striking for the extended version of the near zone metric, where the region in which the $t = 0$ slice is no longer spacelike moves closer to the horizon and the graph of its volume element now crosses that of the near zone in the buffer zone outside of the orbit. But resummation also improves the matching of the original data: The resummed version of the $O(v^4)$ near zone metric agrees more closely with the inner zone metric than does the unresummed version.

2.8.2 Transition functions

We now turn to the process of stitching the inner and near zone metrics together numerically. It is necessary to interpolate between the various metrics in *transition regions* (located inside the buffer zones) in order to stitch the metrics together with no discontinuities. A simple way to do this is to use a weighted average of the metrics, where the precise way this average is carried out is determined by a C^∞ *transition function* $F_{AB} : \mathbb{R}^3 \to [0, 1]$. This function should have the property that $F_{AB}(\vec{x}) = 0$ if $\vec{x} \in C_A \cap O_{AB}^{\complement}$ and $F_{AB}(\vec{x}) = 1$ if $\vec{x} \in C_B \cap O_{AB}^{\complement}$. Here $O_{AB}^{\complement}$ is the complement of the buffer zone between zones C_A and C_B. (These conditions guarantee that the transition takes place completely inside the buffer region.) If we just consider two metrics, $g_{\alpha\beta}^{(A)}$ and $g_{\alpha\beta}^{(B)}$, for simplicity, then the resulting merged metric is given by $[1 - F_{AB}]g_{\alpha\beta}^{(A)} + F_{AB} g_{\alpha\beta}^{(B)}$.

(We have suppressed the position dependence of the transition functions and metrics, for notational convenience.)

In principle, these conditions are all one would impose on possible transition functions. (One might also want to stipulate that F_{AB} be "increasing as one moves from C_A to C_B," where this would have to be interpreted in some appropriate sense.) One could then contemplate minimizing some appropriate norm of the constraint violations of the resulting merged metric (outside, say, the apparent horizons) over all possible transition functions satisfying these requirements [204]. Our approach will be significantly less ambitious, leaving a systematic study of transition functions to later work, probably that accompanying an evolution of the data.

However, as Yunes [151] realized, one can exclude from consideration *a priori* any transition functions that would induce larger (formal) constraint violations in the data than those due to the uncontrolled remainders of the individual metrics. The so-called Frankenstein theorems enunciated in [151] provide conditions on the transition functions that are sufficient to exclude all such functions that lead to this undesirable behavior. These conditions are that the first and second derivatives of F_{AB} be $O(\epsilon_A, \epsilon_B)$ and $O(\epsilon_A^0, \epsilon_B^0)$, respectively. (Here ϵ_A represents the small parameters associated with zone A.) As discussed in Sec. 2.1.1, the theorems imply that initial data obtained using transition functions satisfying these conditions will satisfy the constraint equations to the same formal order as the constituent pieces of the initial data do. We shall explicitly verify that our transition functions respect these conditions.

We have made simple choices for the geometry of the transition regions, using spherical symmetry whenever possible, even though neither the binary nor the holes are spherically symmetric.[10] We have implicitly acknowledged the latter in the inner-to-near transitions by introducing another transition function (called $f_{\rm near}$ and discussed below) that only depends on x, the Cartesian coordinate along the axis passing through the holes at $t = 0$. While we do not have to worry about our transition functions' lack of time dependence (which one would expect to be present, because the transition regions change position as the binary evolves), since we perform all our stitching-together on the initial hypersurface, this time dependence would affect the results if one chose to obtain initial data from the merged 4-metric.

Moreover, we shall only consider one particular form for the transition functions, viz., the same form used in Papers I and II:

$$f(r, r_0, w, q, s) := \begin{cases} 0, & r \leq r_0, \\ \frac{1}{2}\left(1 + \tanh\{(s/\pi)[\chi(r, r_0, w) - q^2/\chi(r, r_0, w)]\}\right), & r_0 < r < r_0 + w, \\ 1, & r \geq r_0 + w, \end{cases} \quad (2.53)$$

where $\chi(r, r_0, w) := \tan[\pi(r - r_0)/2w]$. The effects the parameters have on f is discussed after Eq. (16) in Vega *et al.* [205]. (Vega *et al.*'s x_0 corresponds to our r_0.) Additionally, despite its piecewise definition, f is in fact C^∞ if $s > 0$: One can check directly that f itself is continuous; all its derivatives are continuous since all the derivatives of tanh vanish at infinity. The full

[10] One possibility for obtaining transition functions that better respect the binary's geometry would be to have them be functions of the binary's Newtonian potential (so their level surfaces are equipotentials), possibly supplemented with relativistic terms.

merged metric is thus

$$\begin{aligned} g_{\alpha\beta} = [1 - f_{\rm far}(r)]\Big(f_{\rm near}(x)\{ f_{{\rm inner},1}(r_1) g^{(3)}_{\alpha\beta} + [1 - f_{{\rm inner},1}(r_1)] g^{(1)}_{\alpha\beta}\} \\ + [1 - f_{\rm near}(x)]\{ f_{{\rm inner},2}(r_2) g^{(3)}_{\alpha\beta} + [1 - f_{{\rm inner},2}(r_2)] g^{(2)}_{\alpha\beta}\}\Big) + f_{\rm far}(r) g^{(4)}_{\alpha\beta}, \end{aligned} \tag{2.54}$$

where $g^{(A)}_{\alpha\beta}$ denotes the metric that lives in zone A (see Fig. 2.2 for the numbering system, and recall that we obtain $g^{(2)}_{\alpha\beta}$ from $g^{(1)}_{\alpha\beta}$ using the transformation given at the beginning of Sec. 2.5.1) and

$$\begin{aligned} f_{\rm far}(r) &:= f(r, \lambda/5, \lambda, 1, 2.5), \\ f_{\rm near}(x) &:= f(x, 2.2m_2 - m_1 b/m, b - 2.2m, 1, 2.5), \\ f_{{\rm inner},A}(r_A) &:= f(r_A, 0.256 r_A^{\rm T}, 3.17(m^2 b^5)^{1/7}, 0.2, b/m). \end{aligned} \tag{2.55}$$

Here x denotes the near zone (PN harmonic) x-coordinate; $\lambda = \pi\sqrt{b^3/m}$ is the Newtonian wavelength of the binary's gravitational radiation; and $r_A^{\rm T} = (m_A^3 b^5/m)^{1/7}$ is the "transition radius," obtained by requiring that the leading orders of the uncontrolled remainders be comparable in the inner and near zones [$(m/b)(r_A^{\rm T}/b)^4 = (m_A/r_A^{\rm T})^3$]. For convenience, we shall refer to the value of a parameter appearing in a particular transition function by transferring that transition function's subscript to the parameter's name, e.g., $w_{{\rm inner},A} := 3.17(m^2 b^5)^{1/7}$.

With these choices for the parameters, the transition functions satisfy the hypotheses of the first Frankenstein theorem, given above: For instance, the nth spatial derivatives of $f_{\rm near}$ and $f_{\rm far}$ scale as $w_{\rm near}^{-n} \propto b^{-n} \propto v^{2n}$ and $w_{\rm far}^{-n} = 1/\lambda^n \propto v^n$, respectively. Matters are a bit more complicated for $f_{{\rm inner},A}$: It satisfies the hypotheses since its spatial derivatives decrease rapidly when $v \to 0$. This occurs because these derivatives involve sech with an argument that goes to infinity as $v \to 0$ [since $s_{{\rm inner},A} \propto v^{-2}$] and sech is rapidly decreasing at infinity.

We determined the parameters we use for the transition functions by experimenting with different choices. We found that the values given in Eqs. (2.55) produced the smallest overall constraint violations along the x-axis for our equal-mass test system (with $b = 10m$) of all the choices we tried. Except for the near-to-far zone transition, which is completely new, these choices are very similar to those in Paper II. (In fact, despite the way it is written, our $f_{\rm near}$ agrees exactly with its analogue from Paper II, the function G.) The most important difference is the scaling of the transition width, $w_{{\rm inner},A}$. Both Papers I and II took $w_{{\rm inner},A}$ to scale with $r_A^{\rm T}$, so it depends on the system's mass ratio; in particular, it goes to zero as $m_A \to 0$. (Note that our $f_{{\rm inner},A}$ corresponds to F_A in Papers I and II.) We have found that this choice for $w_{{\rm inner},A}$ results in large transition-induced constraint violations near the smaller black hole for unequal mass ratios. These constraint violations appear to increase without bound as the mass of the smaller hole goes to zero. This is as one would expect, since the gradient of the transition function blows up as the transition width goes to zero, leading to an unbounded increase in constraint violations—see [151] and the above discussion of the Frankenstein theorems.

We can obtain a better-behaved transition function by freezing the dependence of $w_{{\rm inner},A}$ on the mass ratio, as we have done here. (We also have a slightly different coefficient of $r_A^{\rm T}$ than in Paper II, even for an equal-mass system.) The other differences between our $f_{{\rm inner},A}$ and Paper II's F_A are a slightly different coefficient of the transition radius in $r_{0,{\rm inner},A}$, in addition to a new transition radius that reflects the higher-order matching that we have performed here.

(The transition radius, $r_A^{\rm T}$, was slightly misleadingly called the matching radius and referred to as r_A^M in Paper II.)

The choices for the transition functions' parameters determine effective boundaries for the various zones. These are given in Table 2.3 for our equal-mass test binary. This table displays both the formal boundaries (i.e., the numerical values of the boundaries given in Sec. 2.2) as well as the effective boundaries (i.e., the boundaries determined by our choices of parameters for the transition functions). What we call the complete effective boundaries are determined by the entire region in which we use a given metric, even if the coefficient of the metric (due to the transition functions) is very small in a portion of the region. What we refer to as the practical effective boundaries are cut off when the coefficient of the metric becomes smaller in magnitude than 10^{-4} [i.e., much smaller than the magnitude of the uncontrolled remainders, which are $\sim (b/m)^{-5/2} \simeq 3\times 10^{-3}$].

Zone	Formal boundaries	Effective boundaries	
		Complete	Practical
Inner	$r_A \ll 10m$	$r_A \leq 17.4m$	$r_A \leq 11.2m$
Near	$r_A \gg 0.5m$, $r \lesssim 15.8m$	$r_A \geq 0.985m$, $r \leq 119m$	$r_A \geq 1.27m$, $r \leq 109m$
Far	$r \gtrsim 15.8m$	$r \geq 19.9m$	$r \geq 30.4m$

Table 2.3. The zone boundaries for our equal-mass test binary ($b = 10m$).

The effective inner zone boundaries given in Table 2.3 are not quite correct: Since even the practical effective boundaries of the inner zones are greater than half the distance between the holes for $b = 10m$ (as they are for an equal-mass binary, with our choice of transition functions, for $b \lesssim 165m$), one needs to introduce a third transition function, here called $f_{\rm near}$, to effect the transition between the holes. (See Sec. VI B of Paper I for further discussion; this function is referred to as G in Papers I and II.) With our choice of parameters, $f_{\rm near}$ cuts off the complete effective inner zone when the x-coordinate is closer than $1.1m$ to (the x-coordinate of the point particle associated with) the other hole. The practical effective inner zone is cut off when the x-coordinate is $1.93m$ away from the other hole.

In $f_{\rm far}$, one might be concerned that even the practical effective transition region extends well outside of the standard outer boundary of the near zone, viz., $r \simeq \lambda\!\!\!^{-}$. Indeed, it is quite possible that blending in the near zone metric in a region where its perturbative treatment of retardation is not warranted will introduce significant phase errors in the binary's outgoing wave train. However, our choice of transition region is justified (at least for this preliminary construction of transition functions) by the (relatively) large constraint violations of the far zone metric at the inner edge of our transition region, as is shown in Fig. 2.11.

The matching is illustrated in our plots of ψ_4 for the merged and constituent metrics, given in Figs. 2.8 and 2.9. (Recall that we use the full extended version of the data in all plots

unless otherwise noted.) It is clear that the transition functions have introduced undesirable features into the initial data. Some of this is probably unavoidable at a separation of $b = 10m$, which is relatively close for this construction. However, it seems likely that one could choose transition functions that would stitch the metrics together with (at least somewhat) smaller additional features, though we have not investigated this here.

2.8.3 Constraint violations

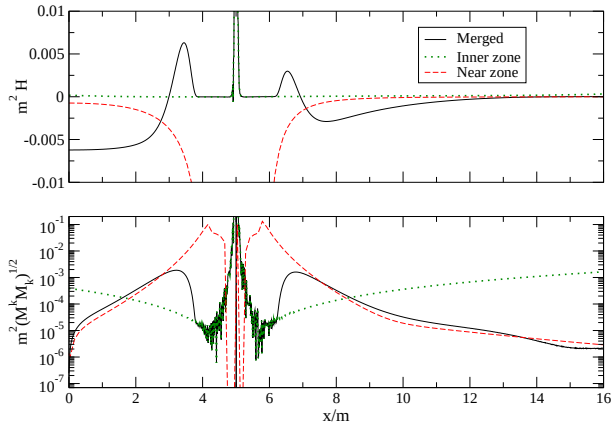

Fig. 2.10. The constraint violations of the merged, inner zone, and near zone metrics. These are plotted along the x-axis around hole 1 for our standard equal-mass test system.

The constraint violations provide a more sensitive check on how well the transition functions are working than the previous subsection's plots, in addition to giving a measure of the accuracy of the entire initial data construction. We compare the constraint violations (computed using BAM [67, 68]) of the individual metrics to those of the merged metric for our equal-mass test system along the x-axis in Figs. 2.10 and 2.11. (We have checked that the constraint violations behave roughly similarly—and are not significantly worse—in the y- and z-directions.) For the norm of the momentum constraint, M_k, we have chosen $\sqrt{M^k M_k}$, where the index is raised using the (merged) metric. [See, e.g., Eqs. (14)–(15) in [137] for expressions for the constraint equations; we denote the Hamiltonian constraint by H.] N.B.: While the plots we display do not cover the entire inner-to-near transition, the constraint violations' behavior in the portion we do not show is analogous to the portion we do show.

All the constraint violations decrease at least as rapidly as $b^{-5/2}$, the expected scaling of the largest uncontrolled remainders. (The expected scaling of the uncontrolled remainders in the near and far zones is b^{-3}, due to the additional terms added in Sec. 2.7 and the constraint violations decrease more rapidly than this in those regions.) This is illustrated in Figs. 2.12 and 2.13 in the inner and near zones, and in Fig. 2.14 in the far zone. In fact, one can see that the decrease of the maximum constraint violations in a given region is *much* more rapid than

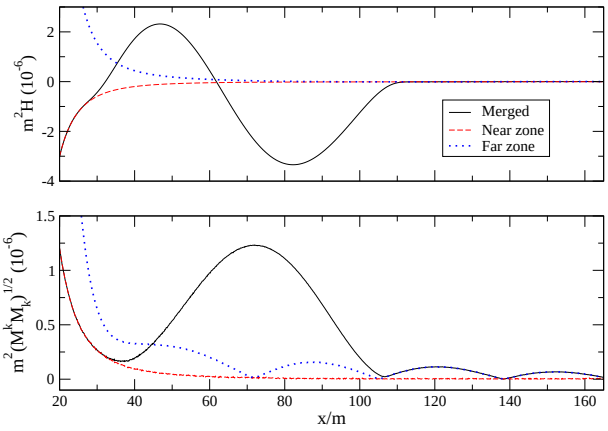

Fig. 2.11. The constraint violations of the merged, near zone, and far zone metrics. These are plotted along the x-axis in a region including the portion of the near-to-far transition region to the right of hole 1. As usual, this is done for our standard equal-mass test binary.

$b^{-5/2}$ (or b^{-3}, in the near and far zones), proceeding at b^{-n}, with $n \gtrsim 5$, for everything except the Hamiltonian constraint in the inner-to-near transition. For the latter it is only slightly more rapid (n slightly larger than $5/2$). This is, in fact, the region (outside of the horizons) where the merged metric has the largest constraint violations. These are likely due in part to the near zone metric's large constraint violations near the horizons, which themselves are primarily attributable to the coordinate singularity at the horizons. (Recall that the horizons are approximately $.5m$ away from the positions of the point particles in our test system—the effects of the new coordinates and tidal distortion are small.) However, it is not clear why the momentum constraint violations in the inner-to-near transition decrease so much faster with b than do the Hamiltonian constraint violations.

The much faster decrease of the constraint violations with increasing b than naïve scaling arguments would predict is not unexpected, at least for the far zone metric, though the reasonably simple arguments we have tried cannot quite reproduce the scaling we observe, just predicting a decrease that is faster than the naïve prediction. In the far zone metric, all the uncontrolled remainders come with a factor of m/r, and since the inner boundary of the far zone scales as $b^{3/2}$ [see the discussion in Sec. 2.2 and around Eqs. (2.55)], this leads to a leading-order scaling of $b^{-9/2}$ in the constraint violations, coming from two spatial derivatives acting (via retarded time dependence) on the v^4 part of uncontrolled remainders of the form $(m/r)v^4$. The observed scaling is b^{-n}, with $n \gtrsim 6.5$. It is possible that at least some of this faster decrease than the naïve prediction is due to the addition of all the higher-order terms (discussed in Sec. 2.7).

For a separation of $10m$, the relatively large constraint violations of the merged initial data compared to those of the individual metrics' initial data are an indication that this separation is close to the minimum for which the hypotheses underlying the data's construction are valid: For instance, as seen above, for this separation (and an equal-mass binary), the two inner-to-near transition regions overlap between the holes, meaning that much of the inner-to-near transition

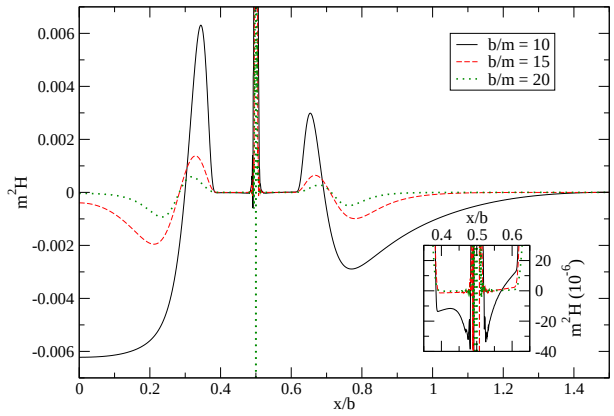

Fig. 2.12. The Hamiltonian constraint around hole 1 for an equal-mass binary with separations of 10m, 15m, and 20m. For ease of comparison, we have scaled the x-axis by b so that (the point particle associated with) hole 1 is always at the same position. In the inset, we zoom in to show how the inner zone constraint violations vary with b.

is effected by f_{near}—see Table 2.3 and the surrounding discussion. Moreover, as we have seen previously, the $t = 0$ slice of the near zone metric is not even spacelike at some points outside the holes' horizons for $b = 10m$. However, this does not adversely affect the merged metric with our choices of transition regions. If one tries closer separations, things are significantly worse. For instance, for a separation of 6m, the maximum constraint violations are larger than those for 10m by a factor of 10 or more. Furthermore, the points at which the near zone metric's $t = 0$ timeslice is no longer spacelike can cause problems for such small separations with our transition functions if one obtains the initial data by merging the individual metrics' initial data sets, as we have done. (However, if one obtains data directly from the merged 4-metric, then the $t = 0$ slice remains spacelike with our transition functions for initial separations at least as small as 5m [206].)

We compared the constraint violations of the new data with the old data (for our standard test system) in Fig. 2.1 and Table 2.1 in Sec. 2.1.1, though we deferred a more detailed discussion to here: First, it is important to realize that the comparison could be somewhat misleading, since each paper's data are in a different coordinate system. (The data from Paper I are in the same harmonic coordinate system as this paper's data in the near zone. However, this is only true perturbatively in the inner zone, where the black hole background is in a coordinate system that is not horizon-penetrating.)

Second, while our data's Hamiltonian constraint violations are not appreciably better than those of the data from Paper II, even though we have matched to higher order, this is not unexpected: Even though we used horizon-penetrating coordinates for the black hole metrics, we used standard PN harmonic coordinates for the PN metric; these coordinates are singular at the horizon. While the merged metric has no coordinate singularities, the PN metric's coordinate singularity increases the constraint violations in the transition regions, making them comparable

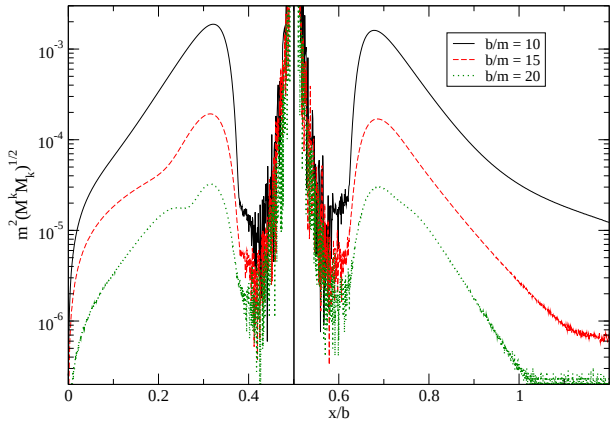

Fig. 2.13. The norm of the momentum constraint around hole 1 for an equal-mass binary with separations of $10m$, $15m$, and $20m$. For ease of comparison, we have scaled the x-axis by b so that (the point particle associated with) hole 1 is always at the same position.

to those from Paper II: Paper II's data use a PN metric with no coordinate singularity as well as even further resummation of the black hole backgrounds than we have employed here, leading to particularly small constraint violations.

Finally, if one compares Fig. 2.1 with, e.g., Figs. 14 and 17 in Paper II, one notices differences in the behavior of the data from Papers I and II close to the hole (and inside the horizon). This is because we have generated the plot using higher-order finite differencing (fourth order vs. second order) and a higher resolution ($0.002m$ vs. $0.008m$) in computing the constraint violations here than we did in first computing them in Paper II. It was necessary to do this to accurately resolve the constraint violations in the inner zone, since the metric components diverge rapidly there. Additionally, we have used the version of Paper II's metric that is in horizon-penetrating coordinates, while Figs. 14 and 17 in Paper II were generated using the version of the data without that additional coordinate transformation: The transformation to horizon-penetrating coordinates introduces further structure in the data's constraint violations.

We can also compare the constraint violations of the full extended data with those of the $O(v^4)$ and $O(v^5)$ versions. We do this in the inner-to-near transition in Fig. 2.15 for a binary with a mass ratio of $3:1$, and in the near-to-far transition, along with the far zone proper, for that binary, as well as an equal-mass binary in Fig. 2.16. [We consider a unequal-mass binary to make the differences between the $O(v^4)$ and $O(v^5)$ versions more pronounced: Most of the $O(v^5)$ terms in the far zone metric vanish for an equal-mass binary.]

In the latter plot (Fig. 2.16), we do not show the differences between the $O(v^4)$ and full extended versions' Hamiltonian constraint in the far zone proper, as they agree up to the level of numerical truncation error. We also do not show the differences between the $O(v^5)$ and full extended versions of the data. These two sets only differ substantially in the far left-hand portion of the transition region, and even there the differences are several orders of magnitude less than those between the $O(v^4)$ and full extended versions. Additionally, we do not show the behavior

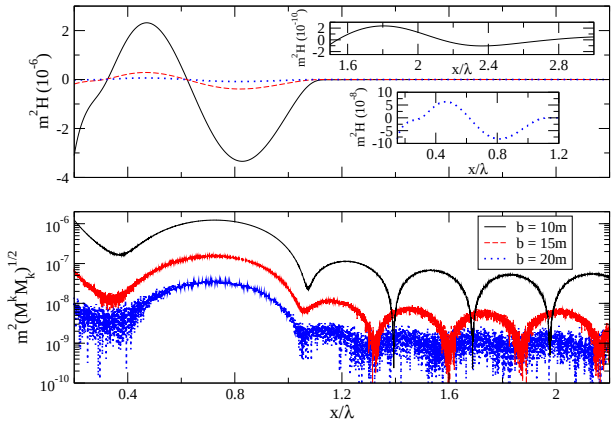

Fig. 2.14. The constraint violations along the x-axis in the portion of the near-to-far transition and far zone proper that lies to the right of hole 1. These are computed for an equal-mass binary with separations of $10m$, $15m$, and $20m$. For ease of comparison, we have scaled the x-axis by $\lambda = \pi\sqrt{b^3/m}$, the Newtonian wavelength of the binary's gravitational radiation. In the two insets, we zoom in to better illustrate the behavior of the Hamiltonian constraint in two situations: In the lower inset, we consider the $b = 20m$ data in the transition region. In the upper inset, we consider the $b = 10m$ data in the far zone proper. (The other data sets also display similar oscillations in their Hamiltonian constraint in the far zone, though the amplitude of these oscillations is too small to be visible on the scale we use to display the oscillations of the $b = 10m$ data's Hamiltonian constraint.)

of the constraint violations to the left of the smaller hole (hole 2): It is qualitatively similar to their behavior to the right of the larger hole shown here, except that for an equal-mass binary, the $O(v^4)$ version of the data has smaller Hamiltonian constraint violations than the full extended version in that region, and for a mass ratio of $3:1$, there is no oscillation in the transition region in the $O(v^4)$ data's momentum constraint violations.

We compare the constraint violations of the different inner zone versions in Fig. 2.17 for binaries with mass ratios of $1:1$ and $3:1$. In this plot, we do not include the version of the inner zone with no fourth order octupole pieces, as the inclusion of those terms does not affect the constraint violations in the inner zone proper at a level above numerical truncation error. However, these terms *do* have a noticable effect on the constraint violations in the inner-to-near transition, as can be seen in Fig. 2.18, which compares the $O(v^4)$ data with and without the fourth-order octupole terms in the inner zone. (The fact that including the fourth order octupole terms in the inner zone metric makes a much larger difference in the merged metric than in the inner zone metric itself in the transition regions suggests that the additional terms that have the most significant effect are the ones in the coordinate transformation, not those in the tidal fields.)

It is also interesting to consider how accurate the data are for different mass ratios. One finds that the constraint violations do not behave quite as well as might be desired in the inner-to-near transition regions as one increases the mass ratio. This is shown in Figs. 2.19 and 2.20,

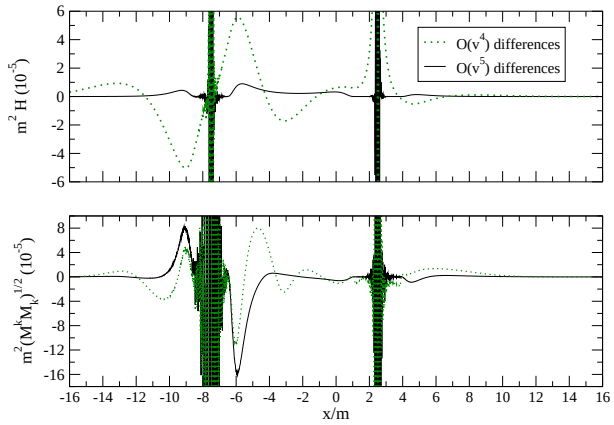

Fig. 2.15. The constraint violations of the $O(v^4)$ and $O(v^5)$ sets of data minus those of the full extended set of data. These are computed along the x-axis in the inner-to-near transition region for a binary with $b = 10m$ and a mass ratio of 3 : 1. (The more massive hole is on the right.)

which plot the Hamiltonian constraint and norm of the momentum constraint for mass ratios of 1 : 1, 3 : 1, 5 : 1, and 10 : 1. The worst behavior is that of the momentum constraint in the transition region near the more massive hole (hole 1), which increases as the mass of that hole increases. The Hamiltonian constraint also increases with mass ratio in the inner zones around both holes. (This is due to the inclusion of the full time dependence of the tidal fields—the inner zone constraint violations decrease with mass ratio if one only uses the version of the inner zone metric with perturbative time dependence.) The behavior of the other constraint violations is nonmonotonic. When one looks at the near-to-far transition and far zone proper one finds much better behavior: The constraint violations decrease with increasing mass ratio in all of those regions, except for a slight increase in the momentum constraint violations in the far zone proper for unequal mass ratios. This is visible for a mass ratio of 3 : 1 in Fig. 2.16; we do not display the results for higher mass ratios, since they are not particularly interesting.

This behavior in the transition regions is primarily attributable to the choices we have made for the transition functions. For instance, it is possible to choose parameters so that the momentum constraint violations *decrease* around the more massive hole as its mass increases. This can be accomplished by taking $w_{\mathrm{inner},A} \propto r_A^{\mathrm{T}}$, as in Papers I and II. However, with this choice, the decrease in momentum constraint violations around hole 1 occurs at the cost of the aforementioned extreme increase in constraint violations around hole 2 as its mass goes to zero. It should be possible to combine the two choices for $w_{\mathrm{inner},A}$ to obtain better behavior for unequal mass ratios, but we have chosen to leave such fine-tuning of transition functions to future work, contenting ourselves with providing examples of workable transition functions here.

It is instructive to compare our data's constraint violations with the constraint violations that occur in an evolution of the data. Of course, one expects that the highly accurate simulations that will provide templates for parameter estimation with Advanced LIGO and LISA will have much smaller evolution-induced constraint violations than current simulations. (And, of course,

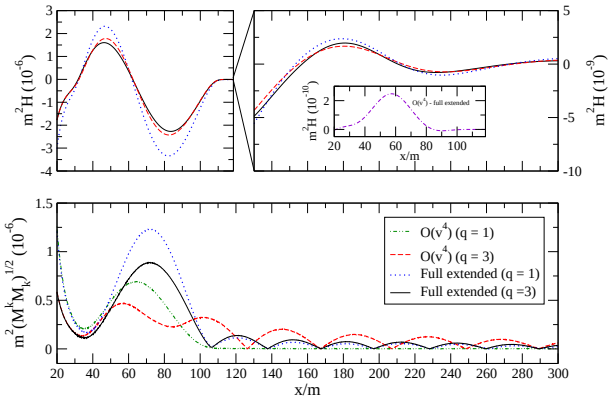

Fig. 2.16. The constraint violations of the $O(v^4)$ and full extended sets of data. These are computed along the x-axis in the near-to-far transition region (and far zone proper) to the right of hole 1 for binaries with $b = 10m$ and mass ratios of $1:1$ and $3:1$. (The more massive hole is on the right.) In the right-hand panel, we zoom in to show the differences in the oscillation of the Hamiltonian constraint in the far zone proper. In the inset, we show the difference between the Hamiltonian constraint violations of the $O(v^4)$ and full extended versions of the data in the near-to-far transition for an equal-mass binary.

the constraint violations do not themselves give an indication of the data's astrophysical realism.) However, current simulations' constraint violations give a convenient scale against which to compare the constraint violations of our data.

The evolution with which we will compare is the equal-mass nonspinning run from the set of 10 runs used in [143] to fix the spin coefficients. It starts at a coordinate separation of $\sim 6.79M$, where M is the binary's mass. (We use M since this mass is in general different from our data's PN mass, m.) The initial constraint violations in this evolution have a maximum magnitude (scaled by M^2) outside the apparent horizons of at least $\sim 10^{-5}$ for the Hamiltonian constraint and $\sim 5\times10^{-6}$ for the norm of the momentum constraint. After a quarter of an orbit, the constraint violations have already increased to $\sim 3\times10^{-4}$ for both the Hamiltonian constraint and the norm of the momentum constraint. The maximum Hamiltonian constraint violations (outside the apparent horizons) remain at about this level for the remainder of the evolution. The momentum constraint violations relax to smaller values as the evolution proceeds, with maxima (outside the apparent horizons) rapidly approaching $\sim 10^{-5}$.

N.B.: Since the apparent horizons were not located numerically in this evolution, we have simply excluded a ball of radius M about each hole. It appears that the apparent horizons of the individual black holes are roughly balls of coordinate radius $M/2$ in an equal-mass evolution with the same computational setup (see Fig. 12 in [68]), but we exclude more of the spacetime to err on the side of caution. We are thus only able to quote lower bounds on the maximum constraint violation outside the apparent horizons.

For an initial separation of $10m$ (which is, admittedly, larger than the comparison run's initial separation) the constraint violations of our data are smaller than the evolution-induced

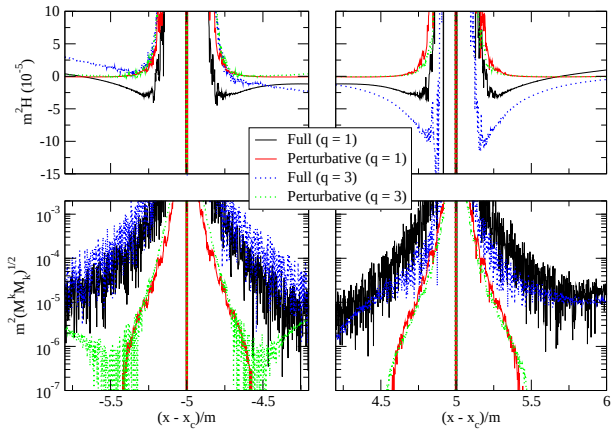

Fig. 2.17. The constraint violations of the versions of the inner zone metric with perturbative and full time dependence for binaries with $b = 10m$ and mass ratios of $1:1$ and $3:1$. We display these in the vicinity of both holes, which we shift in the $3:1$ case so their associated point particles lie at $x = \pm 5m$. [In the figure, $x_c := [1/(q+1) - 1/2]b$.]

constraint violations in that run everywhere except in the inner-to-near transition, where they are much larger. See, e.g., the sup norms given in Table 2.1, along with Figs. 2.12, 2.13, and 2.14. Our data's constraint violations decrease rapidly with increasing separation in the inner-to-near transition, as is shown in the first two figures, and the momentum constraint violations become smaller than the maximal evolution-induced violations discussed above—indeed, close to the "equilibrium" value of $\sim 10^{-5}$—for an initial separation of $20m$. However, even for such a (relatively) large initial separation, our data's maximum Hamiltonian constraint violations are still $\sim 10^{-3}$, close to an order of magnitude larger than the maximum evolution-induced constraint violations seen in the run discussed above.

This is not unexpected, since we are only guaranteed that the constraint violations will decrease as $b^{-5/2}$, due to the uncontrolled remainders in our approximations. As we saw above, the constraint violations actually decrease much more rapidly than this everywhere than in the Hamiltonian constraint in the inner-to-near transition, where the maximum constraint violations (for the three initial separations we considered) are given roughly by $2b^{-5/2}$ (in units of m^{-2}). Thus, for the maximum constraint violations to be $\sim 3\times10^{-4}$, we would need an initial separation of $\sim 34m$. (This is not a completely unreasonable initial separation: It leads to a merger time that is ~ 24 times the longest binary black hole simulation to date, that of [60]. Moreover, it is still small enough that it is unlikely that simulations starting from that initial separation and using conformally flat initial data would be accurate enough to provide templates for parameter estimation with Advanced LIGO and LISA, since $v^4_{\rm initial} \simeq 2\times10^{-3}$.)

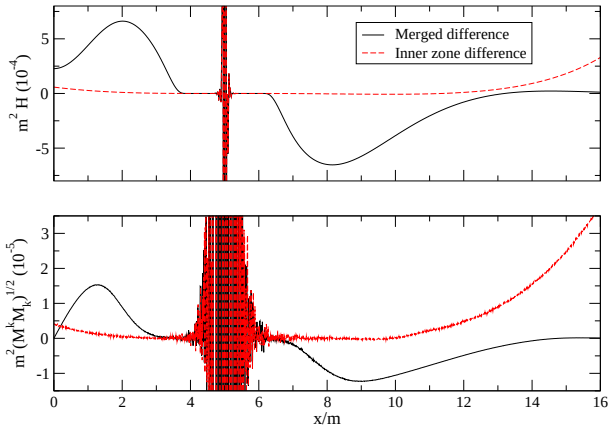

Fig. 2.18. The differences between the constraint violations of the version of the $O(v^4)$ data that omits the fourth-order octupole terms (`04_NoOct`) in the inner zone metric and the version including those terms (`04`). We show them along the x-axis near hole 1 for our standard test binary.

2.9 Conclusions

2.9.1 Summary

We have constructed approximate initial data for a nonspinning black hole binary in a quasicircular orbit. This data set has uncontrolled remainders of $O(v^5)$ throughout the timeslice (including the far zone), along with remainders of $O(v^3[R/b]^4, v^5[R/b]^3)$ in the inner zone. We have verified the scaling of the uncontrolled remainders with v by checking that the constraint violations decrease at least as rapidly as they should when the binary's orbital separation is increased. We constructed this data set by asymptotically matching perturbed black hole metrics onto a PN metric and creating transition functions to smoothly interpolate between the various metrics. The resulting data do not assume conformal flatness and contain the binary's outgoing radiation in addition to the tidal deformations on the holes. (We have included the quadrupole deformations through 1PN along with the lowest-order octupole deformations.)

The results of the matching are given in Sec. 2.5.7 and Eqs. (B.1): Sec. 2.5.7 gives directions for how to put together the coordinate transformation necessary to place the inner zone metric in the same coordinate system as the near zone metric (to the order we have matched). Eqs. (B.1) give explicit expressions for the tidal fields we obtained. [We also found that the inner and near zone mass parameters—i.e., M and m_1—agree through at least $O(v^3)$.] These tidal fields are then inserted into Detweiler's perturbed black hole metric, given in Cook-Scheel coordinates in Eqs. (2.2) and (2.3), to give the inner zone metric. The near and far zone metrics are given in Eqs. (2.4) and (2.48), respectively. We describe our method of computing the binary's past phase evolution, needed for the far zone metric, in Sec. 2.6.1, and the specifics of how we put together the various zones' metrics in Appendix D. Workable (though surely not optimal) transition functions that smoothly interpolate between the various zones' metrics are given in Sec. 2.8.2.

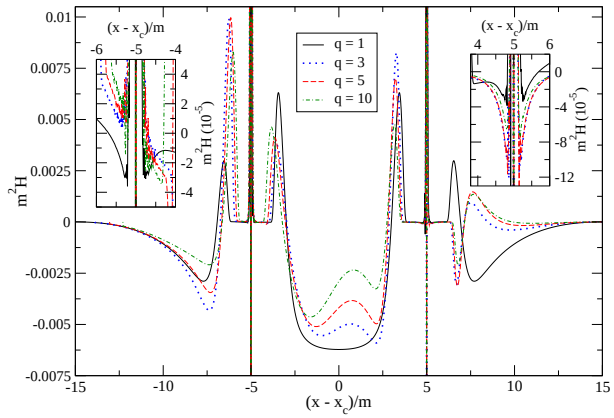

Fig. 2.19. The Hamiltonian constraint along the x-axis for a binary with a separation of $10m$ and mass ratios of $1:1$, $3:1$, $5:1$, and $10:1$ ($q := m_1/m_2$). (The more massive hole—hole 1—is on the right, and the less massive hole—hole 2—is on the left.) For ease of comparison, we have shifted all the data so that the point midway between the two particles is at $x = 0$. [In the figure, $x_c := [1/(q+1) - 1/2]b$.] In the two insets, we zoom in to show how the inner zone metric's constraint violations vary with q, looking at the region around each hole in the inset closest to it.

We have also constructed an extension of these data that is accurate through $O(v^5)$ in the near and far zones. Additionally, this extension includes the additional terms in the purely temporal component of the near zone metric that Blanchet, Faye, and Ponsot [166] give, as well as the matching terms in that component of the far zone metric. (We sketch the computation of these additional terms in Appendix C.) We also calculated the fourth-order octupole pieces of the tidal fields (and the associated piece of the coordinate transformation—see Appendix B.2—and included them, as well. (The 1PN correction to the electric octupole tidal field is among the terms we calculated and add here.) Additionally, we calculated the full time dependence of the tidal fields (for times much less than the radiation reaction timescale) and included it in the inner zone metric. This is discussed in Appendices B.1 and D. See Table 2.2 (in Sec. 2.7) for an overview of the different versions of the metrics we considered in the paper. N.B.: While we did not include this in the table, for the sake of clarity, we considered all the versions of the near zone metrics with and without background resummation, displaying the resulting differences in the volume elements [for the $O(v^4)$ and full extended versions] in Fig. 2.5. We found the full extended (`all`) data set (including background resummation in the near zone) to be the best, overall, considering constraint violations as well as the inclusion of terms that we expect to improve evolutions.

In the process of obtaining these data, we have developed a method of fixing the matching parameters when matching a black hole onto a PN background that differs from that presented by Taylor and Poisson [180] and is more automatable. We have also obtained the 1PN corrections to the magnetic quadrupole and electric octupole for a circular orbit using this method, neither of which Taylor and Poisson computed.

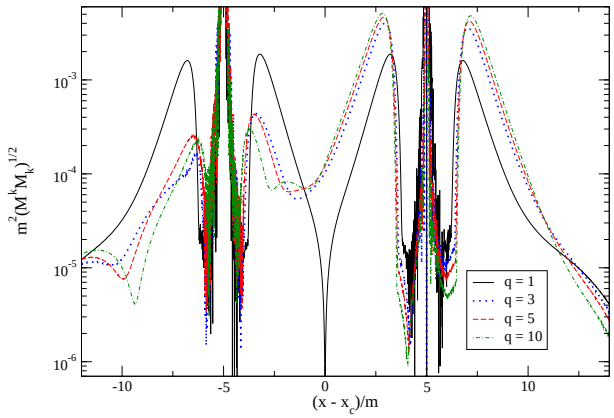

Fig. 2.20. The norm of the momentum constraint along the x-axis for a binary with a separation of $10m$ and mass ratios of $1:1$, $3:1$, $5:1$, and $10:1$ ($q := m_1/m_2$). (The more massive hole—hole 1—is on the right, and the less massive hole—hole 2—is on the left.) For ease of comparison, we have shifted all the data so that the point midway between the two particles is at $x = 0$. [In the figure, $x_c := [1/(q+1) - 1/2]b$.]

The accurate description of the tidal deformations on the holes contained in these data should substantially reduce the high-frequency component of the initial spurious radiation; the use of a high-order PN metric should do the same for the low-frequency component. (The combination of the high-order PN metric, including accurate expressions for the trajectories, and the reduced junk radiation should also give a much better quasicircular orbit—see, e.g., [131, 133].) If these data do indeed reduce the initial spurious radiation, then they can be used to directly quantify the effects of using the conformally flat initial data currently employed, as opposed to data that include many more of the system's expected physical properties. In addition, the waveforms generated using these data would be ideal for the construction of hybrid numerical relativity/post-Newtonian waveforms (as in [207]): Since the initial data are directly connected to the PN approximation, the PN parameters and phasing that are input into the initial data should accurately describe the subsequent evolution.

Of course, one needs to evolve the data to see whether these putative improvements are indeed realized. We have already coded this data set into MAPLE scripts, which were then converted to C code. Both the scripts and codes are freely available online at [152] to anyone who is interested in evolving or otherwise studying the data. Any evolutions of these data will need to use either excision [146, 147], or the turducken approach [150]: The black hole perturbations are not valid all the way to the holes' asymptotically flat ends, preventing the use of standard puncture methods. Additionally, since the data only satisfy the constraint equations approximately, one may want to project them onto the constraint hypersurface before evolution. To do this, one would need to use a code such as [158, 167, 208, 209]: The standard solver for puncture data [210] requires conformal flatness. However, evolutions of data that only approximately solve the constraints are possible: See, e.g., [65, 169].

2.9.2 Possibilities for future initial data constructions with this method

With this work, the asymptotic matching method for generating initial data for nonspinning binary black holes in a quasicircular orbit first essayed by Alvi [62] and further developed in Papers I and II has been taken to the highest order possible without further development in its constituent parts: Including higher multipole orders in the inner zone would require the input of nonlinear black hole perturbation theory (the requisite calculation has now been carried out by Poisson and Vlasov [171]). Iterating to higher orders in v would not only require the higher multipoles, but also an explicit expression for the $O(v^6)$ pieces of the purely spatial components of the near zone metric. Determining the higher-order-in-v pieces of the far zone metric would either require calculation of further contributions from the outer integrals in the DIRE approach [177], or obtaining the far zone metric via matching, following the post-Minkowskian approach of [183].

Nevertheless, it might still be possible to improve the initial data at the (formal) order presented here, as was done in Paper II for the data in Paper I. For instance, one could contemplate converting the near zone metric to Cook-Scheel coordinates (or some other horizon-penetrating coordinate system) in a neighborhood of each black hole. This would regain the complete agreement between background coordinates, with no coordinate singularity at the horizon in the near zone metric, that was found to improve the numerical agreement of the metrics in Paper II. One could also further tweak the transition functions, though this is not likely to produce any dramatic improvements in constraint violations. However, it is possible that different choices for the transition functions could improve the data's properties in evolutions. For instance, in the current near-to-far transition, the near zone metric is used (blended with the far zone metric) for $r \gg \lambda$, where its perturbative treatment of retardation leads to large phasing errors. It might thus be preferable to transition closer to the binary, even at the cost of greater constraint violations. (Resumming the far zone metric is a possibility for reducing these constraint violations, as was discussed briefly in Sec. 2.8.1.)

The prospects for generalizing this construction to include eccentricity or spin are good: The ingredients are nearly all readily available in the literature. Such a generalization—in particular, the inclusion of spin—would be an obvious next step if this initial data set indeed significantly reduces the spurious radiation. Including eccentricity would be straightforward, though algebraically involved, and can be carried out with the ingredients we have used here, perhaps supplemented with the results from [180]. (The evolution of the binary's phase and separation needed in the far zone metric can be obtained through 3PN order using the results of [211].)

However, it would only be possible to obtain the generalization of these data for a spinning binary to $O(v^2)$, formally, while still including all the formal quadrupole pieces in the inner zone. This is true even though the generalization of Blanchet, Faye, and Ponsot's metric to include spin (and spin-orbit coupling) is available [212],[11] as are the expressions for the source multipoles necessary to obtain the matching far zone metric [214]. (The binary's evolution under radiation reaction is also known through 2.5PN [215].) The bottleneck is the available tidally perturbed Kerr metric [216], which only includes the quadrupole perturbations. We have seen that knowledge of the octupole perturbations is necessary to carry out the matching of all the formal quadrupole pieces at $O(v^4)$ [which one would need to do to obtain data that are formally

[11] Errata for the potentials and equations of motion in [212] are given in footnotes 6 and 7 of [213], respectively.

valid through $O(v^3)$]. However, one could use the same philosophy we did when computing our extension and add the higher-order terms in the near and far zones without computing the matching inner zone terms.

Acknowledgments

We would like to thank Luc Blanchet, Steven Detweiler, Lee Lindblom, Eric Poisson, Frans Pretorius, and Clifford Will for useful discussions and clarifications. Additionally, we owe special thanks to Erik Schnetter for giving us an invaluable outsider's perspective on the usability of our codes, thus helping us catch a few typos and correct some unclear exposition. We also wish to thank the anonymous referee for suggesting the plots of ψ_4. This work was supported by the Penn State Center for Gravitational Wave Physics under NSF cooperative agreement PHY-0114375, by NSF grants PHY-0555628 and PHY-0855589 to Penn State, PHY-0652874 and PHY-0855315 to FAU, and PHY-0745779 to Princeton, as well as the Eberly research funds of Penn State.

Chapter 3

Shear modulus of the hadron–quark mixed phase

Hadron–quark hybrid stars are a reasonably robust possibility for exotic phases in compact stars. The lattice of quark and hadronic matter present in the cores of such stars has a large shear modulus, which leads to various interesting astrophysical effects, particularly in the realm of gravitational waves: It can allow the star to sustain a large elastic deformation and emit continuous gravitational waves, due to rotation; the energy stored in the lattice could also power the energetic flares observed from soft gamma repeaters, which are a possible source of gravitational wave bursts. We compute the relevant quantities for these sources in a companion paper, and here only concentrate on the shear modulus itself, which we find can be a few $\times 10^{33}$ erg cm^{-3} over a significant fraction of the maximum mass stable star for certain parameter choices. (As is often done, we describe the quark phase using the bag model plus first-order quantum chromodynamics corrections, and the hadronic phase using a relativistic mean-field model.) In this computation, we include the effects of charge screening (in the Debye model) and the lattice's varying dimension, in addition to angle averaging the full elastic modulus tensor to obtain the effective shear modulus (treating the mixed phase as a polycrystal). Most importantly, we include the contributions to the elastic modulus tensor from changing the cell size; these are necessary for the lower-dimensional phases to be stable. (For each set of equation of state parameters, there is a minimum surface tension for which this contribution is able to stabilize the lower-dimensional phases.) We deal with the varying dimension of the lattice using dimensional continuation, and give a method for computing such dimensionally continued lattice sums.

3.1 Introduction

Due to the high densities present in the centers of neutron stars,[1] it is reasonable to expect that they may contain deconfined quarks, by asymptotic freedom. This possibility was first suggested by Collins and Perry [217] (with previous, less concrete, suggestions due to Itoh [218] and Bodmer [219]—both of these were made before the discovery of asymptotic freedom), and has been much studied since (see, e.g., [87, 220, 221] for some representative work). Glendenning's realization [91, 92] (see also [222, 223] for reviews) that there could be a large region of hadron–quark mixed phase—creating a *hadron–quark hybrid star*—suggests some very interesting astrophysical implications, particularly for gravitational waves. Just like the nuclear "pasta" phases in the crust (first discussed by Ravenhall, Pethick, and Wilson [93]), the hadron–quark mixed phase is thought to form a lattice of varying dimensionality, due to the competition

This chapter is based on work done in collaboration with B. J. Owen which will be submitted to Phys. Rev. D.

[1] We use the term "neutron star" to refer to any compact stars made of cold-catalyzed matter, regardless of its actual composition.

between surface tension and the Coulomb force, as first suggested by Heiselberg, Pethick, and Staubo [224]. (These pasta phases are discussed in more detail in Sec. 3.2.3.)

This lattice will have a large shear modulus, due to a large charge separation (> 100s of elementary charges) and small lattice spacing (on the order of 10s of fm). Such large shear moduli can allow the star to sustain a relatively large nonaxisymmetric deformation (see, e.g., the discussion in [87]), in addition to providing a reservoir of energy that could potentially power large flares, such as those observed from magnetars [87, 225]. Obtaining better estimates for the shear modulus of the hadron–quark lattice is thus of interest to gravitational wave experiments such as LIGO: Nonaxisymmetric deformations of rotating bodies emit gravitational waves, and violent events on neutron stars could lead to a large enough rearrangement of the star's matter to emit gravitational waves (likely through excitation of the star's fundamental modes). Both of these scenarios are the subject of active LIGO searches (see [74, 75, 76, 77, 78, 79, 80, 81, 82, 83]).

One requires a reasonably large region of mixed phase in the star in order to be able to obtain large enough deformations and energies to be of current observational interest. However, there are no observational constraints that suggest that such large regions of mixed phase do not exist: The input parameters to the models of such stars are all unsure enough that there is no conflict between having a very large region of mixed phase, including all the pasta phases down to a quark core, as well a maximum mass compatible with the recent Demorest *et al.* measurement of a $1.97 \pm 0.04\,\mathrm{M}_\odot$ neutron star [95], as illustrated in Weissenborn *et al.* [221].

The shear modulus of this lattice was first estimated very roughly by Owen in [87]. A more careful estimate was made by Nayyar [94], who made a detailed calculation of the equation of state of the star and the structure of the mixed phase following Glendenning [223], though he still neglected many important effects, and had an uncorrected bug in his code.

We improve upon Nayyar's calculation in several ways. First, we give a proper treatment of the varying dimensionality of the pasta phases, including dimensional continuation [following the suggestion that Ravenhall, Pethick, and Wilson [93] made for the nuclear pasta in the crust, then applied to the hadron–quark pasta by Glendenning [222]]. We also perform the associated angle averaging to obtain a shear modulus from the (anisotropic) elastic modulus tensor (here assuming that there are many regions with random orientation, so the mixed phase can be treated as a polycrystal). In the calculation of the shear modulus itself, we perform a full lattice sum, include charge screening (using the Debye model), instead of simply multiplying the standard unscreened shear modulus for a body-centered cubic (bcc) lattice (from Fuchs [226]) by a correction factor, as done by Owen and Nayyar. (However, our linear treatment of charge screening is still quite rough, particularly since we treat the blobs as point charges.)

Perhaps most importantly, we include the contributions to the effective shear modulus that come from perturbations that change the volume of a unit cell (for $d < 3$). (The contributions from the changes to the cell's energy were included by Pethick and Potekhin [227] in considering the nuclear pasta in the crust, though Pethick and Potekhin do not appear to include the change in the charge of the blobs.) These contributions are necessary for the lattice to be stable (since purely electrostatic forces cannot produce a stable equilibrium, by Earnshaw's theorem), and even with their inclusion, we find that large portions of the lattice are unstable for sufficiently small surface tensions.

We use the standard models used by Glendenning [223] for the hadronic and quark equations of state (EOSs), as well as the standard Gibbs method for calculating the bulk properties and

lattice structure of the mixed phase (though we include the contribution from the surface tension to the pressure balance in certain EOSs, following [228, 229, 230, 231]; this is often neglected). Additionally, we use the simple Debye model for charge screening. This is very much a simplified treatment of screening effects, but a proper treatment (following, e.g., [228, 229, 230, 231]) would be much more computationally intensive than the remainder of our approach, so we have left such investigations to future work. Some indication of the magnitude of the error we make in using the Debye model can be seen in the jumps in the shear modulus in the figures in Sec. 3.6. (The recent work by Endo [231] shows that the mixed phase can still occupy a sizable region of the star, even with a full, nonlinear treatment of charge screening, though one cannot draw any definite conclusions about our results from Endo's, since Endo uses rather different EOS parameters.)

In order to perform the dimensionally continued lattice sums, we have developed a generalization of the standard Ewald method [232] (see [233] for a modern treatment). (This method was used by Fuchs [226] in his pioneering calculation of elastic coefficients, and has very recently been used by Baiko [234] in a calculation of the effective shear modulus of the neutron star crust.) The underlying dimensionally continued Poisson summation formula is discussed in Chap. 5. Here we describe the practical implementation to the situation at hand, including the details of the "Ewald screening function," and the dimensional continuation of the specific family of lattices we consider. We use electrostatic units and set $\hbar = c = 1$, so we will generally express masses in terms of MeV and lengths in terms of fm.

The paper is structured as follows: We review the models we use for the hadronic and quark EOSs (including our choices for the many poorly constrained parameters), and how we compute the bulk properties and lattice structure of the mixed phase in Sec. 3.2. We also indicate how we include charge screening (in the Debye model) in Sec. 3.2.4. In Sec. 3.3, we give an overview of the elastic response of the lattice for the various integer dimensions, and how we compute an average shear modulus in a dimensionally continued manner. We describe how to compute the relevant elastic constants in Sec. 3.4, and how to dimensionally continue the resulting lattice sums in Sec. 3.5. We give our results for the shear modulus in Sec. 3.6, along with some discussion, and conclude in Sec. 3.7. We discuss various checks on our computations of the lattice sums in Appendix E.

3.2 Mixed phase

We model the hadronic and quark phases following Glendenning [223], using a relativistic mean field theory model for the hadronic matter (from Glendenning's Chap. 4), and an improved bag model description of the quark matter (from Glendenning's Chap. 8). We have chosen to compute the EOSs "from scratch," instead of using any sort of tabulated EOS for various reasons. Doing this allows us to include the effects of surface tension on the EOS (as discussed in Sec. 3.2.3), and to investigate the effects of different EOS parameters on the shear modulus. It also lets us compute the Debye screening length, for which we need to know how the chemical potentials of the various particle species vary with density. The models we use for the hadronic and quark phases are relatively simple, but should contain at least a rough description of the relevant physics for the situation under consideration. (And given the significant uncertainties associated with any description of cold, dense matter, the use of a more sophisticated model may not be warranted.)

These EOSs depend on a variety of parameters, discussed in more detail in the following subsections. We consider a small collection of representative sets of parameters in this paper, given in Table 3.1. (We also present various results about the mixed phase for these equations of state in that table, as discussed in Sec. 3.6.) All of these parameter sets are chosen to yield a maximum Oppenheimer-Volkov (OV) mass compatible with the recent Demorest *et al.* [95] measurement of a $1.97 \pm 0.04\,\mathrm{M}_\odot$ neutron star. [Since the hadronic EOS we consider is only valid at reasonably high densities (well above neutron drip), we add on a standard low-density EOS for baryon number densities $n_B < 0.08$ fm^{-3}, viz., the combination of the Baym, Pethick, and Sutherland [235] EOS for $n_B < 0.001$ fm^{-3} and the Negele and Vautherin [236] EOS for 0.001 fm$^{-3} < n_B < 0.08$ fm^{-3} used by Lattimer and Prakash [237]. We use the table provided by Kurkela *et al.* [238] at [239]. However, the low-density part of the EOS only has a small effect on the maximum mass of a stable star.]

The Hy1 EOS is taken from Nayyar [94];[2] the Hy1′ EOS changes one of the quark EOS parameters (the bag constant) to obtain a much larger region of mixed phase (with many more pasta phases) in stable stars. The Hy1μ and Hy1σ EOSs each change the treatment of one portion of the calculation to give some indication of how much these affect our results: Hy1μ uses a chemical-potential-dependent quantum chromodynamics (QCD) renormalization scale, while Hy1σ includes the effects of surface tension on the pressure balance of the two phases; Hy1$\mu\sigma$ includes both. Inspired by Weissenborn *et al.* [221], we also considered a case in which we used the hadronic EOS parameters of Lalazissis, König, and Ring (LKR) [240] (known there as the NL3 EOS). These give a very stiff hadronic EOS (a purely hadronic star would have a maximum mass of $2.78\,\mathrm{M}_\odot$), and thus lead to neutron stars with a large region of mixed phase that still satisfy the constraints provided by the Demorest *et al.* measurement. For our LKR1 case, we have picked reasonable-seeming quark EOS parameters that give a sufficiently massive star that still contains a very extensive region of mixed phase, including all the pasta phases. We also considered a case with somewhat generic parameters, generally picking them to be around the midpoint of the accepted range—this is the "generic" parameter set. These were not fine-tuned at all. Additionally, we have considered a variant that uses these more modern hadronic EOS parameters along with a bag constant and QCD coupling constant that yield a larger region of mixed phase—this is the generic′ parameter set.

We plot these EOSs up to the maximum density present in a stable OV star in Fig. 3.1. We do not show the various flavors of the Hy1 EOS here, since the resulting traces are all very similar, though we do show the violations of le Chatelier's principle for the Hy1σ and Hy1$\mu\sigma$ EOSs, compared with the Hy1 EOS in Fig. 3.2. (We do not show the trace for the Hy1μ EOS, as it is almost identical to that for the Hy1 EOS.)

3.2.1 Hadronic EOS

We construct the hadronic EOS following the recipe described in Chap. 4 of Glendenning's book [223], through Sec. 4.9. We thus use a relativistic mean field description, with a Lagrangian that contains the standard scalar and vector (σ and ω) fields, as well as scalar self-interactions, and the isospin asymmetry force, mediated by the vector meson ρ. We also include

[2] There was an error in the code used to perform the calculations in [94], leading to the rather lower maximum mass reported there.

	n_0	$(E/A)_\infty$	K	m^*/m	$a_{\rm sym}$	$B^{1/4}$	α_s	$\bar{\Lambda}_{\rm QCD}$	m_s	σ	$M_{\rm max}$	$M_{\rm min}^{\rm hybrid}$	$R_{\rm max}^{\rm hybrid}/R$	$C_{\rm max}$	densest
	fm^{-3}	MeV	MeV		MeV	MeV		MeV	MeV	MeV fm^{-2}	$M_\odot$	$M_\odot$	%		hybrid phase
Hy1	0.153	−16.3	300	0.7	32.5	180	0.6	300	150	10, 20, 50, 80	2.057	1.747	58.1	0.486	Q, $d = 1.00$
Hy1μ	0.153	−16.3	300	0.7	32.5	180	0.6	$\bar{\mu}_q$	150	80	2.061	1.716	59.5	0.487	Q, $d = 1.01$
Hy1σ	0.153	−16.3	300	0.7	32.5	180	0.6	300	150	80, p	1.997	1.583	63.5	0.480	Q, $d = 1.00$
Hy1$\mu\sigma$	0.153	−16.3	300	0.7	32.5	180	0.6	$\bar{\mu}_q$	150	80, p	2.000	1.545	64.9	0.481	Q, $d = 1.00$
Hy1′	0.153	−16.3	300	0.7	32.5	170	0.6	300	150	80	1.973	1.377	69.3	0.476	H, $d = 1.51$
LKR1	0.148	−16.3	271.76	0.6	37.4	167.5	0.6	300	100	80	1.955	1.096	72.4	0.433	H, $d = 3.00$
generic	0.16	−16	250	0.745	30	200	0.5	$\bar{\mu}_q$	100	80	1.986	1.878	44.0	0.500	Q, $d = 2.10$
generic′	0.16	−16	250	0.745	30	170	0.7	$\bar{\mu}_q$	100	80	1.974	1.534	65.7	0.513	Q, $d = 1.39$

Table 3.1. EOS parameters (or ranges of parameters) that we consider, and the properties of their associated OV stars. In the $\bar{\Lambda}_{\rm QCD}$ column, $\bar{\mu}_q$ denotes the cases where we take the QCD renormalization scale to be given by the average quark chemical potential at each density, as discussed in Sec. 3.2.2. In the σ column, we have denoted the cases in which we include the surface tension contribution to the pressure balance by a "p." $M_{\rm min}^{\rm hybrid}$ gives the masses of stars that first contain hybrid matter; $R_{\rm max}^{\rm hybrid}/R$ denotes the maximum radius fraction occupied by hybrid matter (i.e., the radius fraction for the maximum mass star); and $C_{\rm max}$ denotes the maximum compactness ($2GM/Rc^2$) of a star. We also give the composition of the rare phase ("Q" for quark and "H" for hadronic) and the dimension of the lattice at the center of the maximum mass star.

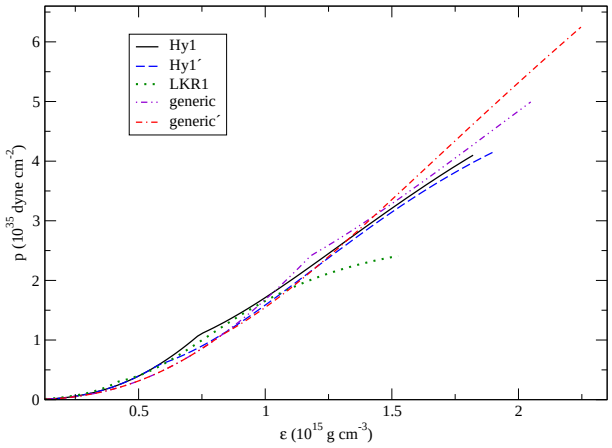

Fig. 3.1. Pressure vs. energy density for the EOSs from Table 3.1, plotted up to the maximum energy density present in a stable OV star.

electrons and muons. See [241] and [94] for further details about the general framework and calculational procedure we used. However, we have used updated parameters in the models, as discussed here.

The model has five input parameters: Two are known reasonably well, viz., the number density and binding energy of nuclear matter at saturation, $n_0 = 0.16 \pm 0.01$ fm^{-3} and $(E/A)_\infty = -16 \pm 1$ MeV. The remaining three are not nearly so well known: The nuclear incompressibility K is thought to lie between 200 and 300 MeV, with many authors placing it in the range 240 ± 10 MeV (see [242]), while the (scaled) Dirac effective mass of the nucleons, m^*/m, is thought to be between ~ 0.53 and 0.96. (Here $m = 938.93$ MeV $= 4.7582$ fm^{-1} is the average of the neutron and proton masses.) The symmetry energy $a_{\rm sym}$ is thought to lie between 28 and 34 MeV, with some evidence pointing to a narrower range of $31 \pm$ a few MeV—see Li *et al.* [243].

All the parameter ranges we have quoted here are taken from Eq. (88) in Steiner *et al.* [244] unless otherwise noted. The range for the Dirac effective mass is computed from that for the Landau effective mass given by Steiner *et al.* following Glendenning's Eq. (4.117) [223], with a Fermi momentum at saturation of 1.33 ± 0.03 fm^{-1}, from the Steiner *et al.* result and Glendenning's Eq. (4.110).

Note that almost all of the LKR parameters fall outside of the ranges we have given. We still consider them for two reasons. First, the LKR EOS is often treated as the paradigmatic stiff hadronic EOS in the literature; in particular, we were inspired to consider these parameters by the LKR EOS's recent use in Weissenborn *et al.* [221]. Second, the LKR parameters are still regarded as providing an excellent fit to the nuclear binding energy and charge radius, explaining why this EOS remains in use.

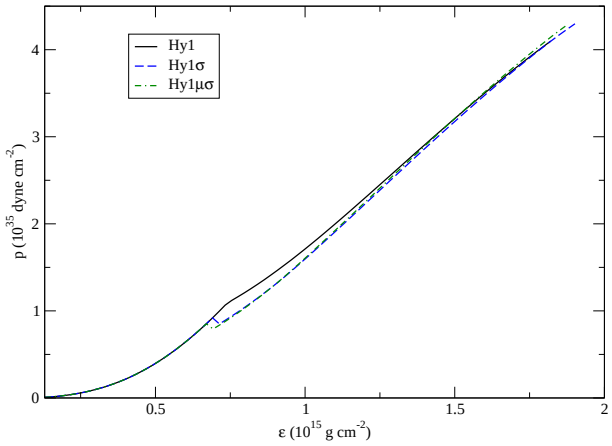

Fig. 3.2. Pressure vs. energy density for the Hy1 EOS and two flavors that include the surface tension contribution to the pressure balance, illustrating the violations of le Chatelier's principle. (Again, each of these is plotted up to the maximum energy density present in a stable OV star.)

3.2.2 Quark EOS

The quark matter is described by the MIT bag model (first given in Chodos *et al.* [245], and discussed briefly in Glendenning [223]), to capture the basic physics of confinement, supplemented with first-order QCD corrections to the thermodynamic potential for free quarks, from Farhi and Jaffe [246], as described in Chap. 8 of Glendenning [223].[3] We take all the quarks to be massive (as opposed to the usual treatment in which only the strange quark is taken to be massive—see, e.g., [220, 247, 221]—but note that Christiansen and Glendenning [248] also take all three quarks to be massive). See Chap. 6 in [94] for further details of the calculation.

Here the parameters are all quite uncertain. The only firm constraint is that nonstrange quark matter is not absolutely stable, since this contradicts the observed existence of nuclei composed of nucleons. In addition, we assume that strange quark matter is not absolutely stable, since we consider hybrid stars, not strange stars. In the pure bag model (with no QCD corrections—i.e., with zero QCD coupling constant), this implies that the fourth root of the bag constant, $B^{1/4}$, is greater than 145 MeV. When one includes QCD corrections, the minimum bag constant decreases—see, e.g., the discussion in Alford *et al.* [220]. There is no known upper bound on B, though for sufficiently large values of B (with all other EOS parameters fixed), stable stars do not contain deconfined quark matter.

We also need to know the QCD coupling constant and quark masses at the energy scale $\bar{\Lambda}_{\rm QCD}$ at which we renormalize the perturbative contributions to the thermodynamic potential. This energy scale is typically taken to be the scale of the quark chemical potentials in the problem. Glendenning uses 300 MeV, though we find that the chemical potentials in the situations

[3] Note that Glendenning corrects a sign error in Farhi and Jaffe's result for the thermodynamic potential in his Eq. (8.14).

we consider are somewhat higher (up to ~ 480 MeV in the densest regions of stable stars), so we also consider a density-dependent renormalization scale, given by $\Lambda_{\overline{\rm QCD}} = \bar{\mu}_q := (\mu_p + \mu_n)/6$, where μ_p and μ_n are the proton and neutron chemical potentials, respectively, so $\bar{\mu}_q$ is an average quark chemical potential. (This was inspired by the treatment of the renormalization scale in Kurkela, Romatschke, and Vuorinen [247], though the specifics of their treatment differ.)

At this scale, the QCD coupling constant α_s is large and not well known—we have considered values between 0.5 and 0.9. The quark masses are similarly uncertain. There are significant uncertainties (up to $\sim 50\%$) even at the 2 GeV scale at which the Particle Data Group [249] quotes the masses, and additional uncertainties in running them to lower energies. For simplicity, we have taken the up, down, and strange quarks to have masses of 2.5, 5, and 105 MeV, respectively, the median of the ranges for the $\overline{\rm MS}$ current masses at 2 GeV given in the 2010 Review of Particle Physics [249].

3.2.3 Hybrid phase and its lattice structure

We determine the bulk properties of the mixed phase using the Gibbs equilibrium conditions, following Glendenning (see, e.g., Chap. 9 in [223]): The appearance of the mixed phase is signaled by quark matter having a larger pressure than hadronic matter. One then determines the volume fractions of the two phases by demanding the equality of the phases' pressures and chemical potentials, in addition to overall electrical neutrality. (One computes the bulk pressure and energy and baryon densities by weighting the contributions from each phase using their volume fractions.)

We also need to obtain the structure of the mixed phase. This requires knowing the surface tension of the hadron–quark interface, σ. While σ has been estimated very roughly in the literature (e.g., [246] and the references given in Endo [231]), its value is still quite uncertain, so we simply take it to range from 10 to 80 MeV fm^{-2} (the lower bound is the default value used by Nayyar [94], and the upper bound is the default value used by Glendenning [223]), making sure that it does not make an appreciable contribution to the overall energy density, since, as Glendenning discusses, the system's energy should not increase upon opening up a new degree of freedom. In the cases we have considered, the blobs' energy density is $\lesssim 2\%$ of the total. Similarly, the lattice's electrostatic pressure is also a small contribution ($\lesssim 3\%$) to the bulk pressure.

Given the competition between this surface tension and the Coulomb energy of the blobs, one expects the blobs to form a lattice—this is a universal feature of systems with such competition. In order to determine the properties of this lattice, we employ the Wigner-Seitz approximation, which divides the lattice up into noninteracting, electrically neutral cells (approximating the lattice's Voronoi cell by a sphere of equivalent volume): Each cell contains a charged blob at its center surrounded by an equal amount of compensating charge. (At lower densities, the blob is formed out of quark matter, and the hadronic matter provides the compensating charge; at higher densities—often not reached in stable stars—the roles are reversed.) The ratios of the volumes of the blob and the cell are fixed, since the baryon and quark volume fractions are fixed. If we denote the the volume fraction of the rare phase by x, then we have $x = (r/R)^d$, where r and R are the radii of the blobs and cells, respectively (the half-thickness of the slabs in the one-dimensional case), and d is the dimensionality of the cell and lattice. If we denote the volume

fraction of the quark phase by χ, then we have

$$x = \begin{cases} \chi, & \chi \leq 1/2, \\ 1-\chi, & \chi > 1/2. \end{cases} \tag{3.1}$$

We then determine r and d by minimizing the cell's energy per unit volume. (We do this per unit volume since we are working at fixed baryon and quark volume fractions.)

Following the suggestion initially made by Ravenhall, Pethick, and Wilson [93] in the nuclear pasta case, we take the lattice's dimension to be a continuous variable—this is a reasonably simple way to deal with the very complicated structure we expect in practice (which can be seen in, e.g., molecular dynamics simulations of nuclear pasta, such as [250, 251, 252, 253]). In the integer dimension cases, we have a bcc lattice of spherical drops in 3 dimensions, a hexagonal lattice of cylindrical rods in 2 dimensions, and equally spaced rectangular slabs in 1 dimension. (These lattices are seen in the molecular dynamics simulations. In particular, Watanabe *et al.* [251] obtain a hexagonal lattice of rods by adiabatically compressing a bcc lattice of drops in their molecular dynamics simulations.)

The expression for the energy per unit volume of a cell is then given by [Eqs. (9.19), (9.23), and (9.24) in Glendenning [223]]

$$\frac{E_{\text{cell}}}{\Omega} = C(x)r^2 + S(x)/r, \tag{3.2}$$

where Ω is the cell volume, and $C(x)$ and $S(x)$ correspond to the Coulomb and surface contributions, respectively, with

$$C(x) := 2\pi[(q_H - q_Q)(\chi)]^2 x f_d(x), \quad S(x) := x\sigma d. \tag{3.3}$$

Here q_H and q_Q are the hadron and quark charge densities [recall that χ is the ratio of hadron to quark volume fractions and x denotes the ratio of the rare to dominant phase volume fractions—see Eq. (3.1)], and [Eq. (9.29) in Glendenning [223]]

$$f_d(x) := \frac{1}{d+2}\left[\frac{2 - dx^{1-2/d}}{d-2} + x\right]. \tag{3.4}$$

The singularity at $d \to 2$ is removable, since the limit exists [and has the expected value; see Eq. (9.30) in Glendenning [223]]. One can now immediately read off the minimizing r [Eq. (9.27) in Glendenning [223]], viz.,

$$r = \left[\frac{S(x)}{2C(x)}\right]^{1/3}. \tag{3.5}$$

One then obtains $d \in [1, 3]$ by minimizing (over that range) the resulting expression for the cell energy (using the minimizing r), viz., $E_{\text{cell}}/\Omega = (3/2)[2C(x)]^{1/3}[S(x)]^{2/3}$ [see Eq. (9.28) in Glendenning [223] for an explicit expression in terms of x, etc.].

As discussed by, e.g., [228, 229, 230, 231] the surface tension contributes to the pressure equality. Explicitly, we have a pressure difference between the dominant and rare phases of [cf.

Eq. (A5) in [248]]

$$p_{\text{dominant}} - p_{\text{rare}} = \frac{(d-1)\sigma}{r}, \tag{3.6}$$

where r is the radius of the blobs. We have included this in our treatment of certain EOSs in a somewhat simplified version: We do not solve for the lattice's dimension (d) self-consistently, but simply take its contribution to this expression to be given by its value at the previous baryon density (calculated using the above expressions). (However, we *do* include the x contribution to the radius of the blobs self-consistently.) Since this correction to the pressure equality is largest at the lowest-density portions of the mixed phase (i.e., the quark drop portions, with $d = 3$), this procedure seems likely to account for the primary effects from the surface tension's contribution to the pressure equality. (Note that we take the bulk pressure to be that of the dominant phase.) With this treatment of the surface tension contribution to the pressure equality, we find a slight violation of le Chatelier's principle (i.e., monotonic increase of pressure with energy density) close to the hybrid transition—this is not present if one does not include the surface tension contribution to the pressure equality (see Fig. 3.2).

3.2.4 Charge screening

The previous discussion has assumed that the charge is uniformly distributed within each blob and in the neutralizing background. This is not the case, in practice: The minimum-energy configuration will have a nonuniform charge distribution, as is discussed in, e.g., [228, 229, 230]. This nonuniform charge distribution—often treated in the perturbative regime as charge screening—will affect the cell energy (and thus the lattice properties, for a given energy density), as well as the lattice's electrostatic energy. Both of these affect the shear modulus. Here we only consider the effects on the lattice's electrostatic energy due to linear charge screening of point charges, using a screened potential. As is commonly done in treatments of the mixed phase (e.g., those by Glendenning), we do not concern ourselves at all with the rearrangement of charge inside the blobs, though this is likely a significant effect (as is discussed in [228, 229, 230]).

In this linearized version, we treat screening as a small perturbation on the overall energy, leading to the expression for the Debye length given in Eq. (1) of [224], viz.,

$$\lambda = \left[4\pi \sum_{\alpha} Q_{\alpha}^{2} \left(\frac{\partial n_{\alpha}}{\partial \mu_{\alpha}} \right) \right]^{-1/2}. \tag{3.7}$$

Here Q_α, n_α, and μ_α are the charge, number density, and chemical potential of particle species α, and the partial derivative is evaluated holding the chemical potentials of all species besides the αth fixed.

To include the effects of charge screening on the electrostatic energy, we dimensionally continue the standard screened potential equation (Yukawa in three dimensions), viz.,

$$(\triangle_d - \lambda^{-2})\phi = -4\pi Q \delta^{(d)}, \tag{3.8}$$

where $\triangle_d$ is the d-dimensional Laplacian, Q is the charge of the blob, and $\delta^{(d)}$ is the d-dimensional Dirac delta distribution. Here we are working in electrostatic units, hence the factor of 4π. Our identification of Q with the charge of the blob requires a little discussion: It is clearly true for $d = 3$, though we should really refer to a charge *density* for $d < 3$ (e.g., a linear charge density

for $d = 2$ and a surface charge density for $d = 1$). We have chosen to reserve the phrase "charge density" for the three-dimensional version (with units of charge per length cubed), and simply refer to the charge of the blob throughout, regardless of the dimensionality.

The resulting potential is

$$\phi(r) = \frac{2Q}{(2\pi\lambda r)^{d/2-1}} K_{d/2-1}(r/\lambda), \tag{3.9}$$

where K_ν is a modified Bessel function of the second kind. This expression can be obtained most easily by noting that it is the same as the Euclidean scalar propagator (up to overall factors), which is given in a dimensionally continued form in Eq. (5) of [254].[4] [However, one can also obtain the same result by either solving the differential equation for ϕ directly, or using that equation's (naturally dimensionally continued) Fourier transform, given in Eq. (3.31), along with the dimensionally continued Fourier transform given in Eq. (3.30).]

This potential clearly represents a simplified treatment of charge screening even in the perturbative limit, since we have used a point charge, instead of the extended charge distribution of a realistic blob, with different screening lengths inside and outside. (We similarly use point charges when calculating the potential energy of other blobs due to this screened potential.) However, it is a practical way for us to account for some of the effects of charge screening. Since we are using this point charge approximation, we compute the screening length using the leptons (i.e., electrons and muons) and the background phase (i.e., the protons when the blobs are made of quarks, and the quarks when the blobs are made of hadrons), since (by symmetry and Gauss's law) the rearrangement of charge within the blob has no (direct) effect on the blob's electrostatic potential (i.e., except through the effects of screening on the blob's size, which we are ignoring here). This switch at $\chi = 1/2$ causes a significant jump in the screening length there. This translates into a jump in the elastic constants, and thus the effective shear modulus, as seen in the figures in Sec. 3.6. The magnitude of this jump gives some indication of the overall error we incur through our simplified treatment of charge screening in the potential. (However, this likely does not give any indication of the errors incurred by neglecting the contribution of charge screening to the cell energy, which we shall see affects the effective shear modulus both directly and indirectly.)

3.3 Elasticity

The elastic response of a crystalline lattice is described by its elastic modulus tensor, S_{klps}, defined by

$$\epsilon = \epsilon_0 + S_{kl} u_{kl} + \frac{1}{2} S_{klps} u_{kl} u_{ps}, \tag{3.10}$$

where ϵ is the deformed lattice's energy density, ϵ_0 is its undeformed energy density, $u_{kl} := \partial_k \delta x_l$ is its displacement gradient (where δx_l denotes the displacement field), and S_{kl} is the first-order piece of the expansion. We have a nonzero first-order piece here, since the undeformed lattice has a nonzero pressure—see Eq. (7) in Baiko [234]. (Wallace [255] gives further discussion.) Explicitly, we have $S_{kl} = -P_{\text{es}} \delta_{kl}$, since the pressure is isotropic. (Note that we shall only

[4] When comparing the two expressions, note that $K_{-\nu} = K_\nu$.

consider the contribution from the lattice's electrostatic pressure $P_{\rm es}$ in our discussion.) Now, we are only interested in the shear stress the lattice generates in response to a shear deformation, and this is given by a different elastic modulus tensor, viz.,

$$B_{klps} = S_{klps} - P_{\rm es}(\delta_{ks}\delta_{lp} - \delta_{kl}\delta_{ps}). \tag{3.11}$$

Specifically, the stress generated by a deformation u_{kl} is given by $B_{klps}(u_{ps} + u_{sp})/2$. [See Eqs. (29) and (30) in Baiko [234].] We can write the components of B_{klps} more simply by using Voigt notation to map them to the two-index object $c_{\alpha\beta}$ using the index mapping given by $\{xx, yy, zz, xy, xz, yz\} \leftrightarrow \{1, 2, 3, 4, 5, 6\}$. With this notation, we note that $c_{11} = S_{1111}$ and $c_{44} = S_{1212}$, while $c_{12} = S_{1122} + P_{\rm es}$. [Note that Baiko's C_{kl} denotes a different tensor.]

Since we are interested solely in the lattice's response to shears, we will be able to focus our attention on a few components of this tensor. If we just consider the cases where a shear strain yields a proportional shear stress (as is the case for isotropic materials), then we will have contributions from the simple shear portions of the tensor, viz., c_{44}, c_{55}, and c_{66}, in addition to the elongational shears $A_{12} := (c_{11} + c_{22})/2 - c_{12}$, $A_{13} := (c_{11} + c_{33})/2 - c_{13}$, and $A_{23} := (c_{22} + c_{33})/2 - c_{23}$. (The simple shears correspond to stresses or strains of the form $2\hat{x}_{(k}\hat{y}_{l)}$, while the elongational shears correspond to stresses or strains of the form $\hat{x}_k\hat{x}_l - \hat{y}_k\hat{y}_l$—i.e., rotations of the simple shears by $\pi/4$.) In the past, certain investigations of shear modulus effects in the crusts of neutron stars have used the simple shear portion of the tensor, c_{44}, as the shear modulus of a bcc lattice (for which $c_{44} = c_{55} = c_{66}$)—see the discussion in Sec. 7.1 of Chamel and Haensel [86]. As Strohmayer *et al.* [256] emphasize, it is inappropriate to simply use one component of the elastic modulus tensor for this purpose. While a truly detailed calculation would use the full elastic modulus tensor, if one considers a polycrystal consisting of many randomly oriented domains, it is possible to use an angle-averaged version and obtain an upper bound.

This upper bound is due to Voigt [257], and involves the elastic constants given above—see Hill [258] for the proof that the Voigt expression gives an upper bound. Hill also discusses a lower bound due to Reuss, but we do not consider it here, since it is constructed from the inverse of the elastic modulus tensor, and thus, for $d < 3$, involves components of the tensor that we do not compute. (Similarly, we do not consider any of the more involved, sharper bounds, such as the oft-used ones by Hashin and Shtrikman [259]. See [260] for a review of such bounds, and [261] for a Hashin-Shtrikman bound for orthorhombic crystals, such as the ones we consider here.) The Voigt result was rediscovered by Ogata and Ichimaru [262] in considering the shear modulus of the neutron star crust. (They used it as an average, as was originally proposed by Voigt, not as an upper bound, as in Hill.) We shall also use the Voigt average for our effective shear modulus (as has also been done by Baiko [234] in a consideration of the shear modulus of the crust, again following Ogata and Ichimaru), giving

$$\mu_{\rm eff} = (A_{12} + A_{13} + A_{23})/15 + (c_{44} + c_{55} + c_{66})/5. \tag{3.12}$$

However, we shall note, as does Baiko, that it is unclear whether this will really provide an appropriate description of the elastic response of a neutron star. In particular, Baiko notes that the lattice will likely want to align itself with the star's magnetic field, leading to large-scale ordered structure.

To dimensionally continue this expression, we need to consider the effects of different dimensionalities on the shear elastic coefficients for lattices of different dimensions. We shall first discuss the integer dimension cases, and then present the dimensionally continued expression for the effective shear modulus at the end. (See Pethick and Potekhin [227] for related discussion about the elasticity of liquid crystals as applied to the pasta phases in the crust.) Our discussion will be simplified by the fact that we can take the elastic constants of all the lattices to have cubic symmetry—this holds for the integer dimension lattices and remains true for the dimensionally continued ones by fiat. However, there will be differences between the elongational shear elastic constants in which the shear takes place completely within the lattice and those that involve an elongation along the rods or slabs. We also will find that the number of nonzero shear elastic constants is reduced due to the translational symmetry along the rods or slabs in lower dimensions. Specifically,

1. In the three-dimensional case, all the shear elastic constants are nonzero, and, by cubic symmetry, the simple and elongational shear elastic constants are each all equal (i.e., $c_{44} = c_{55} = c_{66}$ and $A_{12} = A_{13} = A_{23} =: A_{\text{lat}}$).

2. In the two-dimensional case, only one of the simple shear elastic constants is nonzero, since simple shears along the rods do not lead to a shear stress—i.e., we have $c_{44} \neq c_{55} = c_{66} = 0$, where we have taken the rods to point in the z-direction. The elongational shears are all nonzero, but are not all equal: The one elongational shear perpendicular to the rods has a different elastic constant than do the two elongational shears that involve elongations along the rods, in general. Explicitly, we have $A_{\text{lat}} := A_{12} \neq A_{13} = A_{23} =: A_{\perp}$.

3. In the one-dimensional case, all of the simple shear elastic constants are zero, due to the translational symmetry along the slabs, and the only nonzero elongational shear constants are those that involve elongation along the slabs. (We neglect any change in energy due to shearing one of the slabs.) We thus have $c_{44} = c_{55} = c_{66} = 0$ and, taking the x-direction to be perpendicular to the slabs, $A_{\text{lat}} := A_{12} = A_{13} \neq A_{23} = 0$.

We can now obtain the dimensionally continued version by using the obvious dimensionally continued versions of the relevant basic combinatorial results: The number of independent shears (either simple or elongational) completely within the lattice (i.e., perpendicular to the rods and slabs in the integer dimension cases) is given by $d(d-1)/2$; this gives the multiplicity of the contributions to μ_{eff} from c_{44} and A_{lat}. The number of independent elongational shears with one elongation perpendicular to the lattice and one within it is given by $d(3-d)$; this gives the multiplicity of the contributions from $A_{\perp}$. The dimensionally continued version of Eq. (3.12) is thus

$$\mu_{\text{eff}} = \frac{d}{15}\left[\frac{d-1}{2}A_{\text{lat}} + (3-d)A_{\perp}\right] + \frac{d(d-1)}{10}c_{44}. \tag{3.13}$$

N.B.: In general, one can obtain elongational shear stresses from a strain not proportional to the stress (even for a strain that has no shear component) from the more strongly anisotropic lattices one encounters for $d < 3$. For instance, for $d = 1$, the elongational part of the elastic modulus tensor has the form

$$\mathsf{C}_1 = \begin{bmatrix} c_{11} & c_{13} & c_{13} \\ c_{13} & c_{33} & 0 \\ c_{13} & 0 & c_{33} \end{bmatrix}, \tag{3.14}$$

in Voigt notation. In this notation, the stress due to a shear $\mathbf{u}$ is given by $\mathsf{C}_1\mathbf{u}$. Now, hydrostatic compression is given by the vector $\mathbf{u}_c = \begin{bmatrix}1 & 1 & 1\end{bmatrix}^\top$, while elongational shears in the *xy* and *xz* planes are given by $\mathbf{u}_{xy} = \begin{bmatrix}1 & -1 & 0\end{bmatrix}^\top$ and $\mathbf{u}_{xz} = \begin{bmatrix}1 & 0 & -1\end{bmatrix}^\top$, respectively. Since we have, e.g., $\mathbf{u}_{xy}^\top \mathsf{C}_1 \mathbf{u}_c = c_{11} + c_{13} - c_{33}$ and $\mathbf{u}_{xy}^\top \mathsf{C}_1 \mathbf{u}_{xz} = c_{11} - 2c_{13}$, neither of which is zero, in general, the claim follows. However, such shear stresses are not included in our expression for μ_{eff}, since we have only considered contributions where a shear strain yields a proportional shear stress, as in isotropic materials; this is an appropriate treatment for an effective shear modulus.

3.4 Calculation of the elastic constants

Now looking at how to compute A_{lat}, $A_\perp$, and c_{44}, we can follow Fuchs [226] in expressing these quantities in terms of lattice sums. Specifically, one writes the electrostatic energy of an appropriately deformed lattice as a lattice sum and takes derivatives with respect to the deformation to obtain lattice sum expressions for the elastic constants. In $A_\perp$, we will also need to consider the contributions from the cell energy [obtained using Eq. (3.2)]. One also expects there to be contributions to A_{lat} and c_{44} due to changing the shape of the unit cell (see the discussion in Zach [263]; Christiansen and Glendenning [248] also discuss higher-order shape contributions to the energy from the hadron–quark interface), but we neglect these in our treatment. We do not have to concern ourselves with such contributions for $A_\perp$, even in principle, since we can take the compression inside the lattice to be uniform in all directions.

We also follow Fuchs in using the Ewald method to compute the resulting lattice sums. (See, e.g., [233] for a modern exposition of the Ewald method. Additionally, we make certain modifications to the method so that it is compatible with dimensional continuation—these are discussed in Sec. 3.5.1.) In the Ewald method, one computes the sum of a slowly convergent (indeed, often only conditionally convergent, or even divergent) series by expressing it as the sum of two rapidly convergent series, introducing an Ewald screening function and using the Poisson summation formula. (Actually, the Poisson summation formula is not strictly applicable to the functions being summed in many applications, which is what allows the Ewald method to regularize divergent series, by much the same method as zeta function regularization—see Appendix E for further discussion.)

The Fuchs expressions are obtained by computing the energy of the perturbed lattice. Explicitly, we write the electrostatic energy per unit cell of the lattice (i.e., the energy required to remove a single blob) as [cf. the expression for the potential in Eq. (7) of Johnson and Ranganathan [233] and Fuchs's expression for the energy in Eq. (10) of [226]]

$$W = \frac{Q^2}{2}\left[\sum_{\vec{x}\in\Lambda}{}' (\phi E)(\|\vec{x}\|) + \frac{1}{\Omega}\sum_{\vec{p}\in\Lambda^*}{}' (\widehat{\phi E_c})(\|\vec{p}\|) - \frac{(\widehat{\phi E})(0)}{\Omega}\right]. \tag{3.15}$$

Here Q is the charge of a blob; Λ is the lattice under consideration, with dual lattice Λ^*, and Voronoi cell volume Ω;[5] primes on the sums denote the omission of the zero vector; E is the Ewald screening function, with complement $E_c(x) := 1 - E(x)$; ϕ is the potential due to one of

[5] Here Ω is Fuchs's notation, which we use for the physical volume of a cell. We shall also use Conway and Sloane's [109] notation of $\sqrt{\det\Lambda}$ for the volume without the physical scaling.

the blobs [including the effects of (physical) charge screening]; and the circumflex denotes the Fourier transform of (here three-dimensional) radial functions. (See Sec. 3.5.1 for our Fourier transform conventions.)

We now give the lattice sum expressions for the elastic constants. The most straightforward are those for c_{11} and c_{44}, which are of the form $(d^2W/d\epsilon^2)\big|_{\epsilon=0}/\Omega$, for an appropriate deformation parametrized by ϵ; we have divided by the volume of a Voronoi cell, Ω, here since W gives the energy per unit cell. (Note that we need c_{11} in order to compute $A_\perp$ and the dimensionally continued A_{lat}, even though that elastic constant does not appear in μ_{eff} by itself.) The resulting expressions for elastic constants will be of the form ($\mathfrak{c} \in \{c_{11}, c_{44}\}$)

$$\mathfrak{c} = \frac{Q^2}{2\Omega}\Bigg\{ \sum_{\vec{x}\in\Lambda}{}' \left[(\phi E)'(\|\vec{x}\|)\frac{\partial^2\|\vec{x}\|}{\partial\epsilon^2} + (\phi E)''(\|\vec{x}\|)\left(\frac{\partial\|\vec{x}\|}{\partial\epsilon}\right)^2\right] + \frac{1}{\Omega}\sum_{\vec{p}\in\Lambda^*}{}' \Bigg[2\frac{(\widehat{\phi E_c})(\|\vec{p}\|)}{\Omega^2}\left(\frac{\partial\Omega}{\partial\epsilon}\right)^2 + (\widehat{\phi E_c})^{\bullet}(\|\vec{p}\|)\left(\frac{\partial^2\|\vec{p}\|^2}{\partial\epsilon^2} - \frac{2}{\Omega}\frac{\partial\Omega}{\partial\epsilon}\frac{\partial\|\vec{p}\|^2}{\partial\epsilon}\right) + (\widehat{\phi E_c})^{\bullet\bullet}(\|\vec{p}\|)\left(\frac{\partial\|\vec{p}\|^2}{\partial\epsilon}\right)^2\Bigg] - \frac{2}{\Omega^3}\left(\frac{\partial\Omega}{\partial\epsilon}\right)^2(\widehat{\phi E})(0)\Bigg\}\Bigg|_{\epsilon=0}, \tag{3.16}$$

where the coordinate and Ω derivatives are given by Eqs. (3.17) and (3.18). [Recall that we have $(d\Omega/d\epsilon)|_{\epsilon=0} = 0$ for c_{44}.] The superscript bullets ($\bullet$) denote derivatives taken with respect to $\|\vec{p}\|^2$—cf. the discussion below Eq. (3.17).

To obtain the derivatives needed for the lattice sum expression for c_{44}, we note (following Fuchs [226]) that c_{44} is the only elastic constant that contributes to the change of energy of the lattice if one considers a simple shear deformation. If we take this simple shear to be in the x_1 and x_2 directions, it corresponds to the deformations $x_1 \to x_1 + \epsilon x_2$, $x_2 \to x_2 + \epsilon x_1$ for the direct lattice, and $p_1 \to (p_1 - \epsilon p_2)/(1-\epsilon^2)$, $p_2 \to (p_2 - \epsilon p_1)/(1-\epsilon^2)$ for the dual lattice (x_3 and p_3 are both held fixed). The requisite derivatives are thus

$$\left.\frac{\partial\|\vec{x}\|}{\partial\epsilon}\right|_{\epsilon=0} = \frac{x_1x_2}{\|\vec{x}\|}, \qquad \left.\frac{\partial^2\|\vec{x}\|}{\partial\epsilon^2}\right|_{\epsilon=0} = \frac{x_2^2}{\|\vec{x}\|} - \frac{x_1^2x_2^2}{\|\vec{x}\|^3}, \tag{3.17a}$$

$$\left.\frac{\partial\|\vec{p}\|^2}{\partial\epsilon}\right|_{\epsilon=0} = 2p_1p_2, \qquad \left.\frac{\partial^2\|\vec{p}\|^2}{\partial\epsilon^2}\right|_{\epsilon=0} = 2p_1^2. \tag{3.17b}$$

[N.B.: We have given the derivatives of $\|\vec{p}\|^2$ since the dimensionally continued Fourier transform depends naturally on this quantity—cf. Eq. (3.30). Additionally, all of the right-hand sides of these expressions are evaluated at $\epsilon = 0$ (both here and in all similar situations in the sequel).] For c_{11} (which Fuchs does not compute), we use the deformation $x_1 \to (1+\epsilon)x_1$, $p_1 \to p_1/(1+\epsilon)$ (with all other coordinates held fixed). This perturbation changes the cell volume, so we must

include derivatives of Ω, giving

$$\left.\frac{\partial\|\vec{x}\|}{\partial\epsilon}\right|_{\epsilon=0} = \frac{x_1^2}{\|\vec{x}\|}, \qquad \left.\frac{\partial^2\|\vec{x}\|}{\partial\epsilon^2}\right|_{\epsilon=0} = \frac{x_1^2}{\|\vec{x}\|} - \frac{x_1^4}{\|\vec{x}\|^3}, \tag{3.18a}$$

$$\left.\frac{\partial\|\vec{p}\|^2}{\partial\epsilon}\right|_{\epsilon=0} = -2p_1^2, \qquad \left.\frac{\partial^2\|\vec{p}\|^2}{\partial\epsilon^2}\right|_{\epsilon=0} = 6p_1^2, \tag{3.18b}$$

$$\left.\frac{\partial\Omega}{\partial\epsilon}\right|_{\epsilon=0} = \Omega, \qquad \left.\frac{\partial^2\Omega}{\partial\epsilon^2}\right|_{\epsilon=0} = 0. \tag{3.18c}$$

For A_{lat}, Fuchs uses the elongational shear in the x_1 and x_2 directions, for which the change to the lattice's energy is given by $2A_{\text{lat}}$ alone (and has a lattice sum expression similar to that for c_{44}). However, as we shall see in Sec. 3.5, the resulting expression is not well suited for dimensional continuation, since it contains fourth powers of more than one coordinate [see Eq. (12) in Fuchs [226]]. We can obtain an expression that *is* well-suited to dimensional continuation if we note that $A_{\text{lat}} = c_{11} - c_{12}$ (we have $c_{11} = c_{22}$ by cubic symmetry): We compute c_{11} as above, but obtain $c_{12} = S_{1122} + P_{\text{es}}$ by first using a two-component perturbation to obtain S_{1122}, and then computing P_{es} *à la* Fuchs. The two-component perturbation we use to obtain S_{1122} is $x_1 \to (1+\epsilon_1)x_1$, $x_2 \to (1+\epsilon_2)x_2$, $p_1 \to p_1/(1+\epsilon_1)$, $p_2 \to p_2/(1+\epsilon_2)$ (with x_3 and p_3 held fixed), yielding the derivatives

$$\left.\frac{\partial\|\vec{x}\|}{\partial\epsilon_j}\right|_{\epsilon_{1,2}=0} = \frac{x_j^2}{\|\vec{x}\|}, \qquad \left.\frac{\partial^2\|\vec{x}\|}{\partial\epsilon_1\partial\epsilon_2}\right|_{\epsilon_{1,2}=0} = -\frac{x_1^2x_2^2}{\|\vec{x}\|^3}, \tag{3.19a}$$

$$\left.\frac{\partial\|\vec{p}\|^2}{\partial\epsilon_j}\right|_{\epsilon_{1,2}=0} = -2p_j^2, \qquad \left.\frac{\partial^2\|\vec{p}\|^2}{\partial\epsilon_1\partial\epsilon_2}\right|_{\epsilon_{1,2}=0} = 0, \tag{3.19b}$$

$$\left.\frac{\partial\Omega}{\partial\epsilon_j}\right|_{\epsilon_{1,2}=0} = \Omega, \qquad \left.\frac{\partial^2\Omega}{\partial\epsilon_1\partial\epsilon_2}\right|_{\epsilon_{1,2}=0} = \Omega, \tag{3.19c}$$

where $j \in \{1,2\}$ and $\epsilon_{1,2} = 0 \Rightarrow \epsilon_1 = \epsilon_2 = 0$. One then obtains, from $S_{1122} = \left(\partial^2 W/\partial\epsilon_1\partial\epsilon_2\right)\big|_{\epsilon_{1,2}=0}/\Omega$ and the expression for W in Eq. (3.15),

$$\begin{aligned} S_{1122} = \frac{Q^2}{2\Omega}\Bigg\{ &\sum_{\vec{x}\in\Lambda}{}' \frac{x_1^2x_2^2}{\|\vec{x}\|^2}\left[(\phi E)''(\|\vec{x}\|) - \frac{(\phi E)'(\|\vec{x}\|)}{\|\vec{x}\|}\right] + \frac{1}{\Omega}\sum_{\vec{p}\in\Lambda^*}{}'\Big[(\widehat{\phi E_c})(\|\vec{p}\|) + 2(p_1^2+p_2^2)(\widehat{\phi E_c})^{\bullet}(\|\vec{p}\|) \\ &+ 4p_1^2p_2^2(\widehat{\phi E_c})^{\bullet\bullet}(\|\vec{p}\|)\Big] - \frac{1}{\Omega}(\widehat{\phi E})(0)\Bigg\}\Bigg|_{\epsilon_{1,2}=0}. \end{aligned} \tag{3.20}$$

We calculate P_{es} using the same perturbation we used to obtain c_{11} [with the derivatives given in Eq. (3.18)]. Specifically, $P_{\text{es}} = -\left(dW/d\epsilon\right)|_{\epsilon=0}/\Omega$ [cf. Eq. (3.10), recalling that $S_{kl} = -P_{\text{es}}\delta_{kl}$]. This gives

$$P_{\text{es}} = -\frac{Q^2}{2\Omega}\Bigg\{\sum_{\vec{x}\in\Lambda}{}'\frac{x_1^2}{\|\vec{x}\|}(\phi E)'(\|\vec{x}\|) - \frac{1}{\Omega}(\widehat{\phi E})(0) - \frac{1}{\Omega}\sum_{\vec{p}\in\Lambda^*}{}'\Big[(\widehat{\phi E_c})(\|\vec{p}\|) + 2p_1^2(\widehat{\phi E_c})^{\bullet}(\|\vec{p}\|)\Big]\Bigg\}\Bigg|_{\epsilon=0}. \tag{3.21}$$

We thus have

$$A_{\rm lat} = c_{11} - S_{1122} - P_{\rm es}, \tag{3.22}$$

where c_{11} is given by Eqs. (3.16) and (3.18), and S_{1122} and $P_{\rm es}$ are given by the above expressions.

Now, to obtain $A_\perp$, we need to supplement the expression for c_{11} with the contributions due to changing the cell energy (since we are changing its radius), along with the contributions due to changing the blobs' charge. The contribution due to changing the cell energy is

$$A_{\perp,\rm cell} = \frac{2}{d^2}\frac{E_{\rm cell}}{\Omega}. \tag{3.23}$$

This can be deduced from the scalings of the Coulomb and surface contributions [see Eq. (2) in Pethick and Potekhin [227]], noting that the change in the cell radius with this perturbation is given by

$$\left.\frac{\partial r}{\partial \epsilon}\right|_{\epsilon=0} = \frac{r}{d}, \tag{3.24}$$

which comes from noting that $\Omega = C_{\rm cell} r^d$, where $C_{\rm cell}$ is a constant (since x is fixed, as we are keeping the overall density fixed) and using the expression for $\partial\Omega/\partial\epsilon$ for the c_{11} perturbation given in Eq. (3.18c). [One can also obtain the expression for $A_{\perp,\rm cell}$ by direct (somewhat tedious) calculation, starting from the expression for $E_{\rm cell}/\Omega$ in Eq. (3.2) and using the expression for $\partial r/\partial\epsilon$, plus the analogous one for $\partial^2 r/\partial\epsilon^2$.] For the derivatives of the blobs' charge, we note that the (three-dimensional) charge density is fixed, so that these derivatives can be obtained from those of the cell volume [in Eq. (3.18c)] by replacing the cell volume with the blobs' charge. Explicitly, we have

$$\left.\frac{\partial Q}{\partial \epsilon}\right|_{\epsilon=0} = Q, \qquad \left.\frac{\partial^2 Q}{\partial \epsilon^2}\right|_{\epsilon=0} = 0. \tag{3.25}$$

We now show how to put together all these contributions to obtain the sum that gives $A_\perp$: We have

$$A_\perp = c_{11} + A_{\perp,\rm cell} + A_{\perp,Q}, \tag{3.26}$$

where c_{11} is given by Eqs. (3.16) and (3.18), $A_{\perp,\rm cell}$ is given in Eq. (3.23), and

$$A_{\perp,Q} = \frac{Q^2}{\Omega}\Bigg\{ {\sum_{\vec{x}\in\Lambda}}' \left[(\phi E)(\|\vec{x}\|) + 2\frac{x_1^2}{\|\vec{x}\|}(\phi E)'(\|\vec{x}\|)\right] - \frac{1}{\Omega}{\sum_{\vec{p}\in\Lambda^*}}' \left[(\widehat{\phi E_c})(\|\vec{p}\|) + 4p_1^2(\widehat{\phi E_c})^\bullet(\|\vec{p}\|)\right] + \frac{(\widehat{\phi E})(0)}{\Omega}\Bigg\}\Bigg|_{\epsilon=0}. \tag{3.27}$$

[Recall that the bullet ($\bullet$) denotes derivatives with respect to $\|\vec{p}\|^2$.] As one would expect from Earnshaw's theorem, c_{11} is always negative, so one relies on the contributions from $A_{\perp,\rm cell}$ and $A_{\perp,Q}$ to make $A_\perp$ positive (so that the lattice is stable to shears). (See Sec. 3.6 for further discussion.)

3.5 Dimensional continuation of lattice sums

3.5.1 The dimensionally continued Ewald method

In order to compute these lattice sums numerically, we shall use a generalization of the standard Ewald [232] method used by Fuchs [226]. Recall that this method allows one to convert a slowly convergent (possibly only conditionally convergent, or even divergent) series into a sum of two rapidly convergent series by introducing an Ewald screening function and applying the Poisson summation formula. Showing the standard integer dimension version first, we have, summing a function f over a lattice Λ, with dual lattice Λ^*,

$$\sum_{\vec{x}\in\Lambda} f(\vec{x}) = \sum_{\vec{x}\in\Lambda} (fE)(\vec{x}) + \frac{1}{\sqrt{\det \Lambda}} \sum_{\vec{p}\in\Lambda^*} (\widetilde{fE_c})(\vec{p}). \tag{3.28}$$

Here $\tilde{g}(\vec{p}) := \int_{\mathbb{R}^n} g(\vec{x}) e^{-2\pi i \vec{x}\cdot\vec{p}} d^n x$ is the standard Fourier transform, and $E_c(\vec{x}) := 1 - E(\vec{x})$ is the complement of the Ewald screening function E; we choose E so that both of the sums on the right-hand side converge quickly. [Recall that the classical Poisson summation formula says that $\sum_{\vec{x}\in\Lambda} f(\vec{x}) = (\det\Lambda)^{-1/2} \sum_{\vec{p}\in\Lambda^*} \tilde{f}(\vec{p})$.]

The classic choice for E for Coulombic potentials (dating back to Ewald) is the complementary error function. However, this turns out to be insufficiently flexible to provide good convergence for the sums we consider (particularly for small d). Following Nijboer and de Wette [264] and Fortuin [265], we introduce the incomplete gamma function, $\Gamma(\cdot,\cdot)$, and use the screening function

$$E(\vec{x}) = \Gamma(N/2, \alpha^2 \|\vec{x}\|^2)/\Gamma(N/2). \tag{3.29}$$

This reduces to Ewald's complementary error function for $N = 1$. The extra freedom contained in N allows us to tune E to provide fast convergence for the sums we encounter. We used $N = 10$ and $\alpha = 1.2/a$ in the computations reported in Sec. 3.6. [Here a is the lattice spacing, given in Eq. (3.50).] We could have doubtless obtained faster convergence if we had allowed these parameters to vary with d (and possibly also λ), particularly for d close to 1. However, we found these values to give reasonably good performance, and thus did not perform much experimentation, beyond checking that our results were insensitive to the choices of Ewald screening parameters (within the range of parameter choices that led to convergent results).

In order to dimensionally continue our lattice sums, we need to dimensionally continue the Poisson summation formula. We shall give an overview of the calculational aspects here—see Chap. 5 for more details of the derivations, and a proof of the formula for nicely behaved functions. (The functions we consider here are not well-behaved enough for the formula to apply to them directly, as should be expected, since we are using this Poisson summation formula to regularize conditionally convergent, or even divergent series. If we were to proceed more rigorously, we might, for instance, first introduce a regulator such that the dimensionally continued Poisson summation formula is truly applicable, and then remove the regulator after applying the formula to obtain the final result.) We first introduce the dimensionally continued Fourier transform for spherically symmetric functions, given in Theorem 3.3 of Chap. IV of Stein and Weiss [266],

$$\hat{g}(p) := \frac{2\pi}{p^{d/2-1}} \int_0^\infty g(r) J_{d/2-1}(2\pi p r) r^{d/2} dr \tag{3.30}$$

Here J_ν is a Bessel function of the first kind. (See Sec. 5.2.2 for more details, including an alternative, perhaps slightly neater, expression in terms of a hypergeometric function.) We also note that we can compute the dimensionally continued Fourier transform of the potential from its defining partial differential equation [Eq. (3.8)], giving

$$\hat{\phi}_d(p) = \frac{4\pi}{4\pi^2 p^2 + \lambda^{-2}}. \tag{3.31}$$

[This agrees with the result of the more involved calculation one could perform using the dimensionally continued Fourier integral given in Eq. (3.30).] We use Eq. (3.31) along with the dimensionally continued Fourier integral [Eq. (3.30)] to compute $\widehat{\phi E_c}$ efficiently, writing it as $\hat{\phi} - \widehat{\phi E}$, where the integral giving the second term converges reasonably rapidly.

We then introduce the theta series of a lattice. As is discussed in more detail in Sec. 2.3 of Chap. 2 of Conway and Sloane [109], the theta series of a lattice is the generating function of the number of lattice points on a sphere of a given squared radius, so the theta series of a lattice Λ is defined by

$$\Theta_\Lambda(q) := \sum_{\vec{k}\in\Lambda} q^{\|\vec{k}\|^2}. \tag{3.32}$$

[N.B.: There are several different conventions for theta series and function notation. We have chosen to write all our theta series and functions as functions of the nome, q, unless we note otherwise. This will be the case only in discussions of the Jacobi formula for the theta series of the dual lattice, where it is convenient to treat the theta series as a function of a complex variable z, with $q = e^{i\pi z}$. We shall denote this by an overbar—e.g., $\bar{\Theta}_\Lambda(z) := \Theta_\Lambda(e^{i\pi z})$. Conway and Sloane treat all their theta functions as functions of z, even when they write their expansions in terms of the nome.] Thus, if we define the power series coefficients of the theta series using

$$\Theta_\Lambda(q) =: \sum_{l=0}^{\infty} A_l q^{B_l}, \tag{3.33}$$

we can write the sum of a spherically symmetric function F over Λ as

$$\sum_{\vec{k}\in\Lambda} F(\|\vec{k}\|) = \sum_{l=0}^{\infty} A_l F(\sqrt{B_l}). \tag{3.34}$$

The dimensionally continued Poisson summation formula then has the obvious form

$$\sum_{l=0}^{\infty} A_l F(\sqrt{B_l}) = \frac{1}{\sqrt{\det\Lambda}} \sum_{l=0}^{\infty} A_l^* \hat{F}(\sqrt{B_l^*}). \tag{3.35}$$

Here, A_l^* and B_l^* are obtained from Λ^* analogously to their counterparts for Λ [in Eq. (3.33)]. The theta series for Λ^* can be calculated from Θ_Λ using the Jacobi formula [Eq. (3.40)], which is already in dimensionally continued form. [N.B.: The dimensionally continued Poisson summation formula presented in Chap. 5 omits the factor of $(\det\Lambda)^{-1/2}$, since, as discussed there, this factor cancels against a similar one present in the Jacobi transformation formula. We include the factor here, since we obtain a simpler result for the theta series of the dual lattice by using the

standard Jacobi transformation formula.] Of course, we need to sum more than just spherically symmetric functions [see Eqs. (3.16)–(3.21)], but, as we shall see shortly, this dimensionally continued Poisson summation formula will be sufficient for our needs.

3.5.2 Dimensional continuation of the lattice

Turning now to the problem of dimensionally continuing the lattices themselves, recall that the integer dimension lattices are [up to an overall scaling, which we determine in Eq. (3.50)] a bcc lattice for $d = 3$, a hexagonal lattice for $d = 2$, and $\mathbb{Z}$, the (one-dimensional) lattice of integers, for $d = 1$. We have not discovered any canonical way of dimensionally continuing sums over this family of lattices,[6] but it is possible to perform the dimensional continuation if we treat the dimensionally continued lattice as a union of hyperlattices (i.e., lattices of one dimension fewer than the overall lattice)[7] whose separation is given by a freely specifiable function f^{lat} that interpolates between the integer dimension separations. One then finds that the sums over the hyperlattices dimensionally continue in a natural way, and that the final result for the shear modulus is rather insensitive to the choice of f^{lat} (provided that it satisfies some reasonable properties, discussed below).

Explicitly, the integer dimension lattices can be written (up to the overall scaling) as $[f^{\text{lat}}(d)\mathbb{Z}_{\text{even}}] \times \mathbb{Z}^{d-1} + [f^{\text{lat}}(d)\mathbb{Z}_{\text{odd}}] \times [\mathbb{Z}^{d-1} + (1/2)^{d-1}]$, where $f^{\text{lat}}(d)\mathbb{Z}_{\text{even}}$ and $f^{\text{lat}}(d)\mathbb{Z}_{\text{odd}}$ denote the even and odd integers, respectively, both scaled by $f^{\text{lat}}(d)$, $\mathbb{Z}^{d-1}$ denotes the $(d-1)$-dimensional lattice of integers, and, in Conway and Sloane's notation [109], $\mathbb{Z}^{d-1} + (1/2)^{d-1}$ denotes the same shifted by the [$(d-1)$-dimensional] vector all of whose components are $1/2$. This is illustrated in Fig. 3.3 (we take x_1 to be in the direction orthogonal to the hyperlattices).

Here $f^{\text{lat}}(d)$ is freely specifiable, except that it must satisfy $\{1, 2, 3\} \mapsto \{1, \sqrt{3}/2, 1/2\}$. Additionally, it makes sense to choose it to be smooth, nonincreasing, and concave. A particularly attractive possibility that satisfies all these criteria is

$$f^{\text{lat}}_{\cos}(d) := \cos\left(\frac{\pi}{6}[d-1]\right), \tag{3.36}$$

which we will use in all our results unless otherwise indicated. (What is perhaps even more satisfying is that all the other simple—though generally not *quite* so simple—possibilities we tried all agree quite well with $f^{\text{lat}}_{\cos}$.) To get some idea as to how much variation is possible in f^{lat}, given our requirements of it, we can consider the envelope of all possible functions satisfying

[6] While the root lattice family A^*_d interpolates between the desired lattices for $d \in [1, 3]$, there are two difficulties: First, its theta series is written in terms of a sum whose number of terms depends upon dimension—see, e.g., Eq. (56) in Chap. 4 of Conway and Sloane [109] for the theta series for A_d, from which the theta series for the dual lattice can be obtained using Jacobi's formula [our Eq. (3.40)]. The sum is over dth roots of unity, so one could contemplate writing it as an integral, using Cauchy's theorem, and proceeding that way. However, even disregarding the complications this would involve, it is not clear how to compute the sums involving x_1^4 that we need (for, e.g., c_{11}) in this framework, or, alternatively, how to implement the requisite distortions to the lattice at the level of its theta series.

[7] Note that most of these hyperlattices are actually shifted lattices, mathematically speaking.

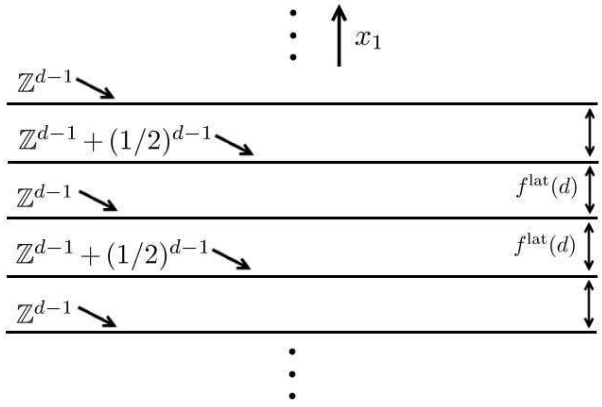

Fig. 3.3. A schematic of the decomposition of the full lattice into hyperlattices.

the requirements. The bounds on this envelope are

$$f^{\text{lat}}_{\text{inf}}(d) = \begin{cases} (\sqrt{3}/2 - 1)(d-1) + 1, & 1 \le d < 2, \\ [(1 - \sqrt{3})(d-2) + \sqrt{3}]/2, & 2 \le d \le 3, \end{cases} \tag{3.37a}$$

$$f^{\text{lat}}_{\text{sup}}(d) = \begin{cases} 1, & 1 \le d < d', \\ [(1 - \sqrt{3})(d-2) + \sqrt{3}]/2, & d' \le d < 2, \\ (\sqrt{3}/2 - 1)(d-1) + 1, & 2 \le d \le 3, \end{cases} \tag{3.37b}$$

where $d' := 3 - 1/(\sqrt{3} - 1) \simeq 1.63$. See Fig. 3.4 for an illustration. [It would be natural to choose f^{lat} so that the dimensionally continued lattice had effective cubic symmetry (discussed in Sec. 3.5.3). However, it is not possible to do so, since the choice of f^{lat} that satisfies this criterion for the $d = 1$ and $d = 2$ lattices does not do so for the $d = 3$ lattice.]

Now, we dimensionally continue the sums over the hyperlattices using the hyperlattice's theta series, which are naturally dimensionally continued. Specifically, the theta series of $\mathbb{Z}^d$ and $\mathbb{Z}^d + (1/2)^d$ are ϑ_3^d and ϑ_2^d, where

$$\vartheta_2(q) := \sum_{k \in \mathbb{Z}} q^{(k+1/2)^2}, \qquad \vartheta_3(q) := \sum_{k \in \mathbb{Z}} q^{k^2}, \qquad \vartheta_4(q) := \sum_{k \in \mathbb{Z}} (-q)^{k^2}. \tag{3.38}$$

[See, e.g., Sec. 5 of Chap. 4 of Conway and Sloane [109], but recall the differences in their theta function notation, discussed below Eq. (3.32); we introduce ϑ_4 here since it appears in the theta series of the dual lattice.]

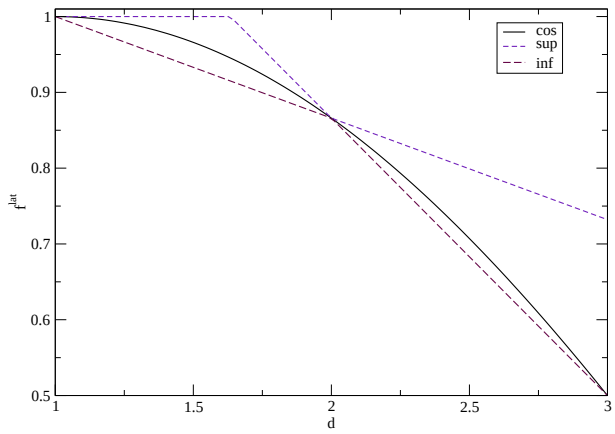

Fig. 3.4. Plots of $f^{\rm lat}_{\rm cos}$ [given in Eq. (3.36)], along with the pointwise sup and inf over all such possibilities [$f^{\rm lat}_{\rm sup}$ and $f^{\rm lat}_{\rm inf}$, given in Eqs. (3.37)].

The theta series of the full lattice is thus

$$\begin{aligned}\bar\Theta_\Lambda(z) &= \sum_{k\in\mathbb{Z}}\left\{q^{[2kf^{\rm lat}(d)]^2}\left[\bar\vartheta_3(z)\right]^{d-1} + q^{[(2k+1)f^{\rm lat}(d)]^2}\left[\bar\vartheta_2(z)\right]^{d-1}\right\} \\ &= \bar\vartheta_3([2f^{\rm lat}(d)]^2 z)\left[\bar\vartheta_3(z)\right]^{d-1} + \bar\vartheta_2([2f^{\rm lat}(d)]^2 z)\left[\bar\vartheta_2(z)\right]^{d-1}.\end{aligned} \tag{3.39}$$

[Recall our overbar notation for theta functions—e.g., $\bar\vartheta_3(z) := \vartheta_3(e^{i\pi z})$.] One can check that this reduces to the appropriate expressions for $d \in \{1, 2, 3\}$; the theta series for the 3-dimensional bcc lattice and 2-dimensional hexagonal lattice are given in Eqs. (96) and (60) of Chap. 4 of Conway and Sloane [109]. For $d = 1$, we obtain the theta series for $\mathbb{Z}$ in a nonstandard form—one can convert it to the standard one given above by using the identity $\bar\vartheta_2(4z) + \bar\vartheta_3(4z) = \bar\vartheta_3(z)$ from Eq. (22) in Chap. 4 of Conway and Sloane.

We use Jacobi's formula (which is already dimensionally continued) to obtain the theta series of the dual lattice, viz., [e.g., Eq. (5.4), or Eq. (19) in Chap. 4 of Conway and Sloane [109]]

$$\bar\Theta_{\Lambda^*}(z) = \sqrt{\det\Lambda}(i/z)^{d/2}\bar\Theta_\Lambda(-1/z). \tag{3.40}$$

When applying Jacobi's formula, we take the volume of the lattice's Voronoi cell to be dimensionally continued in the obvious way, viz., $\sqrt{\det\Lambda} = f^{\rm lat}(d)$. [N.B.: This expression neglects the overall scaling of the lattice, which we fix in Eq. (3.50).] We then obtain, upon use of the

theta function identities in Eq. (21) of Chap. 4 in Conway and Sloane,

$$\begin{aligned}\bar{\Theta}_{\Lambda^*}(z) &= \left\{\bar{\vartheta}_3(z/[2f^{\text{lat}}(d)]^2)\left[\bar{\vartheta}_3(z)\right]^{d-1} + \bar{\vartheta}_4(z/[2f^{\text{lat}}(d)]^2)\left[\bar{\vartheta}_4(z)\right]^{d-1}\right\}\Big/2 \\ &= \frac{1}{2}\sum_{k\in\mathbb{Z}}\left\{q^{[k/f^{\text{lat}}(d)]^2}\left(\left[\bar{\vartheta}_3(z)\right]^{d-1} + \left[\bar{\vartheta}_4(z)\right]^{d-1}\right) + q^{[(k+1/2)/f^{\text{lat}}(d)]^2}\left(\left[\bar{\vartheta}_3(z)\right]^{d-1} - \left[\bar{\vartheta}_4(z)\right]^{d-1}\right)\right\}.\end{aligned} \tag{3.41}$$

The second expression tells us that we can treat the dual lattice as a union of hyperlattices separated by a distance of $[2f^{\text{lat}}(d)]^{-1}$, where the even hyperlattices are D_{d-1} and the odd ones are $D_{d-1} + (0^{d-2}1)$ (cf. the schematic of the direct lattice shown in Fig. 3.3). Here D_d is the d-dimensional root lattice discussed in Sec. 7.1 of Chap. 4 of Conway and Sloane [109], and $D_d + (0^{d-1}1)$ denotes the same lattice shifted by a unit in one coordinate direction. These lattices' theta series are $(\vartheta_3^d \pm \vartheta_4^d)/2$ [Eqs. (87) and (89) of Chap. 4 of Conway and Sloane [109]], with the upper [resp. lower] sign corresponding to D_d [resp. $D_d + (0^{d-1}1)$]. This interpretation is convenient, as it allows us to compute the sums over the dual lattice using the same technology as for the direct lattice.

3.5.3 Lattice sums

From the expressions in Eqs. (3.16)–(3.21), we see that we need to dimensionally continue sums involving a spherically symmetric function times either x_1^n ($n \in \{0, 2, 4\}$), x_2^2, or $x_1^2 x_2^2$. In order to do this with our method, we note that we can express x_1^n in terms of $f^{\text{lat}}(d)$ and the index of the hyperlattice (k, in our discussion below), due to our method of dimensionally continuing the lattice. For x_2^2, we note that the hyperlattices have effective cubic symmetry, so we have

$$\sum_{\vec{x}\in\mathcal{H}_{d-1}\cap S_r} x_2^2 = \frac{n_{\mathcal{H}}(r)r^2}{d-1}, \tag{3.42}$$

where $\mathcal{H}_{d-1} \cap S_r$ denotes the intersection of a hyperlattice $\mathcal{H}_{d-1}$ (with dimension $d-1$) with a $(d-2)$-sphere of radius r centered at the origin, and $n_{\mathcal{H}}(r)$ is the number of points in this intersection (obtained from $\mathcal{H}_{d-1}$'s theta series). Unfortunately, this method is not applicable to x_2^4 (which appears in the Fuchs expression for A_{lat} along with x_1^4), which is why we compute A_{lat} using the more involved method discussed above. However, note that we can compute P_{es} (and thus A_{lat}) and c_{44} two ways—the lattice sums we use do not contain fourth powers of any of the coordinates, so we can also compute them with the index substitution $1 \leftrightarrow 2$. We find that the two choices differ by $\lesssim 10\%$.

We now give the explicit expressions for the computation of the requisite lattice sums in a dimensionally continued manner. If we consider summing $G(x_1, x_2)F(\|\vec{x}\|)$ over the d-dimensional lattice Λ_d, where $G(x_1, x_2)$ is either one of x_1^n ($n \in \{0, 2, 4\}$), x_2^2, or $x_1^2 x_2^2$, then we have to evaluate the following double sum:

$$\sum_{\vec{x}\in\Lambda_d} G(x_1, x_2)F(\|\vec{x}\|) = \sum_{k=0}^{\infty}\sum_{l=0}^{\infty}\left\{\iota_k N_l^{[3]}\mathcal{A}_G F(\mathcal{R}^{[3]}) + 2N_l^{[2]}\mathcal{B}_G F(\mathcal{R}^{[2]})\right\}, \tag{3.43}$$

where

$$\mathcal{A}_{x_1^n} = [2k f^{\text{lat}}(d)]^n, \qquad \mathcal{B}_{x_1^n} = [(2k+1) f^{\text{lat}}(d)]^n, \tag{3.44a}$$

$$\mathcal{A}_{x_2^2} = l/(d-1), \qquad \mathcal{B}_{x_2^2} = l/(d-1) + 1/4, \tag{3.44b}$$

$$\mathcal{R}^{[3]} := \sqrt{[2k f^{\text{lat}}(d)]^2 + l}, \qquad \mathcal{R}^{[2]} := \sqrt{[(2k+1) f^{\text{lat}}(d)]^2 + l + [d-1]/4}, \tag{3.44c}$$

and one obtains the coefficients for the $x_1^2 x_2^2$ case by multiplication (e.g., $\mathcal{A}_{x^2y^2} = \mathcal{A}_{x^2}\mathcal{A}_{y^2}$). [The slightly counterintuitive-appearing superscript "[2]" and "[3]" come from the names of the theta functions that give the pertinent hyperlattices' theta series—see Eq. (3.46).] The l-sum comes from summing over an individual hyperlattice, and the k-sum then sums over all hyperlattices. We have introduced

$$\iota_k := \begin{cases} 1, & k = 0, \\ 2, & \text{otherwise}, \end{cases} \tag{3.45}$$

so we can take k to run only over the positive integers, while the hyperlattice index runs over *all* integers. [One counts all the nonnegative integers except zero twice when writing the sum of an even function over $\mathbb{Z}$ as a sum over the positive integers.] The structure of the hyperlattices is accounted for by the theta series coefficients $N_l^{[j]}$, defined by

$$\sum_{l=0}^{\infty} N_l^{[3]} q^l := [\vartheta_3(q)]^{d-1}, \qquad \sum_{l=0}^{\infty} N_l^{[2]} q^l := \left[\frac{\vartheta_2(q)}{q^{1/4}}\right]^{d-1} \tag{3.46}$$

[recall that the hyperlattices' theta series are ϑ_2^{d-1} and ϑ_3^{d-1}; the theta functions are defined in Eq. (3.38)]. Similarly, for the dual lattice, we have

$$\sum_{\vec{p}\in\Lambda_d^*} G(p_1, p_2) F(\|\vec{p}\|) = \sum_{k=0}^{\infty} \sum_{l=0}^{\infty} \left\{ \iota_k N_l^+ C_G F(\mathcal{R}^+) + 2 N_l^- \mathcal{D}_G F(\mathcal{R}^-) \right\}, \tag{3.47}$$

where

$$C_{p_1^n} = [k/f^{\text{lat}}(d)]^n, \qquad \mathcal{D}_{p_1^n} = [(2k+1)/2 f^{\text{lat}}(d)]^n, \tag{3.48a}$$

$$C_{p_2^2} = 2l/(d-1), \qquad \mathcal{D}_{p_2^2} = (2l+1)/(d-1), \tag{3.48b}$$

$$\mathcal{R}^+ := \sqrt{[k/f^{\text{lat}}(d)]^2 + 2l}, \qquad \mathcal{R}^- := \sqrt{[(2k+1)/2 f^{\text{lat}}(d)]^2 + 2l + 1} \tag{3.48c}$$

(with the same multiplication for the $p_1^2 p_2^2$ case as for the direct lattice), and the theta series coefficients are given by

$$\sum_{l=0}^{\infty} N_l^{\pm} q^l := \left\{ [\vartheta_3(q)]^{d-1} \pm [\vartheta_4(q)]^{d-1} \right\} \Big/ 2 \tag{3.49}$$

[recall that the dual hyperlattices' theta series are $\vartheta_3^{d-1} \pm \vartheta_4^{d-1}$].

We can now calculate the elastic constants by combining together these results with our previously derived expressions. For c_{44}, these are given by Eqs. (3.16) and (3.17). For A_{lat}, the

sum is given in Eq. (3.22). For $A_\perp$, we start from Eq. (3.26), computing c_{11} using Eqs. (3.16) and (3.18), $A_{\perp,\mathrm{cell}} = (3/2)E_{\mathrm{cell}}/\Omega$ using Eq. (3.2), and $A_{\perp,Q}$ using Eq. (3.27).

We also need to determine the scaling of the lattice for a given energy density. This is given by the cell radius, R, computed in Sec. 3.2.3: Equating the volume of a d-dimensional sphere with this radius to the volume of the lattice's Voronoi cell [given by $f^{\mathrm{lat}}(d)a^d$] determines the lattice's spacing, a. Explicitly, we have

$$a = \frac{\pi^{1/2}}{[f^{\mathrm{lat}}(d)\Gamma(d/2+1)]^{1/d}}R, \tag{3.50}$$

using the dimensionally continued expression for the volume of a unit d-ball, viz., $\pi^{d/2}/\Gamma(d/2+1)$. Additionally, we compute Q, the charge of the blob, using the charge density of the rare phase (i.e., the quarks for $\chi \leq 1/2$ and the hadrons for $\chi > 1/2$), and the (d-dimensional) volume of the blob.

3.6 Results and discussion

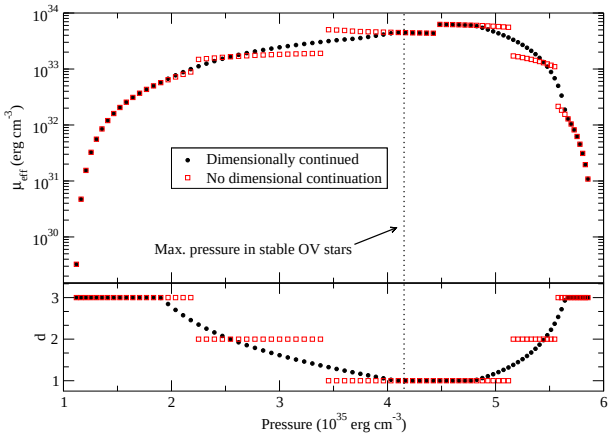

Fig. 3.5. The effective shear modulus and lattice dimensionality versus pressure for the Hy1 EOS both with and without dimensional continuation. We have also indicated the maximum pressure one obtains in a stable OV star using this EOS.

Here we present the shear moduli for the various EOS parameters we consider (given in Table 3.1). First, to give an indication of the effects of dimensional continuation, we plot in Fig. 3.5 the effective shear modulus μ_{eff} [see Eq. (3.13)] and lattice dimensionality d versus pressure with and without dimensional continuation, for the Hy1 EOS with a surface tension of $\sigma = 80$ MeV fm^{-2} [and the $f^{\mathrm{lat}}_{\mathrm{cos}}$ lattice interpolation function from Eq. (3.36)]. We have shown all the pasta phases, even though only the first few appear in stable stars, as is indicated in the

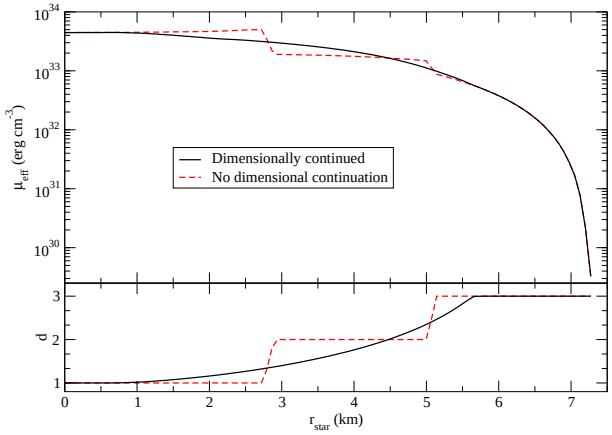

Fig. 3.6. The (interpolated) effective shear modulus and lattice dimensionality versus OV (Schwarzschild coordinate) radius for the maximum mass stable star with the Hy1 EOS both with and without dimensional continuation.

figure. The jump in the effective shear modulus occurs at the halfway point in the mixed phase—i.e., equal amounts of quark and hadronic matter—and is due to the switch on the screening length λ at that point (see the discussion in Sec. 3.2.4). Also note that the lattice becomes unstable for a small range of d slightly less than 3—see the discussion below. We additionally show $\mu_{\rm eff}$ and d versus the (Schwarzschild coordinate) OV stellar radius $r_{\rm star}$ for the maximum mass star in Fig. 3.6. Here we have used the same logarithmic interpolation used to compute maximum quadrupoles and elastic energy in Chap. 4.

Even if the effective shear modulus is positive, the lattice can still be unstable to shear strains. This is in fact the case for small regions of the lattice whose effective shear modulus is shown in Fig. 3.5: For d slightly less than 3, $A_{\rm lat}$ becomes negative. However, this is only true when one uses $f^{\rm lat}_{\rm cos}$, $f^{\rm lat}_{\rm inf}$, or something similar for the lattice interpolation function. If one uses $f^{\rm lat}_{\rm sup}$, then $A_{\rm lat}$ remains positive; this is illustrated in Fig. 3.7 for the standard Hy1 $\sigma = 80$ MeV fm^{-2} case with the lattice interpolation function $f^{\rm lat}_{\rm cos}$, as well as the sup and inf over all interpolation functions [shown in Fig. 3.4]. However, even though different choices of the lattice interpolation function lead to qualitatively different stability results, they only lead to differences of a few percent in the effective shear modulus, as illustrated in Fig. 3.8.[8] (N.B.: Since c_{11} is always negative, $A_\perp$ is made positive by the other contributions, primarily that from $A_{\perp,{\rm cell}}$ [cf. Eq. (3.26)], though for $d \simeq 2.99$ one also needs the contribution from $A_{\perp,Q}$ in certain cases—but note that $A_{\perp,Q}$ also becomes negative for $d \lesssim 2$.)

[8]We have used the two bounds of the envelope on all the interpolation functions we consider to show that even the greatest possible variation is small. The bounds themselves would not be admissible interpolation functions, according to our criteria: They are not smooth, and $f^{\rm lat}_{\rm sup}$ does not even take on the correct value at $d = 3$. (As one would expect, the variation is smaller if one considers a smoother lattice interpolation function that takes on the correct value at $d = 3$ instead of $f^{\rm lat}_{\rm sup}$.)

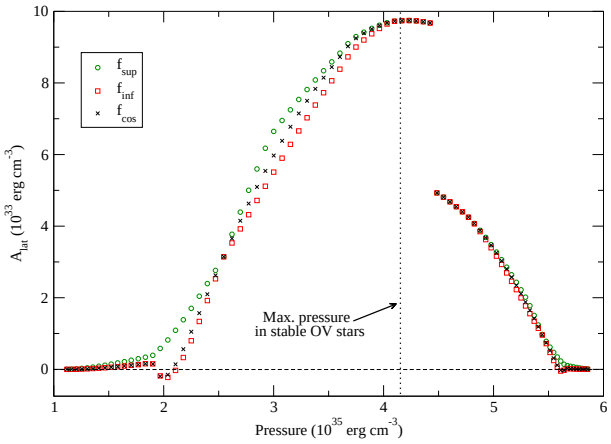

Fig. 3.7. The (dimensionally continued) $A_{\rm lat}$ versus pressure for the Hy1 EOS and a variety of lattice interpolation functions ($f^{\rm lat}$).

The largest effect of the equation of state parameters on observable quantities involving the shear modulus is, of course, the extent of the mixed phase in stable stars. (See Weissenborn *et al.* [221] for a survey of the dependence of the mixed phase's extent on the bag constant and QCD coupling constant for two hadronic EOS parameter sets.) The largest effect on the shear modulus itself, however, comes from the surface tension, σ; this is illustrated for the Hy1 EOS in Fig. 3.9. (Note that the shear modulus is greater for smaller surface tensions for d close to 3.) Additionally, σ has a direct, and quite substantial, effect on the lattice's stability—if σ is too small, then the lattice will become unstable to shears (indicated by $A_\perp$ becoming negative) as the dimensionality decreases, as illustrated for the Hy1 EOS and two low values of σ in Fig. 3.10. (And, of course, a surface tension that is too high will make forming the lattice at all too energetically expensive—we do not consider σs nearly that large.) To illustrate the relatively small effect of the other EOS parameters on the effective shear modulus for a fixed surface tension, in Fig. 3.11 we plot $\mu_{\rm eff}$ versus the quark volume fraction χ for a representative sample of the EOSs from Table 3.1 (all with $\sigma = 80$ MeV fm^{-2}). (The different flavors of Hy1 EOS—i.e., Hy1, Hy1μ, Hy1σ, and Hy1$\mu\sigma$—all have quite similar shear moduli for a fixed surface tension. The largest difference is caused by the inclusion of the surface tension contribution to the pressure balance, as would be expected. We have not shown this, to avoid a cluttered figure.)

3.7 Conclusions

We have made a far more careful calculation of the shear modulus of the hadron–quark mixed phase than has previously been attempted. In particular, we have computed all the lattice's (anisotropic) elastic constants, before averaging to obtain an isotropic effective shear modulus (for a polycrystal); we have also dealt with the lattice's changing dimension in both the electrostatic potential and the geometrical effects on the elastic constants. Perhaps most importantly, we have included the contributions to the elastic constants from changing the size of the blobs that

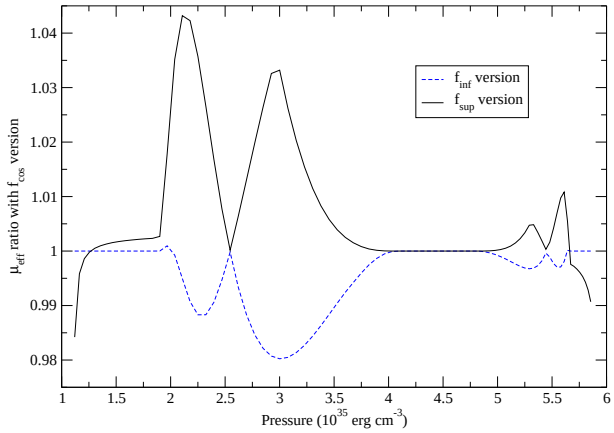

Fig. 3.8. Ratios of the effective shear modulus computed using $f^{\rm lat}_{\rm sup}$ and $f^{\rm lat}_{\rm inf}$ to that computed using $f^{\rm lat}_{\rm cos}$ [see Eqs. (3.36) and (3.37)] plotted versus pressure for the Hy1 EOS and $\sigma = 80$ MeV fm^{-2}.

are present for $d < 3$. These act to stabilize the lattice for lower dimensions (and significantly increase the shear modulus of these portions of the lattice), though only for sufficiently large surface tensions: We have found that most of the lower-dimensional portions of the lattice are unstable to shear perturbations if the surface tension is too small.

These calculations depend upon a wide variety of poorly constrained parameters. While we found that the shear modulus of the mixed phase itself depends most sensitively on the surface tension, astrophysical effects depend on the amount of mixed phase present in a given star, which is primarily determined by the standard hybrid EOS parameters. We will see this in more detail when we use the shear moduli calculated here to compute the maximum elastic quadrupolar deformations and elastic energy of these hybrid star models in Chap. 4.

The obvious place where the calculation could be improved significantly is the treatment of charge screening. Here one would like to perform a nonlinear calculation, as done in [267, 231] (or at least use the Thomas-Fermi approximation), and, perhaps most importantly, include the effects of charge screening on the cell energy: This will affect the shear modulus both by changing the cell size and spacing, as well as through the cell energy's direct contribution to one of the elastic constants for lower dimensions. (In particular, the contributions from this elastic constant are necessary to stabilize the lattice.) Since Endo *et al.* [267, 231] find that charge screening has a noticeable effect on the extent of the mixed phase in stars (in addition to changing the blob size and lattice spacing), it would be very interesting to see whether our discovery that the lattice is only stable for sufficiently large surface tensions still holds when one includes charge screening. (One expects that there will be, in effect, degeneracy pressure contributions to the cell energy in a proper treatment, for instance.)

One might also want to investigate the effects of using different descriptions of the hadronic and quark matter. For instance, one could use the higher-order perturbative calculations of Kurkela, Romatschke, and Vuorinen [247] or the Nambu–Jona-Lasinio treatment (e.g., [268]),

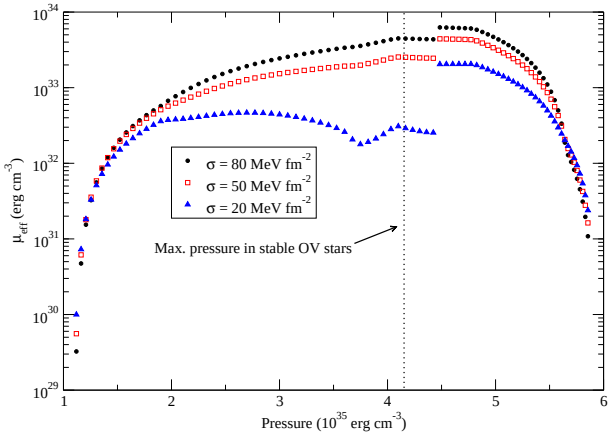

Fig. 3.9. The (dimensionally continued) effective shear modulus versus pressure for the Hy1 EOS and a variety of surface tensions, σ.

for the quark matter, while Dirac-Brückner-Hartree-Fock (e.g., [268]) would be a possibility for the hadronic matter. Other possibilities would be including more exotica (hyperons, for instance, as in, e.g., [269]), and, in particular, magnetic fields (cf. the discussion in Baiko [234]).

Acknowledgments

This work was supported by NSF grants PHY-0555628 and PHY-0855589 and the Eberly research funds of Penn State.

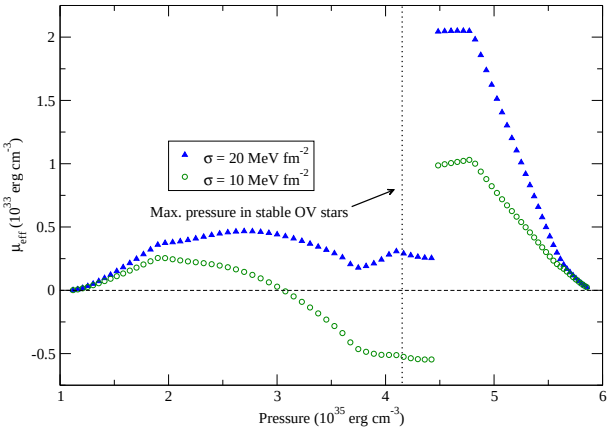

Fig. 3.10. The (dimensionally continued) effective shear modulus versus pressure for the Hy1 EOS and two choices of σ, showing the negative values for $\sigma = 10$ MeV fm^{-2}.

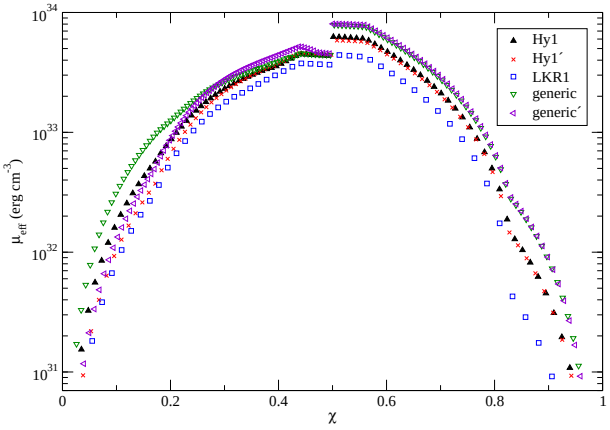

Fig. 3.11. The (dimensionally continued) effective shear modulus versus χ for a representative selection of the EOSs from Table 3.1 and $\sigma = 80$ MeV fm^{-2}. (We have left off a few points at either extreme of χ with low shear moduli to better show the differences between the different predictions where the shear moduli are the highest.)

Chapter 4

Maximum quadrupole deformations and elastic energy of relativistic stars

We present a method for calculating the maximum elastic quadrupolar deformation of a relativistic star, generalizing previous Newtonian, Cowling approximation treatments. (We also show how to drop the Cowling approximation in the Newtonian case.) We then apply this formalism to two possible cases: We consider the standard case of a crustal deformation, applicable to all neutron stars, as well as deformations in the core, applicable to stars that contain exotica. In particular, we consider deformations supported by the shear modulus of the hadron–quark mixed phase in hybrid stars. In both the crust and core cases, we find suppressions of the quadrupole due to relativity, particularly for compact stars. For core deformations, these suppressions can be ~ 3 (compared to the standard, Cowling approximation calculation), while for crustal deformations, they can be ~ 6. We also make more simplistic estimates of the elastic energy stored in these deformations. However, even with the relativistic suppression, we find that hybrid stars can support quadrupole moments of a few $\times 10^{41}$ g cm^2 in fairly realistic cases, and a few $\times 10^{42}$ g cm^2 in more extreme cases [corresponding to (Newtonian) ellipticities of $\sim 5\times 10^{-4}$ and a few $\times 10^{-3}$ with a fiducial moment of inertia of 10^{45} g cm^2] and store an elastic energy of $\sim 10^{49}$ ergs (this maximum does not vary so much between realistic and extreme cases). In the crustal case, we have maximum quadrupoles of a few $\times 10^{39}$ g cm^2 (ellipticities of a few $\times 10^{-6}$) and maximum elastic energies of $\sim 10^{46}$ ergs for $1.4\,M_\odot$ stars, using a somewhat rough model for the crust's shear modulus.

4.1 Introduction

Neutron stars can sustain large quadrupole deformations, which can store considerable amounts of energy; these quantities can be especially large if the star contains some sort of exotic matter. In particular, quark-hadron hybrid stars can have an extensive region of mixed phase with a large shear modulus. (This shear modulus was calculated carefully in Chap 3.) Knowing these maximum quadrupoles and elastic energy is important for gravitational wave searches: The quadrupole moments lead to continuous wave signals, currently being searched for in data from the LIGO and Virgo gravitational wave observatories [74, 75, 76, 77, 78, 79, 80]. See Pitkin [270] for a recent review.

The maximum elastic energy is relevant for searches for gravitational wave bursts from magnetars [81, 82, 83], since the relevant energies can be obtained by cracking exotic cores (as suggested by Corsi and Owen [225]), provided that the large breaking strain (of 0.1) found for the crust by Horowitz and Kadau [271] is applicable to such cores. (This seems likely to be the

This chapter is based on work done in collaboration with B. J. Owen which will be submitted to Phys. Rev. D.

case, since the primary source of the strength appears to be the system's large pressure, but see Chugunov and Horowitz [272] for further discussion of these breaking strains.) In both cases, knowing the maxima of these quantities for a variety of possible interior models allows one to motivate searches (if the maxima are sufficiently large for reasonable theoretical models), as well as to interpret upper limits (and possible detections).

Here we compute the maximum quadrupole moments and elastic energy associated with the large shear moduli of quark-hadron hybrid stars, performing a full general relativistic calculation of the quadrupole moment and using the values for the shear modulus obtained in Chap. 3; to date, these quantities have only been estimated very roughly [87, 225]. We also apply our relativistic calculation to the more commonly considered case of a quadrupole generated by elastic deformations in the crust. Previous investigations of the maximum quadrupole (for either crustal deformations, or deformations of stars containing quark matter) [87, 88, 89, 90, 99, 273] have all been Newtonian and almost all used the basic expression in terms of the star's shear modulus, breaking strain, and local gravitational acceleration obtained in the Cowling approximation (i.e., neglecting the contribution from the self-gravity of the perturbation) by Ushomirsky, Cutler, and Bildsten (UCB) [98]. [Haskell *et al.* [88] use the formalism developed in Haskell, Jones, and Andersson (HJA) [99], which lets them drop the Cowling approximation, but is still Newtonian.]

We also use UCB's basic formalism in our calculations, but significantly extend their results, first dropping the Cowling approximation, and then doing the full general relativistic (GR) version. We follow UCB's approach much more closely than do HJA, and obtain an analogous integral expression to UCB's for the maximum quadrupole moment. This is advantageous for a number of reasons: First, it lets us assess the differences in the contributions from the shear modulus at different radii in the star in the three different cases (Newtonian Cowling, Newtonian no Cowling, and GR). Second, it allows us to verify that the maximally strained case indeed leads to the maximum quadrupole moment in all the cases we have considered. UCB were able to show this generally in the Newtonian Cowling case, and we can check that it remains true without the Cowling approximation in both the Newtonian and GR cases.

In our general relativistic calculation, we use the relativistic theory of elasticity given by Carter and Quintana [274] (revisited and placed in a somewhat more modern guise by Karlovini and Samuelsson [275]), though all we need from it is the relativistic form of the elastic stress-energy tensor, which can be obtained by simple covariance arguments, as noted by Schumaker and Thorne [276]. We also use the standard Thorne and Campollataro [277] Regge-Wheeler gauge [278] formalism for perturbations of static relativistic stars, following Hinderer's recent calculation [100] of the quadrupole moment of a tidally deformed relativistic star.

Even though we are interested in the gravitational radiation emitted by rotating stars, it is sufficient for us to calculate the static quadrupole deformation. As discussed by Ipser [279], and then proved for more general situations by Thorne [24], this static quadrupole (obtained from the asymptotic form of the metric) will give the emitted gravitational radiation in the fully relativistic, slow-motion limit. [This approximation has uncontrolled remainders of order ω/ω_K, where ω and ω_K are the star's angular velocity and its maximum angular velocity—i.e., its Kepler velocity. This ratio is $\lesssim 10^{-2}$ for the pulsars for which LIGO has been able to beat the spindown limit. (These pulsars are discussed in [77].)]

We make far less sophisticated calculations of the energy contained in the perturbation, only calculating the purely elastic part—i.e., ignoring the contributions due to the changes in the

star's structure—though we do include the corrections due to the star's curved spacetime. We leave more involved calculations to future work.

We shall generally show G and c explicitly, though we shall take $G = c = 1$ during the most calculationally intense portion of Sec. 4.3. This part also involved reasonably extensive use of the computer algebra system MAPLE and the associated tensor manipulation package GRTENSORII [181]. (However, we used MATHEMATICA to perform the numerical computations presented in Sec. 4.5.)

The paper is structured as follows: In Sec. 4.2, we review UCB's formalism and extend it to compute the maximum Newtonian quadrupole deformation without making the Cowling approximation. In Sec. 4.3, we further generalize to the fully relativistic case, and in Sec. 4.4, we describe how to compute the star's elastic energy. In Sec. 4.5, we display the Green functions for the maximum quadrupole for various equations of state (EOSs), as well as showing the maximum quadrupoles and elastic energy for the various hybrid EOS parameters considered in Chap. 3. We also show the maximum quadrupoles in the crustal deformation case (using a rough model for the crust's shear modulus). We discuss these results in Sec. 4.6, and finally summarize and conclude in Sec. 4.7.

4.2 Newtonian calculation of the quadrupole

We first demonstrate how to compute the Newtonian quadrupole without making the Cowling approximation. This provides a warm-up before we tackle the full relativistic case, and also will allow us to verify some of the statements made by UCB and HJA. We use the basic formalism of UCB, modeling the star as nonrotating, with a stress-energy tensor of a perfect fluid plus shear terms, and treating the shear contributions as a first-order perturbation. (This perturbative treatment should be quite a good approximation: The maximum shear stress we consider is $\lesssim 5 \times 10^{-4}$ times the star's energy density.)

It is convenient to start by realizing that the quadrupole moment can be written in terms of the surface value of the perturbation to the star's Newtonian potential. We start from UCB's definition of

$$Q_{22} := \int_0^\infty \delta\rho(r) r^4 dr \tag{4.1}$$

(where we take the density perturbation $\delta\rho$ and all similar perturbed quantities to have only an $l = m = 2$ part). [Note that this quadrupole moment differs by an overall constant from the one defined by Thorne [24]—e.g., his Eq. (5.27a).] We then recall that the perturbed Poisson equation is (writing out the explicit radial Laplacian for an $l = 2$ perturbation, $\triangle_2$, and denoting radial derivatives by primes)

$$(\triangle_2 \delta\Phi)(r) := \frac{1}{r^2}[r\delta\Phi(r)]'' - \frac{6}{r^2}\delta\Phi(r) = 4\pi G\delta\rho, \tag{4.2}$$

with boundary conditions of

$$\delta\Phi(0) = 0, \qquad R(\delta\Phi)'(R) = -3\delta\Phi(R). \tag{4.3}$$

[See, e.g., Eqs. (2.15) and (2.16) in [280]—their Φ_{22} is our $\delta\Phi$.] If we now substitute the expression for $\delta\rho$ in terms of $\delta\Phi$ into the expression for Q_{22} and integrate by parts, using the boundary

conditions, we obtain

$$Q_{22} = -\frac{5R^3}{4\pi G}\delta\Phi(R). \tag{4.4}$$

[N.B.: There is an equivalent expression (specialized to an $l = 2$, $m = 0$ perturbation) in Eq. (A4) of Cutler, Ushomirsky, and Link [281]. This sort of expression is more commonly seen in the relativistic case, where it is necessary to obtain the quadrupole in this manner by looking at the perturbation's asymptotic behavior—see the discussion in Sec. 4.3.]

We now wish to obtain an equation for $\delta\Phi$ in terms of the shear stresses. We follow UCB in decomposing the perturbed stress tensor as [see their Eqs. (38)–(40)]

$$\delta\tau_{ab} = -\delta p Y_{lm} g_{ab} + t_{rr} Y_{lm}(\hat{r}_a\hat{r}_b - e_{ab}/2) + t_{r\perp} f_{ab} + t_\Lambda(\Lambda_{ab} + e_{ab}/2). \tag{4.5}$$

Here δp is the pressure perturbation, Y_{lm} is a spherical harmonic, t_{rr}, $t_{r\perp}$, and t_Λ are the components of the shear stresses, g_{ab} denotes the metric of flat, 3-dimensional Euclidean space, $e_{ab} := g_{ab} - \hat{r}_a\hat{r}_b$, $f_{ab} := 2r\hat{r}_{(a}\nabla_{b)}Y_{lm}/\beta$ [$\beta := \sqrt{l(l+1)} = \sqrt{6}$], and $\Lambda_{ab} := r^2\nabla_a\nabla_b Y_{lm}/\beta^2 + f_{ab}/\beta$. (We have corrected the dropped factor of β^{-1} multiplying f_{ab} in UCB's definition of Λ_{ab}—this was also noticed by HJA [99].) We also have $t_{ab} = 2\mu\sigma_{ab}$, where μ is the shear modulus, and σ_{ab} is the strain tensor. (This is a factor-of-2 correction to the expression in UCB, as noted in [87].) Now, a convenient expression can be obtained from the perturbed equation of hydrostatic equilibrium

$$\nabla^a\delta\tau_{ab} = \delta\rho g(r)\hat{r}_b + \rho\nabla_b\delta\Phi \tag{4.6}$$

(∇_a denotes the flat-space covariant derivative), substituting for $\delta\rho$ using the Poisson equation [Eq. (4.2)] and projecting along $\hat{r}^b$, yielding

$$\frac{\triangle_2\delta\Phi}{4\pi G} + \frac{\rho}{g(r)}\delta\Phi' = \frac{\hat{r}^b\nabla^a\delta\tau_{ab}}{g(r)} = \frac{1}{g(r)}\left[-\delta p' + t'_{rr} + \frac{3}{r}t_{rr} - \frac{\beta}{r}t_{r\perp}\right]. \tag{4.7}$$

We then project Eq. (4.6) along $\nabla^b Y_{lm}$ to express δp in terms of the shear stresses t_{rr}, $t_{r\perp}$, and t_Λ, along with ρ and $\delta\Phi$, giving

$$\delta p = -\rho\delta\Phi - \frac{t_{rr}}{2} + \frac{r}{\beta}t'_{r\perp} + \frac{3}{\beta}t_{r\perp} + \left(\frac{1}{\beta^2} - \frac{1}{2}\right)t_\Lambda. \tag{4.8}$$

Substituting this into Eq. (4.7), we thus obtain

$$\triangle_2\delta\Phi - \frac{4\pi G}{g(r)}\rho'\delta\Phi = \frac{4\pi G}{g(r)}\left[\frac{3}{2}t'_{rr} - \frac{4}{\beta}t'_{r\perp} - \frac{r}{\beta}t''_{r\perp} - \left(\frac{1}{\beta^2} - \frac{1}{2}\right)t'_\Lambda + \frac{3}{r}t_{rr} - \frac{\beta}{r}t_{r\perp}\right]. \tag{4.9}$$

We now wish to obtain an integral expression for Q_{22} that generalizes UCB's Eq. (64) to the case where we do not make the Cowling approximation. We shall do this by obtaining the Green function for the l.h.s. of Eq. (4.9), and then integrating by parts; we will be able to discard all of the boundary terms, since the stresses vanish at the star's surface and the integrand vanishes at the star's center. We can obtain the Green function using the standard Sturm-Liouville expression in terms of the solutions of the homogeneous equation [e.g., Eq. (10.103) in Arfken and Weber [282]]; we obtain the appropriate solution to the homogeneous equation numerically,

for a given background star model. The equation for the Green function is

$$(\mathcal{L}\mathcal{G})(r,\bar{r}) := \frac{\partial}{\partial r}\left[r^2\frac{\partial}{\partial r}\mathcal{G}(r,\bar{r})\right] - \left[6 + \frac{4\pi G r^2}{g(r)}\rho'\right]\mathcal{G}(r,\bar{r}) = \delta(r-\bar{r}), \tag{4.10}$$

with

$$\mathcal{G}(0,\bar{r}) = 0, \qquad R\partial_1\mathcal{G}(R,\bar{r}) = -3\mathcal{G}(R,\bar{r}), \tag{4.11}$$

where ∂_1 denotes a partial derivative taken with respect to the first "slot" of the function.

If we then write $G_{\rm Newt}(r) := -5R^3r^2\mathcal{G}(R,r)/g(r)$ [including the factor of r^2 to account for multiplying through by it in obtaining the operator $\mathcal{L}$, and also including the factor of $1/g(r)$ that multiplies all of the r.h.s. of Eq. (4.9), for notational convenience], we have

$$\begin{aligned} Q_{22}^{\rm Newt} &= \int_0^R G_{\rm Newt}(r)\left[\frac{3}{2}t'_{rr} - \frac{4}{\beta}t'_{r\perp} - \frac{r}{\beta}t''_{r\perp} - \left(\frac{1}{\beta^2}-\frac{1}{2}\right)t'_\Lambda + \frac{3}{r}t_{rr}(r) - \frac{\beta}{r}t_{r\perp}(r)\right]dr \\ &= -\int_0^R\left\{\left[\frac{3}{2}G'_{\rm Newt}(r) - \frac{3}{r}G_{\rm Newt}(r)\right]t_{rr}(r) + \left[\frac{r}{\beta}G''_{\rm Newt}(r) - \frac{2}{\beta}G'_{\rm Newt}(r) + \frac{\beta}{r}G_{\rm Newt}(r)\right]t_{r\perp}(r) \right. \\ &\quad \left. + \left(\frac{1}{2}-\frac{1}{\beta^2}\right)G'_{\rm Newt}(r)t_\Lambda(r)\right\}dr \end{aligned} \tag{4.12}$$

We have freely integrated by parts in obtaining the second expression, noting that the boundary terms are zero, since $G_{\rm Newt}(r)$ vanishes sufficiently rapidly as $r \to 0$, and the stress is zero at the surface of the star.[1] This reduces to UCB's Eq. (64) if we take $G_{\rm Newt}(r) \to r^4/g(r)$, corresponding to the Green function for $\triangle_2$ (i.e., for the radial part of the Poisson equation for a perturbation with $l = 2$ angular dependence).

To obtain an analogue of the expression for the maximum quadrupole given in Eq. (5) of Owen [87], we note that UCB's argument about the maximum strain leading to the maximum quadrupole still holds here for the stars we consider, since the coefficients of the stress components in the integrand are all positive. (We have checked this numerically for each background star model we have considered.) We thus recall that $t_{ab} = 2\mu\sigma_{ab}$, where σ_{ab} is the star's strain tensor, and write $\sigma_{rr} = (32\pi/15)^{1/2}\bar{\sigma}_{\rm max}$, $\sigma_{r\perp} = (3/2)^{1/2}\sigma_{rr}$, and $\sigma_\Lambda = 3\sigma_{rr}$, giving the case where the star is maximally (and uniformly) strained—see Eqs. (67) in UCB. (The breaking strain $\bar{\sigma}_{\rm max}$ is given by the von Mises expression, $\sigma_{ab}\sigma^{ab} = 2\bar{\sigma}_{\rm max}^2$; it thus corresponds to assuming that the lattice yields when it has stored a maximum energy density.) We then have

$$\frac{|Q_{22}^{\rm max,Newt}|}{\bar{\sigma}_{\rm max}} = \sqrt{\frac{32\pi}{15}}\int_0^R \mu(r)\left[rG''_{\rm Newt}(r) + 3G'_{\rm Newt}(r)\right]dr. \tag{4.13}$$

This reduces to Eq. (5) in Owen [87] if we use the Cowling approximation result for $G_{\rm Newt}$, viz., $G_{\rm Newt}(r) \to r^4/g(r)$.

Note that there is no direct contribution from ρ' to $G''_{\rm Newt}$ in the no Cowling case, despite what one might expect from the equation for $\mathcal{G}$ [Eq. (4.10)]: Writing $\bar{\mathcal{G}}(r) := \mathcal{G}(R,r)$ for

[1] Note that Haskell, Jones, and Andersson [99] claim that UCB's expression does not include distributional contributions due to sudden changes in the shear modulus. This is not the case—these are included due to UCB's integration by parts (cf. the definition of the distributional derivative).

notational simplicity, the ρ' contribution from

$$\bar{\mathcal{G}}''(r) = (2/r)\bar{\mathcal{G}}'(r) + [6/r^2 + 4\pi G\rho'(r)/g(r)]\bar{\mathcal{G}}(r) \tag{4.14}$$

is exactly canceled by one from

$$g''(r) = 6Gm(r)/r^4 - 8\pi G\rho(r)/r + 4\pi G\rho'(r) \tag{4.15}$$

in

$$G''_{\rm Newt}(r) = -5R^3r^2[\bar{\mathcal{G}}''(r)/g(r) - \bar{\mathcal{G}}(r)g''(r)/\{g(r)\}^2 + \{\text{terms with no } \rho'\}]. \tag{4.16}$$

However, there is a contribution from ρ' to $G''_{\rm Newt}$ (via g'') if we make the Cowling approximation [i.e., take $G_{\rm Newt}(r) \to r^4/g(r)$, as discussed above]; we shall see that this leads to a significant difference in the resulting contributions to the quadrupole moment from regions of the star surrounding a sharp change in density (e.g., near the crust-core interface, which will be relevant for the quadrupoles supported by crustal elasticity considered by UCB and others).

Numerically, we compute $G_{\rm Newt}$ by solving $\mathcal{L}F = 0$ [with the operator $\mathcal{L}$ given by Eq. (4.10)] with the boundary conditions $F(r_0) = 1$ and $F'(r_0) = 2/r_0$, where r_0 is the small inner radius used in the solution of the Oppenheimer-Volkov equations, as discussed in Sec. 4.5.1 [though $F(r_0) = 0$, $F'(r_0) = C \neq 0$ gives much the same result], and writing

$$\mathcal{G}(R, r) = -\frac{F(r)}{3RF(R) + R^2F'(R)} \tag{4.17}$$

[cf. Eq. (10.103) in Arfken and Weber [282]]. We obtain such a simple form because $r < R$ for the situation in which we are interested, and we have evaluated the Wronskian at the star's surface, using the boundary condition there to eliminate the contribution from the other solution to the homogeneous equation.

Our Green function method might not seem to be the best choice for obtaining the maximum quadrupole numerically (though the formulation is ideal for showing that maximum stress gives the maximum quadrupole, or in seeing how much stresses at different radii contribute to the total quadrupole) since we have to integrate the numerical solution to a differential equation. However, this method appears to be the simplest way of dealing with any potential distributional contributions from the derivatives of the shear modulus, since they are automatically taken care of by the integration by parts.

4.3 General relativistic calculation of the quadrupole

Here we compute the maximum quadrupole moment in general relativity, using the Regge-Wheeler gauge [278] relativistic stellar perturbation theory developed by Thorne and Campollataro [277], as in the similar calculation of the tidal Love number of a relativistic star by Hinderer [100]. We start by writing down the line element corresponding to a static, even-parity, $l = 2$ first-order perturbation of a static, spherical, relativistic star in the Regge-Wheeler gauge [cf. Eq. (14) in Hinderer [100]]:

$$ds^2 = -[1 + H_0(r)Y_{lm}]f(r)dt^2 + [1 + H_2(r)Y_{lm}]h(r)dr^2 + [1 + K(r)Y_{lm}]r^2(d\theta^2 + \sin^2\theta d\phi^2). \tag{4.18}$$

Here we have used the notation of Wald [283] for the background, so f and h are the standard Schwarzschild functions for the unperturbed star, with $f = e^{2\phi}$, where

$$\phi'(r) = \frac{G}{c^2}\frac{m(r) + 4\pi r^3 p/c^2}{r[r - 2Gm(r)/c^2]}, \tag{4.19}$$

with $\phi(R) = \log(1 - 2GM/Rc^2)/2$, and

$$h(r) = \left[1 - \frac{2Gm(r)}{rc^2}\right]^{-1}. \tag{4.20}$$

In these expressions, $m(r) := 4\pi \int_0^r \rho(\bar{r})\bar{r}^2 d\bar{r}$. We have also written our expressions in terms of l, for clarity, following UCB, even though we have specialized to $l = 2$.

The metric perturbation is determined by H_0, H_2, and K, which here are sourced by the perturbation to the star's stress-energy tensor. The appropriate stress-energy tensor can be obtained directly from the standard Newtonian expression [given in Eq. (4.5)] by simple covariance arguments, as in Schumaker and Thorne [276], or from the detailed relativistic elasticity theory of Carter and Quintana [274] [see their Eq. (6.19)]; this is also discussed in Karlovini and Samuelsson [275] [see their Eq. (128)]. All we really need for our purposes is to note that the shear contribution is tracefree with respect to the background metric, so we can use the obvious covariant generalization of the decomposition given by UCB,[2] giving

$$\delta T_{ab} = [\delta\rho \hat{t}_a\hat{t}_b + \delta p(g_{ab} + \hat{t}_a\hat{t}_b) - t_{rr}(\hat{r}_a\hat{r}_b - q_{ab}/2)]Y_{lm} - t_{r\perp} f_{ab} - t_\Lambda(\tilde{\Lambda}_{ab} + h^{1/2}Y_{lm}q_{ab}/2), \tag{4.21}$$

with the full stress-energy tensor given by

$$T_a{}^b = \rho \hat{t}_a\hat{t}^b + p(\delta_a{}^b + \hat{t}_a\hat{t}^b) + \delta T_a{}^b. \tag{4.22}$$

Here, indices now run over all four spacetime dimensions and g_{ab} denotes the background (spacetime) metric (which we use to raise and lower indices). Additionally, we have introduced the background temporal and radial unit vectors $\hat{t}_a$ and $\hat{r}_a$; q_{ab} is the metric on the unit 2-sphere; $f_{ab} := 2r\hat{r}_{(a}\nabla_{b)}Y_{lm}/\beta$ [this is the same definition as f_{ab} in the Newtonian case, given below Eq. (4.5), hence the same name, except that $\hat{r}_a$ and ∇_a now have their curved-space meanings]; and $\tilde{\Lambda}_{ab} = r^2h^{1/2}\nabla_a\nabla_b Y_{lm}/\beta^2 + f_{ab}/\beta$.

Our $\tilde{\Lambda}_{ab}$ differs from the Newtonian Λ_{ab} (from UCB) due to the insertion of $h^{1/2}$. This insertion is necessary for $\tilde{\Lambda}_{ab}$ to be transverse and orthogonal to f_{ab}. The same logic leads to the introduction of the factor of $h^{1/2}$ multiplying q_{ab} in the t_Λ term in Eq. (4.21); it is there so that the t_Λ term is orthogonal to the t_{rr} term. We have used UCB's convention for the relative sign between the perfect fluid and shear portions of the stress-energy tensor, though we have reversed the overall sign. (However, we have used the UCB convention proper in Sec. 4.2.) The factor of $h^{1/2}$ in the coefficient of t_Λ leads to a factor of h^{-1} in the strain σ_Λ that corresponds to a maximum von Mises breaking strain given by $\sigma_{ab}\sigma^{ab} = 2\bar{\sigma}^2_{\max}$. We thus have $\sigma_\Lambda = 3\sigma_{rr}/h$ [with $\sigma_{rr} = (32\pi/15)^{1/2}\bar{\sigma}_{\max}$ and $\sigma_{r\perp} = (3/2)^{1/2}\sigma_{rr}$, as before].

[2] It is instructive to note that we never use any sort of Hookean property of the star's material, only that there is a tracefree contribution to its stress-energy tensor whose maximum value is given by the material's shear modulus and von Mises breaking strain.

One can now obtain equations for H_0, H_2, and K using various components of the perturbed Einstein equations [written in mixed form—i.e., as $G_\alpha{}^\beta = (8\pi G/c^4)T_\alpha{}^\beta$], as in Hinderer [100]: From the ${}_\theta{}^\phi$-component, we obtain (taking $G = c = 1$ for the moment)

$$H_2 = 16\pi r^2 h^{1/2} t_\Lambda/\beta^2 - H_0. \tag{4.23}$$

From the ${}_r{}^\theta$-component, we obtain

$$K' = -H_0' + (H_2 - H_0)\phi' + (H_0 + H_2)/r + 16\pi r h^{1/2} t_{r\perp}/\beta. \tag{4.24}$$

From the difference of the ${}_t{}^t$ and ${}_r{}^r$ components, we obtain

$$-K'' + \left(\phi' + \psi' - \frac{2}{r}\right)K' + \frac{H_0' + H_2'}{r} - \frac{\beta^2 h}{2r^2}H_0 + \left[\frac{\beta^2 h}{2r^2} - \frac{2}{r}(\phi' + \psi')\right]H_2 = 8\pi h(\delta\rho + \delta p - t_{rr}), \tag{4.25}$$

where $\psi := (1/2)\log h$. [We have checked these equations against Eqs. (19) in Ipser [279] (taking the static limit—i.e., $\Omega = 0$ in Ipser's notation); the concordance for notation is $\nu = 2\phi$, $e^\nu = f$, $\lambda = 2\psi$, $e^\lambda = h$, $\rho_1 = -\delta\rho$, $p_1 = -\delta p$, $\mathfrak{P}_2 = t_{rr}$, $\mathfrak{Q}_1 = h^{1/2}t_{r\perp}/\beta$, and $\mathfrak{S} = h^{1/2}t_\Lambda/\beta^2$. Additionally, Ipser's H_0 is the negative of ours.] We can now use the first two equations to write the third as an expression for H_0 in terms of the source terms, viz.,

$$H_0'' + \left(\frac{2}{r} + \phi' - \psi'\right)H_0' + \mathcal{P}(r)H_0 = 8\pi h^{1/2}\mathcal{S}(r), \tag{4.26}$$

where

$$\mathcal{P}(r) := 2\phi'' + 2\phi'\left(\frac{3}{r} - \phi' - \psi'\right) + \frac{2\psi'}{r} - \frac{\beta^2}{r^2}h \tag{4.27}$$

and

$$\begin{aligned}\mathcal{S}(r) &:= h^{1/2}(\delta\rho + \delta p - t_{rr}) + 2\left\{(3 - r\phi')\frac{t_{r\perp}}{\beta} + r\frac{t_{r\perp}'}{\beta} + [r^2\phi'' + r\phi'(5 - r\phi') + r\psi' - \beta^2 h/2 + 1]\frac{t_\Lambda}{\beta^2}\right.\\ &\quad \left. + r^2\phi'\frac{t_\Lambda'}{\beta^2}\right\}\\ &=: h^{1/2}(\delta\rho + \delta p) + \mathcal{S}_{[t]}(r),\end{aligned} \tag{4.28}$$

and we have written $\mathcal{S}_{[t]}$ for the contributions from shear stresses. These expressions can be checked against Eqs. (27)–(28) in Ipser [279], and we find exact agreement.

We now wish to eliminate $\delta\rho$ and δp in favor of the shear stresses, as in the Newtonian version. We use the same projections of stress-energy conservation as in the Newtonian case (projecting onto the quantities defined by the background spacetime, for simplicity) along with the Oppenheimer-Volkov (OV) equations, giving

$$\delta\rho + \delta p = \frac{1}{\phi'}\left[-\frac{H_0'}{2}(\rho + p) - \delta p' + t_{rr}' + \left(\frac{3}{r} + \phi'\right)t_{rr} - \frac{\beta}{r}h^{1/2}t_{r\perp}\right] \tag{4.29}$$

and

$$\delta p = -\frac{H_0}{2}(\rho + p) - \frac{t_{rr}}{2} + \frac{1}{\beta h^{1/2}}\left[(3 + r\phi')t_{r\perp} + rt'_{r\perp}\right] + h^{1/2}\left(\frac{1}{\beta^2} - \frac{1}{2}\right)t_\Lambda. \tag{4.30}$$

Using the second expression to substitute for $\delta p'$ in the first, we have

$$\begin{aligned}\delta\rho + \delta p = \frac{1}{\phi'}\Bigg\{&\frac{H_0}{2}(\rho' + p') + \left[\frac{3}{r} + \phi'\right]t_{rr} + \frac{3}{2}t'_{rr} + \frac{1}{\beta h^{1/2}}\Bigg[\left(\psi'[3 + r\phi'] - \phi' - r\phi'' - \frac{\beta^2 h}{r}\right)t_{r\perp} \\ &- (4 + r[\phi' - \psi'])t'_{r\perp} - rt''_{r\perp}\Bigg] + \left(\frac{1}{2} - \frac{1}{\beta^2}\right)h^{1/2}(\psi' t_\Lambda + t'_\Lambda)\Bigg\} \\ =:\ &\frac{H_0}{2\phi'}(\rho' + p') + \frac{\mathcal{S}_{[\delta\rho,\delta p]}(r)}{\phi'}.\end{aligned} \tag{4.31}$$

The equation for H_0 thus becomes

$$\begin{aligned}(\mathcal{L}_{\rm GR}H_0)(r) &:= H_0'' + \left(\frac{2}{r} + \phi' - \psi'\right)H_0' + \left[\mathcal{P}(r) + 4\pi h\frac{\rho' + p'}{\phi'}\right]H_0 \\ &= 8\pi h^{1/2}[h^{1/2}\mathcal{S}_{[\delta\rho,\delta p]}(r)/\phi' + \mathcal{S}_{[t]}(r)],\end{aligned} \tag{4.32}$$

[see Eq. (4.27) for the definition of $\mathcal{P}(r)$ and Eqs. (4.28) and (4.31) for the definitions of the source terms]. As expected, this reduces to Eq. (4.9) in the Newtonian limit [where we have $H_0 \to 2\delta\Phi$ and $c^2\phi' \to g(r)$].

We now want to write the equation for H_0 in Sturm-Liouville form, in order to obtain its Green function easily. To do this, we note that the appropriate "integrating factor" (for the first two terms) is $r^2(f/h)^{1/2}$, which gives

$$[r^2(f/h)^{1/2}H_0']' + r^2(f/h)^{1/2}\left[\mathcal{P}(r) + 4\pi h\frac{\rho' + p'}{\phi'}\right]H_0 = 8\pi r^2 f^{1/2}[h^{1/2}\mathcal{S}_{[\delta\rho,\delta p]}(r)/\phi' + \mathcal{S}_{[t]}(r)]. \tag{4.33}$$

We also need the boundary conditions, which are given by matching H_0 onto a vacuum solution at the surface of the star. The vacuum solution that is regular at infinity is given by Eq. (20) in Hinderer [100] with $c_2 = 0$, viz.,

$$H_0(R) = c_1\left[\left(\frac{2}{C} - 1\right)\frac{C^2/2 + 3C - 3}{1 - C} + \frac{6}{C}\left(1 - \frac{1}{C}\right)\log(1 - C)\right], \tag{4.34}$$

where we have evaluated this at the star's surface—i.e., $r = R$—and defined the star's compactness,

$$C := 2GM/Rc^2 \tag{4.35}$$

(now returning to showing factors of G and c explicitly). We require that H_0 and H_0' be continuous at the star's surface. The value of c_1 obtained from this matching of the internal and external solutions gives us the quadrupole moment. If we use the quadrupole moment amplitude that reduces to the UCB integral in the Newtonian limit, we have

$$Q_{22} = \frac{G^2}{c^4}\frac{M^3 c_1}{\pi}. \tag{4.36}$$

[This expression comes from inserting a pure $l = m = 2$ density perturbation into Eq. (2) in Hinderer [100], contracting the free indices with unit position vectors, performing the angular integral, for which the expressions in Thorne [24] are useful, and noting that the result is $(8\pi/15)Y_{22}$ times the UCB integral—i.e., UCB's Eq. (1). The given result then follows immediately from Hinderer's Eqs. (7), (9), and (22); we reverse the overall sign since we have reversed the UCB sign convention for the stress-energy tensor.]

We then have a Green function for Q_{22} of

$$\mathcal{G}_{\rm GR}(R,r) = \left(\frac{2GM}{c^2}\right)^3 \left(1 - \frac{2GM}{Rc^2}\right)^{-1} \frac{\mathcal{U}(r)}{c^2R^2[\mathcal{U}'(R)H_0(R) - \mathcal{U}(R)H_0'(R)]} \tag{4.37}$$

(including the overall factor of $8\pi G/c^4$ that multiplies the source). Here $\mathcal{U}$ is given by $\mathcal{L}_{\rm GR}\mathcal{U} = 0$ [$\mathcal{L}_{\rm GR}$ is given by Eq. (4.32)], with $\mathcal{U}(r_0) = 1$ and $\mathcal{U}'(r_0) = 2/r_0$ [cf. Eq. (10.103) in Arfken and Weber [282], as well as our Newtonian version above; recall that r_0 denotes the small inner radius we use in our solution of the OV equations and that $(f/h)^{1/2}(R) = 1 - 2GM/Rc^2$]. Here $H_0(R)$ and $H_0'(R)$ are given by the boundary conditions [Eq. (4.34)] with $c_1 \to 1$. [One obtains this expression from the Green function for $H_0(R)$, dividing through by the quantity in brackets in Eq. (4.34) to obtain c_1, and then using Eq. (4.36) to obtain Q_{22}.] We thus define, for notational simplicity, two relativistic generalizations of $G_{\rm Newt}(r)$: One,

$$G_{\rm GR}(r) := \frac{r^2(fh)^{1/2}\mathcal{G}_{\rm GR}(R,r)}{\phi'}, \tag{4.38}$$

for the contributions from $\mathcal{S}_{[\delta\rho,\delta p]}$, and one,

$$\bar{G}_{\rm GR}(r) := r^2 f^{1/2}\mathcal{G}_{\rm GR}(R,r), \tag{4.39}$$

for the contributions from $\mathcal{S}_{[t]}$.

With these definitions, the integral expression for the quadrupole in terms of the stresses (and the structure of the background star) is

$$\begin{aligned} Q_{22} &= \int_0^R \left[G_{\rm GR}(r)\mathcal{S}_{[\delta\rho,\delta p]}(r) + \bar{G}_{\rm GR}(r)\mathcal{S}_{[t]}(r)\right] dr \\ &= \int_0^R (C_{rr}t_{rr} + C_{t\perp}t_{r\perp} + C_\Lambda t_\Lambda) dr, \end{aligned} \tag{4.40}$$

where

$$C_{rr} := \left(\frac{3}{r} + \phi'\right) G_{\rm GR}(r) - \frac{3}{2}G_{\rm GR}'(r) - h^{1/2}\bar{G}_{\rm GR}(r), \tag{4.41a}$$

$$C_{r\perp} := -\frac{\beta h^{1/2}}{r}G_{\rm GR}(r) + \frac{2 + r(\phi' + \psi')}{\beta h^{1/2}}G_{\rm GR}'(r) - \frac{r}{\beta h^{1/2}}G_{\rm GR}''(r) + \frac{4 - 2r\phi'}{\beta}\bar{G}_{\rm GR}(r) - 2\frac{r}{\beta}\bar{G}_{\rm GR}'(r), \tag{4.41b}$$

$$C_\Lambda := \left(\frac{1}{\beta^2} - \frac{1}{2}\right) h^{1/2}G_{\rm GR}'(r) + \frac{2r\phi'(3 - r\phi') + 2r\psi' - \beta^2 h + 2}{\beta^2}\bar{G}_{\rm GR}(r) - \frac{2r^2\phi'}{\beta^2}\bar{G}_{\rm GR}'(r), \tag{4.41c}$$

and we have freely integrated by parts twice to obtain the second equality in Eq. (4.40), using the same argument as in the Newtonian calculation.

We now look at the maximum quadrupole. This is still given by the uniformly maximally strained case—we have checked numerically that the coefficients of the three stress terms are all negative for all the background stars we consider. We thus have a maximum quadrupole given (as discussed previously) by $t_{ab} = 2\mu\sigma_{ab}$ and $\sigma_{rr} = (32\pi/15)^{1/2}\bar{\sigma}_{\rm max}$, $\sigma_{r\perp} = (3/2)^{1/2}\sigma_{rr}$, and $\sigma_\Lambda = 3\sigma_{rr}/h$, yielding

$$\frac{|Q_{22}^{\rm max,GR}|}{\bar{\sigma}_{\rm max}} = \sqrt{\frac{32\pi}{15}}\int_0^R \mu(r)\Bigg\{\left[\frac{6}{r}(h^{1/2}-1) - 2\phi'\right]G_{\rm GR}(r) + \left[3 - \frac{r}{h^{1/2}}(\phi'+\psi')\right]G'_{\rm GR}(r) + \frac{r}{h^{1/2}}G''_{\rm GR}(r) + Q^{\rm stress}\Bigg\}dr, \tag{4.42}$$

where

$$Q^{\rm stress} := 2\left[\frac{r\phi'(r\phi'-3) - r\psi' + \beta^2 h/2 - 1}{h} + r\phi' + h^{1/2} - 2\right]\bar{G}_{\rm GR}(r) + 2r\left(\frac{r\phi'}{h}+1\right)\bar{G}'_{\rm GR}(r) \tag{4.43}$$

is the contribution from the stresses' own gravity. We have split it off both for ease of notation, and because it is generally quite negligible, except for the most massive, compact stars, as illustrated below. (The factor of $1/\phi'$ is what makes the contributions from the density and pressure perturbations so much larger.)

4.4 Computation of the energy

As in the computation of the maximum quadrupole, we compute both the Newtonian and relativistic versions of the elastic energy, to give an indication of how much difference the relativistic treatment makes. However, our computations will be much less sophisticated: We shall not include the contributions from the deformation of the star, only the energy due to the elastic deformation of the lattice itself.

We first note that the energy density of a lattice with shear modulus $\mu(r)$ and shear strain σ_{ab} is given by $\mu(r)\sigma_{ab}\sigma^{ab}/2$, so the Newtonian elastic energy of a spherical star (of radius R) with this shear modulus, stressed to its maximum von Mises breaking strain, with $\bar{\sigma}^2_{\rm max} = \sigma_{ab}\sigma^{ab}/2$, is thus given by

$$E^{\rm max}_{\rm Newt} = 4\pi\bar{\sigma}^2_{\rm max}\int_0^R \mu(r)r^2dr. \tag{4.44}$$

In the relativistic case, we have a different measure (coming from the curved background), and also need to introduce a redshift factor, since we want to compute the energy measured at infinity [see, e.g., Eq. (47b) in Schumaker and Thorne [276], as well as the discussion in Sec. V*b* of Ipser [279]]. The spherically symmetric measure is now given by $4\pi h^{1/2}r^2dr$, and the gravitational redshift factor is $f^{1/2}$ [where f and h are the background metric coefficients introduced in Eq. (4.18)], so the relativistic energy is given by

$$E^{\rm max}_{\rm GR} = 4\pi\bar{\sigma}^2_{\rm max}\int_0^R \mu(r)(fh)^{1/2}r^2dr. \tag{4.45}$$

Of course, if one is interested in obtaining the maximum energy available to be radiated in gravitational waves, one really wants to consider the Hamiltonian of the perturbed spacetime. This Hamiltonian is considered in Schumaker and Thorne [276], as well as, e.g., Detweiler and Ipser [284] and Schutz [285]. All of these references show that their Hamiltonian satisfies a conservation law involving the star's gravitational energy loss. However, none of these are immediately applicable to our case, since they assume either a perfect fluid perturbation (Detweiler and Ipser, Schutz) or a purely elastic, odd-parity perturbation (Schumaker and Thorne). (We have even parity perturbations of both perfect fluid and elastic variables.) We leave the derivation of an appropriate Hamiltonian for future work. (The Lagrangian density for nonradial perturbations of a relativistic star with an isotropic shear modulus given in Finn [286] may be useful in this regard.)

4.5 Results

4.5.1 Green functions for Q_{22} for various EOSs

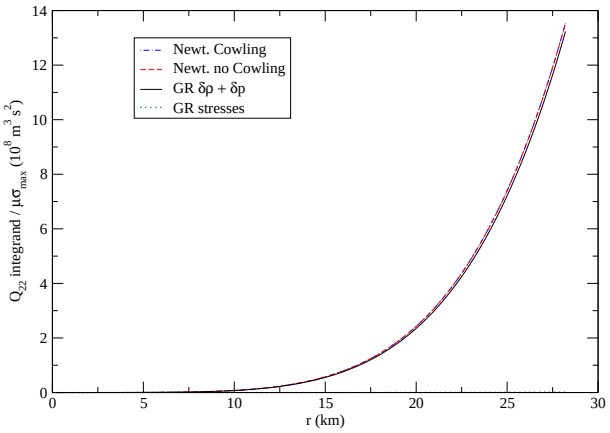

Fig. 4.1. The Q_{22} integrands (without the factor of $\mu\bar{\sigma}_{\max}$) for the SLy EOS and an $0.124\,\mathrm{M}_\odot$ star, with a compactness of 0.013. (The two Newtonian curves lie on top of each other, and the stress contribution is barely visible above the r-axis.)

We now show how the different maximal strain Q_{22} Green functions [given by the integrands in Eqs. (4.13) and (4.42) without the factors of μ (but including the prefactor)] vary with EOS, as well as with the mass of the star, for a given EOS, to give an indication of how much difference the various approximations make in different situations. We start with the unified SLy EOS [287], obtained by Haensel and Potekhin [288] (using the table provided by the Ioffe group [289] at [290]). Here we illustrate the changes in the Green functions with mass for stars with masses ranging from $0.124\,\mathrm{M}_\odot$ (close to this EOS's minimum mass of $0.094\,\mathrm{M}_\odot$, and similar to the masses considered by Horowitz [273]) to the maximum mass of $2.05\,\mathrm{M}_\odot$; see

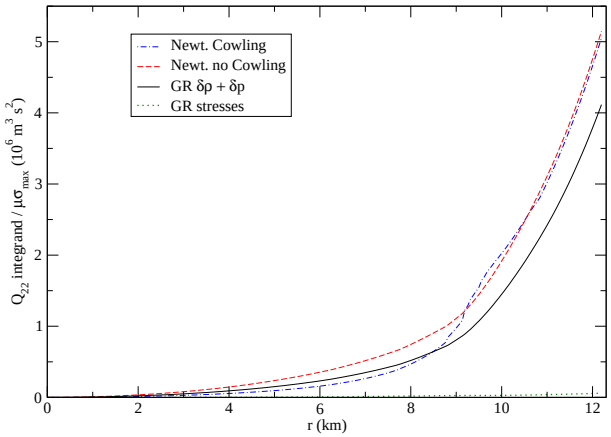

Fig. 4.2. The Q_{22} integrands (without the factor of $\mu\bar{\sigma}_{\rm max}$) for the SLy EOS and an $0.500\,{\rm M}_\odot$ star, with a compactness of 0.12.

Figs. 4.1, 4.2, 4.3, 4.4, 4.5, and 4.6. These stars' compactnesses[3] range from ~ 0.01 to 0.6. Note that Figs. 4.1 and 4.6 have different vertical scales than the other plots in the series.

We illustrate the ratios of the various Q_{22} Green functions to the Newtonian Cowling approximation one for the maximum mass ($2.05\,{\rm M}_\odot$) hybrid star using the Hy1 EOS (see Table 3.1) in Fig. 4.7.[4] Note that we compute the stellar background fully relativistically, using the OV equations, in all cases; we identify the OV equations' Schwarzschild radial coordinate with the Newtonian radial coordinate. We have used the enthalpy form of the OV equations given by Lindblom [55], and implemented the inner boundary condition by taking the star to have an inner core of radius $r_0 = 100$ cm, whose mass is given by $(4/3)\pi r_0^3 \epsilon_0$, where ϵ_0 is the energy density corresponding to the central enthalpy that parametrizes the solution. In all cases, we have used MATHEMATICA 7's native methods to solve the differential equations, find roots, etc. (We may need to choose a smaller value of r_0, or use a higher-order expansion for the inner boundary condition to avoid the spike in the relativistic Green function seen around $r = 0$ in Fig. 4.7. However, this appears to make at most a few percent correction to the results for the quadrupoles, and thus can likely be ignored. Nevertheless, we will revisit all the numerics and ensure that everything is working correctly, particularly for the stars that only contain hybrid matter in the innermost portions of their core.)

[3]Recall that we define the compactness as $2GM/Rc^2$ (as do, e.g., Binnington and Poisson [291]), so that a Schwarzschild black hole has a compactness of unity. We emphasize our definition here, since one finds other quantities referred to as the compactness in the literature. For instance, Damour and Nagar [292] define their compactness without the factor of 2, and Lattimer and Prakash [293] use the reciprocal of Damour and Nagar's definition, which has the unusual property that a Newtonian star has a larger compactness than a black hole.

[4]As discussed in Chap. 3, for our low-density EOS, we use the same combination of the Baym, Pethick, and Sutherland (BPS) [235] EOS for $n_B < 0.001\,{\rm fm}^{-3}$ and the Negele and Vautherin [236] EOS for $0.001\,{\rm fm}^{-3} < n_B < 0.08\,{\rm fm}^{-3}$ used by Lattimer and Prakash [237]. These were obtained from the table provided by Kurkela *et al.* [238] at [239].

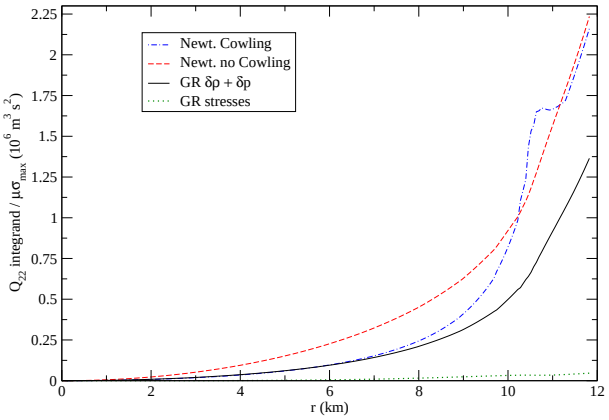

Fig. 4.3. The Q_{22} integrands (without the factor of $\mu\bar{\sigma}_{\rm max}$) for the SLy EOS and a 1.00 $M_\odot$ star, with a compactness of 0.25.

4.5.2 Maximum Q_{22} and elastic energy for hybrid stars

Here we display the maximum quadrupole deformations and elastic energy as a function of stellar mass, for each of the hybrid EOS parameter sets considered in Chap. 3. We start by showing these values calculated in the various approximations using the Hy1 EOS (with a surface tension of $\sigma = 80$ MeV fm^{-2}; see Table 3.1) in Figs. 4.8 and 4.9, and then restrict our attention to the relativistic results. We also show how the maximum relativistic quadrupole varies with the surface tension for the Hy1 EOS in Fig. 4.10. (The variation of the maximum elastic energy is almost identical.) The slightly larger quadrupoles for lower surface tensions at low masses are expected, due to a slightly larger shear modulus at low pressures for lower surface tensions—see Fig. 3.9. Finally, we show the maximum quadrupoles and elastic energy for different hybrid EOSs in Figs. 4.11 and 4.12. The considerable differences are due to the substantial variations in the extent of the mixed phase in stable stars with EOS parameters, as well as the EOS-dependence of the stars' compactnesses (see Table 3.1). In particular, the LKR1 EOS produces stars with a very large region of mixed phase—up to 72.6% of the star's radius—and a (relatively) small maximum compactness—only 0.433. (Note that our quadrupole and energy curves for the LKR1 EOS end slightly short of the EOS's maximum mass of 1.955 $M_\odot$, only going to 1.948 $M_\odot$, due to problems with the numerics.) In fact, despite the greater than an order of magnitude differences in high-pressure shear modulus for the Hy1 EOS in going from a surface tension of 20 MeV fm^{-2} to one of 80 MeV fm^{-2} (see Fig. 3.9), the differences in the resulting maximum quadrupoles and elastic energy are at most a factor of a few (for large masses). This is not unexpected: These quantities are dominated by the portions of the mixed phase further out in the star, where the shear moduli have a much lesser dependence on the surface tension. (Additionally, larger surface tensions lead to smaller shear moduli at low pressures, which also helps to minimize the effect, though the maximum quadrupoles still increase with increasing surface tension for high masses, as expected.)

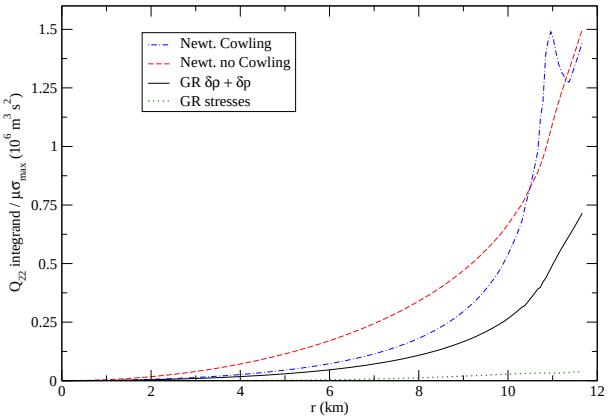

Fig. 4.4. The Q_{22} integrands (without the factor of $\mu\bar{\sigma}_{\rm max}$) for the SLy EOS and a 1.40 $M_\odot$ star, with a compactness of 0.35.

In addition to the quadrupole moments, we also show the "LIGO ellipticity" $\epsilon_{\rm LIGO} = \sqrt{8\pi/15}Q_{22}/I_{zz}$ [e.g., Eq. (2) of [87]; I_{zz} is the star's principal moment of inertia, for which we use the fiducial LIGO value of $I_{zz} = 10^{38}$ kg m^2 = 10^{45} g cm^2]. We do this for easy comparison with the observational papers (e.g., [75, 77]), since they frequently quote results in terms of ellipticity, instead of quadrupole moment. Note that LIGO's current upper bounds on ellipticity (with this fiducial moment of inertia) are $\sim 10^{-4}$, corresponding to a quadrupole moment of $\sim 10^{41}$ g cm^2. N.B.: We present these LIGO ellipticities *only* for comparison with LIGO results, not to give any indication of the shape of the star. While the true ellipticity (computed with the star's actual principal moment of inertia, which may differ from the fiducial LIGO one by at least a factor of a few) indeed gives a clear measure of the star's shape in the Newtonian case, it does not do so in any obvious way in the relativistic case. If one wished to know the star's true, relativistic shape, one would need to calculate it using the same perturbative setup used to obtain the quadrupole moment.

4.5.3 Maximum Q_{22} and elastic energy for crustal deformations

Here we give a rough indication of how much relativistic effects affect contributions to quadrupole from elastic deformations in the crust, as originally considered by UCB. We use the SLy EOS considered above, and take the shear modulus to be 10^{16} cm^2 s^{-2} times the star's energy density; this rough method of obtaining the shear modulus was used by HJA (though the actual shear modulus is likely a factor of a few greater—see their Fig. 2); they also used the SLy EOS (though they did not give it that name). (We also use the Horowitz and Kadau breaking strain of 0.1 [271].) Additionally, we take the bottom of the crust to be located at a density of either 2.1×10^{14} g cm^{-3} or 1.6×10^{14} g cm^{-3}, again following HJA. [Note, however, that Douchin and Haensel [287] place the crust-core interface at a pressure of 5.37×10^{32} erg cm^{-3} (corresponding to a density of 1.28×10^{14} g cm^{-3}) for the SLy EOS.] HJA take the first, thick crust case to compare with UCB; for the second, thin crust case, they are following a suggestion

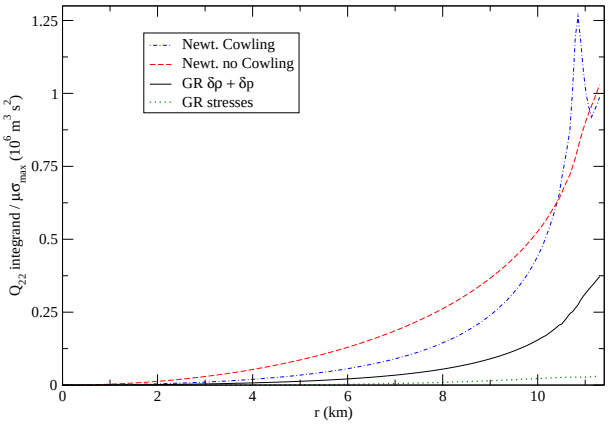

Fig. 4.5. The Q_{22} integrands (without the factor of $\mu\bar{\sigma}_{\rm max}$) for the SLy EOS and a 1.75 $M_\odot$ star, with a compactness of 0.46.

by Haensel [294]. We plot the quadrupole moment and ellipticity, as above, for masses between $\sim$ 1.2 $M_\odot$ (around the minimum observed neutron star mass—see [293]) and the SLy EOS's maximum mass of 2.05 $M_\odot$ in Fig. 4.13.

In addition to the expected relativistic suppression of the quadrupole (which becomes quite dramatic for compact, high-mass stars), we also find that the Newtonian Cowling approximation slightly overestimates the quadrupole (by $\sim$ 25–50%), as found by HJA (though they find the overestimate to be considerably greater, around a factor of at least a few), as opposed to the underestimate seen in the hybrid case. This overestimate is due to the cancellation of contributions from ρ' when one drops the Cowling approximation (see the discussion at the end of Sec. 4.2). We also see that the contributions from the stresses' gravity to the maximum quadrupole are slightly more significant in the crustal case, where they are $\lesssim$ 14%, than they are in the hybrid case, where they are $\lesssim$ 10%.

We also compute the elastic energy in this case, for comparison. We show it in Fig. 4.14 for the same stellar masses and other parameters used in the above quadrupole computation. We see that the smallest-mass stars we consider have maximum energies of $\sim 10^{46}$ ergs in the thick crust case, comparable to the electromagnetic energy released in the 2004 giant flare from SGR 1806-20 [295, 296, 297]. We also find that the relativistic corrections to the maximum energy are completely negligible here ($< 1\%$), as should be expected, since the correction factor $(fh)^{1/2}$ [see Eq. (4.45)] goes to its Schwarzschild value of unity at the star's surface.

4.6 Discussion

Previous studies of the tidal and magnetic deformations of compact stars have found similar relativistic suppressions of quadrupole moments with compactness. In the tidal case, the multipoles the star develops in response to an external tidal field are determined by the star's Love numbers, which have recently been computed in a number of papers [100, 291, 292, 298,

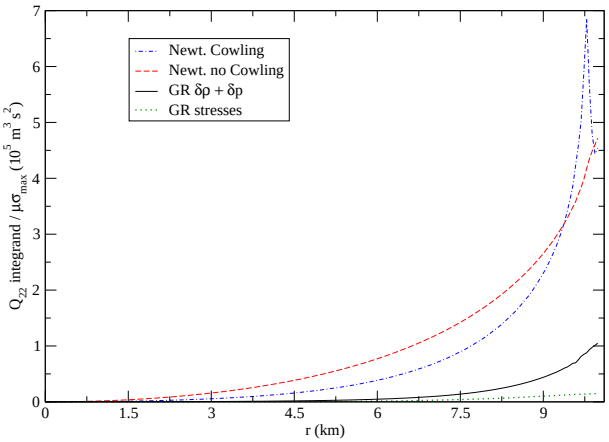

Fig. 4.6. The Q_{22} integrands (without the factor of $\mu\bar{\sigma}_{\rm max}$) for the SLy EOS and a maximum mass, $2.05\,{\rm M}_\odot$ star, with a compactness of 0.60.

299], for a variety of equations of state (both polytropic and realistic). All of these calculations find that the Love number of a maximally compact star is a factor of $\gtrsim 3$ smaller than that for a Newtonian star (for the polytropic cases). For realistic non-self-bound EOSs, they find that the Love number decreases with increasing compactness after an initial rise from zero at zero compactness. In particular, Damour and Nagar [292] compute the Love number for the maximally compact incompressible star (with a compactness of $8/9 \simeq 0.89$) analytically, and find that the Love number is over 400 times smaller for this case than for an incompressible Newtonian star, and there are suppressions of over an order of magnitude for other low-order polytropes (i.e., ones with a polytropic index ≤ 1).

In the case of magnetic deformations, the expected suppressions are seen by, e.g., Ioka and Sasaki [300] and Ciolfi, Ferrari, and Gualtieri (CFG) [301]. In fact, since the largest compactness considered in those papers is only 0.36 (in CFG), one imagines that they overestimate the maximum quadrupoles by at least a factor of a few for more compact stars.

These suppressions can primarily be attributed to something akin to the no-hair theorem, since the largest suppression comes from the boundary conditions. This implies that the stiffness of spherically symmetric curved vacuum spacetime suppresses the quadrupole. The quadrupole is also suppressed by a larger effective gravitational acceleration (given by ϕ').

Our results imply that all of the Newtonian computations of quadrupoles due to elastic mountains on relativistic stars overestimate the quadrupole moment, often by at least a factor of a few. (The only exceptions we have found are for low-mass stars of around $0.5\,{\rm M}_\odot$, where the Newtonian Cowling approximation is a slight underestimate for contributions to the quadrupole from elastic stresses in the core, though the Newtonian no Cowling version is still an overestimate—see Fig. 4.2. But note that neutron stars with these masses are not known to exist in nature.) This overestimate can be ~ 6 for massive stars whose quadrupole is being generated by an elastic deformation near the crust-core interface, as considered by UCB and others; this is

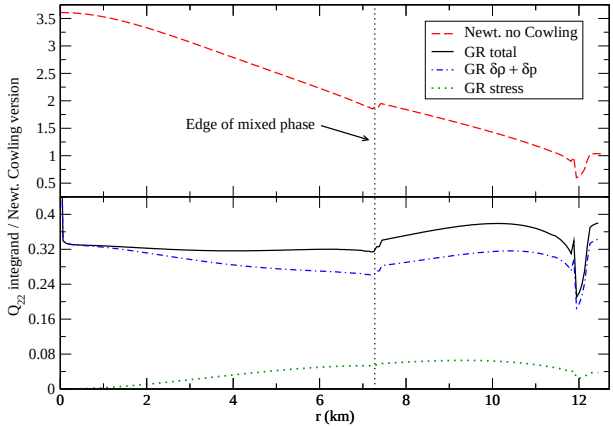

Fig. 4.7. Ratios of the Q_{22} integrands with the Newtonian Cowling approximation integrand for the Hy1 EOS and a maximum mass, 2.06 $M_\odot$ star, with a compactness of 0.49.

due to the sudden changes in density at that interface entering directly through g'', as discussed at the end of Sec. 4.2.

However, the calculations by Horowitz [273] only receive negligible corrections (of $\lesssim$ 5%), since he considers quite nonrelativistic (compactnesses of ~ 0.01) low-mass neutron stars. In fact, one makes even smaller errors in using the Cowling approximation to treat these stars (see Fig. 4.1), since the gravitational field is much larger than the changes in density in the crust. However, it is unclear what relevance Horowitz's calculation has for neutron stars in the universe, as no neutron stars with such low masses have ever been observed (nor is there a compelling mechanism for forming them).

Nevertheless, Horowitz remarks that gravitational wave detection of gravitational waves from elastically deformed neutron stars will, *ceteris paribus*, be biased towards low(er) mass neutron stars, if one considers deformations generated by crustal stresses. This is an important point, particularly when considering the astronomical interpretation of detections (or even upper limits), and the results we present here make the bias against high-mass stars even stronger.

Of course, one must remember that all of these values are maxima, assuming a maximally strained star, while there is no reason for a given star to be maximally strained. Moreover, as UCB and HJA note, these calculations assume that all the strain goes into the $l = m = 2$ perturbation, though strain in other modes (e.g., the $l = 2$, $m = 0$ mode due to rotation) can push the lattice closer to its breaking strain while not increasing the $l = m = 2$ quadrupole.

4.7 Conclusions and outlook

We have presented a method for calculating the maximum elastic quadrupole deformation of a relativistic star with a known shear modulus and applied it to stars whose elastic deformations are supported either by a shear modulus from a hadron–quark mixed phase in the core, or the Coulomb lattice of nuclei in the crust. We find that the relativistic quadrupole is always

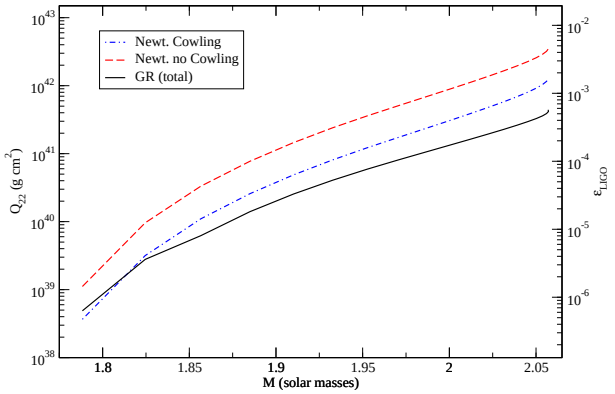

Fig. 4.8. The Newtonian Cowling, Newtonian no Cowling, and full relativistic (including stress contributions) values for the maximum quadrupole deformations (and LIGO ellipticity) of hybrid stars versus mass, using the Hy1 EOS with a surface tension of $\sigma = 80$ MeV fm^{-2} and a breaking strain of 0.1.

suppressed, compared with the standard, Newtonian Cowling approximation calculation of the quadrupole, at least for stars with masses of $\gtrsim 1\,M_\odot$ (corresponding to the observed masses of neutron stars) and the EOSs we have investigated. These suppressions can be up to ~ 3 in the hybrid case, and ~ 6 in the crustal case (though note that our crustal calculations use a rough approximation for the shear modulus). These suppressions strengthen the Horowitz [273] argument that searches for gravitational waves from elastically deformed neutron stars supported by crustal stresses are biased towards lower-mass stars. (However, this argument does not apply to quadrupole deformations of hybrid stars, since the increase in the size of the region of mixed phase with increasing mass dominates the relativistic suppressions.) These results imply that many of the previous calculations of elastic quadrupoles (e.g., [88, 89, 90, 98, 99]) will need their results revised downwards.

But even with these suppressions, we obtain maximum quadrupole deformations of a few $\times\, 10^{42}$ g cm^2 in the hybrid case for a very stiff hadronic EOS, and a few $\times\, 10^{41}$ g cm^2 for more realistic cases (in both situations, the maximum quadrupoles are given by the most massive stars); these values assume that the Horowitz and Kadau [271] breaking strain of 0.1 is applicable to the mixed phase. Such large quadrupole deformations were previously thought only to be possible for solid quark stars (see [87]), or from crustal deformations in the very low-mass neutron stars considered by Horowitz [273]. These large deformations (corresponding to LIGO ellipticities of a few $\times\, 10^{-3}$ in the extreme case, and $\sim 5 \times 10^{-4}$ in a more realistic case) would be able to be detected by current LIGO searches for gravitational waves from certain known neutron stars. (However, we must note that there is no reason to assume that such isolated stars are anywhere near maximally strained, even neglecting the uncertainties in the description of their interiors.) The prospects for crustal quadrupoles are now somewhat less optimistic, and definitely favor lower-mass stars. We also calculated the elastic energy stored in the quadrupole deformation of the hybrid stars, and found it to be $\sim 10^{49}$ ergs (in our rather simplistic treatment),

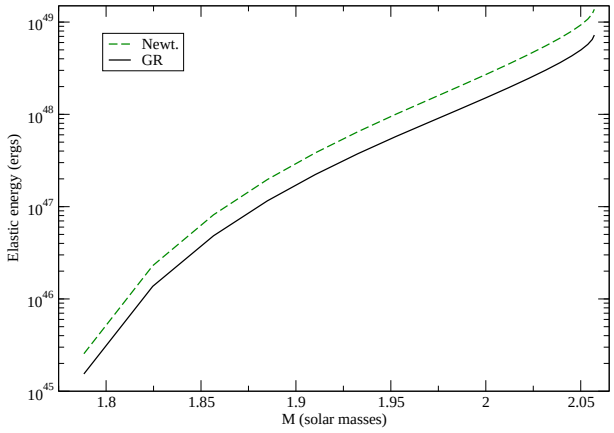

Fig. 4.9. The Newtonian and relativistic values for the maximum elastic energy of hybrid stars versus mass, using the Hy1 EOS with a surface tension of $\sigma = 80$ MeV fm^{-2} and a breaking strain of 0.1.

for the same parameters that give the maximum quadrupole deformation. It would be useful to calculate the full energy of the deformed star (i.e., including the contributions from the change to the star's structure), which we will do in future work.

Other future work will include calculating the relativistic quadrupoles from crustal deformation with a more realistic shear modulus than our rather rough one. We will start by using the more careful version considered by HJA, which includes the changing composition calculated by Douchin and Haensel [287]. We might also consider the more recent expressions for the shear modulus due to Baiko [234] and Horowitz and Hughto [302], though these are small corrections to the Ogata and Ichimaru [262] expression used by HJA. Far more important is the difference between accreted and non-accreted crusts, which we can also explore following HJA [99]. We will likely also consider a variety of other EOSs, to see how these affect the relativistic suppression of the quadrupole.

It might also be interesting to see if one can obtain an analytic Green function for the relativistic quadrupole for the maximally compact incompressible star case. The relativistic electric Love number for this case was computed analytically by Damour and Nagar [292], who found a very large suppression compared with the analogous Newtonian case. (Similarly, one might investigate the Tolman VII exact solution.) A considerably more ambitious (but still potentially quite informative) analytic investigation would be to search for an exact solution describing an elastically deformed (i.e., nonspherical) static star supported by a physically reasonable EOS and shear modulus—one would almost surely want to start with the axisymmetric case. One might also want to consider the shape of the surface of the deformed star in the relativistic case, since one can no longer simply use the Newtonian ellipticity. Additionally, it would be interesting to consider the possible interaction of elastic and magnetic deformations.

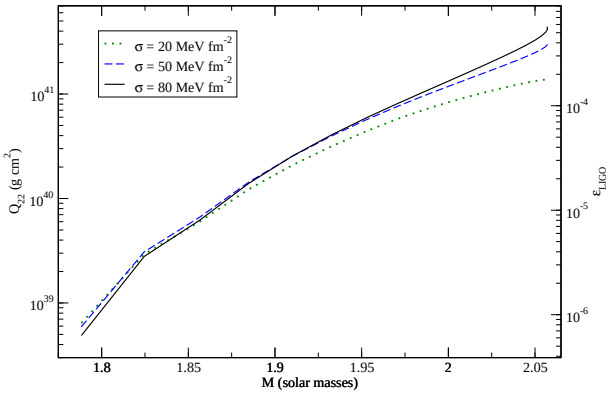

Fig. 4.10. The full relativistic maximum quadrupole deformations (and LIGO ellipticity) of hybrid stars versus mass, using the Hy1 EOS with various surface tensions, σ, and a breaking strain of 0.1.

Acknowledgments

This work was supported by NSF grant PHY-0855589 and the Eberly research funds of Penn State.

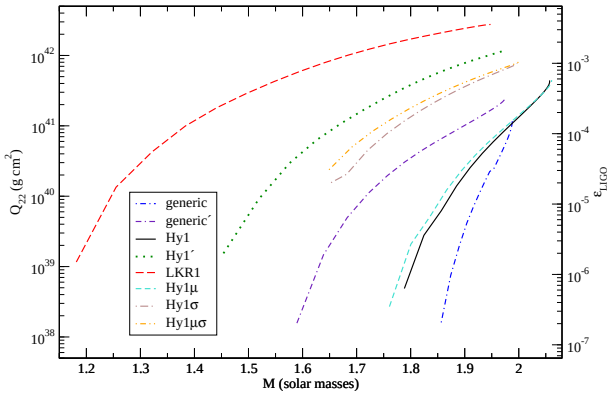

Fig. 4.11. The full relativistic maximum quadrupole deformations (and LIGO ellipticity) of hybrid stars versus mass, using various EOSs from Table 3.1, all with a surface tension of σ = 80 MeV fm^{-2} and a breaking strain of 0.1.

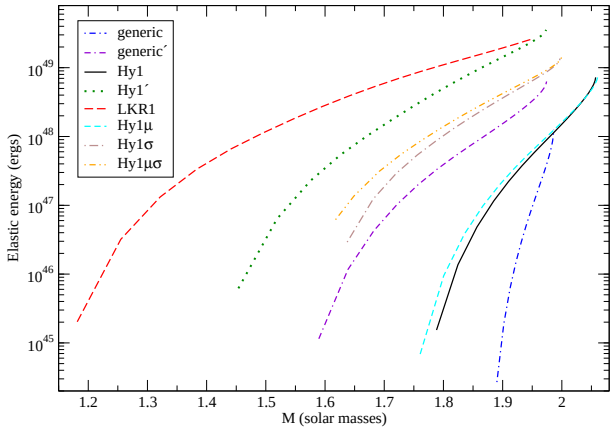

Fig. 4.12. The maximum relativistic elastic energy of hybrid stars versus mass, using various EOSs from Table 3.1, all with a surface tension of σ = 80 MeV fm^{-2} and a breaking strain of 0.1.

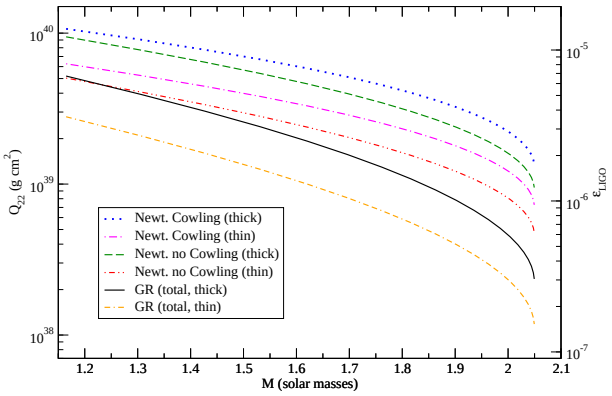

Fig. 4.13. The Newtonian Cowling, Newtonian no Cowling, and full relativistic (including stress contributions) values for the maximum quadrupole deformations (and LIGO ellipticity) due to crustal stresses versus mass. These are computed using the SLy EOS with the rough HJA recipe for the shear modulus (and two crustal thicknesses) and a breaking strain of 0.1.

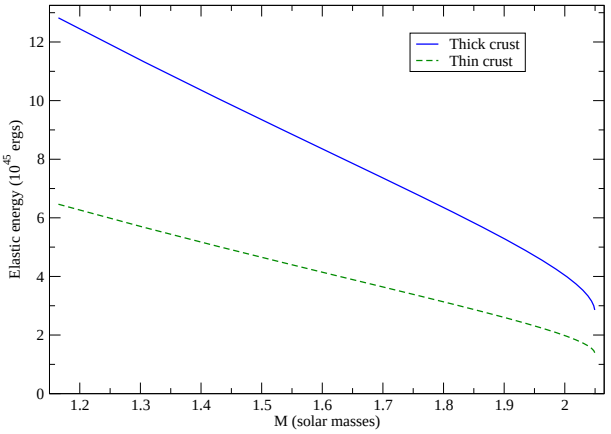

Fig. 4.14. The maximum elastic energy for a crustal deformation versus mass, calculated using the SLy EOS with the rough HJA recipe for the shear modulus (and two crustal thicknesses) and a breaking strain of 0.1.

Chapter 5

A dimensionally continued Poisson summation formula

...entre deux vérités du domaine réel, le chemin le plus facile et le plus court passe bien souvent par le domaine complexe. —Paul Painlevé [303]

We generalize the standard Poisson summation formula for lattices so that it operates on the level of theta series, allowing us to introduce noninteger dimension parameters (using the dimensionally continued Fourier transform). When combined with one of the proofs of the Jacobi imaginary transformation of theta functions that does not use the Poisson summation formula, our proof of this generalized Poisson summation formula also provides a new proof of the standard Poisson summation formula for dimensions greater than 2 (with appropriate hypotheses on the function being summed). In general, our methods work to establish the (Voronoi) summation formulae associated with functions satisfying (modular) transformations of the Jacobi imaginary type by means of a density argument (as opposed to the usual Mellin transform approach). Additionally, our result relaxes several of the hypotheses in the standard statements of these summation formulae. The density result we prove for Gaussians in the Schwartz space may be of independent interest.

5.1 Introduction

Consider a lattice $\Lambda \subset \mathbb{R}^n$ and a sufficiently well-behaved function $F : \mathbb{R}^n \to \mathbb{R}$. [Taking F to belong to the Schwartz space $\mathscr{S}(\mathbb{R}^n)$ is sufficient, and is what we shall do in our later generalization.] The standard Poisson summation formula then says that

$$\sum_{k\in\Lambda} F(k) = \frac{1}{\sqrt{\det \Lambda}} \sum_{p\in\Lambda^*} \tilde{F}(p). \tag{5.1}$$

Here Λ^* is the lattice dual to Λ, $\det \Lambda$ denotes the volume of a Voronoi cell of Λ, and

$$\tilde{F}(p) := \int_{\mathbb{R}^n} F(x) e^{-2\pi i x\cdot p} dx$$

denotes the Fourier transform of F. (We use a tilde here so that we can reserve the circumflex for our more general, dimensionally continued Fourier transform.) We wish to construct a dimensionally continued version of this result.

The paper on which this chapter is based is arXiv:1011.3790 [math.CA], which has been submitted to J. Fourier Anal. Appl.

This problem was originally inspired by a condensed matter physics investigation involving the dimensional continuation of electrostatic lattice sums, computed using the Ewald method (see, e.g., [233] for a modern exposition of this method). However, the ensuing discussion is a purely mathematical offshoot of this investigation. For one thing, the results we were able to prove do not include the physically relevant case of a slowly decaying function, even though we have numerical evidence that the results still hold in this case. Nevertheless, the methods used here might also be applicable to the dimensional regularization of lattice sums: See [304] for an approach using zeta functions and the Mellin transform.

If we specialize to the case where F is a radial function, we can obtain a dimensionally continued Poisson summation formula in terms of the lattice's theta series—see Theorem 1 for the (particularly simple) version for $\mathbb{Z}^d$ ($d > 1$). This result even holds when one uses, instead of a theta series derived from a lattice (or lattice-like object), a function Υ that merely possesses the appropriate modular transformation properties (with sufficiently strong bounds on the growth of its power series coefficients). This more general result is given in Theorem 2. The following Proposition shows that a large family of Υs satisfying the hypotheses of Theorem 2 can be constructed from Jacobi theta functions. This family contains all the theta series given in Chap. 4 of Conway and Sloane [109] (except for the general forms of those for the root lattice A_d and its translates). The final Corollary states the resulting summation formula explicitly.

This relation between modular transformations and summation formulae is not new—though the dimensional continuation is. The relation has reached its most refined form in the association between automorphic forms and Voronoi summation formulae (see, e.g., Miller and Schmid [111] for a review of recent work). However, work on this correspondence first arose in the context of transformations related to the functional equation for the zeta function, inspired by a question by Voronoi on analogues of the Poisson summation formula—see, e.g., [305] and references therein. (We call particular attention to the work of Ferrar [306]; see Theorem 10.2.17 in Cohen [307] for a more modern discussion of a very similar result.) Additionally, Baake, Frettlöh, and Grimm [308] give a (distributional) radial Poisson summation formula in their Theorem 3 in a form that is very similar to our dimensionally continued form. However, they do not show how to dimensionally continue the lattice (or, indeed, mention theta functions explicitly), and their proof (which relies on the standard Poisson summation formula) only holds for integer dimensions. There are also discussions of similar formulae—these derived from modular transformations—at the beginning of Chapter 4 of Iwaniec and Kowalski [309], and in Sec. 10.2 of Huxley [310]—what Huxley terms the Wilton summation formula. These formulae are presented in what appears to be a dimensionally continued form, though their hypotheses assume integer dimensions. Regardless, the summation formula in Iwaniec and Kowalski and Huxley's Wilton summation formula are derived from cusp forms, while our result (in the language of modular forms) does not require that the constant term in the form's Fourier series vanish. (Indeed, we do not mention modular forms *qua* modular forms at all in the sequel.)

The work presented here gives a view of these matters that differs from all the other investigations we have seen. In particular, our method of proof bears no resemblance to any of the other proofs of which we are aware. The other proofs that begin with a modular transformation rely heavily on the Mellin transform (possibly supplemented with heavy specialized machinery), while the standard proof of the classical Poisson summation formula uses the lattice's periodicity and Fourier series. Our primary analytic tool is a density result for Gaussians in the Schwartz space (established by basic functional analytic means). The remainder of the proof uses basic

real and complex analysis (primarily Taylor's theorem, the Lebesgue dominated convergence theorem, and Cauchy's integral formula) to show that the dimensionally continued Poisson summation formula holds for the Gaussians (in essence, by reversing the usual derivation of the Jacobi imaginary transformation using the Poisson summation formula), and that it remains true in the limit in the Schwartz space.

5.2 Ingredients

5.2.1 Theta series

Here we recall various facts about theta series and theta functions that we shall need for the rest of our discussion, following Chap. 4 of Conway and Sloane [109]. The theta series of a lattice Λ is defined by

$$\Theta_\Lambda(q) := \sum_{k\in\Lambda} q^{|k|^2}.$$

(This is often treated as a formal series, but converges for $q \in \mathbb{C}$, $|q| < 1$.) The utility of the theta series stems from the fact that the coefficient of q^l in the expansion of $\Theta_\Lambda(q)$ in powers of q gives the number of points in the intersection of the lattice and a sphere of radius $\sqrt{l}$ centered at the origin. Thus, if we write

$$\Theta_\Lambda(q) =: \sum_{l=0}^{\infty} N_l q^{A_l}, \tag{5.2}$$

then

$$\sum_{k\in\Lambda} f(|k|) = \sum_{l=0}^{\infty} N_l f(\sqrt{A_l}).$$

[N.B.: We have written the radial function F as $f(|\cdot|)$, and shall only consider these radial parts in the sequel.] Examples of dimensionally continued theta series for families of lattices include the d-dimensional cubic lattice $\mathbb{Z}^d$, with $\Theta_{\mathbb{Z}^d}(q) = \vartheta_3^d(q)$, and the root lattice D^d, with $\Theta_{D^d}(q) = [\vartheta_3^d(q) + \vartheta_4^d(q)]/2$. (See Chap. 4 in Conway and Sloane [109] for further examples.) Here

$$\vartheta_2(q) := 2q^{1/4}\sum_{l=1}^{\infty} q^{l^2-l}, \qquad \vartheta_3(q) := 1 + 2\sum_{l=1}^{\infty} q^{l^2}, \qquad \vartheta_4(q) := 1 + 2\sum_{l=1}^{\infty}(-q)^{l^2} \tag{5.3}$$

are Jacobi theta functions (where ϑ_2 is defined for future use).

N.B.: It is often customary to take theta functions and theta series to be functions of a complex variable z, instead of the nome $q = e^{i\pi z}$ that we have used here. We have chosen to regard the nome as fundamental since we are primarily interested in the expansions of these functions in powers of q. However, when discussing transformations of these functions, it is considerably more convenient to regard them as functions of z. On the few occasions where we do this, we shall use an overbar to denote the difference, e.g., $\bar{\Theta}_\Lambda(z) := \Theta_\Lambda(e^{i\pi z})$. (In the literature on summation formulae derived from automorphic forms, one thinks of our expansions of Θ_Λ in q as the Fourier coefficients of $\bar{\Theta}_\Lambda$.)

Since the Poisson summation formula involves the dual lattice, we need to know how to obtain its theta series. This is given by the Jacobi formula [Eq. (19) in Chap. 4 of Conway and

Sloane [109]], which states that

$$\bar{\Theta}_{\Lambda^*}(z) = \sqrt{\det \Lambda}(i/z)^{d/2}\bar{\Theta}_{\Lambda}(-1/z), \tag{5.4}$$

where d is the dimension of the lattice. The Jacobi formula is typically proved using the Poisson summation formula [see, e.g., the discussion leading up to our Eq. (5.8)]. However, all we need in our discussion is the intimately related Jacobi imaginary transformation of the Jacobi theta functions (also known as the modular identity or reciprocity formula for the theta functions), i.e.,

$$\bar{\vartheta}_2(-1/z) = (z/i)^{1/2}\bar{\vartheta}_4(z), \qquad \bar{\vartheta}_3(-1/z) = (z/i)^{1/2}\bar{\vartheta}_3(z). \tag{5.5}$$

(The first of these is also true with the labels 2 and 4 switched.) The standard proof of these identities is a direct application of the Poisson summation formula, but there are alternative proofs that are independent of it. For instance, one such proof is given in Sec. 21.51 of Whittaker and Watson [311], while Bellman's text [108] discusses several others—see, in particular, Sec. 30 for Polya's derivation—in addition to the standard Poisson summation version (in Sec. 9). Our discussion will thus be independent of the standard Poisson summation formula (with the exception of a brief appeal to establish Theorem 1 for $d = 1$).

5.2.2 The dimensionally continued Fourier transform

We also need to dimensionally continue the Fourier transform. Stein and Weiss give a dimensionally continued version of the Fourier transform for radial functions in Theorem 3.3 of Chap. IV of [266], viz.,

$$\begin{aligned}\hat{f}(p) &:= \frac{2\pi}{p^{d/2-1}}\int_0^\infty f(r)J_{d/2-1}(2\pi pr)r^{d/2}dr \\ &= \frac{2\pi^{d/2}}{\Gamma(d/2)}\int_0^\infty f(r){}_0F_1(d/2;-\pi^2p^2r^2)r^{d-1}dr.\end{aligned} \tag{5.6}$$

(This reduces to the standard Fourier transform for a radial function when $d \in \mathbb{N}$.) Here the first equality gives the expression from Stein and Weiss (J_ν is a Bessel function) and the second gives an equivalent (perhaps slightly neater) expression in terms of the confluent hypergeometric limit function ${}_0F_1$. The hypergeometric expression has the advantage of only involving one appearance of p (and being manifestly regular at $p = 0$ for all $d \geq 1$), in addition to showing the d-dimensional polar coordinate measure for radial functions explicitly. We shall thus use the hypergeometric expression exclusively in the sequel. (One can obtain the hypergeometric expression using the Stein and Weiss derivation—the only difference is that one uses a different special function to evaluate the final integral.[1])

For this expression to be well-defined, it is sufficient to take $d \geq 1$: One assumes $d > 1$ when using integral representations to express the result in terms of either of the two given special functions, and can also check that the integral is convergent for all $p \in \mathbb{R}$ in that case, provided that $f \in L^1(\mathbb{R}_+)$. Additionally, Eq. (5.6) reduces to the expected expression for $d = 1$

[1]The integral representation for ${}_0F_1$ we used is 07.17.07.0004.01 on the Wolfram Functions Site [312].

[using $J_{-1/2}(z) = \sqrt{2/\pi z}\cos z$ or ${}_0F_1(1/2;-z) = \cos(2\sqrt{z})$].[2] (Stein and Weiss restrict to $d \geq 2$ so that the integral they use in their derivation is well-defined, since they are only considering integer dimensions.) This restriction to $d > 1$ is necessary for other parts of our discussion, though we have numerical evidence that it can be relaxed.

The following result is central to understanding why this dimensionally continued Fourier transform agrees with the dimensional continuation of the theta series.

Lemma 1. *For $d \geq 1$, the dimensionally continued Fourier transform (for radial functions) defined in Eq.* (5.6) *takes a Gaussian $\mathcal{G}_\alpha(r) := e^{-\alpha r^2}$, $\operatorname{Re}\alpha > 0$ to another Gaussian, $\hat{\mathcal{G}}_\alpha(p) = (\pi/\alpha)^{d/2} e^{-\pi^2 p^2/\alpha}$.*

Remark. Intuitively, this result follows from dimensionally continuing the well-known integer-dimension result. We should get the same result from direct calculation using Eq. (5.6) since that expression was obtained using the same dimensional continuation procedure.

Proof. The case $d = 1$ is classical. For $d > 1$, we use ${}_0F_1$'s defining series,

$$ {}_0F_1(d/2; -\pi^2 p^2 r^2) = \sum_{n=0}^{\infty} \frac{(-\pi^2 p^2 r^2)^n}{(d/2)_n n!} \tag{5.7} $$

[$(\cdot)_n$ denotes the Pochhammer symbol] and integrate term-by-term, evaluating each integral using the gamma function.[3] The resulting series is the Maclaurin series for the expression we gave for $\hat{\mathcal{G}}_\alpha$. The term-by-term integration is justified by the Lebesgue dominated convergence theorem. To see this, we use the same integral representation for ${}_0F_1$ used in the derivation of Eq. (5.6), which gives, for any $N \in \mathbb{N}$,

$$ \left| \sum_{n=0}^{N} \frac{(-\pi^2 p^2 r^2)^n}{(d/2)_n n!} \right| \leq {}_0F_1(d/2; \pi^2 p^2 r^2) \leq K \cosh(2\pi p r) \int_0^1 (1-t^2)^{(d-3)/2} dt, $$

where $K > 0$ is a constant.[4] This allows us to apply the dominated convergence theorem, since the integral in the final term is finite for $d > 1$ and $\int_0^\infty \cosh(2\pi p r)|e^{-\alpha r^2}|dr$ is finite for $\operatorname{Re}\alpha > 0$. □

Remark. The importance of this result to our discussion comes in its use in obtaining the integer dimension Jacobi transformation formula (and thus also the Jacobi imaginary transformations of the Jacobi theta functions) via the standard Poisson summation formula: For a lattice Λ of dimension $n \in \mathbb{N}$, we have (taking $\operatorname{Im} z > 0$ so that everything converges)

$$ \bar{\Theta}_\Lambda(z) := \sum_{k\in\Lambda} e^{i\pi z|k|^2} = \frac{1}{\sqrt{\det\Lambda}} \left(\frac{i}{z}\right)^{n/2} \sum_{p\in\Lambda^*} e^{-i\pi|p|^2/z} = \frac{1}{\sqrt{\det\Lambda}} \left(\frac{i}{z}\right)^{n/2} \bar{\Theta}_{\Lambda^*}(-1/z), $$

which can be written as

$$ \bar{\Theta}_{\Lambda^*}(z) = \sqrt{\det\Lambda}(i/z)^{n/2} \bar{\Theta}_\Lambda(-1/z), \tag{5.8} $$

[2] These identities are 03.01.03.0004.01 and 07.17.03.0037.01, respectively, on the Wolfram Functions Site [312].

[3] The Maclaurin series for ${}_0F_1$ is 07.17.02.0001.01 on the Wolfram Functions Site [312].

[4] N.B.: We denote the set of positive integers by $\mathbb{N}$, and the set of nonnegative integers by $\mathbb{N}_0$.

the Jacobi transformation formula. We thus expect that the dimensionally continued dual theta series that we obtain using this formula will agree with the dimensionally continued Fourier transform to give a dimensionally continued Poisson summation formula.

5.3 The dimensionally continued Poisson summation formula for $\mathbb{Z}^d$

With these results in hand, we can thus write Eq. (5.1) [for a radial function $F =: f(|\cdot|)$] as

$$\sum_{l=0}^{\infty} N_l f(\sqrt{A_l}) = \frac{1}{\sqrt{\det \Lambda}} \sum_{l=0}^{\infty} N_l^* \hat{f}(\sqrt{A_l^*}),$$

where the starred quantities come from writing the theta series of Λ^* in the power series form given by Eq. (5.2), and we calculate $\hat{f}$ by taking the dimension parameter d to be the dimension of the lattice. (As we shall see later, what is important is that the d one uses here is the same d that appears in the Jacobi transformation formula.) It is clear that this equality holds when $d \in \mathbb{N}$, by the standard Poisson summation formula. What is perhaps surprising is that the equality still holds for, e.g., $\Lambda = \mathbb{Z}^d$, with $d \in \mathbb{R}$ ($d \geq 1$). We shall first prove the result for this simple case ($\mathbb{Z}^d$ is self-dual, $\det \mathbb{Z}^d = 1$, and $A_l = l$), where it becomes

Theorem 1. *If $f \in \mathscr{S}^{\mathsf{E}}(\mathbb{R})$ (i.e., f is an even Schwartz function) and $d \geq 1$, then*

$$\sum_{l=0}^{\infty} N_l f(\sqrt{l}) = \sum_{l=0}^{\infty} N_l \hat{f}(\sqrt{l}), \tag{5.9}$$

where the N_l are given by the power series expansion of the theta series of $\mathbb{Z}^d$, viz.,

$$\Theta(q) = \vartheta_3^d(q) = \left[1 + 2\sum_{k=1}^{\infty} q^{k^2}\right]^d =: \sum_{l=0}^{\infty} N_l q^l,$$

and $\hat{f}$ is computed using Eq. (5.6).

However, the simplifications are primarily notational. As we shall see in the discussion in Sec. 5.6, the proof works with minimal modifications for a much larger class of Θ, including functions that cannot be the theta series of a lattice (even though they have an integer dimension parameter).

Remark. The restriction that f be an even function should not be surprising: In integer dimensions, it corresponds to the lack of a cusp at the origin for the full radial function $F = f(|\cdot|)$. Moreover, as Miller and Schmid note [111], the standard one-dimensional Poisson summation formula is a trivial $0 = 0$ for odd functions.

5.4 A Schwartz space density result

Since the proof proceeds by noting that the desired formula holds almost trivially for the Gaussians from Lemma 1, and then extends to an interesting set of functions [viz., $\mathscr{S}^{\mathsf{E}}(\mathbb{R})$] by density, we start by establishing the requisite density result.

Lemma 2. $\overline{\text{Span}\{x \mapsto e^{-\alpha x^2} | \alpha > 0\}}^{\mathscr{S}(\mathbb{R})} = \mathscr{S}^{\mathsf{E}}(\mathbb{R})$ *[i.e., the Schwartz space closure of the given family of Gaussians is all the even Schwartz functions].*

Proof. We shall prove this by showing that

$$\mathcal{X} := \text{Span}\{x \mapsto e^{-\alpha x^2} | \alpha > 0\} + \text{Span}\{x \mapsto x e^{-\alpha x^2} | \alpha > 0\}$$

is dense in $\mathscr{S}(\mathbb{R})$, so its even part, $\text{Span}\{x \mapsto e^{-\alpha x^2} | \alpha > 0\}$, is thus dense in $\mathscr{S}^{\mathsf{E}}(\mathbb{R})$. We shall use Corollary IV.3.14 from Conway's text [313], which states that a linear manifold (here $\mathcal{X}$) is dense in a locally convex topological vector space [here $\mathscr{S}(\mathbb{R})$] if and only if the only element of the dual of the topological vector space that vanishes on all elements of the linear manifold is the zero element. We then reduce the problem to the standard fact that a holomorphic function that is zero on a set with an accumulation point is zero everywhere.

It is most convenient to proceed by identifying $\mathscr{S}(\mathbb{R})$ with a sequence space, following Simon [110]. Here the sequence space is given by the coefficients of the Hermite function expansion of elements of $\mathscr{S}(\mathbb{R})$, and provides a particularly nice characterization of the tempered distributions [the elements of $\mathscr{S}'(\mathbb{R})$, the dual of $\mathscr{S}(\mathbb{R})$]. Namely, if a_n are the Hermite coefficients of $f \in \mathscr{S}(\mathbb{R})$ [i.e., $a_n := \int_{\mathbb{R}} f(x) h_n(x) dx$, where h_n is the nth Hermite function], then $\varphi \in \mathscr{S}'(\mathbb{R})$ can be written as $\varphi(f) = \sum_{n=0}^{\infty} c_n a_n$, where c_n are the Hermite coefficients of φ, with $|c_n| \leq C(1+n)^m$ for some $C, m > 0$. (This is Theorem 3 in Simon [110].) Note that Simon defines the Hermite functions to be L^2 normalized, so, we have, from the first equation in Sec. 2 of Simon,[5]

$$h_n(x) := \frac{e^{-x^2/2}}{\sqrt{\pi^{1/2} 2^n n!}} H_n(x), \qquad H_n(x) := (-1)^n e^{x^2} \frac{d^n}{dx^n} e^{-x^2},$$

where the H_n are the Hermite polynomials, with generating function[6]

$$\sum_{n=0}^{\infty} H_n(x) \frac{t^n}{n!} = e^{2tx - t^2}.$$

We can now use this generating function to show that the Hermite coefficients of $x \mapsto e^{-\alpha x^2}$ are given by

$$a_n = \mathcal{N}_n \frac{d^n}{dt^n} \left[\int_{\mathbb{R}} e^{-(\alpha x^2 + x^2/2 - 2tx + t^2)} dx \right] \Bigg|_{t=0} = \mathcal{N}_n \frac{d^n}{dt^n} \left[\sqrt{\pi\beta} e^{(\beta - 1)t^2} \right] \Big|_{t=0},$$

where $\mathcal{N}_n := (\pi^{1/2} 2^n n!)^{-1/2}$ is the Hermite functions' normalization factor and $\beta := 1/(\alpha + 1/2)$. We thus have $a_{2n} = \mathcal{N}_{2n} (\pi/\beta)^{1/2} (\beta - 1)^n / n!$, $a_{2n+1} = 0$, by the series expansion of the exponential. [We used Lemma 2.2 in Chap. 13 of Lang [314] to interchange differentiation and integration. We only need to consider the case where t lies in some neighborhood of 0, so the t-derivatives of the integrand are each bounded by a polynomial in x times a Gaussian in x (for

[5] N.B.: Simon defines the h_n without the factor of $(-1)^n$ (that here comes from our H_n). We have included the $(-1)^n$ for notational simplicity (since we use the standard convention for the Hermite polynomials). This does not have any effect on Simon's Theorem 3, since it simply amounts to a sign change of the odd Hermite coefficients.

[6] This is 05.01.11.0001.01 on the Wolfram Functions Site [312].

all t in the neighborhood), and those functions of x are integrable over $\mathbb{R}$.] Similarly, the Hermite coefficients of $x \mapsto xe^{-\alpha x^2}$ are $b_{2n} = 0$ and $b_{2n+1} = \mathcal{N}_{2n+1}(\pi/\beta^3)^{1/2}(\beta-1)^n/n!$. Thus, we consider

$$E_{\beta,\pm}(x) := (\beta/\pi)^{1/2}e^{-\alpha x^2} \pm (\beta^3/\pi)^{1/2}xe^{-\alpha x^2},$$

which has Hermite coefficients of $(\pm 1)^n \mathcal{N}_n(\beta-1)^{\lfloor n/2 \rfloor}/\lfloor n/2 \rfloor!$, where $\lfloor \cdot \rfloor$ denotes the greatest integer less than or equal to its argument.

Now, for any $\varphi \in \mathscr{S}'(\mathbb{R})$, $\mathcal{E}_\pm(\beta) := \varphi(E_{\beta,\pm})$ is a holomorphic function of β. To see this, we note that

$$\mathcal{E}_\pm(\beta) = \sum_{n=0}^{\infty}(\pm 1)^n c_n \mathcal{N}_n \frac{(\beta-1)^{\lfloor n/2 \rfloor}}{\lfloor n/2 \rfloor!} = \sum_{n=0}^{\infty}(\mathcal{N}_{2n}c_{2n} \pm \mathcal{N}_{2n+1}c_{2n+1})\frac{(\beta-1)^n}{n!}, \tag{5.10}$$

where c_n are the Hermite coefficients of φ. Since the c_n are bounded by a polynomial in n, the series converges for all $\beta \in \mathbb{C}$, giving holomorphy. Thus, if $\mathcal{E}_\pm(\beta) = 0$ for all β in an interval (as is the case here), then all of $\mathcal{E}_\pm$'s power series coefficients are zero. Applying this result to the two choices of sign, we obtain (since the $\mathcal{N}_n$ are never zero) $c_n = 0 \; \forall \; n \in \mathbb{N}_0 \Rightarrow \varphi \equiv 0$, which thus proves the lemma. □

Remark. This result may be of wider applicability, particularly in harmonic analysis, due to the ubiquity of the Gaussian. We thus note that the proof of the lemma shows that α need merely belong to some subset of the right half-plane with an accumulation point to guarantee density. One could have also proved this result more abstractly (and without recourse to the Hermite expansion) by a slightly indirect application of the Stone-Weierstrass theorem, though the basic Hahn-Banach argument (contained in the Corollary from Conway we use) remains the same [315].

5.5 Proof of Theorem 1

We first note that Eq. (5.9) is clearly true for $d = 1$ (indeed, $d \in \mathbb{N}$) by the standard Poisson summation formula for lattices (applied to $\mathbb{Z}^d$). To prove the result for $d > 1$, we shall first establish that it holds for the Gaussians from Lemma 1, and then show that the equality still holds in the limit in the Schwartz space topology. The control afforded by demanding convergence in the Schwartz space makes this quite straightforward. The primary result that needs to be shown is that two functions that are ϵ-close in the Schwartz space topology have dimensionally continued Fourier transforms that are $C\epsilon$-close in a given Schwartz space seminorm (where the constant C depends on the seminorm under consideration, as well as d).

To show that Eq. (5.9) holds when $f = \mathcal{G}_\alpha$, we first consider the left-hand side and note that

$$\sum_{l=0}^{\infty} N_l e^{-\alpha l} = \Theta(e^{-\alpha}). \tag{5.11}$$

Convergence is guaranteed because Θ is analytic inside the unit disk. [To see that Θ is analytic inside the unit disk, note that ϑ_3 is analytic there, and, moreover, nonzero, so its dth power is analytic, as well. It is easiest to see that ϑ_3 is nonzero inside the unit disk from its infinite product expansion, given in, e.g., Eq. (35) in Chap. 4 of Conway and Sloane [109].] Using Lemma 1,

the right-hand side of Eq. (5.9) becomes

$$\left(\frac{\pi}{\alpha}\right)^{d/2} \sum_{l=0}^{\infty} N_l e^{-\pi^2 l/\alpha} = \left(\frac{\pi}{\alpha}\right)^{d/2} \Theta(e^{-\pi^2/\alpha}).$$

Now, the Jacobi imaginary transformation for ϑ_3 [Eq. (5.5)] implies that $(\pi/\alpha)^{d/2}\Theta(e^{-\pi^2/\alpha}) = \Theta(e^{-\alpha})$, so we have thus established the result for $\mathcal{G}_\alpha$.

We shall now show that this equality continues to hold in the limit. The equality is clearly true for any finite linear combination of the Gaussians from Lemma 1, so we use Lemma 2 to approximate an arbitrary $f \in \mathscr{S}^{\mathsf{E}}(\mathbb{R})$ by a finite linear combination of these Gaussians, g. Specifically, we have $\|f-g\|_{n,m} < \epsilon \;\forall\; n, m \in \mathbb{N}_0$, where $\|f\|_{n,m} := \sup_{x\in\mathbb{R}} |x^n f^{(m)}(x)|$ is the family of seminorms that gives the Schwartz space topology. (We denote the mth derivative of f by $f^{(m)}$.) We wish to bound the difference between the two sides of Eq. (5.9) by a constant times ϵ. We have

$$\left|\sum_{l=0}^{\infty} N_l f(\sqrt{l}) - \sum_{l=0}^{\infty} N_l \hat{f}(\sqrt{l})\right| \leq \left|\sum_{l=0}^{\infty} N_l (f-g)(\sqrt{l})\right| + \left|\sum_{l=0}^{\infty} N_l (\hat{f}-\hat{g})(\sqrt{l})\right|, \tag{5.12}$$

where we used the fact that the dimensionally continued Poisson summation formula holds for g, along with the triangle inequality. We can bound the two sums on the right-hand side by constants times ϵ using the assumption about the closeness of f to g in the Schwartz space topology and the fact that N_l grows at most polynomially with l. The latter fact also shows that the two sums on the left converge for $f \in \mathscr{S}(\mathbb{R})$.

5.5.1 Bounds on the growth of N_l and on the right-hand side of Eq. (5.12)

We obtain the polynomial bound on N_l using Cauchy's integral formula with the contour C_R, a circle of radius $R \in (0,1)$, centered at the origin (and oriented counterclockwise):

$$|N_l| = \left|\frac{1}{2\pi i}\int_{\mathsf{C}_R} \frac{\vartheta_3^d(z)}{z^{l+1}} dz\right| = \frac{1}{2\pi}\left|\int_0^{2\pi} \frac{\vartheta_3^d(Re^{i\theta})}{R^l e^{il\theta}} d\theta\right| \leq \frac{2^d}{R^l(1-R)^d}.$$

Here we have used $|\vartheta_3(q)| \leq 2/(1-|q|)$ (for $|q|<1$, obtained using the geometric series). The right-hand side attains its minimum [for $R \in (0,1)$] at $R = l/(l+d)$, so we have

$$|N_l| \leq 2^d (1+d/l)^l (1+l/d)^d \leq C_d l^d,$$

where $C_d > 0$ is some constant (and the second inequality only holds for $l \geq 1$). [We have used the fact that $(1+1/r)^r < e$ for $r > 0$.]

If we write $h := f - g$, then this bound implies that $|N_l h(\sqrt{l})| \leq C_d l^d |h(\sqrt{l})| \leq \epsilon C_d / l^2$ (for $l \geq 1$), where the second inequality follows from the fact that h is ϵ-close to 0 in the Schwartz space topology. [Explicitly, we have $|x^{2d+4}h(x)| \leq \epsilon \;\forall\; x > 1 \Rightarrow l^d |h(\sqrt{l})| \leq \epsilon/l^2 \;\forall\; l \in \mathbb{N}$. The first inequality comes from noticing that for any $\gamma \geq 0$, we have $|x^\gamma h(x)| \leq |x^{\lceil\gamma\rceil} h(x)| \leq \epsilon$ for $x \geq 1$, where $\lceil\cdot\rceil$ denotes the smallest integer greater than or equal to its argument.] We shall show that $|p^{2n}\hat{h}(p)| \leq K_d \epsilon \;\forall\; n \in \mathbb{N}$, $p \in \mathbb{R}$ (where K_d is some n-dependent constant), so we have $|p^{2d+4}\hat{h}(p)| \leq K_d \epsilon \;\forall\; p \in \mathbb{R}$. We can thus apply the same argument to the second sum and hence

bound both sums by constants times ϵ (since $\sum_{l=1}^{\infty} l^{-2}$ is finite), showing that the dimensionally continued Poisson summation formula is true in the limit [since we will have shown that the right-hand side of Eq. (5.12) is bounded by a constant times ϵ].

5.5.2 Bound on $|p^{2n}\hat{h}(p)|$

To prove the bound on $|p^{2n}\hat{h}(p)|$, we first dimensionally continue some standard Fourier results.

Lemma 3. *If we define the d-dimensional Laplacian for radial functions by*

$$\triangle_d f(r) := f''(r) + \frac{d-1}{r} f'(r), \tag{5.13}$$

then, for $d > 1$,

i) $\mathcal{F}_p(r) := {}_0F_1(d/2; -\pi^2 p^2 r^2)$ *satisfies* $\triangle_d \mathcal{F}_p = -4\pi^2 p^2 \mathcal{F}_p$, *so*

ii) $\widehat{\triangle_d^n f}(p) = (-1)^n (2\pi p)^{2n} \hat{f}(p)$ *for* $f \in \mathscr{S}(\mathbb{R})$.

Proof. Part *i* follows from the fact that $y_a(r) := {}_0F_1(a; r)$ satisfies $r y_a''(r) + a y_a'(r) = y_a(r)$.[7] [Alternatively, it can be obtained by direct calculation using Eq. (5.7), justifying term-by-term differentiation using analyticity.] Part *ii* is then obtained by induction, applying Eq. (5.6) to $\triangle_d^{n-1} f$ and integrating by parts twice. [The boundary terms at infinity vanish because $f \in \mathscr{S}(\mathbb{R})$; those at 0 vanish because $d > 1$ (or cancel amongst themselves).] □

We can thus write $|p^{2n}\hat{h}(p)| = (2\pi)^{-2n} |\widehat{\triangle_d^n h}(p)|$. Then, since we shall show below that $|r^k \triangle_d^n h(r)| \le \mathcal{D}\epsilon$, where $\mathcal{D}$ is some (n- and d-dependent constant), we obtain [using Eq. (5.6) and the fact that ${}_0F_1(a; r)$ is a bounded function of r, as was seen in the proof of Lemma 1]

$$\begin{aligned} |p^{2n}\hat{h}(p)| &\le C \int_0^\infty |\triangle_d^n h(r)| r^{d-1} dr \\ &\le C \left[\int_0^1 |\triangle_d^n h(r)| dr + \int_1^\infty |\triangle_d^n h(r)| r^{d-1} dr \right] \\ &\le C\mathcal{D} \left[1 + \int_1^\infty r^{d-1-s} dr \right] \epsilon, \end{aligned}$$

where $C > 0$ is some (n- and d-dependent) constant and we used $|r^k \triangle_d^n h(r)| \le \mathcal{D}\epsilon$ with $k = 0$ and $k = s$. We can choose $s > d$, so the integral in the final term is finite, thus giving the desired result.

[7] This differential equation for ${}_0F_1$ is 07.17.13.0003.01 on the Wolfram Functions Site [312].

5.5.3 Bound on $|r^k \triangle_d^n h(r)|$

To see that $|r^k \triangle_d^n h(r)|$ is bounded by some (n- and d-dependent) constant (called $\mathcal{D}$ above), we first note that we can use induction to write

$$\triangle_d^n h(r) = \sum_{j=1}^{2n} a_j \frac{h^{(j)}(r)}{r^{2n-j}} \tag{5.14}$$

for some (n- and d-dependent) constants a_j (and an arbitrary differentiable h). Thus, for $|r| \geq 1$, we have $|r^k \triangle_d^n h(r)| \leq \epsilon \sum_{j=1}^{2n} a_j$. For $|r| < 1$, matters are considerably more subtle, and we have to rely on the fact that h is even to see that $\triangle_d^n h$ remains bounded at the origin. The argument goes as follows: We write $h = \mathcal{P} + \mathcal{R}$, where $\mathcal{P}$ is h's $(2n)$th-degree Maclaurin polynomial (necessarily even, since h is) and $\mathcal{R}$ is the associated remainder. We then have $|r^k \triangle_d^n h(r)| \leq |r^k \triangle_d^n \mathcal{P}(r)| + |r^k \triangle_d^n \mathcal{R}(r)|$. Since $\triangle_d$ maps even polynomials to even polynomials [as can be seen from Eq. (5.14)], $|r^k \triangle_d^n \mathcal{P}(r)|$ is bounded by a (k-, n-, and d-dependent) constant times ϵ for $|r| \leq 1$. [Since the coefficients of $\mathcal{P}$ are given by derivatives of h, they are bounded by constants times ϵ, by hypothesis.] To deal with $|r^k \triangle_d^n \mathcal{R}(r)|$, we first need to establish an identity for derivatives of $\mathcal{R}$, viz., (for $j \leq 2n$)

$$\mathcal{R}^{(j)}(r) = \frac{h^{(2n+1)}(\xi_j)}{(2n+1-j)!} r^{2n+1-j},$$

for some $\xi_j \in (0, r)$. This follows from differentiating $h = \mathcal{P} + \mathcal{R}$ j times, and comparing the resulting expression with the $(2n-j)$th order Maclaurin expansion (with Lagrange remainder) of $h^{(j)}$. The polynomial pieces are the same, while the remainder pieces give the two sides of the equality. Combining this identity with Eq. (5.14), we obtain

$$\triangle_d^n \mathcal{R}(r) = r \sum_{j=1}^{2n} b_j h^{(2n+1)}(\xi_j),$$

where the b_j are (n- and d-dependent) constants. This shows that $|r^k \triangle_d^n \mathcal{R}(r)|$ is bounded by an (n- and d-dependent) constant times ϵ for $|r| \leq 1$, so $|r^k \triangle_d^n h(r)|$ is, as well, proving the desired result, and hence the theorem. □

Remark. The restrictions on f and d in the statement of the theorem are surely not optimal: There is numerical evidence that the given result holds for $d \in \mathbb{C}$, $\mathrm{Re}\, d > 0$ and less smooth f [e.g., $f(r) = e^{-|r|^3}$]. (The evidence also extends to the generalization given in Theorem 2 and is provided by a MATHEMATICA notebook, available online.[8]) While one could use a slightly larger function space than $\mathscr{S}^{\mathsf{E}}(\mathbb{R})$ without any change to the proof—the proof does not need control over $\|f - g\|_{n,m}$ for all n and m—we did not investigate this in any detail: The resulting function space would still require a fair amount of differentiability (while we have numerical evidence that the formula remains true for at least some functions with a cusp at the origin), and faster decay than the standard Poisson summation formula. Moreover, the closure of the family of Gaussians in this less restrictive topology would almost surely be more recondite than $\mathscr{S}^{\mathsf{E}}(\mathbb{R})$.

[8] The notebook is available at `http://gravity.psu.edu/~nathanjm/Dim_cont_PSF_test.nb`.

5.6 Generalization of Theorem 1

Since there are other families of lattices with dimensionally continued theta series besides $\mathbb{Z}^d$ (e.g., the root lattice D^d mentioned in Sec. 5.2.1), it is reasonable to expect that Theorem 1 can be generalized by replacing Θ with some more general function Υ. In fact, we have the following

Theorem 2. *Assume that we have a function Υ and $d > 1$ such that*

i) We can write

$$\Upsilon(q) = \sum_{l=0}^{\infty} N_l q^{A_l},$$

where

1. *$A_{l+1} > A_l$, $A_0 \geq 0$.*
2. *$\sum_{l=1}^{\infty} A_l^{-m} < \infty$ for some $m \in \mathbb{N}$.*
3. *There exists $L \in \mathbb{N}$ and $C, n > 0$ such that $|N_l| \leq C A_l^n$ for all $l \geq L$,*
4. *The A_l are such that the series converges inside the unit disk.*[9]

ii) If we define

$$\overline{\Upsilon}^*(z) := (i/z)^{d/2} \overline{\Upsilon}(-1/z)$$

(recall the overbar notation introduced in the nota bene *in Sec. 5.2.1), then we can write*

$$\Upsilon^*(q) = \sum_{l=0}^{\infty} N_l^* q^{A_l^*},$$

with the same hypotheses about the series as in part i.

Then, for any $f \in \mathscr{S}^{\mathsf{E}}(\mathbb{R})$, we have the summation formula

$$\sum_{l=0}^{\infty} N_l f(\sqrt{A_l}) = \sum_{l=0}^{\infty} N_l^* \hat{f}(\sqrt{A_l^*}),$$

where we compute $\hat{f}$ using Eq. (5.6) *(with the d used in part* ii*).*

Remark. The definition of Υ^* is just the dimensionally continued Jacobi transformation [Eq. (5.4)] of Υ with the factor of $\sqrt{\det \Upsilon}$ omitted. (We leave off this factor, since it would just cancel against the one present in the standard Poisson summation formula [cf. Eq. (5.1)].)

Proof. The proof is almost the same as that for Theorem 1 (replacing Θ by Υ, and noting that we can no longer appeal to the standard Poisson summation formula for $d = 1$, so we simply exclude

[9] The ratio test and the given bound on N_l provide sufficient conditions for convergence inside the unit disk, viz., $A_{l+1} - A_l \geq \delta$ for some $\delta > 0$ and $\lim_{l\to\infty} A_{l+1}/A_l = 1$. (These are satisfied by the specific examples we consider.) However, one could relax the requirement of convergence to some subset of the unit disk, as the remark following Lemma 2 reveals.

that case). Our hypotheses are such that the only new part is checking that $\sum_{l=0}^{\infty} |N_l h(\sqrt{A_l})| \to 0$ as $\epsilon \to 0$ if h is ϵ-close to 0 in the Schwartz space topology [and similarly for $\sum_{l=0}^{\infty} |N_l^* h(\sqrt{A_l^*})|$]. To do this, we simply note that we have $|N_l h(\sqrt{A_l})| \leq C A_l^n |h(\sqrt{A_l})|$, by hypothesis, and that $x^{2(n+m)}|h(x)| \leq \epsilon \; \forall \; x \in \mathbb{R} \Rightarrow A_l^n |h(\sqrt{A_l})| \leq \epsilon / A_l^m$, from which the desired result follows immediately. (The same argument holds for the starred quantities, since the hypotheses are identical.) □

Remark. This theorem can likely be interpreted as a trace formula for the dimensionally continued, spherically symmetric Laplacian [Eq. (5.13)], since the kernel of the dimensionally continued Fourier transform is an eigenfunction of this operator (see Lemma 3). See, e.g., Sec. 1.3 (particularly Theorem 1.3) of Uribe [316] for a presentation of the standard Poisson summation formula for an integer dimension lattice as a trace formula for the Laplacian.

It is not clear how to construct the most general Υ satisfying the hypotheses of Theorem 2.[10] Nevertheless, it is easy enough to write down a reasonably general, yet fairly simple family of functions that does satisfy these hypotheses, viz., finite linear combinations of products of the three basic theta functions given in Eq. (5.3). Specifically, we can consider products of the form

$$\Upsilon_d(q) := \prod_{m=1}^{M} \vartheta_2^{\lambda_m}(q^{s_m}) \vartheta_3^{\rho_m}(q^{t_m}) \vartheta_4^{\sigma_m}(q^{u_m}), \tag{5.15}$$

where $\lambda_m, \rho_m, \sigma_m \geq 0$, $\sum_{m=1}^{M}(\lambda_m + \rho_m + \sigma_m) = d$, and $s_m, t_m, u_m \in \mathbb{Q}_+$. The extension to finite linear combinations of Υ_ds with the same d is trivial, by linearity. One can write all the theta series given in Chap. 4 of Conway and Sloane [109] as such finite sums of Υ_ds, except for the general form of the theta series of the root lattice A^d and its translates. In fact, theorems in Conway and Sloane (Theorems 7, 15, and 17 in Chap. 7 and Theorem 5 in Chap. 8) show that the theta series of large classes of lattices can be written in such a form. However, the expression in terms of Υ_ds is considerably more general, since one only requires $\lambda_m, \rho_m, \sigma_m \in \mathbb{N}_0$ to reproduce the theta series in Conway and Sloane, while here they can be arbitrary nonnegative real numbers. One can also use the general template provided by Eq. (5.15) to construct other admissible Υs from, e.g., automorphic forms, or other such functions ψ that satisfy the relation $\bar{\psi}(-1/z) = (z/i)^\eta \bar{\phi}(z)$ for some $\eta \in \mathbb{R}$ (where ϕ and ψ are well-behaved enough that the power series of the Υ constructed using these functions satisfies the hypotheses of Theorem 2).

We now want to establish the following

Proposition. *Υ_d [defined in Eq. (5.15)] satisfies the requirements given in the statement of Theorem 2.*

Proof. First note that the Jacobi imaginary transformations of the theta functions [given in Eq. (5.5)] imply that

$$\Upsilon_d^*(q) = \prod_{m=1}^{M} \frac{\vartheta_2^{\sigma_m}(q^{1/u_m}) \vartheta_3^{\rho_m}(q^{1/t_m}) \vartheta_4^{\lambda_m}(q^{1/s_m})}{\sqrt{s_m^{\lambda_m} t_m^{\rho_m} u_m^{\sigma_m}}}, \tag{5.16}$$

[10] However, Ryavec characterizes all admissible Υs (under certain assumptions) for $d = 1$ in [317]. We also call attention to the work of Córdoba [318, 319], who shows that in integer dimensions, large classes of generalized Poisson summation formulae arise from the standard Poisson summation formula applied to the finite disjoint union of (integer dimensional) lattices.

so the arguments we give for Υ_d can be applied to Υ_d^* immediately. Now, we have

$$A_l = (l + \mathcal{A})/V, \qquad \mathcal{A} := \sum_{m=1}^{M} V\lambda_m s_m/4$$

where V is the least common denominator of s_m, t_m, and u_m (for all m). [We have the additive constant $\mathcal{A}$ due to the overall factor of $q^{1/4}$ in $\vartheta_2(q)$.] Thus the first required property (positivity and monotonicity of the A_l) is obviously true, and the second (convergence of the series whose terms are A_l^{-m}) is clearly true for $m = 2$ (and $L = 1$), as before.

For the third property (polynomial boundedness of the N_l), we use the same Cauchy's integral formula argument used in Sec. 5.5.1. Here N_l is given by the lth term in the Maclaurin expansion of $\Upsilon_d(q^V)/q^{\mathcal{A}}$, so we have

$$\begin{aligned} |N_l| &= \left| \frac{1}{2\pi i} \int_{\mathsf{C}_R} \prod_{m=1}^{M} \frac{\vartheta_2^{\lambda_m}(z^{Vs_m})\vartheta_3^{\rho_m}(z^{Vt_m})\vartheta_4^{\sigma_m}(z^{Vu_m})}{z^{V\lambda_m s_m/4} z^{l+1}} dz \right| \\ &\le 2^d \prod_{m=1}^{M} \frac{1}{R^l(1 - R^{Vs_m})^{\lambda_m}(1 - R^{Vt_m})^{\rho_m}(1 - R^{Vu_m})^{\sigma_m}} \\ &\le \frac{2^d}{R^l(1 - R)^d}, \end{aligned}$$

where C_R is the same contour used previously. We have used the geometric series to obtain the bound $|\tau(q)| \le 2/(1 - |q|)$, where $\tau(q)$ is any of $\vartheta_2(q)/q^{1/4}$, $\vartheta_3(q)$, or $\vartheta_4(q)$. Additionally, we have used the fact that $\kappa \ge 1$, where κ is any of Vs_m, Vt_m, or Vu_m, so $|1 - R^\kappa| \ge 1 - R$, since $R \in (0, 1)$. We also recalled that $\lambda_m, \rho_m, \sigma_m \ge 0$ and $\sum_{m=1}^{M}(\lambda_m + \rho_m + \sigma_m) = d$. Since there is an $R \in (0, 1)$ such that $2^d/[R^l(1 - R)^d] \le C_d l^d$ (for $l \ge 1$), as was shown in Sec. 5.5.1, we are done.

The fourth property (convergence of the q-series in the unit disk) follows from the analyticity and lack of zeros of the theta functions inside the unit disk, as in the argument given below Eq. (5.11). Specifically, $\Upsilon(q^V)/q^{\mathcal{A}}$ is an analytic function of q inside the unit disk; the lack of zeros can be seen from the infinite product representations of ϑ_2 and ϑ_4 given, e.g., in Eqs. (34) and (36) in Chap. 4 of Conway and Sloane [109]. □

For clarity, we present the summation formula given by the Proposition and Theorem 2 explicitly (and without any reference to the transformation formula) as the following

Corollary. *Let Φ be a finite linear combination of Υ_ds [from Eq.* (5.15)*; all with the same $d > 1$] and let Ψ be the analogous linear combination of the Υ_d^*s given in Eq.* (5.16) *(i.e., with the same parameters and coefficients as for the Υ_ds). If we write*

$$\Phi(q) =: \sum_{l=0}^{\infty} N_l q^{A_l}, \qquad \Psi(q) =: \sum_{l=0}^{\infty} P_l q^{B_l},$$

then, for any $f \in \mathscr{S}^{\mathsf{E}}(\mathbb{R})$, we have

$$\sum_{l=0}^{\infty} N_l f(\sqrt{A_l}) = \sum_{l=0}^{\infty} P_l \hat{f}(\sqrt{B_l}),$$

where $\hat{f}$ *is computed using Eq.* (5.6).

Remark. This result shows that one can apply this extended Poisson summation formula to lattice-like objects whose theta series have coefficients of both signs, so they do not exist as a lattice, even though $d \in \mathbb{N}$: For a trivial example, consider $d = 2$ and $\Phi(q) = \vartheta_4^2(q) = 1-4q+4q^2+\cdots$. Of course, this is in some sense too trivial, since one can write $\vartheta_4^2 = 2\Theta_{D^2} - \Theta_{\mathbb{Z}^2}$, and then apply the standard Poisson summation formula to each of those lattices to establish the result in this case (cf. the discussion in Córdoba [319]). However, in more complicated higher-dimensional cases, it will likely not be clear how to construct the lattice(s) associated with the theta series (if they indeed exist).

Acknowledgments

It is our pleasure to thank George Andrews, Jingzhi Tie, and Shuzhou Wang for encouragement and useful comments, John Roe for mentioning an alternative proof of the density result, and Artur Tšobanjan for helpful remarks about the exposition. We also thank Ben Owen for comments on the manuscript and for suggesting the physics problem that sparked these investigations. This work was supported by NSF grants PHY-0555628 and PHY-0855589 and the Eberly research funds of Penn State.

Chapter 6

Multimessenger observations of white dwarf binaries with gravitational and electromagnetic radiation

The sensitivity and astrophysical significance of gravitational wave measurements can frequently be enhanced by combining them with observations using other messengers. For instance, one can combine gravitational wave and electromagnetic observations of white dwarf binaries to obtain the individual masses of the binaries' components. This is a measurement that cannot be made using either messenger alone, in practice, except in certain exceptional situations (or by invoking considerable modeling). We consider two possible methods of performing this measurement with upcoming or proposed observatories, and evaluate the anticipated accuracy of the measurement using an extension of the standard Fisher matrix formalism (combined with a rough model for the galaxy's population of binary white dwarfs). In one case, the gravitational radiation from the binary is strong, allowing a low-frequency gravitational wave observatory (e.g., LISA) to measure the amplitudes of the higher harmonics of the gravitational radiation. Combining these gravitational wave measurements with an electromagnetic parallax measurement (from, e.g., GAIA) gives a very clean measurement of the individual masses. We found that one can measure at least one of the individual masses of ~ 10 high-frequency systems with an accuracy of better than 40% using LISA and GAIA. In the other case, applicable to weaker sources, one also measures the system's mass function (spectroscopically), thus avoiding the need for the higher harmonics. One can then measure the individual masses of at least a hundred binaries in our population model with accuracies of tens of percent (assuming reasonable errors in the mass function; we do not model the specifics of the observation). If one has a mass function and gravitational wave higher harmonics but no parallax, one obtains distance and mass measurements, though we find that these would be quite inaccurate, in practice.

6.1 Introduction

White dwarf binaries are by far the most numerous population of compact binaries in the galaxy: Current population synthesis estimates place the number of systems at a few $\times$ 10^8 [116, 117, 320]. Of this population, only 52 systems have been detected to date [116]; see [113] and Table 1 in any of [117, 321, 322] for lists), and this sample is biased towards longer periods. Additionally, the masses and distances to these systems are often highly uncertain—see, e.g., [113]. The proposed Laser Interferometer Space Antenna (LISA) mission [10] is anticipated to greatly expand this sample, particularly at short periods, resolving 10^3–10^4 systems [320, 323].

This chapter is based on work done in collaboration with M. J. Koop, H. S. Langdon, A. R. Lundberg, and L. S. Finn, which will eventually be submitted to Mon. Not. R. Astron. Soc.

In addition to discovering many new white dwarf binaries, LISA will also be able to determine many of the basic parameters characterizing these systems, often with good accuracy. It is well known that LISA will be able to measure (with varying degrees of accuracy) the sky location, period, and inclination angle of all the white dwarf binaries it resolves, as is discussed in, e.g., [324]. Additionally, it is commonly thought there will be a small set of systems for which LISA will directly determine the system's distance and a certain combination of its individual masses, the so-called chirp mass (defined in Sec. 6.2). These are the systems for which the frequency evolution is both "clean" (i.e., the same as for a point mass binary, to a tolerance appropriate for the desired measurement accuracy) and rapid enough that LISA is able to measure it over its observation period (which might be as short as a year, in the worst possible case).

However, if one combines the LISA measurements with electromagnetic observations, one can measure the chirp mass—and, indeed, the binary's component masses—without relying on this frequency evolution. Moreover, not only do the electromagnetic observations supply information about the binary's parameters that supplements the LISA measurements, but they also increase LISA's measurement accuracy by giving the system's position and frequency evolution with sufficient accuracy that one can take them to be known precisely in the LISA data analysis.

This multimessenger approach allows one to measure the individual masses of a larger and more diverse sample of binaries than do purely gravitational wave observations. In particular, the multimessenger approach is applicable to mass transferring systems, for which the evolution is emphatically not clean. Additionally, there are some nearby systems in our population model whose masses we can measure with good precision for which LISA would not be able to measure the chirp in > 10 years, much less the 1 year in which we envision making the measurement. Nevertheless, it is possible in principle to obtain the individual masses using gravitational wave measurements alone, despite the statement to the contrary in Webbink [325]. (Webbink did not consider the possibility of measuring the higher harmonics.)

We shall describe three such possible combinations of observations that yield measurements of the binaries' component masses. Two of these measurements involve measuring higher harmonics with LISA, which has not previously been explored in the context of white dwarf binaries with LISA, even though it is well known that including such higher harmonics improves the parameter estimation of binary black holes (e.g., [326, 327, 328, 329]; see also Sec. 6.5.5 in [330]).[1] The higher harmonics (specifically, the mass octupole and current quadrupole radiation) are useful for us because their amplitude depends on a different combination of the masses than does the amplitude of the lowest harmonic, mass quadrupole radiation. The mass octupole and current quadrupole radiation's amplitude is reduced by a factor of v/c, compared to the amplitude of the mass quadrupole radiation, where v is the binary's orbital velocity and c is the speed of light. However, $v/c \gtrsim 5 \times 10^{-3}$ for the highest-frequency white dwarf binaries. Since LISA will observe these binaries' mass quadrupole radiation with large signal-to-noise ratios (SNRs) of up to ~ 1000, it will thus be able to measure the amplitudes of the higher harmonics with SNRs of a few or more.

[1] Note that the authors of [327] incorrectly attribute the higher harmonics to the nonlinearity of the field equations of general relativity. The higher harmonics are all present in the linear approximation, as would be expected, since such higher harmonics are present in electromagnetic wave generation, and the Maxwell equations are linear. See Theorem 1 in Blanchet [19] for an expression for an expression for the general solution to the linearized Einstein equations in terms of the various multipoles (which yield the higher harmonics).

Of course, these higher harmonics vanish in the equal-mass case, though we shall see that this does not lead to difficulties in measuring the masses of systems with equal masses (or close to equal masses), since we simply have the same uncertainties due to noise concerning the amplitudes of the higher harmonics in all cases. The vanishing of the higher harmonics for face-on binaries *does* lead to difficulties for small inclination angles, however, since the known suppression of the higher harmonic amplitudes (the inclination angle can be determined with just the lowest-order radiation) makes the measurement much more sensitive to noise at the higher harmonics' frequencies.

The two electromagnetic measurements that are useful for us are parallactic measurements of distance (from, e.g., the astrometry mission GAIA, discussed in, for instance, [331]) and mass function measurements (from observations of the system as a single-line spectroscopic binary). One can combine either of these two measurements with the GW measurements (including the higher harmonics) to obtain the masses of the binary's components. (In principle, one also obtains the binary's distance from the case with the mass function, though in practice we have found that this measurement cannot be made precisely enough to be useful.) One can also obtain the system's masses by combining both the electromagnetic measurements with the GW measurements. Here one only needs the lowest-order mass quadrupole radiation to make the measurement, though we include the higher harmonics in our analysis. (They will increase the accuracy of the measurement, even if only very slightly.) (Both Nelemans [332], and later Stroeer, Vecchio, and Nelemans [324] have suggested studying white dwarf binaries by combining LISA measurements with these specific electromagnetic measurements, though they did not consider the higher harmonics, and did not make any calculations of accuracy.)

For all of these measurements, we envision the following general scheme: LISA first discovers a population of white dwarf binaries with strong signals, obtaining an accurate period and rough sky localization (which can be as good as a few square arcminutes or better for strong systems) for each of those systems. One expects that these systems' electromagnetic emission will vary at (integer multiples of) the orbital frequency (due to eclipses and/or hot spots, or even just ellipsoidal variability [333]; the last of these has recently been observed in the two shortest-period detached double white dwarfs discovered to date [334, 335]). One can thus search for the systems electromagnetically using the known period and approximate sky location. (See [325] for further discussion.) Once one has obtained a precise electromagnetic sky location for the binaries, one can monitor the system's frequency evolution electromagnetically. For systems brighter than 20th GAIA magnitude (which is $\sim V$ magnitude), one can consult the GAIA catalog to obtain a distance. (The GAIA mission anticipates publishing their catalog around 2021, well before LISA flies—see e.g., [331].) One can also attempt to measure the mass function—this measurement will likely be successful for relatively bright systems with somewhat long periods (provided that the system has a sharp enough spectral line).

In order to assess the accuracy with which these measurements can be made, we use the standard Fisher matrix approach common from gravitational wave applications—see, e.g., [336, 337]—which we have extended to include the anticipated errors of the electromagnetic measurements. We then construct a population model using population synthesis results from the literature and determine the number and properties of systems whose masses could be measured to a given accuracy using the three combinations. (We assume the minimal LISA mission in our analysis—viz., one year, with only two arms working—so our numbers are somewhat pessimistic.)

We find that one can combine a GAIA parallactic distance measurement with LISA measurements (including the higher harmonics) to measure at least one of the masses of ~ 10 systems, both detached and Roche-lobe overflow (RLOF), with an accuracy of better than 40% (often $\sim 20\%$; $\sim 12\%$ in the best case). It would be difficult to measure the masses of these high frequency systems any other way. The LISA + mass function measurement is, unfortunately, only able to obtain an accurate mass measurement in a few cases, and even in these few cases, one only obtains good accuracy for the companion to the star for which the mass function is measured—one expects that this companion will be the more massive star, as is generally the case in observed systems (e.g., [334, 338]).

The LISA + GAIA + mass function case allows one to measure the masses of hundreds of systems (many detached and some RLOF, plus a few verification binaries, most notably ES Cet) with accuracies of between $\sim 5\%$ to $\sim 30\%$, assuming realistic statistical uncertainties for the mass function measurements. (However, this presumes that one is able to measure the mass function at all—one is not guaranteed the existence of a strong enough line from at least one of the stars for all the systems considered.) Since one is more likely to be able to measure the mass function accurately for longer-period systems, this is a complementary measurement to the one involving just LISA and GAIA: That measurement requires LISA to be able to measure the higher harmonics, which can only be done accurately for short-period systems. (When considering longer-period systems, one has to worry about possible confusion, in principle, due to the large number of systems at lower frequencies. However, we only consider the systems whose SNRs are high enough that they should be easily resolvable above the irreducible confusion noise; see the discussion in Crowder and Cornish [114] and Sec. 6.7.)

But note that there can be significant systematic errors in the mass function measurements of white dwarf binaries (particularly close and/or RLOF ones), primarily due to so-called K-corrections (see the discussion in Sec. 6.5.3). While there are no systematic uncertainties in the parallax measurements, there are some in the gravitational radiation, due to finite size effects. Nevertheless, these only have a significant effect on the current quadrupole radiation, and the correction is smaller than the accuracy of the measurements we expect to be able to make (see the discussion in Sec. 6.6 and Appendix F).

We start with a more detailed discussion of the information provided by each of the observations in Sec. 6.2 and give a careful exposition of the GW waveform we use in Sec. 6.3. We then discuss the specifics of our Fisher matrix analysis of the combined gravitational wave and electromagnetic measurements in Sec. 6.4. In Sec. 6.5, we discuss the models for the uncertainties of the electromagnetic measurements, including our population model. We give the results in Sec. 6.6 and discuss them in Sec. 6.7. In Sec. 6.8 we summarize and conclude. We discuss finite size effects in the gravitational radiation from white dwarf binaries in Appendix F.

6.2 Observational data

Here we briefly outline the parameters measured by each of the observations we consider; we shall expand on the specifics of the measurements in the following sections. The electromagnetic measurements will always give us the system's sky location and phase evolution (i.e., its frequency and frequency evolution); the latter will likely be able to be determined from photometry, since one expects that these systems will exhibit brightness variations at their orbital periods. Additionally, if a system is sufficiently close, then one can measure its (geometric)

parallax and thus obtain its distance, r. GAIA will obtain highly accurate parallaxes (errors of 300 μas, at worst) for all stars brighter than 20th (GAIA) magnitude (very similar to V magnitude). This corresponds to distance uncertainties of at most a few tens of percent for objects near 20th magnitude around a kpc away, with correspondingly better determinations for brighter and/or closer stars; see the discussion in Sec. 6.6. If one is able to observe a clear spectral line on one of the stars at an exposure time of significantly less than the orbital period, then one can measure that star's radial velocity semi-amplitude, K_1, and combine it with the system's period, P, to obtain the mass function,

$$f_M := \frac{m_2^3 \sin^3\theta}{(m_1 + m_2)^2} = \frac{PK_1^3}{2\pi G}. \tag{6.1}$$

Here m_2 is the mass of the companion to the star whose radial velocity is measured (that star's mass is m_1), θ is the inclination angle, and G is Newton's constant. (The second equality follows from Kepler's third law, assuming a circular orbit.)

As discussed in the next section, the gravitational wave signal will supply the system's inclination angle, along with two different combinations of the systems' individual masses and distance. One can obtain the inclination angle and one of the combinations of masses and distance by measuring (both polarizations) of the dominant harmonic. To obtain the second combination of masses and distance, one needs to measure at least one of the next two harmonics. The gravitational wave observations also provide the system's sky position and frequency evolution, though to a substantially lesser accuracy than electromagnetic observations are able to provide. We thus do not include these in our calculation of the overall measurement accuracy. (As discussed in Sec. 6.4.4, we are able to take the sky position and frequency evolution to be known precisely.) However, these measurements are important, in that they allow electromagnetic observations to identify the systems LISA discovers. Additionally, one obtains the system's gravitational wave polarization angle, though that is not needed explicitly in our measurements.

6.3 Gravitational radiation from white dwarf binaries

Since the systems under consideration are not strongly relativistic (with orbital velocities $\lesssim 0.04c$ for the systems in our population model; see Sec. 6.6),[2] we can obtain an accurate description of their radiation using the post-Newtonian approximation. In this approximation, the waveform is expressed as a series in v/c, where v is the system's orbital velocity. More specifically, one writes the waveform in terms of the binary's (mass and current) multipole moments, which are themselves expanded in v/c; these multipoles will be important in later discussions. (See, e.g., [19] for a review of the application of the post-Newtonian approximation to compact binaries.)

While the post-Newtonian expansion of the gravitational waveform from a nonspinning point particle system in a circular orbit has been worked out to the impressively high order of $(v/c)^6$ (past the lowest-order "quadrupole formula" expression) [339], we shall only need the corrections through v/c for this study: $(v/c)^2 \lesssim 2 \times 10^{-3}$ for the binaries we consider, while

[2]The upper bound comes from considering a binary with a period of 86 s, the shortest period in our population model, and both stars with masses of 1.4 $M_\odot$, close to the Chandrasekhar mass.

the very best accuracies we expect to obtain in our measurement are a few percent. Moreover, even if we could measure these higher-order corrections accurately, we would not be able to break any further degeneracies: While the amplitudes start to depend on the symmetric mass ratio $\eta := m_1 m_2/(m_1+m_2)^2$ at $(v/c)^2$, η is not independent of $\zeta := (m_1-m_2)/(m_1+m_2)$, which we obtain from the lower-order pieces.[3] Specifically, $\eta = (1-\zeta^2)/4$.

We take the explicit expression for the waveform from Eq. (238) in [19], keeping corrections to the "Newtonian" mass quadrupole result only through $O(v/c)$, by the above discussion. Reproducing the resulting expression here to fix notation, we have, using the expression for Blanchet's x given in his Eq. (192) and defining convenient quantities,

$$h_+ = -2A\left(1+\cos^2\theta\right)\cos 2\Phi - \frac{B}{4}\sin\theta\left[\left(5+\cos^2\theta\right)\cos\Phi + 9\left(1+\cos^2\theta\right)\cos 3\Phi\right], \tag{6.2a}$$

$$h_\times = -4A\cos\theta\sin 2\Phi - \frac{3}{4}B\sin 2\theta\left(\sin\Phi - 3\sin 3\Phi\right), \tag{6.2b}$$

where Φ denotes the binary's orbital phase (recall that θ denotes the system's inclination angle)

$$A := \frac{(G\mathcal{M})^{5/3}\omega^{2/3}}{c^4 r}, \qquad B := \frac{G^2\mathfrak{m}^2\omega}{c^5 r}, \tag{6.3a}$$

$$\mathcal{M} := \frac{(m_1 m_2)^{3/5}}{(m_1+m_2)^{1/5}}, \qquad \mathfrak{m} := \left[\frac{m_1 m_2|m_1-m_2|}{(m_1+m_2)}\right]^{1/2}. \tag{6.3b}$$

Here $\mathcal{M}$ is known as the chirp mass, while $\mathfrak{m}$ is a "scaled mass difference." In Eqs. (6.2), the mass quadrupole terms are those that involve 2Φ, while the mass octupole terms involve 3Φ and Φ. The current quadrupole terms only involve Φ, and make a contribution of $-(4/3)B\sin\theta\cos\Phi$ to h_+ and $-(2/3)B\sin 2\theta\sin\Phi$ to $h_\times$. (Note that the Φ and 3Φ terms provide redundant information.)

Now, even though the systems' orbital velocities are small enough that their gravitational radiation is very well described by the first few terms of the post-Newtonian expansion, we still must justify using the standard circular orbit, nonspinning point particle waveform. First, absent dynamical interactions with other objects, double white dwarfs are expected to have circular orbits, due to tidal interactions (see, e.g., [115, 340]).[4] Of course, the orbital radii of these binaries change secularly, either decreasing due to the emission of gravitational radiation, or increasing due to mass transfer, so the orbits are at best quasicircular. However, the changes in the systems in which we are interested occur adiabatically (we are not interested in systems where there is catastrophic mass transfer or tidal disruption), so we can still take the orbit to be instantaneously circular.

[3] While one obtains dependence upon m_1+m_2 alone in a higher-order correction at $O([v/c]^6)$ [see Eq. (8.9g) in Blanchet *et al.* [339]; this contribution is singled out in their Eq. (8.12)], this is a hereditary contribution (specifically, a tails-of-tails contribution), which depends on the binary's entire past history. Blanchet *et al.* [339] calculate it assuming that the binary's frequency evolution is solely (point mass) GW-driven, so even if we could measure such high-order contributions accurately, this term would be modified in unknown ways by finite size effects (through their effect on the binary's phase evolution).

[4] While significant dynamical interactions are anticipated to occur in globular clusters, the resulting population of eccentric binaries in the LISA band is expected to be small, consisting of only a few systems [340].

These secular changes in the orbital radius will affect the frequency and amplitude of the resulting gravitational radiation, but we can ignore these in our analysis: The frequency changes can be ignored since we assume that we have a sufficiently accurate phase-connected solution from electromagnetic observations. This is quite reasonable, as is discussed in Sec. 6.4.4. The amplitude changes over the course of a year are small in all except the most highly mass-transferring systems (which we simply exclude from our analysis and population model), and thus will have a negligible effect on the accuracy of the measurement. Specifically, they are $\lesssim 1\%$ for a purely (point mass) GW-driven inspiral for the $2 \times 1.4\,\mathrm{M}_{\odot}$, 86 s binary mentioned above, and considerably smaller for binaries with smaller chirp masses. During conservative mass transfer, they are a few times larger, except in the extreme, short-lived cases that we do not consider. (See, e.g., the discussion in [341].)

Since white dwarfs are not compact (their radii are $\gtrsim 10^3$ times their Schwarzschild radii, and can be a significant fraction of the orbital separation for the systems in which we are interested), it might seem a poor approximation to treat them as point masses. However, the point mass approximation is exact for the mass multipoles if the individual stars are spherically symmetric, so it only obtains corrections due to tidal effects. As realized by Clark [342], these are always small for binary systems, since mass transfer (or tidal disruption) places an upper bound on the ratio of the size of an object to its orbital separation. We estimate the corrections for our case *à la* Chau [343] (whose work Clark was following) in Appendix F, finding that the fractional corrections to the mass octupole are larger than those to the mass quadrupole.

One obtains significantly larger finite size effects in the current multipoles, since they are sensitive to the components' structure through their spins at Newtonian order, even for spherical components (we assume corotation in our analysis—see Appendix F for further discussion); the contribution from corotation does not appear to have been appreciated in the literature. (The standard PN analyses of spin consider truly compact objects, whose radii are at most a few times their Schwarzschild radii, and in this case, the spin contributions are taken to be higher post-Newtonian effects, due to the suppression from the bodies' small size, even though they are otherwise Newtonian effects. See, e.g., the discussion in [213].) These finite size effects are up to a 6% correction to the amplitude of the radiation at the binary's orbital frequency for certain of the systems in our population model whose masses we can measure well. However, the resulting correction to the inferred masses is only $\sim 3\%$, considerably smaller than the most accurate mass measurements in our population model (of $\sim 15\%$). We thus ignore it. (For comparison, if we do not use the radiation at the binary's orbital frequency in our analysis, then we decrease the accuracy of our mass measurements by ~ 5 percentage points.) We thus appear to be justified in our use of point particle, nonspinning, circular orbit waveforms to better accuracy than we anticipate being able to make mass measurements of realistic systems with LISA and GAIA.

6.4 Prediction of measurement uncertainties

In order to quantify the expected accuracy with which we can measure the physical parameters of the binary white dwarf system, we use the techniques of the Fisher matrix (a.k.a. the covariance matrix). Here we detail the slight modifications necessary to incorporate independent (electromagnetic) observations into the general Fisher matrix formalism, after first reviewing the standard application to gravitational wave observations, following Finn [336].

In general, we consider measuring of the set of parameters $\boldsymbol{\mu}$ that uniquely characterize an observed signal, based on an observed data stream

$$g(t) = n(t) + s(t; \tilde{\boldsymbol{\mu}}). \tag{6.4}$$

Here $\tilde{\boldsymbol{\mu}}$ are the true source parameters, $s(t; \tilde{\boldsymbol{\mu}})$ is the signal the source would produce in the detector in the absence of noise, and $n(t)$ is the detector's noise, which we take to be stationary and Gaussian. Due to this noise, the measured parameters $\hat{\boldsymbol{\mu}}$ differ from their true counterparts, with a difference we shall write as $\delta\boldsymbol{\mu} := \tilde{\boldsymbol{\mu}} - \hat{\boldsymbol{\mu}}$. We define the measurement's signal-to-noise ratio (SNR) in terms of $\hat{\boldsymbol{\mu}}$

$$\rho^2 = 2\left\langle s(\hat{\boldsymbol{\mu}}), s(\hat{\boldsymbol{\mu}})\right\rangle. \tag{6.5}$$

Here we have introduced the noise-weighted inner product

$$\langle s, u\rangle := \int_{-\infty}^{\infty} \frac{\tilde{s}(f)\tilde{u}^*(f)}{S_n(|f|)} df, \tag{6.6}$$

where

$$\tilde{u}(f) := \int_{-\infty}^{\infty} u(t) e^{2\pi i f t} dt \tag{6.7}$$

denotes the Fourier transform of u, the asterisk denotes complex conjugation, and S_n is the detector's one-sided noise power spectral density.

We now turn to our primary concern: the probability distribution of $\delta\boldsymbol{\mu}$. As is shown in Finn [336], this distribution is a multivariate Gaussian in the high-SNR limit, viz.,

$$p(\delta\boldsymbol{\mu}|\hat{\boldsymbol{\mu}}) = \frac{\exp\left[-\boldsymbol{\Delta}^\top \mathsf{C}^{-1}\boldsymbol{\Delta}/2\right]}{\left[(2\pi)^N \det \mathsf{C}\right]^{1/2}}. \tag{6.8}$$

Here $\boldsymbol{\Delta} := \delta\boldsymbol{\mu} - \overline{\delta\boldsymbol{\mu}}$ (an overbar denotes an average over all instances of noise), superscript $\top$ denotes the transpose, C is the covariance matrix, and N is the number of parameters. The covariance matrix is the primary output of this analysis, since its components give us the variances σ_i^2 and correlation coefficients r_{ij} of $\delta\boldsymbol{\mu}$, viz.,

$$\begin{aligned} \sigma_i^2 &:= \Delta_i^2 = C_{ii}, \\ r_{ij} &:= \sigma_i^{-1}\sigma_j^{-1}\Delta_i\Delta_j = \frac{C_{ij}}{\sigma_i^{-1}\sigma_j^{-1}} \end{aligned} \tag{6.9}$$

(with no implied sums). The components of the inverse covariance matrix can be calculated from the signal by

$$C_{ij}^{-1} = 2\left\langle \frac{\partial s}{\partial \mu_i}(\hat{\boldsymbol{\mu}}), \frac{\partial s}{\partial \mu_j}(\hat{\boldsymbol{\mu}})\right\rangle. \tag{6.10}$$

Let us now generalize this expression to the case of multiple, independent detectors (gravitational wave or otherwise), labeled by the index α. We start by noting that since the detectors' noise is independent, the probability distribution of the full uncertainties is a product of the probability distributions of the uncertainties of the individual observations. This implies [by Eq.(6.9)] that the inverse of the full covariance matrix is the sum of the inverse covariance matrices of the

individual observations. Here we treat the individual covariance matrices as acting on the full set of parameters, even though any individual detector can only measure a subset of the parameters. All the individual inverse covariance matrices will thus necessarily be singular,[5] though their sum will be invertible, except in degenerate cases—e.g., when the binary is face-on.)

To obtain this expression for the full inverse covariance matrix, first introduce some notation: Let $\boldsymbol{\mu}_{\rm TOT}$ be the full set of independent parameters which together uniquely characterize the signals observed by all the detectors. Additionally, let the uncertainties in the αth detector's observations be given by the covariance matrix C_α. Now, these covariance matrices include the effect of the priors introduced in the analysis of the detectors' data. We ignore these in our derivation, since we want to consider only the cases where the data are more restrictive than the priors, so we can take the priors to be flat over the region where the is probability is most strongly peaked. We also assume that the most likely values of the parameters inferred by each detector are very close to those that would be inferred in a maximal likelihood analysis using the entire suite of detectors, allowing us to ignore the fact that the various covariance matrices are evaluated at different parameter values, in general.

With these assumptions, the probability distribution of the uncertainties in this full parameter set is given (up to a small remainder, due to the slight differences in inferred parameter values) by

$$p(\delta\boldsymbol{\mu}_{\rm TOT}|\hat{\boldsymbol{\mu}}_{\rm TOT}) \propto \prod_\alpha \exp\left[-\boldsymbol{\Delta}_{\rm TOT}^{\rm T}\mathsf{C}_\alpha^{-1}\boldsymbol{\Delta}_{\rm TOT}/2\right]. \tag{6.11}$$

(Here all the "TOT" quantities are defined analogously to the single detector case; recall that we take each C_α to act on the full set of parameters.) This implies that the inverse of the full covariance matrix $\mathsf{C}_{\rm TOT}$ is given by

$$\mathsf{C}_{\rm TOT}^{-1} = \sum_\alpha \mathsf{C}_\alpha^{-1}. \tag{6.12}$$

[N.B.: While we compute the gravitational wave covariance matrix using Eq. (6.10), the electromagnetic covariance matrices are simply obtained from the anticipated standard deviations of the observations; there are no correlations to be concerned about. (We neglect any possible correlations between the parallax and mass function measurements due to correlations between the system's masses and luminosity.)]

6.4.1 LISA's measurement of the gravitational wave signal

As mentioned in the introduction, for this analysis we are assuming the minimal LISA mission, with an observation time of one year and only two working arms. We also assume that electromagnetic observations have provided us with the binary's position and phase evolution to the requisite accuracy. This is a reasonable assumption, as will be discussed in Sec. 6.4.4. This knowledge simplifies the analysis considerably, since we can neglect all the phase modulations due to LISA's orbital motion and transfer functions: The phase shifts these introduce are

[5] This means that referring to these individual inverse covariance matrices as such is something of a misnomer, since they are not the inverse of any matrix, when taken to act over the entire parameter set. However, we retain the terminology, since they *are* invertible when taken to act over the parameter set appropriate to that detector, and we calculate those portions of the matrix in the usual way.

dependent only on the source's position and phase evolution (once one has fixed LISA's initial orientation), so one can remove them in data analysis. [See, e.g., Eq. (14) of [344] for an explicit expression for how the phase shifts enter into the observed strain.] We can thus take LISA's barycenter to be located at the solar system's barycenter, so the only effects of LISA's orbital motion will be the yearly rotation of the plane of the constellation about the perpendicular to the ecliptic plane and the constellation's yearly counter-rotation in its own plane. (In principle, the Doppler shifts to the observed frequency due to LISA's orbital motion affect the signal-to-noise ratio, since they change where the signal falls on LISA's noise curve. However, we can neglect these changes in practice, since they are quite small: The Doppler shifts to the frequency are at most $\sim 10^{-4}$.)

In order to calculate the gravitational wave contribution to the covariance matrix [using Eq. (6.10)], we need to know the signal, m. This will depend on LISA's response functions, which allow one to convert the metric perturbation describing an incident gravitational wave into the strain measured by the detector. We use LISA's Michelson observable, and compute LISA's response in the rigid adiabatic approximation (RAA) of [345], simplifying to the low-frequency approximation (also discussed in [345]) whenever possible.

However, we cannot use the low-frequency approximation throughout, because we cannot ignore LISA's transfer functions at high frequencies: Even though we can ignore the phase modulations due to LISA's transfer functions in our analysis, by the argument above, we still must consider the amplitude modulations caused by the transfer functions. These enter into LISA's Michelson response (in the RAA) as

$$s = (l_1^a l_1^b S_1 - l_2^a l_2^b S_2) h_{ab}/2, \tag{6.13}$$

where l_I^a are unit vectors along LISA's arms ($I \in \{1, 2\}$ labels the arms),

$$S_I := \frac{1}{2}\left\{\mathrm{sinc}\left[\frac{f}{2f_*}(1 - l_I^a P_a)\right] + \mathrm{sinc}\left[\frac{f}{2f_*}(1 + l_I^a P_a)\right]\right\} \tag{6.14}$$

[$\mathrm{sinc}(x) := \sin(x)/x$, f is the GW frequency, $f_* := c/(2\pi L) \simeq 9.5$ mHz is LISA's transfer frequency ($L = 5\times10^9$ m is its armlength), and P^a is the unit vector in the direction of propagation], and h_{ab} is the metric perturbation. We have $S_I \to 1$ for $f \to 0$, so the low-frequency approximation consists of setting all the S_I to 1. This is a good approximation for $f \lesssim f_*$, and always gives an upper bound on the signal. It is also calculationally convenient, since we can obtain analytic expressions for the integrals involving the transfer functions that enter into our covariance matrix in this approximation. (N.B.: The larger effect of the transfer functions on the accuracy of parameter estimation at low frequencies found by Vecchio and Wickham [344] is due to the transfer functions' modulation of the signal's phase, which is not relevant for our case, where we take the source's frequency and sky location to be known precisely.)

6.4.2 LISA's response functions

If the incident gravitational wave contains polarization states h_+ and $h_\times$, then the measured strain is

$$s = R_+(h_+ \cos 2\psi - h_\times \sin 2\psi) + R_\times(h_+ \sin 2\psi + h_\times \cos 2\psi), \tag{6.15}$$

where $R_{+,\times}$ are LISA's response functions and ψ is the polarization angle. These response functions are given by substituting $h_{ab} \to e^{+,\times}_{ab}$ in Eq. (6.13), where the polarization tensors $e^{+,\times}_{ab}$ are given in terms of the the gravitational wave's polarization vectors, u^a and v^a, by

$$e^{+}_{ab} := u_a u_b - v_a v_b \tag{6.16a}$$

$$e^{\times}_{ab} := 2u_{(a}v_{b)}. \tag{6.16b}$$

To calculate these response functions for a source at ecliptic coordinates $\{\beta, \lambda\}$, we first compute the polarization vectors for this source position, using the convention that $\boldsymbol{u}$ is parallel to the ecliptic. We then compute LISA's arm vectors using Euler angles, assuming that the arms have an arbitrary initial orientation. As we shall see shortly, we only need the time averaged (over one year, i.e., one LISA orbit) products of the response functions in constructing the Fisher matrix. We can calculate these analytically (using MAPLE) in the low-frequency limit, giving

$$\left\langle R_+^2 \right\rangle = P_{\rm LISA}\left[\frac{45}{256}\cos^2\beta - \frac{9}{128}\cos^4\beta - \frac{27}{512}\sin^2\beta + \left(\frac{111}{8192} + \frac{243}{4096}\sin^2 2\lambda\right)(1+\sin^2\beta)^2\right], \tag{6.17a}$$

$$\left\langle R_\times^2 \right\rangle = P_{\rm LISA}\left[\frac{45}{256}\cos^2\beta + \left(\frac{489}{2048} - \frac{972}{4096}\sin^2 2\lambda\right)\sin^2\beta\right], \tag{6.17b}$$

$$\langle R_+ R_\times \rangle = -\frac{243}{4096} P_{\rm LISA}(\sin\beta + \sin^3\beta)\sin 4\lambda, \tag{6.17c}$$

where $\langle \cdots \rangle := \int_0^{P_{\rm LISA}} (\cdots) dt$ and $P_{\rm LISA} = 1$ yr is LISA's orbital period. To obtain these expressions, we have chosen LISA's initial orientation such that the bisector of the two arms points in the $\lambda = 0$ direction. Since we are using an observing period of one year, any other initial orientation would be equivalent to changing the ecliptic longitude (λ) of the source.

Calculating the individual elements of the covariance matrix from the gravitational wave measurements requires evaluating noise weighted inner products [cf. Eq. (6.10)] using the signal calculated using Eq. (6.13). Here we can make a number of reasonable approximations to simplify this calculation. (See [346] for a discussion of similar techniques.) First, the functions for which we are calculating inner products all have Fourier transforms that are strongly peaked around the three frequencies $f_{\rm bin}$, $2f_{\rm bin}$, and $3f_{\rm bin}$, where $f_{\rm bin}$ is the binary's orbital frequency (see Sec. 6.3), since these are the three frequencies present in the signal; the spread in the Fourier domain is introduced by our finite observing time. (We only consider the peaks that lie in the LISA band; the noise strongly suppresses all contributions at other frequencies.) We can thus take the contributions from the different frequencies to be orthogonal, and compute their inner products with themselves in the time domain (evaluating the noise at the frequency under consideration in each term).

The second approximation is based on the fact that the binary periods we consider are much less than our fiducial observation time of one year (indeed, $\lesssim 1$ hour). This allows us to use the stationary phase approximation to "integrate out" the fast variation of the binary's oscillation compared to the slow variation of LISA's response function. (The fractional remainders are thus on the order of $1\,{\rm hr}/1\,{\rm yr} \simeq 10^{-4}$.) The remaining integrals appearing in the evaluation of Eq. (6.10) for such sources are just the averaged products of response functions considered in Eqs. (6.17).

6.4.3 LISA's noise

We use the model for LISA's noise given in Table 1 of the LISA flowdown guide [347]. This model represents the instrumental sensitivity demanded by LISA's science requirements. However, we use LISA's strain noise, not the equivalent metric perturbation noise that is output directly by Table 1 in the flowdown document. In other words, we leave off the factors of $\sqrt{5}$ (due to averaging over polarization), $2/\sqrt{3}$ (due to the 60° angle between LISA's arms), and $T(f)$ (the transfer function), since we use LISA's response functions to obtain the strain from the metric perturbation (and do not need to perform any averaging at this stage, since we measure the polarization angle). (These factors are discussed further in Sec. 3.1 of [348].) Explicitly, we have a strain amplitude spectral density of

$$S_n(f) = \frac{1}{L^2}\left[S_{\rm IMS}(f) + 4\frac{S_{\rm DRS}(f)}{(2\pi f)^4}\right], \tag{6.18}$$

where

$$S_{\rm IMS}(f) = C_{\rm IMS}\left[1 + \left(\frac{f_0}{f}\right)^4\right], \tag{6.19a}$$

$$S_{\rm DRS}(f) = C_{\rm DRS}\left[1 + \left(\frac{f}{f_H}\right)^4\right]\left[1 + \frac{f_L}{f}\right], \tag{6.19b}$$

with $C_{\rm IMS} = \left(12\times10^{-12}\right)^2$ m^2/Hz, $C_{\rm DRS} = \left(30\times10^{-16}\right)^2$ m^2/(s^{4}Hz), $f_0 = 2$ mHz, $f_H = 8$ mHz, and $f_L = 0.1$ mHz. (Recall that $L = 5\times10^9$ m is LISA's armlength.) N.B.: We corrected the value for ΔX_0 given in the table in our expression for $C_{\rm IMS}$: The correct value of 12 is given in Table 2 and the first equation in Sec. 5 of the flowdown guide; Table 1 of that document contains the incorrect value of 18.

6.4.4 Optical measurements of the binary system

Here we consider the contribution of the electromagnetic measurements to our analysis. Suppose an electromagnetic observation gives us a value for some relevant parameter, χ (here either the parallax or the mass function), and an associated variance of that parameter, σ_χ^2. To simplify calculations, we choose χ to be one of the parameters $\boldsymbol{\mu}$ we use to describe the system parameters. Specifically we choose $\boldsymbol{\mu} = \{\boldsymbol{\xi}, \chi\}$ where $\boldsymbol{\xi}$ consists of the remainder of the undetermined parameters (all of which come from the gravitational wave observation). The inverse covariance matrix associated with the electromagnetic measurement then only has a single nonzero element, i.e., $\mathsf{C}_{\rm EM}^{-1} = {\rm diag}(0,\cdots,0,\sigma_\chi^{-2})$. We then generate the full covariance matrix by combining this electromagnetic inverse covariance matrix with the inverse covariance matrix associated with the gravitational wave observations, viz.,

$$C^{-1}_{ij,{\rm GW}} = \begin{bmatrix} C^{-1}_{11,{\rm GW}} & \cdots & C^{-1}_{15,{\rm GW}} & 0 \\ \vdots & \ddots & \vdots & \vdots \\ C^{-1}_{15,{\rm GW}} & \cdots & C^{-1}_{55,{\rm GW}} & 0 \\ 0 & \cdots & 0 & 0 \end{bmatrix}. \tag{6.20}$$

We can take the binary's sky position to be known exactly, since the precision of an optical measurement will be much greater than LISA's angular resolution. Checking this explicitly, we note that the sky location enters our measurement through LISA's response functions, as discussed in Sec. 6.4.1, thus affecting the modulation of both the amplitude and phase. If we have arcsecond-level localization accuracy (and we expect far greater accuracy; for instance, GAIA is expected to measure parallaxes at the sub-milliarcsecond level), then LISA's signal will be affected at the 5×10^{-6} level in the amplitude, and at even smaller levels in the phase ($\lesssim 10^{-11}$, much smaller than LISA's frequency resolution for an observation time of 1 year of $1\ \mathrm{yr}^{-1} \simeq 3 \times 10^{-8}$ Hz). The phase requirement (from LISA's frequency resolution) is more stringent, but still quite reasonable. For instance, the phase-connected solution for HM Cnc (a.k.a. RX J0806.3+1527; period of ~ 322 s) given by Strohmayer [349] has an uncertainty of $\sim 2.5 \times 10^{-9}$ Hz over one year, well under LISA's frequency resolution.

6.4.5 Choice of variables

To simplify the algebra, we compute the gravitational wave covariance matrix using the variables $\{A, B, \theta, \phi, \psi\}$, to which we adjoin whichever electromagnetically determined parameter (r or f_M) is appropriate to obtain our full parameter set. (In the LISA + GAIA + mass function case, we adjoin r and transform the mass function's inverse covariance matrix to the resulting coordinates before adding it to the other inverse matrices.) We then transform the the full covariance matrix to more physically meaningful mass and distance parameters (e.g., $\{m_1, m_2, r\}$, or other, less highly correlated mass parameters) using a coordinate transformation. (The covariance matrix transforms like a covariant 2-tensor under coordinate transformations.)

6.5 Models

We now wish to obtain a rough idea of the number and properties of the systems whose masses we will be able to measure to a given accuracy using this method. In order to do this, we have created a rough population model using results in the literature, and estimated the expected errors in the GAIA and mass function measurements.

6.5.1 Population model

The basis for our population model is the period distribution of double white dwarf binaries given in Fig. 2 of Nelemans *et al.* [320]. We have taken the distribution to be flat in the logarithm of the period in each bin and cut it off at periods above $10^{-1.5}$ days $\simeq 2732$ s (this cutoff may cause us to lose some low-frequency systems in the LISA + GAIA + mass function case), so there are $449,345$ systems in the model.[6] (While an extrapolation of the results in Fig. 2 of [320] suggests that there will be ~ 30 systems at periods shorter than ~ 86 s that are not shown in that figure, we have not included these, due to low statistics and a high uncertainty in their apparent magnitudes, due to the competing effects of, e.g., tidal heating and extinction.) This is a flat in $\log a$ distribution (a denotes a system's semimajor axis), corresponding to the

[6] Note that estimates for the total number of binaries vary by a factor of ~ 3 in the literature; the Nelemans *et al.* [320] number is the lowest, and the Liu *et al.* [117] number is the highest.

assumed shape of the initial period distribution used by Nelemans *et al.* (the population synthesis evolution maintains the shape of the distribution). Thus, one might want to convert the histogram back to the underlying smooth distribution, though we will not attempt this here.

Following the proportions of detached and RLOF systems found in the overall disk model of Ruiter *et al.* [115], we take there to be 155,821 detached binaries (34.7%) and 293,524 (65.3%) RLOF systems. While one might expect that these fractions would change with period, Figs. 1–2 in [115] suggest that the fractions are still approximately correct for the short period systems we are considering. For each of these systems, we select a position in the galactic disk using a standard model for its density (discussed below), along with an inclination angle (chosen from a distribution that is uniform on the 2-sphere), and a polarization angle (chosen from a uniform distribution). (We take the sky position to be a fixed $\lambda = 8$ hours and $\beta = 50°$, for simplicity.)

All that remains is to obtain the masses. This is rather more complicated, since the range of possible masses depends on the system's period and whether it is RLOF or not. The allowed ranges are given in [341], with fits to the boundaries in the frequency-chirp mass plane given in Sec. 5.1 of that paper.[7] For the distribution of chirp masses within the allowed range for a given period, we have used the Gaussian fit from Liu *et al.* [117], with a mean and standard deviation of $0.347\,M_\odot$ and $0.128\,M_\odot$, respectively, cut off at the appropriate population boundaries (which are discussed in more detail below). (N.B.: This Gaussian fit misses some secondary peaks in the distribution, particularly at low masses—see Fig. 7 in Liu *et al.* [117].) Then, once we have selected the binary's period and chirp mass, we pick out an appropriate mass ratio: If the system is RLOF, then we obtain the mass ratio by taking the smaller-mass star to have the same radius as the volume radius of its Roche lobe (using the standard Eggleton fits). If the system is detached, then we pick its mass ratio from a flat distribution between the equal-mass case and the smallest mass ratio the system can have and remain detached (using the same Eggleton fits as in the RLOF case), with its more massive component having a mass less than the Chandrasekhar mass.

The galactic distribution model is the same one used by, e.g., Ruiter *et al.* and Nelemans *et al.* [115, 320], where the spatial density of binaries is

$$\rho(r) = \frac{N}{4\pi R_0 z_0} \exp(-R/R_0)\,\mathrm{sech}^2(z/z_0). \tag{6.21}$$

Here N is the total number of binaries, R and z are galactic cylindrical coordinates, and R_0 and z_0 are the radial and vertical scales of the Galaxy, respectively. We follow Liu [351] in taking $R_0 = 2.5$ kpc and $z_0 = 90$ pc. (However, this vertical scale height may be rather on the small side for disk white dwarfs—it might easily be as large as 500 pc; see, e.g., the discussion in [115, 352].) We also take the Sun to be 8 kpc from the galactic center and 30 pc off the galactic plane. The lower cutoff for the chirp mass for detached systems of a given period is given by Eq. (37) in Kopparapu and Tohline [341] [after converting mass quadrupole GW frequency to period and GW amplitude to chirp mass and frequency; see, e.g., Eq. (10) in [341]]. The upper cutoff is always $1.25\,M_\odot$, the chirp mass of a $2 \times 1.44\,M_\odot$ binary. For RLOF systems, the upper and lower cutoffs are given by Eqs. (37) and (39) in [341], respectively. (In order to speed

[7] N.B.: These boundaries were determined using the zero-temperature mass-radius relation. We have used these expressions instead of the finite-entropy results given in [350], for simplicity; this is in keeping with the general roughness of our population model.

computation in the RLOF case, where the chirp mass boundaries are much more restrictive, we take the boundaries to be constant over each of the period bins from Fig. 2 of Nelemans *et al.* [320]. Specifically, we take the lower [resp. upper] cutoff to be the minimum [resp. maximum] chirp mass possible for the smallest [resp. largest] period in that bin.

We find that in certain regions of the parameter space the covariance matrix is close to singular and our code becomes numerically unstable. To avoid these instabilities and speed the computations, we introduce a number of cutoffs for problem areas of the parameter space. (We do not lose any important information in doing this, since the excluded systems would all have very large errors in the determination of their parameters.) First, we reject binaries that are more than 6 kpc from the Sun. Secondly, in the LISA + GAIA and LISA + mass function cases, we reject binaries with small higher harmonic gravitational wave amplitudes, specifically when $\mathcal{M} \sin\theta / rP < 2 \times 10^{-4}\ \mathrm{M}_\odot\ \mathrm{s}^{-1}\ \mathrm{kpc}^{-1}$. Finally, we also reject cases where $\theta < 0.3$ radians.

6.5.2 GAIA parallax uncertainties

In any cases where we assume we have the parallax distance to the binary as measured by GAIA, we must also generate an uncertainty associated with that measurement. We use the expression for the expected sky-averaged GAIA parallax errors in terms of the GAIA magnitude of the system given in Eq. (5.1) of Lindegren [331]. (We neglect the corrections due to ecliptic latitude given in Lindegren's Table 3; they are $\lesssim 30\%$.) In order to obtain the GAIA magnitude, we use a model for the system's absolute V magnitude, its distance (as given by the population model), and a model for extinction. (We neglect all color corrections in the conversion to GAIA magnitude, for simplicity.)

For the RLOF systems, we use the model for the absolute V magnitude of the disk of an AM CVn system in terms of the system's period, given in Fig. 5 of Nelemans *et al.* [353]. We find that $M_V = 5.5 + 7.3 \log_{10}(P/10^{2.4}\ \mathrm{s})$ is a reasonable match for the model predictions between $10^{2.4}$ s $\simeq$ 250 s and $10^{3.6}$ s $\simeq$ 3980 s. In the absence of models for the (optical) luminosity of shorter-period systems, we take $M_V = 5.5$ for all periods below 250 s.

In using a model for the disk magnitude of an AM CVn system, we have neglected the case of direct-impact accretion, where no disk is formed. According to [353], this is the dominant case for short-period systems; see their Fig. 4. Even though such systems do not possess a disk, the (relatively) more numerous short-period systems are likely luminous enough (due to the effects of accretion, irradiation, and tidal heating) that we do not err too greatly in taking them to be $M_V = 5.5$. However, if one takes the fiducial distance of 5 kpc for HM Cnc from [119], one obtains $M_V = 7.6$; this neglects extinction, but HM Cnc is on a low-extinction sightline away from the galactic plane (total galactic extinction of < 0.1 V mag, according to the NED calculator [354], which uses the model of Schlegel *et al.* [355]). This may mean that our short-period AM CVn results are too optimistic. Nevertheless, this model likely underestimates the AM CVn disk magnitudes: If we compare its predictions to later measurements of absolute magnitudes made using accurate parallactic distances (see, e.g., [113, 356]), the measured values appear to be brighter by as much as $\sim$ 2 magnitudes. We neglect this, since the model for extinction we use has a much larger uncertainty, as discussed below.

For detached systems, we take use the dependence of the luminosities on the stars' masses and ages computed by [357] with the fit given in Appendix A of [353]. (However, this model predicts that the more massive star is more luminous, while one usually only observes the less

massive, larger star in these systems; the resulting luminosities should thus be treated with caution.) We take the white dwarfs to have been cooling for 10^8 years, based on the typical detached evolution discussed in Sec. 3.1 of Ruiter *et al.* [115]. We also apply a bolometric correction of -0.2 mag, following [358] (though this is small enough that it is probably not really worth worrying about). This estimate neglects tidal heating, which might be $\gtrsim 3$ mag for the shortest period systems in our model, according to Fig. 6 in [359]. As above, we justify our neglect of these by noting that there are even greater uncertainties in our model for extinction.

For extinction, we use the Bahcall-Soniera model [Eqs. (7)–(8) in [360]] to get the rough dependence of extinction on galactic latitude, realizing that the actual extinction might vary by several magnitudes in the plane; see, e.g., the figures in Joshi [361]. Note that Joshi plots selective $(B - V)$ extinction and takes the total V-band extinction to be 3.1 times this. This multiplier is appropriate for the diffuse interstellar medium, though a multiplier of 5 would be appropriate for dense molecular clouds, as is discussed in [362]. We shall thus quote the distribution of systems we can observe accurately if we assume unrealistically small parallax errors (of 10^{-5}) to give an idea of how much the GAIA errors (thus including the models for luminosity and extinction) affect our measurement.

6.5.3 Mass function uncertainties

In cases where we assume the mass function has been measured by electromagnetic observations, we need a characteristic uncertainty associated with this measurement. Since we are assuming that the binary period P will be known very accurately, the uncertainty in the mass function will be dominated by the uncertainty in the radial velocity semi-amplitude, K_1. Overall, the fractional uncertainty in the mass function will be three times the fractional uncertainty of K_1. [See the expression given in Eq. (6.1).] This assumes that the radial velocity is measured from a spectral line emitted from the center of mass of the brighter component of the binary. If the spectral line originates from a different region of the star (possibly due to an asymmetry from tidal distortion or accretion) a "K-correction" term must be introduced to account for the difference between the radial velocity of the center-of-mass of the binary component and the radial velocity of the emission location (see, e.g., [363] for a computation of this effect for an irradiated Roche-lobe filling star, where it can easily be a 20% correction, and may even be a few times larger).

To find a reasonable range for the expected mass function errors, we consider the white dwarf binary measurements of Kilic *et al.* [334, 335, 338]. Using the errors associated with the K measurements as described above, we find fractional mass function errors ranging from $\sim 1\%$ to $\sim 17\%$ in the binaries they consider. (N.B.: The mass function errors quoted in [338] are incorrect, due to an error in their code [364]. The errors we quote are thrice those in the radial velocity semi-amplitude.) The periods of these binaries are in the 12 minute to 6 hour range (and the best accuracies—of $\lesssim 3\%$—are obtained for the shortest-period systems, in [334, 335]). Since LISA is more sensitive to shorter period binaries, we also consider the Roelofs *et al.* [119] measurements of HM Cnc, a ~ 322 s period binary. (These measurements are also interesting because HM Cnc is an AM CVn system, while all the Kilic *et al.* measurements were of detached systems.) Roelofs *et al.* quote K measurements for three features in the spectrum of this system, with corresponding fractional errors in the mass function ranging from 23% to 46%. (Note that these are purely statistical errors, and neglect the necessity of applying a K-correction.)

In actuality, we expect the mass function error to depend on the binary's individual properties. In particular, even disregarding the issue of whether the binary has a clear spectral line, for short-period binaries it is also difficult to get a large enough SNR in the spectra to obtain a well-resolved line with the short exposures necessary to resolve the binary's phase: See, for instance, the difficulties involved in obtaining phase-resolved observations of HM Cnc [119, 365]. However, it is difficult to accurately quantify exactly how these errors would be introduced without choosing a specific observing setup. Instead, we consider two cases, either a constant, highly optimistic $10^{-5}\,M_\odot$ (used in the LISA + mass function case), or a constant fractional error of 20% (used in both the LISA + mass function and LISA + GAIA + mass function cases). (This fiducial 20% error comes from taking taking the optimistic side of the Roelofs *et al.* [119] HM Cnc measurement, since many of the systems that can be measured accurately in this case have longer periods than HM Cnc.) Given this roughness, it also seems appropriate for us to neglect any correlations between the mass function and distance measurements, since they would be even more model-dependent.

6.6 Results

Here we illustrate how well we can perform the various measurements on the systems in our population model. We first show how the accuracy depends on the various binary parameters by picking typical values for the systems in our population for which we can measure the masses well and then varying one parameter at a time. We choose our fiducial system to be detached, since one is not able to vary a RLOF system's period, chirp mass, and mass ratio independently and have it remain RLOF. Our fiducial system has a period of 500 s, a distance of 400 pc, a chirp mass of $0.45\,M_\odot$, mass ratio of 0.75, inclination angle of 60°, polarization angle of 150°, galactic latitude of 3.5° (used in the Bahcall-Soneira extinction model), and ecliptic coordinates of $\lambda = 120°, \beta = 50°$. The system has masses of $0.45\,M_\odot$ and $0.60\,M_\odot$, which LISA + GAIA can measure with accuracies of 19% and 20%, respectively. Its absolute and apparent V magnitudes are 8.0 and 16.7, respectively (the GAIA magnitude is almost equal to the V magnitude); GAIA would obtain the distance with an accuracy of 2%. (The correlations are ~ -0.99 for m_1 and m_2 and ~ 0.06 for the masses and distance.)

For the LISA + GAIA case, we plot the dependence of the fractional errors in the determination of the masses on the detached system's distance, period, chirp mass (holding the mass ratio fixed), mass ratio (holding the chirp mass fixed), inclination angle, polarization angle, and sky location in Figs. 6.1 through 6.8. For the plots versus sky location, we have chosen to plot along several representative slices in both ecliptic latitude and longitude. (Overall, we find that the sky position can change the measurement accuracies of the individual masses by up to 8 percentage points.) Additionally, we did not use the RAA for these sky location plots, for ease of computation. For each case, we only show the parameters that are physically realistic for a detached system, and that lead to fractional mass errors of $\lesssim 0.4$. (In particular, the minimum period plotted is given by the requirement that the system remain detached, and the minimum distance is a rough lower bound obtained from our population model results.) Note that there may be some slight inaccuracies in the quoted mass errors (here and in the rest of the presentation of results), given our method for inverting the Fisher matrix—we estimate that these may be $\sim 10\%$ for the shortest-period systems we consider.

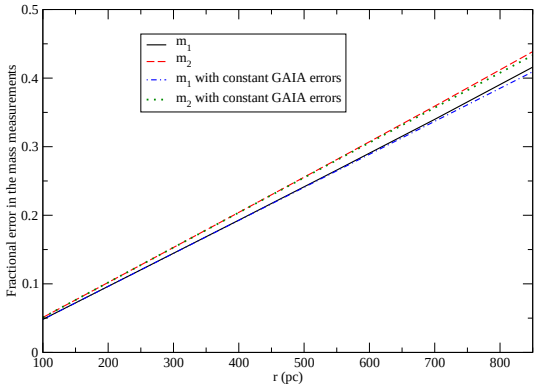

Fig. 6.1. The fractional mass errors vs. distance, *r*, for our fiducial system in the LISA + GAIA case. We have plotted these with the realistic GAIA errors and also with a constant fractional error in the distance determination of 10^{-5} to indicate how much the GAIA errors affect the overall errors.

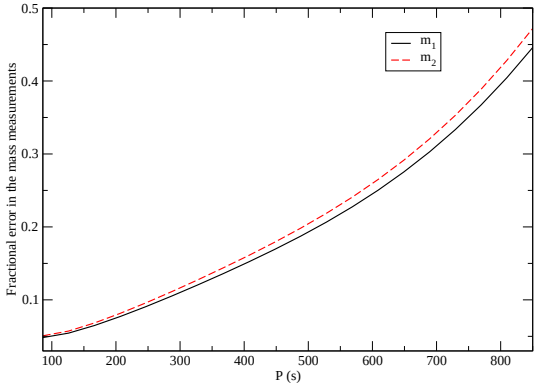

Fig. 6.2. The fractional mass errors vs. period, *P*, for our fiducial system in the LISA + GAIA case.

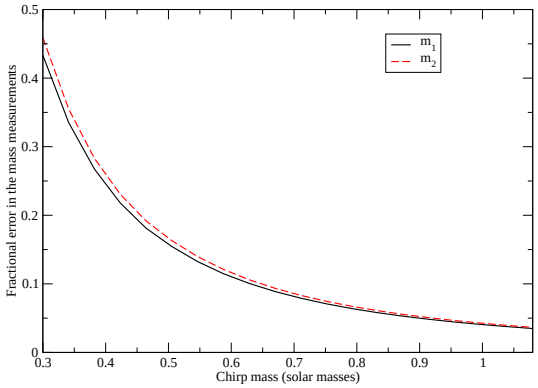

Fig. 6.3. The fractional mass errors vs. chirp mass, $\mathcal{M}$, for our fiducial system in the LISA + GAIA case. (We have not shown the version with a constant fractional mass error of 10^{-5}, since the resulting errors are almost indistinguishable from those with realistic GAIA errors.)

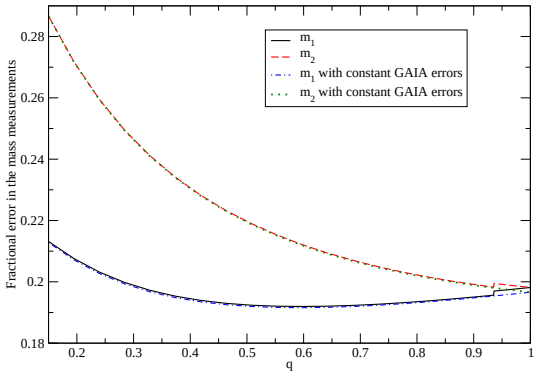

Fig. 6.4. The fractional mass errors vs. mass ratio, q, for our fiducial system in the LISA + GAIA case. The sudden jump in the errors with realistic luminosity at a mass ratio of ~ 0.94 is due to a discontinuity in the dependence of the luminosity on the stars' masses in the model from [353] we use. To illustrate this, we have also plotted the mass errors with a constant fractional mass error of 10^{-5}.

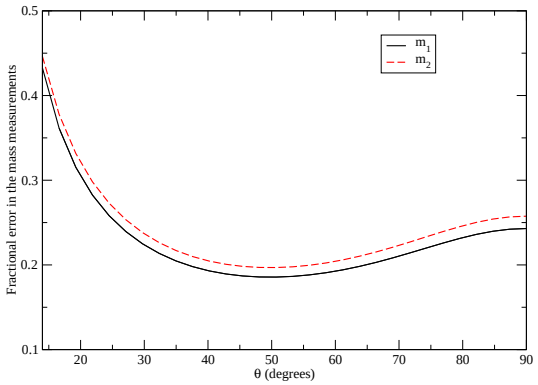

Fig. 6.5. The fractional mass errors vs. inclination angle, θ, for our fiducial system in the LISA + GAIA case.

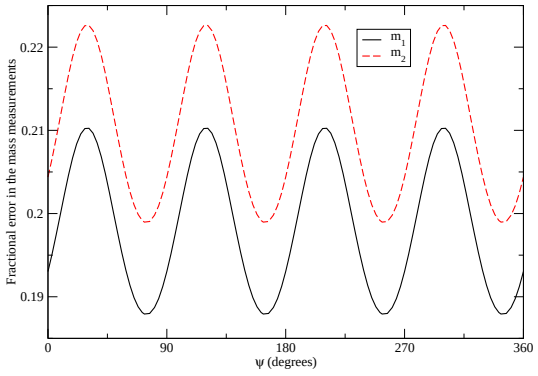

Fig. 6.6. The fractional mass errors vs. polarization angle, ψ, for our fiducial system in the LISA + GAIA case.

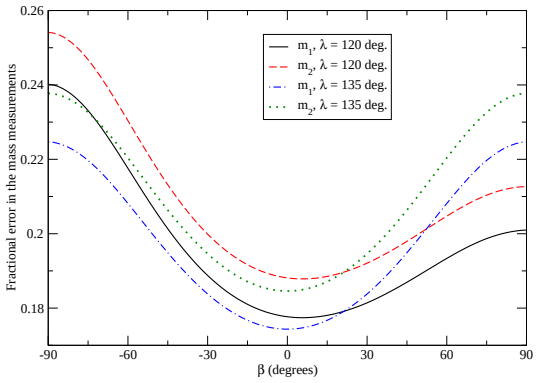

Fig. 6.7. The fractional mass errors vs. ecliptic latitude, β, in the LISA + GAIA case, for $\lambda = 120°$ and $135°$ and our fiducial system, computed using the low-frequency approximation.

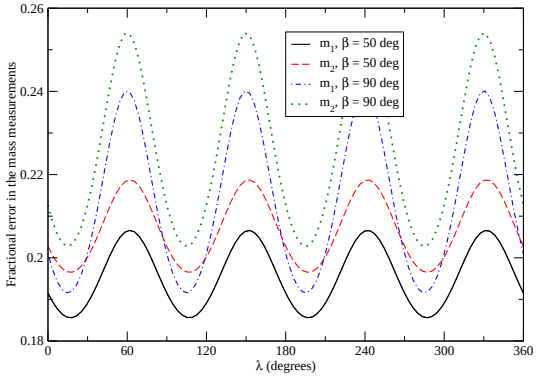

Fig. 6.8. The fractional mass errors vs. ecliptic longitude, λ, in the LISA + GAIA case, for $\beta = 50°$ and $90°$ and our fiducial system, computed using the low-frequency approximation.

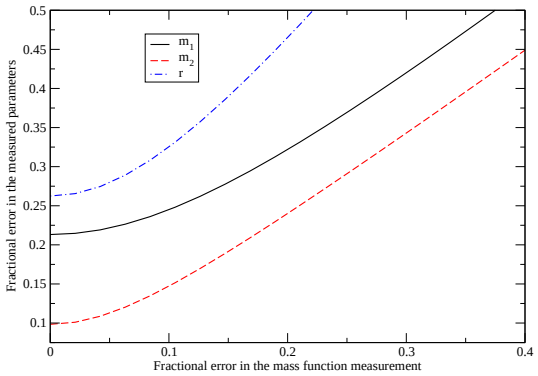

Fig. 6.9. The fractional errors in the parameters vs. the error in the mass function measurement, in the LISA + mass function case, for the fiducial system, with a very optimistic distance of 100 pc.

For the LISA + mass function case, we only show the dependence of the errors on the error in the mass function; see Fig. 6.9. In order to display this dependence clearly, we have used a very optimistic distance of 100 pc in order to obtain small fractional errors in the masses and distance for a small fractional error in the mass function. (Note that we take the smaller mass to be the one whose radial velocity is measured in determining the mass function.)

For the LISA + GAIA + mass function case, we use the parameters of the AM CVn system ES Cet given by Nelemans [113] for our test system, viz., a period of 621 s, a distance of either 350 or 1000 pc, masses of 0.062 and 0.6 $M_\odot$ (corresponding to a chirp mass and mass ratio of 0.154 $M_\odot$ and 0.11, respectively), an inclination angle of 60°, and an apparent V magnitude of 16.9.[8] (We keep the same arbitrary polarization angle and sky location as for the LISA + GAIA systems, for convenience.) We plot the fractional error in the determination of the masses versus the fractional accuracy of the mass function measurement in Fig. 6.10. (Note that while we include the higher harmonics in our analysis, they make a negligible contribution to the accuracy for ES Cet.) We could have also considered one of the other bright white dwarf binaries given by Nelemans [113] (e.g., AM CVn itself, or WD 0957-666), though there we would not have been able to improve upon the statistical uncertainties of the mass measurements quoted by Nelemans for those systems. However, our method *would* provide an independent measurement, with different systematics—the current mass measurements use various assumptions and models, all of which seem reasonable, but it would be good to have an independent check.

Turning to the population model results themselves, we find that we can only measure a handful of systems with good accuracy in the LISA + GAIA case, and even fewer in the LISA + mass function case. We plot the fractional mass errors versus the systems' distances, periods, and individual masses in Figs. 6.11, 6.12, and 6.13. All of these mass errors are calculated using realistic GAIA errors (including the models for extinction and the source's absolute magnitude

[8]Note that the masses and inclination are Nelemans's "best guesses," which he warns may be "completely wrong."

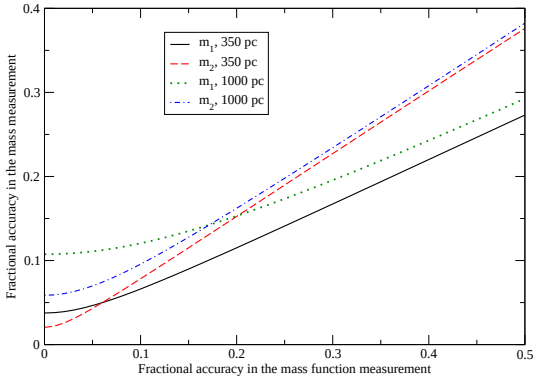

Fig. 6.10. The fractional mass errors vs. the fractional accuracy in the mass function measurement, for the LISA + GAIA + mass function case, computed for the fiducial ES Cet system.

discussed in Sec. 6.5). We also calculated the errors assuming an unrealistically small, constant fractional distance error (of 10^{-5}) and plot them in Fig. 6.14 to show how much of the errors are intrinsic to the LISA portion of the measurement.

In the LISA + mass function case, we observe even fewer systems with good accuracy, and for those this good accuracy only applies to the mass of the more massive star. (Recall that we assume that the less massive star is the one whose radial velocity is measured.) In Fig. 6.15 we show the errors that result if we assume unrealistically small mass function errors of 10^{-5} $M_{\odot}$, as well as a more realistic fractional error of 20%. The three detached systems that can be measured with reasonable precision have apparent V magnitudes of between 15 and 16, so a fairly precise mass function measurement might not be out of the question (though one still will have to worry about K-corrections). The RLOF system has an apparent V magnitude of $\sim$ 22. (Its faintness is due to its being more than 4 times as far away as the detached systems.) However, if we consider the detached systems in the LISA + GAIA case, we can measure their masses with considerably improved accuracies (between 12% and 20%, assuming realistic GAIA errors). (N.B.: These systems do not appear in the LISA + GAIA plots, since the LISA + mass function case was studied using a different realization of the galactic population than the LISA + GAIA case, so we could make different cuts on the distribution.)

In the LISA + GAIA + mass function case, we can measure a large number of systems with good accuracy, assuming a constant fractional error of 20% in the mass function measurement (as is reasonable, even for relatively short-period systems; see the discussion in Sec. 6.5.3), and taking the same realistic GAIA errors as above. The histograms of errors are given in Figs. 6.16, 6.17, 6.18, and 6.19. For reasons of computational speed, we only simulated $\sim$ 55% of the RLOF systems for these plots. Also, none of these plots were made using the RAA, though that will not lead to significant differences, since the shortest period considered is $\sim$ 180 s, and most are considerably longer. We also show the dependence of the errors of the mass measurement on the system's distance, period, and individual masses in Figs. 6.20, 6.21, 6.22, 6.23, 6.24, and 6.25 for the detached systems. The sudden increase in binaries at periods

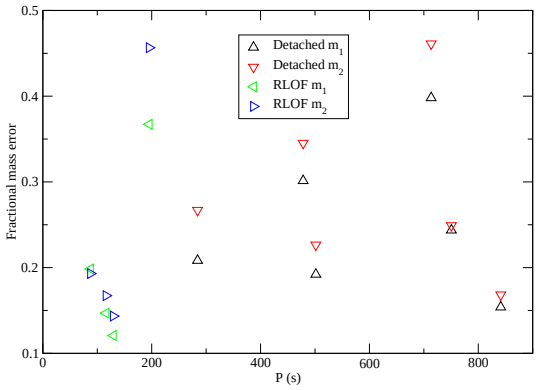

Fig. 6.11. In the LISA + GAIA case, the fractional mass errors vs. the system's orbital period for the systems in our population model for which we can measure at least one of the masses with a fractional accuracy of better than 0.4.

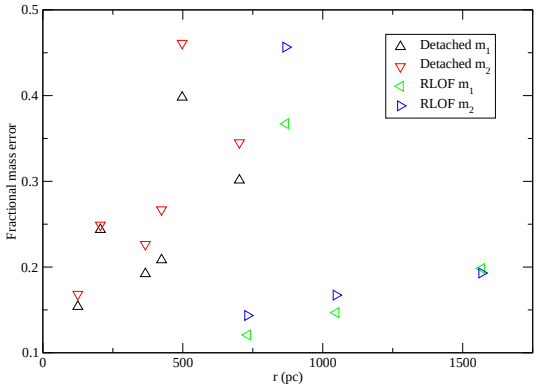

Fig. 6.12. In the LISA + GAIA case, the fractional mass errors vs. the system's distance for the systems in our population model for which we can measure at least one of the masses with a fractional accuracy of better than 0.4.

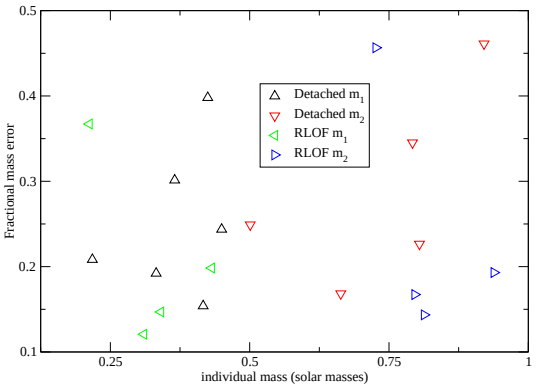

Fig. 6.13. In the LISA + GAIA case, the fractional mass errors vs. the individual masses for the systems in our population model for which we can measure at least one of the masses with a fractional accuracy of better than 0.4.

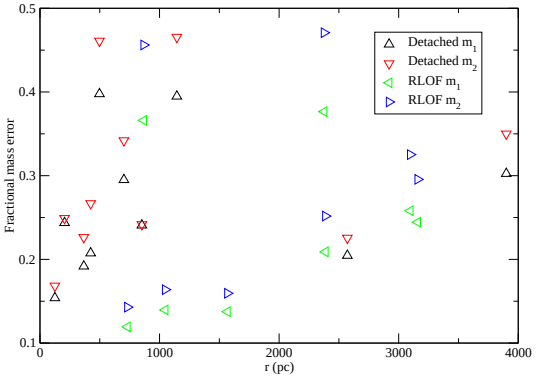

Fig. 6.14. In the LISA + distance measurement case, the fractional mass errors vs. the system's distance for the systems in our population model for which we can measure at least one of the masses with a fractional accuracy of better than 0.4, assuming an unrealistically small, constant fractional error of 10^{-5} in the distance measurement.

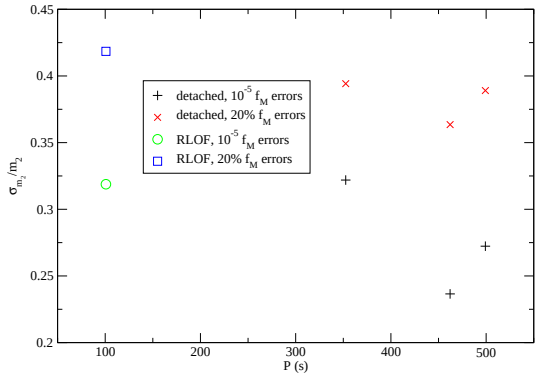

Fig. 6.15. In the LISA + mass function case, the fractional errors in the larger mass vs. the system's period for the systems in our population model for which we can make the measurement with a fractional accuracy of better than 0.4. We have plotted these with an unrealistic mass function error of $10^{-5}\,M_{\odot}$, as well as a more realistic 20% fractional error.

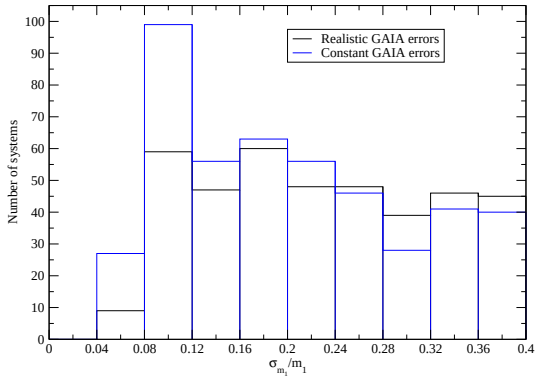

Fig. 6.16. A histogram of the fractional errors in the determination of m_1 in the LISA + GAIA + mass function case for the detached systems in our population model.

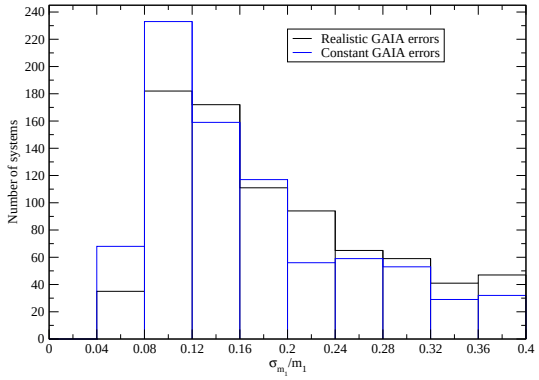

Fig. 6.17. A histogram of the fractional errors in the determination of m_2 in the LISA + GAIA + mass function case for the detached systems in our population model.

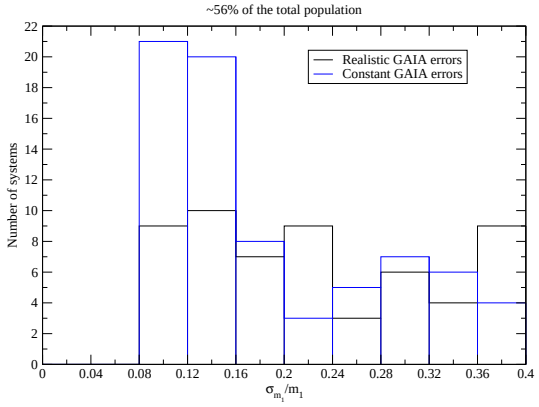

Fig. 6.18. A histogram of the fractional errors in the determination of m_1 in the LISA + GAIA + mass function case for the RLOF systems in our population model.

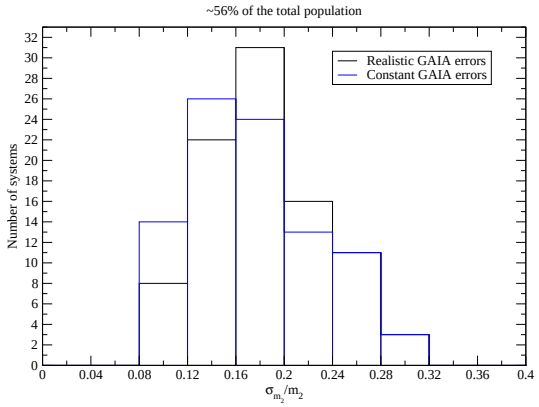

Fig. 6.19. A histogram of the fractional errors in the determination of m_2 in the LISA + GAIA + mass function case for the RLOF systems in our population model.

of $\gtrsim 1750$ s is due to a step in the period distribution (see Fig. 2 in [320]); the cutoff for periods beyond 2732 s was put in by hand. Future work will use a smooth period distribution and include more low-frequency systems.

6.7 Discussion

Since we anticipate that LISA will discover the vast majority of the binaries for which these measurements will be applicable, we should consider LISA's ability to localize the binaries, thus allowing for an electromagnetic detection. (Webbink [325] discusses some of the specifics of how these detections could take place.) In the LISA + GAIA case, LISA will be able to localize the binaries very well [within an area of about a few square arcminutes or less, using the rough fit to the results of Cutler [366] given in Eq. (10) of Webbink [325]], since these are high-frequency systems, observed with high SNRs (hundreds or larger).[9] In the LISA + GAIA + mass function case, the SNRs are not uniformly so high (most are in the tens or smaller), and the frequencies are generally significantly smaller, so most systems will only be localized to within hundreds of square degrees. However, the systems which we are guaranteed to be able to resolve will have SNRs in the tens or greater, and these systems have proportionally better localizations (the area of the error ellipse goes as $1/\mathrm{SNR}^2$), on the order of tens of square degrees or better.

Since we consider many longer-period systems in the LISA + GAIA + mass function case, we wish to allay any possible concerns about the confusion noise. We thus note that the confusion noise is primarily due to low-SNR systems—LISA will be able to resolve most of the high-SNR systems, particularly those with SNRs of a few tens or more (see, e.g., Crowder and Cornish [114]), and most of the systems we can measure well in the LISA + GAIA + mass

[9] We do not need to include a correction to account for only assuming that LISA has two arms working: As Cutler [366] notes, for monochromatic sources, the additional arms aid LISA's angular resolution almost solely by increasing the SNR.

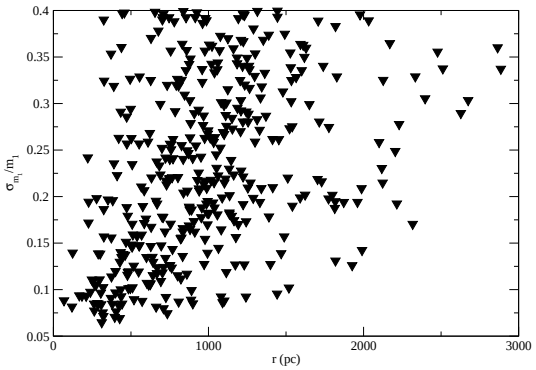

Fig. 6.20. The fractional errors in the determination of m_1 vs. distance in the LISA + GAIA + mass function case for the detached systems in our population model.

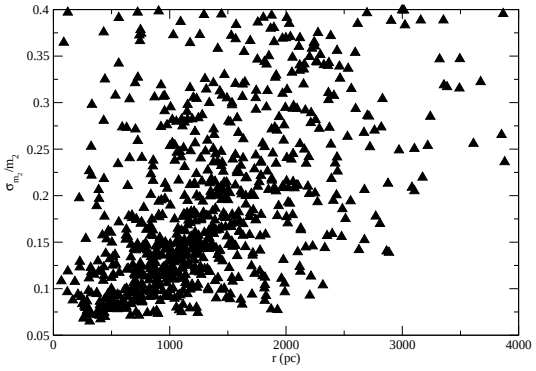

Fig. 6.21. The fractional errors in the determination of m_2 vs. distance in the LISA + GAIA + mass function case for the detached systems in our population model.

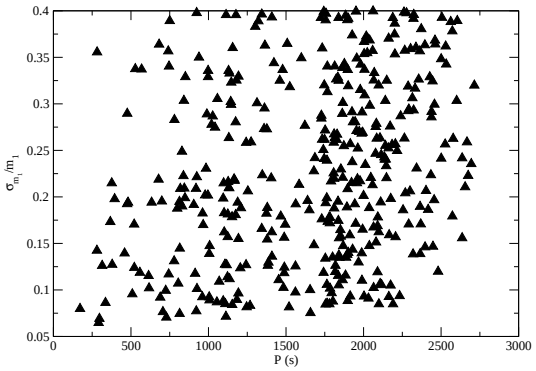

Fig. 6.22. The fractional errors in the determination of m_1 vs. period in the LISA + GAIA + mass function case for the detached systems in our population model.

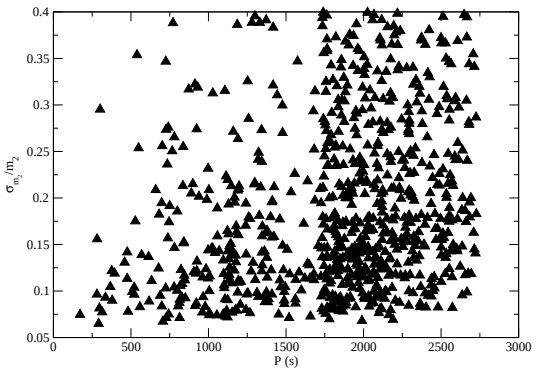

Fig. 6.23. The fractional errors in the determination of m_2 vs. period in the LISA + GAIA + mass function case for the detached systems in our population model.

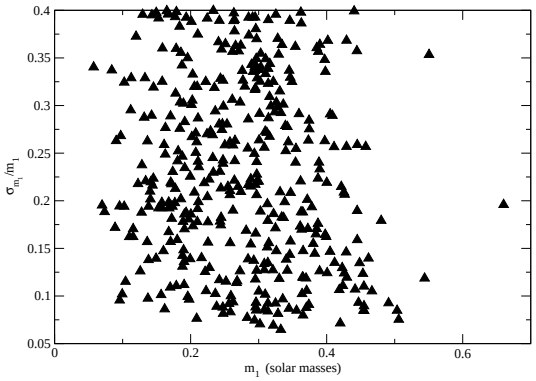

Fig. 6.24. The fractional errors in the determination of m_1 vs. m_1 in the LISA + GAIA + mass function case for the detached systems in our population model.

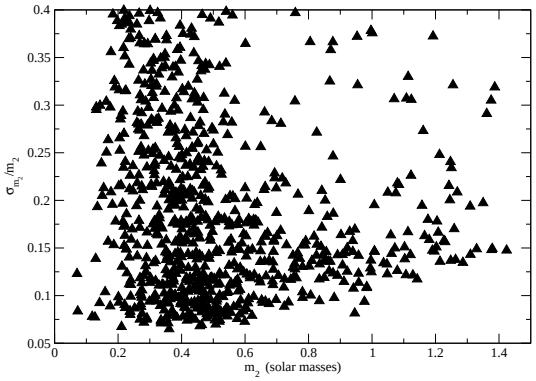

Fig. 6.25. The fractional errors in the determination of m_2 vs. m_2 in the LISA + GAIA + mass function case for the detached systems in our population model.

function case are detected with such SNRs: See the plots of SNR versus fractional error in m_2 in Figs. 6.26 and 6.27 and the associated histograms in Figs. 6.28 and 6.29. (N.B.: These SNRs were calculated using the low-frequency approximation to LISA's response, for computational ease. However, since none of the periods considered are too short, this leads to errors of $\lesssim 10\%$ in the computed SNRs.)

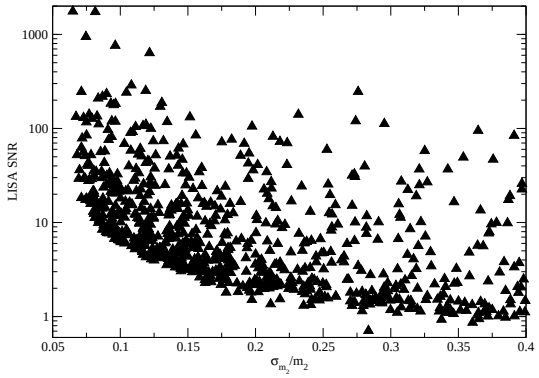

Fig. 6.26. LISA's SNR versus the fractional error in m_2 for the LISA + GAIA + mass function case and the detached systems in our population model.

We also note that the one obtains significantly smaller errors (by factors of ~ 2 to ~ 5) for the systems we can measure well in the LISA + GAIA case if one considers observing them in the LISA + GAIA + mass function case. However, obtaining the fiducial 20% mass function errors for these systems' generally short periods would likely be difficult (though some of the techniques discussed by Webbink [325] may be relevant).

It is also useful to consider the size of the chirp in the detached systems for which we can measure the masses to good accuracy in the LISA + GAIA case (neglecting finite size effects), to determine how many of them would have a large enough chirp that LISA could measure it in a year (and thus make the electromagnetic component of the observations superfluous, in principle; in practice, including the electromagnetic observations will always improve the accuracy, even discounting the difficulty of determining whether a system is detached based solely on gravitational wave observations). (We do not consider the chirp of the RLOF systems, since it will be dominated by mass transfer effects, and thus will not directly encode the system's chirp mass.) Only one of the six detached systems shown in Fig. 6.11 has a change in frequency over a year that is larger than one of LISA's one year frequency bins, and there it shifts by less than 2 bins (considering the lowest order radiation at twice the orbital frequency). Of course, if we monitor the system's frequency evolution electromagnetically, as we assume to be the case for the measurement we consider, then we are able to measure smaller changes in its frequency; see the discussion in Sec. 6.4.4. However, we have not considered adding this information into our analysis in the current discussion.

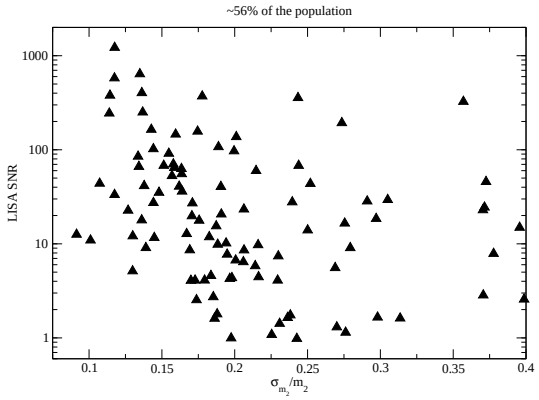

Fig. 6.27. LISA's SNR versus the fractional error in m_2 for the LISA + GAIA + mass function case and the RLOF systems in our population model.

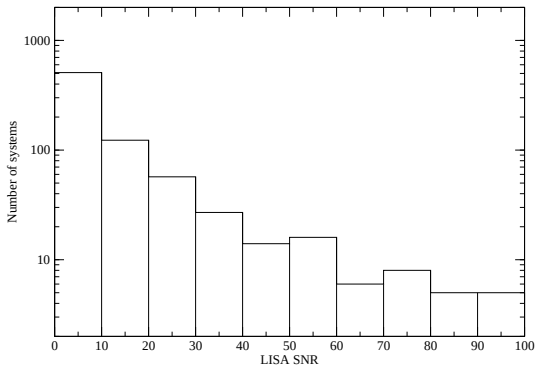

Fig. 6.28. A histogram of LISA's SNR for SNRs between 0 and 100 for the detached systems in our population model for which $\sigma_{m_2}/m_2 < 0.4$ in the LISA + GAIA + mass function case.

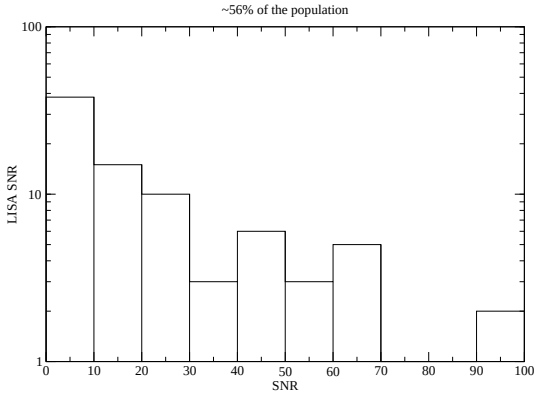

Fig. 6.29. A histogram of LISA's SNR for SNRs between 0 and 100 for the RLOF systems in our population model for which $\sigma_{m_2}/m_2 < 0.4$ in the LISA + GAIA + mass function case.

Finally, we consider the finite size contributions to the amplitude of the gravitational radiation from these binaries. While white dwarfs are not truly compact objects (with radii $\gtrsim 10^3$ times their Schwarzschild radii), finite size contributions to the amplitudes of the gravitational radiation from white dwarf binaries are only significant for the higher harmonics for the binaries whose masses we can measure to good precision in the LISA + GAIA case. And even then they are at most a $\sim$ 5% correction to the amplitude of the radiation at the binary's orbital frequency and a $\sim$ 1% correction to the amplitude of the radiation at thrice the binary's orbital frequency. (There are, of course, also corrections to the amplitude of the radiation at twice the orbital frequency, but these turn out to be much less than 1% for the systems whose masses we can measure well in the LISA + GAIA case. There would also be corrections to the point mass frequency evolution, but we do not consider these here, since they would be the largest for RLOF systems, where they would be completely dominated by the effects of mass transfer. However, these corrections could be calculated quite straightforwardly following [367, 368].) See Appendix F for the expressions used to reach these conclusions. (Note that these expressions assume corotation, which is generally taken to be the case for compact binaries. However, Willems, Deloye, and Kalogera [369] found that the corotation timescale is significantly longer than the gravitational wave inspiral timescale for detached binaries in their model. If the system is not corotating, then the finite size effects will likely be smaller, since they are dominated by the stars' corotation-induced spins. However, they could be larger if one of the white dwarfs is an asynchronous rapid rotator, as is the white dwarf in HD 49798/RX J0648.0-4418 [370]. We have also neglected any contributions from possible accretion discs—we save considering these for future work.)

We also note that three of the four RLOF systems in our population model whose masses we can measure with good accuracy (i.e., at least one with a better fractional accuracy than 0.4) in the LISA + GAIA case are eclipsing. We determined this using the inclinations assigned to these systems in the population model and the Eggleton fit for the mass-radius relationship of zero-temperature white dwarfs [quoted in, e.g., Eq. (12) in [341]]. (However, one of the systems

only has eclipses of very shallow amplitude.) But none of the detached systems we can measure well in the LISA + GAIA case are eclipsing, by this criterion.

In the LISA + GAIA + mass function case, there are many more eclipsing systems, even detached ones: 174 ($\sim$ 20% of the detached systems whose masses we can measure with good accuracy in this case), of which 25 experience total eclipses. There are, fractionally, even more RLOF systems whose masses we can measure with good accuracy in this case that are eclipsing than detached systems, viz., 43 ($\sim$ 40% of the well-measured population), of which 17 experience total eclipses. However, even accounting for the fact that we only simulated $\sim$ 56% of the total RLOF population in this case, the total number of detached eclipsing binaries is $\sim$ twice as large (though the number of totally eclipsing binaries is comparable, with the correction for the simulation size). (It would be useful to investigate the amplitudes of brightness variation expected of the population due to ellipsoidal variability, following Morris and Naftilan [333], but we leave this for future work.)

It is also interesting to see how many potential Type Ia supernova progenitors (i.e., systems with total masses greater than the Chandrasekhar mass) there are in the sample. None of the systems in our population model whose masses we can measure well in the LISA + GAIA case have such large masses. However, in the LISA + GAIA + mass function case, there are 32 such systems (all of which are detached, as would probably be expected).

6.8 Conclusions

We have seen that one can combine LISA measurements of the gravitational radiation from a white dwarf binary with electromagnetic measurements to obtain the individual masses of the stars in the binary. The three possible measurements are LISA + GAIA [i.e., gravitational waves (with higher harmonics) + a distance measurement (from parallax)]; LISA + mass function [gravitational waves (with higher harmonics) + a mass function measurement (from spectroscopy)]; and LISA + GAIA + mass function [gravitational waves (just the lowest harmonic needed, though including the higher harmonics will slightly increase the measurement accuracies) + distance + mass function]. We have evaluated the accuracies with which these measurements could be made, using the Fisher matrix (including the anticipated errors in the electromagnetic observations in our Fisher matrix analysis), and a rough population model.

We found, in particular, that if one combines LISA measurements with GAIA measurements of parallax, then one is able to measure at least one of the masses of 10 systems (6 detached, 4 RLOF) in our population model with fractional accuracies of 40% or better (see, e.g., Fig. 6.11). Half of these (including all the RLOF systems) are high-frequency systems (with periods of $\lesssim$ 300 s), for which it would likely be difficult to obtain the masses any other way. We find that the LISA + mass function case is likely not worth pursuing, in practice: Even assuming negligible mass function errors, one is only able to measure one (and *only* one) of the individual masses to better than 40% for four systems in our population model. Moreover, all four of these systems have short enough periods that even obtaining a mass function measurement with the fiducial 20% errors would likely be difficult, though the larger mass of the three detached systems can still be measured with an accuracy of better than 40% with such errors. (Additionally, while one obtains the distance in this case, in principle, it is not measured accurately enough for the systems in our population model to make this measurement worthwhile, in practice.) In the

LISA + GAIA + mass function case, one can measure at least one of the masses with an accuracy of tens of percent for over a hundred binaries, assuming 20% errors in the mass function; see, e.g., Fig. 6.17.

In all of these cases, we assume that LISA will discover the vast majority of the binaries for which these measurement will be made, particularly in the LISA + GAIA case, for which accurate measurements cannot be made for any of the known verification binaries. Of course, there are active campaigns to detect more white dwarf binaries before LISA flies (e.g., a search by Levitan *et al.* with the Palomar Transient Factory [371], Kilic *et al.*'s ELM program to look for companions of extremely low-mass white dwarfs [334, 335, 372, 373], the Rapid Temporal Survey [374], and the Supernova Progenitor Survey [375]), but they will likely have the same general bias towards longer-period systems as the searches that have found the 52 systems we know now. In the LISA + GAIA case, all the binaries for which mass measurements can be made accurately will have high LISA SNRs, leading to good sky localization (on the order of a few square arcminutes), making it relatively easy to search electromagnetically for these systems, using the known period from LISA; see [325] for further discussion. In the LISA + GAIA + mass function case, we can make mass measurements of many more systems with good accuracy, though most of these systems are detected with far smaller SNRs than in the LISA + GAIA case, and thus are poorly localized. However, there are still hundreds of systems that are detected at SNRs of tens or greater (see Fig. 6.28), and thus have localizations on the order of tens of square degrees or better, allowing them to be detected electromagnetically without too great an effort. Additionally, there will likely be systems that are discovered electromagnetically for which this measurement will be able to be made with good accuracy, since one can measure the masses of ES Cet (one of LISA's currently known verification binaries; see [113]) to good accuracy with this method, assuming its fiducial parameters (and a reasonably accurate mass function measurement); see Fig. 6.10.

We have not considered the case where LISA measures the binary's masses on its own. This is possible, in principle, for the systems for which LISA measures a clean chirp, though it is unclear whether there will be any systems for which the measurement will be able to be made, in practice, particularly if LISA is only able to observe for a year or so. Not only does this measurement require LISA to be able to measure the system's frequency evolution, so it is only applicable to the short-period systems which have significant frequency evolution, but it requires some way of determining whether the chirp is clean. The surest way to accomplish this is to measure the system's braking index—see, e.g., [324]—though this is difficult, as it involves the second derivative of the frequency. However, since we are considering measuring the masses, one could invoke some modeling of the system (primarily a mass-radius relationship) and determine the probability that the system is detached, based on the observation, though this would not be a particularly clean measurement. We leave a more detailed analysis of this case for future work.

Other future work on this measurement will likely include considering a much more refined population model (as in [115, 116, 117]). This work might also use a Monte Carlo treatment of the uncertainties in the measurement, since the errors are not very small, which suggests that the Fisher matrix predictions may not be a good indication of the true errors. (One would at least want to make a semianalytic assessment of the reliability of the Fisher matrix predictions following [376].) Finally, one would likely wish to improve the models for the systems' apparent magnitude and the rough estimates of the mass function error.

In general, we have made pessimistic assumptions about LISA's abilities, since we assumed its minimal mission. If we consider the optimistic case, where it observes for 5 years with all three links working, then the uncertainties would be $2\sqrt{5} \simeq 4$ times smaller. Looking further into the future, this measurement can be made by some of the other low-frequency gravitational wave detectors that have been proposed. In particular, DECIGO (see, e.g., Kawamura *et al.* [12]) will be able to make significant improvements to these measurements, particularly for high-frequency systems (periods of $\lesssim 200$ s). ASTROD [11] would be able to improve upon the measurements of low-frequency systems (periods of $\gtrsim 1000$ s); these would mostly be made in the ASTROD + GAIA + mass function case.

We have seen that finite size effects in the amplitude are not important for these observations, for the systems in our population model. However, they are large enough that DECIGO will likely be able to measure them for some realistic systems (particularly if these systems are corotating), based on the predicted noise curve given by Yagi and Tanaka [377] (which is more pessimistic than that given in Kawamura *et al.* [12]), allowing us to directly probe the internal structure of the white dwarfs in a binary. (LISA would be able to make this measurement if it observes a nearby high-frequency binary, of course, particularly in the optimistic case with a five year mission with all three arms working.) We leave a careful consideration of the accuracy with which this measurement can be made—and the precise properties of white dwarfs that can be inferred from it—to future studies. However, we note that one can detect some finite size effects even without knowing the system's distance, since they lead to different amplitudes for the higher harmonics. We also note that very high-frequency binaries (orbital periods of around half a minute) would be allow DECIGO to make highly precise measurements of many finite size effects, even without assuming corotation. Such binaries are rather extreme cases [since they will be tens of years from coalescence, and have to be fairly massive, so that they did not coalesce sooner], but would be bright enough that one would be able to make this measurement out to several kpc.

While direct measurements of finite size effects offer all sorts of possibilities for interesting white dwarf science (in particular, checking models for the internal structure and corotation), just measuring the individual masses of a large sample of white dwarf binaries is interesting enough, astrophysically. In particular, it would allow one to place constraints on population synthesis models. Additionally, this measurement gives the system's total mass, and thus lets one identify potential Type Ia supernova progenitors, as suggested by Webbink [325]. (However, identifying the potential progenitors that will coalesce soon will likely be a task for LISA alone, as they are likely all far enough away and sufficiently obscured that they would not be observed by GAIA, or be able to have their parallax determined any other way. Nevertheless, if they are indeed close to coalescence, then they will be bright sources for LISA, so it will have a good chance of observing their frequency evolution, and thus obtaining their distance itself.)

Acknowledgments

We thank Chris Belczynski, Matt Benacquista, Tanja Hinderer, Richard O'Shaughnessy, Ashley Ruiter, Robin Stebbins, Justin Vines, and Richard Wade for valuable conversations. NKJ-M acknowledges the support of NSF award PHY-0855589; LSF acknowledges the support of NSF award PHY-0653462.

Appendix A

Comparing Cook-Scheel and PN harmonic coordinates

In the quasi-Cartesian form of Cook-Scheel coordinates [172], the Schwarzschild metric is

$$\begin{aligned} g_{00}^{\mathrm{CS}} &= -\frac{R-M}{R+M}, & g_{0k}^{\mathrm{CS}} &= \frac{4M^2}{(R+M)^2}\frac{X_k}{R}, \\ g_{kl}^{\mathrm{CS}} &= \left(1+\frac{M}{R}\right)^2\delta_{kl} + \frac{M^2}{R^2}\frac{R-M}{R+M}\left[1+\frac{4MR}{(R+M)^2}\right]\frac{X_kX_l}{R^2}. \end{aligned} \tag{A.1}$$

[The transformation from Schwarzschild to Cook-Scheel coordinates is given in Eqs. (2.1).] For comparison, the Schwarzschild metric in PN harmonic coordinates is

$$g_{00}^{\mathrm{har}} = -\frac{R-M}{R+M}, \qquad g_{kl}^{\mathrm{har}} = \left(1+\frac{M}{R}\right)^2\left(\delta_{kl}-\frac{X_kX_l}{R^2}\right)+\frac{R+M}{R-M}\frac{X_kX_l}{R^2}, \tag{A.2}$$

where $g_{0k}^{\mathrm{har}} = 0$. (One obtains PN harmonic coordinates from Schwarzschild coordinates by $R = \mathcal{P} - M$, where $\mathcal{P}$ is the Schwarzschild radial coordinate. This is just the spatial part of the Schwarzschild-to-Cook-Scheel transformation.) Obviously, these coordinates have preserved the coordinate singularity of the Schwarzschild metric in Schwarzschild coordinates.

Note that the purely temporal component of the Cook-Scheel version has the same form as in PN harmonic coordinates, but all the other components are different. In particular, the Cook-Scheel version has nonzero spatiotemporal components as well as a slightly more involved nondiagonal piece of the spatial components. Explicitly, the differences between the PN harmonic and Cook-Scheel versions of the Schwarzschild metric components are

$$\begin{aligned} g_{00}^{\mathrm{CS}} - g_{00}^{\mathrm{har}} &= 0, \\ g_{0k}^{\mathrm{CS}} - g_{0k}^{\mathrm{har}} &= \frac{4M^2}{(R+M)^2}\frac{X_k}{R}, \\ g_{kl}^{\mathrm{CS}} - g_{kl}^{\mathrm{har}} &= -\frac{16M^4}{(R-M)(R+M)^3}\frac{X_kX_l}{R^2}. \end{aligned} \tag{A.3}$$

(Of course, this must be interpreted purely algebraically, since we are subtracting components in different coordinate systems.) The difference of the purely spatial components scales as $O([M/R]^4)$ as $M/R \to 0$, which is clearly higher order in the near zone. However, the difference of the spatiotemporal components is $O([M/R]^2)$, which is of the same order as the terms we do keep in the spatial metric. And, indeed, the first term in this expansion appears in our coordinate transformation—see Sec. 2.5.7.

Appendix B

Tidal fields

B.1 Comparison with Taylor and Poisson's results

To facilitate the comparison of our expressions for the tidal fields with those obtained by Taylor and Poisson [180], we collect the results of our matching here. These include the results of the fourth order octupole matching from the next subsection, and are all put together using Eqs. (2.13) to give explicit expressions for the tidal fields about hole 1:

$$\mathcal{E}_{kl}(t) = \frac{m_2}{b^3}\left\{\left[1 - \frac{1}{2}\frac{m_2}{b}\right][\delta_{kl} - 3\hat{x}_k\hat{x}_l] + \frac{1}{2}\frac{m}{b}[4\hat{x}_k\hat{x}_l - 5\hat{y}_k\hat{y}_l + \hat{z}_k\hat{z}_l] - 6\sqrt{\frac{m}{b}}\frac{t}{b}\hat{x}_{(k}\hat{y}_{l)} + O\left(\left[\frac{m_2}{b}\right]^2, \frac{t^2}{b^2}\right)\right\}, \tag{B.1a}$$

$$\mathcal{B}_{kl}(t) = \frac{m_2}{b^3}\sqrt{\frac{m_2}{b}}\left\{\left[-6\sqrt{\frac{m}{m_2}} + \frac{m_2}{b}\left\{5\left(\frac{m}{m_2}\right)^{3/2} + 7\sqrt{\frac{m}{m_2}} - 3\sqrt{\frac{m_2}{m}}\right\}\right]\hat{x}_{(k}\hat{z}_{l)} - 6\frac{m}{m_2}\sqrt{\frac{m_2}{b}}\frac{t}{b}\hat{y}_{(k}\hat{z}_{l)} + O\left(\left[\frac{m_2}{b}\right]^{3/2}, \frac{t^2}{b^2}\right)\right\}, \tag{B.1b}$$

$$\mathcal{E}_{klp}(t) = \frac{m_2}{b^4}\left\{\left[1 - 3\frac{m_2}{b}\right][15\hat{x}_k\hat{x}_l\hat{x}_p - 9\delta_{(kl}\hat{x}_{p)}] + 3\frac{m}{b}[5\hat{y}_{(k}\hat{y}_l\hat{x}_{p)} - 3\delta_{(kl}\hat{x}_{p)}] + O\left(\left[\frac{m_2}{b}\right]^2, \frac{t}{b}\right)\right\}, \tag{B.1c}$$

$$\mathcal{B}_{klp}(t) = \frac{9}{2}\frac{m_2}{b^4}\sqrt{\frac{m}{b}}\left\{5\hat{x}_{(k}\hat{x}_l\hat{z}_{p)} - \delta_{(kl}\hat{z}_{p)} + O\left(\left[\frac{m_2}{b}\right]^{1/2}, \frac{t}{b}\right)\right\}. \tag{B.1d}$$

Here, for the purposes of comparison with Taylor and Poisson's results, we have included the time dependent pieces we know in the quadrupole fields (the time dependence falls into the uncontrolled remainders in the octupole fields). These are ordinarily contained in $\dot{\mathcal{E}}_{kl}$ and $\dot{\mathcal{B}}_{kl}$, since we usually treat them as independent tidal fields. We have also written out all of the STF projections explicitly.

Taylor and Poisson give explicit expressions for the quadrupole tidal fields for a binary in a circular orbit in their Eqs. (1.10)–(1.14) [and with alternate notation in Eqs. (7.25)–(7.29)]. The parts of the quadrupole fields that Taylor and Poisson and we have both computed agree: These consist of the electric quadrupole, including its 1PN corrections; the time derivative of the electric quadrupole with no corrections; and the magnetic quadrupole with no corrections, all evaluated at $t = 0$. In fact, we can recover all of Taylor and Poisson's expressions for the tidal fields, including the full time dependence, if we evaluate our expressions for the tidal fields at $t = 0$ and then make the substitutions $\hat{x}_k \to \hat{x}_k \cos\omega t + \hat{y}_k \sin\omega t$ and $\hat{y}_k \to -\hat{x}_k \sin\omega t + \hat{y}_k \cos\omega t$. (This is, of course, only accurate for times much less than the radiation reaction time scale.)

Thus, even though we are not given the full time dependence directly from the matching, we can obtain it from our results, since they are true for any point in the orbit.

While we have computed certain higher-order contributions to the tidal fields that Taylor and Poisson did not, we cannot improve upon the formal accuracy of their 1PN result for the tidal heating: The 2PN correction to the expression for the tidal heating involves the unknown 2PN correction to the electric quadrupole.

We can also check the lowest-order pieces of all the tidal fields we found are the expected Newtonian ones: The Newtonian pieces of the tidal fields can be computed independently using Eqs. (5.45), (5.50), and (5.56) in [194], along with the obvious generalization of that reference's Eqs. (5.45) and (5.50) for the magnetic octupole, viz., $\mathcal{B}^{\rm Newt}_{klp} = -(3/8)\epsilon^{su}{}_{(k}\partial_{lp)s}\beta_u$, where β^k is given by Eq. (5.56b) of [194]. (To reproduce our results exactly, one needs to evaluate all of these expressions for the Newtonian parts of the tidal fields at $r_1 = 0$. Also, since these expressions for the Newtonian parts of the tidal fields are valid in the rest frame of hole 1, we need to use the relative velocity of the holes in calculating β^k.) Our expression for the 1PN correction to the magnetic quadrupole can be checked in the extreme mass ratio limit against that computed by Poisson in [378]: This result is given in an appropriate form for comparison in an unnumbered equation in Sec. VII E of Taylor and Poisson [180] and agrees with our computation.

B.2 1PN corrections to the fourth order octupole fields

Even though we cannot obtain all the inner zone octupole pieces at fourth and fifth orders without including the hexadecapole fields (since these will give octupole contributions to the nonpolynomial part at these orders), it *is* possible to match only the polynomial parts, and, in doing so, read off the 1PN corrections to the octupole tidal fields. As an illustration, we shall read off the 1PN correction to the electric octupole (along with the lowest-order piece of the time derivative of the magnetic quadrupole) by matching the octupole parts of the polynomial pieces at fourth order.

Except for the added algebraic complication of keeping higher-order multipole terms, this calculation proceeds precisely analogously to the fourth order calculation involving the quadrupole-and-lower multipoles of the polynomial part in Sec. 2.5.6. The only subtlety that we should mention is one that was already present in our original fourth order calculation. However, it was not a potential source of confusion there because we were computing both the polynomial and nonpolynomial parts at once. Now that we want to compute the polynomial part by itself, we need to bear in mind that two nonpolynomial pieces can produce a polynomial piece when multiplied together (e.g., $\tilde{r}$ is a nonpolynomial piece, but $\tilde{r}^2$ is a polynomial piece). Therefore, contributions to the near zone metric involving terms such as $n_1^{(k}n_{12}^{l)}/S^2$ will contain polynomial pieces, since n_1^k contains a factor of $1/\tilde{r}$, and $1/S^2$ contributes a factor of $\tilde{r}$. The final results are

$$(\bar{\mathcal{E}}_{kl})_2 = 0, \qquad (\bar{\mathcal{E}}_{klp})_2 = 15\frac{m}{m_2}\hat{y}_{\langle k}\hat{y}_l\hat{x}_{p\rangle} - 45\hat{x}_{\langle k}\hat{x}_l\hat{x}_{p\rangle}, \tag{B.2a}$$

$$(\bar{\mathcal{B}}_{kl})_1 = -6\frac{m}{m_2}\frac{1}{b}\hat{y}_{(k}\hat{z}_{l)}, \qquad (\bar{\mathcal{B}}_{klp})_1 = 0, \tag{B.2b}$$

with an accompanying polynomial piece of the coordinate transformation of

$$
\begin{aligned}
\left(X_\alpha^{\rm P}\right)_{4,3} = {}& \frac{\tilde{x}t}{b^3}\left\{\left[\frac{3}{2}\frac{m}{m_2}-2\right]\tilde{x}^2-\frac{m}{m_2}\frac{t^2}{6}+\left(\frac{3}{2}-\frac{9}{2}\frac{m}{m_2}\right)y^2+\frac{1}{2}\left(1-\frac{m}{m_2}\right)z^2\right\}\hat{t}_\alpha \\
&+\frac{1}{b^3}\left\{\left[\frac{m}{m_2}\left(\frac{t^2}{4}+\frac{\tilde{x}^2}{8}+y^2-\frac{3}{2}z^2\right)+y^2+z^2\right]\tilde{x}^2\right. \\
&\qquad \left.-\frac{m}{m_2}\left[\frac{t^4}{24}+\frac{y^4-z^4}{8}+\frac{(y^2+z^2)t^2}{4}\right]-\frac{(y^2+z^2)^2}{4}\right\}\hat{x}_\alpha \\
&+\frac{\tilde{x}y}{b^3}\left\{3\tilde{x}^2-\frac{9}{4}(y^2+z^2)+\frac{m}{m_2}\left[\frac{t^2}{2}-\frac{5}{2}\tilde{x}^2+\frac{9}{4}y^2+\frac{3}{4}z^2\right]\right\}\hat{y}_\alpha \\
&+\frac{\tilde{x}z}{b^3}\left\{3\tilde{x}^2-\frac{9}{4}(y^2+z^2)+\frac{m}{m_2}\left[\frac{t^2}{2}-\frac{\tilde{x}^2}{2}+\frac{7}{4}y^2+\frac{z^2}{4}\right]\right\}\hat{z}_\alpha .
\end{aligned}
\tag{B.3}
$$

Continuing on to fifth order to obtain the 1PN corrections to the magnetic octupole and time derivative of the electric quadrupole would be algebraically more complicated, but would otherwise proceed as above. At sixth order we are not so fortunate. If we tried to carry out even the quadrupole part of the sixth order polynomial matching, so as, e.g., to read off the 2PN correction to the electric quadrupole, we would be stymied by our lack of knowledge of $\left(X_\alpha^{\rm NP}\right)_{4,3}$: The $\tilde{r}$-times-a-polynomial-in-$\tilde{x}^\alpha$ pieces of $\left(X_\alpha^{\rm NP}\right)_{4,3}$ (which we expect to be present, as there have been such terms at all lower multipole orders) will contribute to $(h^{\rm P}_{\alpha\beta})_6$ via the $b\,(1/R)_4$ term.

Appendix C

Extended far zone metric

As discussed in Sec. 2.7, we were not able to use all of the PN near zone metric provided by Blanchet, Faye, and Ponsot [166] in our matching, but chose to include the higher-order terms [viz., the $O(v^6)$ and $O(v^7)$ terms in g_{00} and the $O(v^6)$ terms in g_{0k}] in an extension to our data. Here we describe how we obtain the matching additional terms in the far zone, following Pati and Will [177, 178], as in Sec. 2.6.

The requisite ingredients are nearly all readily available, and the ones that are not are almost all quite easily calculable: We need to know how to obtain the metric from the metric perturbation, and the expression Pati and Will give for this [in, e.g., Eqs. (4.2) of [177]] is of sufficiently high order for our purposes. We also need to know how to obtain the metric perturbation by differentiating multipoles: Here we need to add on to Pati and Will's result [reproduced in our Eq. (2.45)] by computing the $O(v^6)$ and $O(v^7)$ pieces of h^{00}, which are

$$\frac{1}{6}\partial_{klps}\left[\frac{\mathcal{I}^{klps}(u)}{r}\right] - \frac{1}{30}\partial_{klpsv}\left[\frac{\mathcal{I}^{klpsv}(u)}{r}\right], \tag{C.1}$$

and the $O(v^6)$ pieces of h^{0k}, which are

$$-\frac{1}{6}\partial_{lps}\left[\frac{\dot{\mathcal{I}}^{klps}(u)}{r}\right] + \frac{1}{2}\epsilon^{lkp}\partial_{psv}\left[\frac{\mathcal{J}^{lsv}(u)}{r}\right]. \tag{C.2}$$

These were obtained by substituting the expressions for M^Q (in terms of $\mathcal{I}^Q$ and $\mathcal{J}^Q$) from Pati and Will's Eqs. (4.7) into their Eq. (2.13) (both from [177]). (Recall that Q is a multi-index.)

In these expressions, we have omitted the nonlinear terms arising from the outer integral. While it would be, in principle, reasonably straightforward to compute them, following the procedure given by Pati and Will [177], the calculation would be involved enough that we do not attempt it here. In fact, if we change our order counting to the strict Pati-Will order counting [i.e., disregarding post-Minkowskian powers of G, so *all* powers of $1/r$ after the first are counted as $O(v)$], then we can ignore the unknown outer integral term that would contribute to g_{0k} at $O(v^6)$ if we used the order counting we used in the $O(v^4)$ version of the data (detailed in Sec 2.6): This term comes from the first term of Eq. (4.4b) in [177],[1] and looks, schematically, like $\mathcal{I}\mathcal{J}^k/r^3$, which is $O(v^7)$ with the strict Pati-Will order counting. This new order counting does not cause us to drop any of the outer integral terms that we were previously keeping, and with it, we have consistent $O(v^5)$ initial data in both the near and far zones.

[1] It is not present in the more specific expression Pati and Will give in Eq. (6.5b) of [177], because they have specialized that expression—using their "quick and dirty" rule—to look at contributions to the near zone, where this term does not contribute until a much higher order than they are considering.

However, even with the new order counting, there are still some unknown $O(v^7)$ outer integral terms in h^{00}, e.g., ones that look like $\mathcal{I}\ddot{\mathcal{I}}^{kl}\hat{n}^{<kl>}/r^2$ [see Eq. (6.5a) in [177]]. We shall simply neglect these terms here: Since we are adding the $O(v^7)$ terms to the initial data without regard to formal accuracy, it does not make sense to go to the trouble of calculating the $O(v^7)$ outer integral terms. This is particularly true since we are not even sure that we have all the terms we need in the 1PN correction to the mass octupole, as we shall discuss below.

Finally, we need expressions for all the source multipoles, to the appropriate PN order: We need $\mathcal{I}$ to 2PN, which we can obtain from the expression Blanchet gives for the system's binding energy in Eq. (170) of [19] (to which add the mass of the point particles to get $\mathcal{I}$). We also need $\mathcal{J}^k$, $\mathcal{I}^{kl}$, and $\mathcal{I}^{klp}$ to 1PN. The first of these can be obtained from the expression Kidder, Will, and Wiseman give for the system's angular momentum in Eq. (2.13b) of [379]. The second is given in Eq. (2.46c). However, the third has to be obtained from the three-index Epstein-Wagoner (EW) moment, $I^{klp}_{\rm EW}$, given in, e.g., Eq. (6.6b) in Will and Wiseman [179]: The result is $\mathcal{I}^{klp} = m_1 x_1^{klp}(1 + v_1^2/2 - m_2/2b) + (1 \leftrightarrow 2) + O(v^4)$, up to possible terms of the form $m_1^2 b\delta^{(kl}x_1^{p)} + (1 \leftrightarrow 2)$. The caveat is due to Will and Wiseman's omission of the terms in $I^{klp}_{\rm EW}$ that are pure traces in the first two indices (since they were just interested in computing the waveform, which is tracefree). Fortunately, we do not need to know the 1PN correction to $\mathcal{I}^{klp}$ to obtain consistent $O(v^5)$ data, though it is necessary to obtain the even higher-order terms we include in the purely temporal component of the far zone metric.

The given expression for $\mathcal{I}^{klp}$ comes from the relation $\dot{\mathcal{I}}^{klp} = 3I^{(klp)}_{\rm EW}$, which itself comes from taking a time derivative of the definition of $\mathcal{I}^{klp}$ [given in, e.g., Eq. (4.5b) in [177]], using the conservation law $\partial_\beta \tau^{\alpha\beta} = 0$ to write $\partial_0 \tau^{\alpha 0} = -\partial_k \tau^{\alpha k}$, and integrating the result by parts. The result is an expression that equals $3I^{(klp)}_{\rm EW}$ up to surface terms [see the definition of $I^{(klp)}_{\rm EW}$ in Eq. (2.19b) of [179]]. To obtain the given result for $\mathcal{I}^{klp}$, we merely antidifferentiate $3I^{(klp)}_{\rm EW}$ with respect to t. We have to worry about missing terms that are constant in time (up to radiative effects) when doing this, but it turns out that any such terms are zero for a circular orbit. This follows from considering all possible constant-in-time 1PN contributions to $\mathcal{I}^{klp}$ and finding that they vanish for a circular orbit because $\vec{A}$, the Laplace-Runge-Lenz vector, does. (The only other vectorial Newtonian constant of the motion is the binary's angular momentum, and that cannot contribute to $\mathcal{I}^{klp}$ at 1PN since it is odd under time reversal, while $\mathcal{I}^{klp}$ is even.)

Finally, we need $\mathcal{J}^{klp}$, $\mathcal{I}^{klps}$, and $\mathcal{I}^{klpsv}$ to Newtonian order: These can be obtained from Eq. (D1) in [178]. With all these ingredients, we can put together the far zone metric in the same way as we did in Sec. 2.6. We thus obtain its various components to the same order as we are keeping the near zone metric (with the above caveats about missing terms), viz., with uncontrolled remainders of $O(v^8)$ in the purely temporal component, $O(v^7)$ in the spatiotemporal components, and $O(v^6)$ in the purely spatial components.

Appendix D

Computation of the metrics

Here we detail exactly how the metrics are computed in the MAPLE scripts that were used (along with BAM) to compute the constraint violations and create the plots. The scripts themselves and the resulting C code (based on MAPLE's C output) are available online at [152].

D.1 Inner zone

To compute the inner zone metric around hole 1, we substitute the tidal fields given in Eq. (B.1) into the expression for Detweiler's perturbed Schwarzschild metric in Cook-Scheel coordinates that we give in Eqs. (2.2) and (2.3), taking $M = m_1$. We then transform using the coordinate transformation given in Sec. 2.5.7. The resulting metric thus includes terms through $O(v^5)$ all components, though, as discussed in Sec. 2.1.3.1, initial data derived from this metric will only have a formal accuracy of $O(v^4)$. We also do not perform any expansions after substituting the tidal fields and performing the coordinate transformation, so the final, transformed metric also contains various other higher-order-in-v terms. The inner zone metric around hole 2 is obtained by the same procedure, along with the transformations detailed at the beginning of Sec. 2.5.1.

We have considered three versions of the inner zone metric: The first version (contained in `04_NoOct`) comes directly from the matching performed in Sec. 2.5 and only contains the pieces that we were able to match onto the near zone metric while including all of the multipolar contributions at a given order [i.e., up to octupole order through $O(v^3)$ and then only up to quadrupole order through $O(v^5)$]. The second version (contained in `04`) also incorporates the results of the fourth-order octupole matching carried out in Appendix B.2—this includes the 1PN correction to the electric octupole, but only the polynomial part of the accompanying coordinate transformation. The third version (contained in `05` and `all`) adds on the time dependence of all the tidal fields (for a circular orbit), obtained in the manner described in Appendix B.1, though it still uses the same coordinate transformation as before. (We use the 1PN expression for ω when substituting for the unit vectors in obtaining the full time dependence. We leave off the known higher-order corrections to ω here since the expressions for the tidal fields we obtained by matching came from using the 1PN version of ω.)

We calculate the third version by substituting $T\dot{\mathcal{E}}_{kl} \to (T-t)\dot{\mathcal{E}}_{kl}(0)$ and similarly for $\dot{\mathcal{C}}_{klp}$ in Eq. (2.3) before substituting in the tidal fields (with full time dependence). These substitutions are necessary because the $T\dot{\mathcal{E}}_{kl}$ and $T\dot{\mathcal{C}}_{klp}$ terms in Eq. (2.3) come from the expansions of $\mathcal{E}_{kl}$ and $\mathcal{C}_{klp}$ (with full dependence on V, the ingoing Eddington-Finkelstein coordinate) about $V = 0$. We, however, are only including the full time dependence on t, the near zone time coordinate, in the tidal fields, due to our method of obtaining this dependence. These expressions will thus will only contain the $t\dot{\mathcal{E}}_{kl}$ and $t\dot{\mathcal{C}}_{klp}$ pieces (when expanded about $t = 0$), so we make the above substitutions to retain the linear T-dependence given by the matching while not including the

linear t-dependence twice. (We experimented with including the full time dependence of the tidal fields using T instead of t and found that the constraint violations increased.)

This method of computing the metric deliberately does *not* include the effects of the full time dependence on the spatial variation of the tidal fields' contributions to the metric [due to their dependence on V; see the discussion following Eq. (2.3)], since these would enter at the same order as the unknown time derivatives of the tidal fields (second derivatives of the quadrupole fields, and first derivatives of the octupole fields). Of course, the terms we are keeping are higher-order as well, but since they would enter with explicit factors of t in the multipole expansion, they would not be entangled with the explicit appearances of unknown time derivatives. (This follows because the Schwarzschild metric is time-independent in the coordinates we use.) What we have done is equivalent to repeating the matching we have performed at each value of (near zone time) t, up to orbital shrinkage effects, which are higher-order than the terms we are considering here. (We also have not attempted to include the full time dependence of the coordinate transformation for the reasons discussed in Sec. 2.7.)

D.2 Near zone

We compute the near zone metric by substituting the trajectories for the point particles (obtained in the manner discussed in Sec. 2.6.1) into Blanchet, Faye, and Ponsot's metric [given in Eqs. (7.2) of [166]], including the background resummation given in Sec. 2.8.1. Here there are, again, three versions of the metric, one giving $O(v^4)$ data, one $O(v^5)$ data, and one containing the complete 2.5PN metric.[1] N.B.: In order to perform background resummation on the purely temporal component of the complete 2.5PN metric, one needs to also subtract the $O([m_1/r_1]^3)$ portion of the expansion of the background, viz., $2m_1^3/r_1^3$, in Eq. (2.51). All these versions are constructed by truncating the metric components to the desired order before substituting in the trajectories. No expansions are performed after that substitution, since we do not want to drop the higher-order terms that we are keeping in the trajectories (discussed in Sec. 2.6.1) for conformity with the far zone metric. Due to an oversight, we did not include the 3PN corrections to the relative-to-COM relation in the $O(v^4)$ version of the near zone metric used to obtain the plots given in this paper, but have included them in the version available online at [152].

D.3 Far zone

The calculation of the far zone metric follows the DIRE approach, detailed in Sec. 2.6, differentiating multipole moments to obtain the metric. We have the same three versions of the far zone metric as for the near zone metric, and obtain them in the same manner: We expand to the desired order after performing all the substitutions except for ϕ, ω, and b (i.e., the contributions that vary due to secular radiation reaction effects and are discussed in Sec. 2.6.1). We also do not include any of the terms due to derivatives acting on b: These would give nonzero contributions, due to the separation's retarded time dependence from orbital shrinkage, but these terms are quite small, both formally and practically—unlike those due to the radiation reaction effects in the phase or undifferentiated separation—so we neglect them. [For instance, the

[1] Recall that one needs all the components through $O(v^4)$ [resp. $O(v^5)$] in addition to the $O(v^5)$ [resp. $O(v^6)$] terms in the spatiotemporal components in order to obtain $O(v^4)$ [resp. $O(v^5)$] data.

lowest-order contribution due to the nonzero time derivative of b in the $\partial_{kl}[\mathcal{I}^{kl}(u)/r]$ contribution to g_{00} is formally $O(v^9)$. It is also numerically small: The largest contribution has a magnitude of $\sim 10^{-7}$ when evaluated at the intersection of the x-axis and the inner boundary of the near-to-far transition for our equal-mass test binary, viz., $x \simeq 20m$—see Sec. 2.8.2. For comparison, the contribution of the uncorrected $(m_1/r)v_1^2 + (1 \leftrightarrow 2)$ term in that situation is $\sim 10^{-4}$.]

The $O(v^4)$ version uses a slightly different order counting than the $O(v^5)$ and full extended versions: As discussed in Sec. 2.6, we choose to keep the outer integral terms—here these are the terms that look like $(m/r)^2$—in the $O(v^4)$ data due to post-Minkowskian considerations, even though those terms are $O(v^5)$ if one interprets the Pati-Will order counting strictly. However, as mentioned in Appendix C, we do not know any of the higher-order outer integral terms, so we simply drop them [using the strict Pati-Will order counting to justify doing so in the $O(v^5)$ data].

Appendix E

Checks of lattice sums

We have checked that our code can reproduce all the relevant results for elastic constants presented in the literature, and detail these checks here: For a three-dimensional unscreened bcc lattice, we have checked that we can reproduce the results of Fuchs [226] (for c_{44} and $A_{\rm lat}$) and Ho [380] (for c_{11}), and also that we are in agreement with the very recent and much more precise calculation of all three elastic constants (to 8 significant digits) by Baiko [234]. For three-dimensional bcc lattice with screening, we have checked against the results from Horowitz and Hughto [302]. We have also checked that the surprisingly simple results we obtain in the unscreened two-dimensional hexagonal case agree with those obtained analytically using zeta function regularization.

We do not reproduce the Fuchs results exactly, though we agree to better than 0.25% for $A_{\rm lat}$ and 0.015% for c_{44}. Moreover, we agree with Baiko's results to all five significant figures to which we have calculated them (using a screening length of $10^{10}a$, where a is the lattice spacing). (Baiko claims agreement with Fuchs, and does not comment on the discrepancy.[1]) We agree to better than 0.015% with Ho's result; here the discrepancy could simply be due to rounding. (Baiko does not compare with Ho.)

Horowitz and Hughto computed $A_{\rm lat}$ (twice their b_{11})[2] for a screening length of $\lambda = 0.863a$. We agree to better than 1% for $A_{\rm lat}$ and 0.011% for c_{44}. The discrepancy for c_{44} could be due to rounding, though the discrepancy for $A_{\rm lat}$ is more likely to be indicative of a less than accurate result by Horowitz and Hughto, since they give caveats about that portion of their calculation (of $\sim 1\%$). (In particular, they are using a "brute force" summation over the direct lattice, which will not have nearly as rapid convergence as our Ewald method.) Specifically, our results are (using Fuchs's units of $Q^2/2a$, where Q is the charge on the blob) $A_{\rm lat} = 0.18047\ldots$ and $c_{44} = 0.69017\ldots$, while Horowitz and Hughto give 0.1787 and 0.6901, respectively. [We converted the Horowitz and Hughto elastic constants and screening length from their expressions in terms of the ion sphere radius $a_{\rm HH} = [3/(4\pi n)]^{1/3}$, where n is the number density of the blobs, into Fuchs units. To do this, we used Eq. (3.50) to express n in terms of a, the lattice spacing, using the volume of the Voronoi cell, which gives $a = (8\pi/3)^{1/3}a_{\rm HH}$ for $d = 3$.]

For the two-dimensional unscreened hexagonal lattice, we obtain what appear, numerically, to be simple fractions for the elastic constants (when expressed in Fuchs-type units of Q^2). Explicitly, we have $A_{\rm lat} = 1/2$, $c_{11} = -1/4$, and $c_{44} = 1/4$.

---

[1] This discrepancy with the Fuchs results should not be surprising, since Baiko and we are using modern computational technology, which facilitates summation of the many terms required to achieve convergence to quite a few decimal places.

[2] N.B.: Horowitz and Hughto's [302] expression for b_{11} in terms of c_{11} and c_{12} in their Eq. (13) is missing a factor of $1/2$, which can be seen to be present by starting from Eq. (7) in [262] and noting that $c_{31} = c_{12}$ for a cubic lattice.

We can show that these elastic constants indeed take the expected, extremely simple forms by calculating them analytically, using analytic continuation of an Epstein zeta function, as discussed in, e.g., [304, 381]. We first note that the 2-dimensional Coulomb potential is $-2Q \log r$,[3] so the sums that give the elastic constants will all have the formal (and divergent) form

$$\sum_{\vec{x}\in\Lambda_{\text{hex}}}{}' \alpha, \tag{E.1}$$

where α is some constant (and Λ_{hex} is the hexagonal lattice). To see this explicitly for c_{11}, we have (writing it in Fuchs-type units)

$$c_{11}^{\text{hex}} = -\sum_{\vec{x}\in\Lambda_{\text{hex}}}{}' \left(\frac{x_1^2}{\|\vec{x}\|^2} - 2\frac{x_1^4}{\|\vec{x}\|^4} \right) = \sum_{\vec{x}\in\Lambda_{\text{hex}}}{}' \frac{1}{4}, \tag{E.2}$$

where we have used the substitutions $x_1^2 \to \|\vec{x}\|^2/2$ and $x_1^4 \to (3/8)\|\vec{x}\|^4$ (valid when summing over a hexagonal lattice) to obtain the final expression. (One can obtain these substitutions by direct calculation, for which it is convenient to write the lattice points as elements of $\mathbb{C}$, so one can multiply a given point by sixth roots of unity to obtain all the other lattice points the same distance from the origin.)

Of course, this sum diverges, but, as indicated in Sec 3.4, we expect to obtain a regularized version from our Ewald sum procedure. Indeed, it seems reasonable (possibly even likely) that we should obtain the same result using Ewald sums as one obtains using zeta function regularization, since both methods rely at their root on the Jacobi imaginary transformation of theta functions: See, for instance, the discussion in Chap. 5, where we obtain the Poisson summation formula used in the Ewald method from the Jacobi transformation, and the discussion in Appendix B of [304], which uses the Jacobi transformation (referred to by its alternate name of the modular property of the theta function) to analytically continue the Epstein zeta function.

We thus begin by defining the Epstein zeta function ζ_Λ associated with an arbitrary lattice Λ. This is given [cf. the version for $\mathbb{Z}^d$ in Eq. (B1) of [304] and the more general version in Eq. (2.5) of [381]] by

$$\zeta_\Lambda(s) := \sum_{\vec{x}\in\Lambda}{}' \frac{1}{\|\vec{x}\|^{2s}} \tag{E.3}$$

for $\operatorname{Re} s > d/2$ (where d is the dimension of Λ), and analytically continued to $s \in \mathbb{C}$ (except for isolated poles) by Riemann's integral-splitting procedure and the Jacobi imaginary transformation, as in [304, 381]. We have $\zeta_\Lambda(0) = -1$ for any lattice [of positive dimension—cf. the third property given in Appendix B of [304] and Eq. (2.13) in [381]], so we obtain $c_{11} = -1/4$, in Fuchs-type units, as advertised above. We obtain the values for c_{44} and A given above by the same procedure, except that we also need to use the additional hexagonal lattice sum substitution $x_1^2 x_2^2 \to \|\vec{x}\|^4/8$.

[3] If one computes the $\lambda \to \infty$ limit of our dimensionally continued screened potential [Eq. (3.9)] for $d = 2$, one does not quite obtain this expression for the potential. However, the two expressions only differ by the addition of a term that is constant with respect to r, so one obtains the same results for the elastic constants.

Appendix F

Finite size effects in gravitational radiation from close, corotating binaries

While finite size effects are a classical consideration in the study of the (Newtonian) orbital evolution of close binaries—see, e.g., [382, 383][1]—finite size effects on the gravitational wave emission from these sources have been given comparatively little attention in the literature, apart from discussions of the effects of tidal disruption on the pre-merger signal in neutron star binaries (e.g., [385]). However, finite size effects were found to have potentially detectable effects on the phase evolution of double neutron star binaries during inspiral in analytical calculations by Flanagan and Hinderer [298, 386], later also seen in numerical calculations by Read *et al.* [387, 388]; earlier analytical studies include [367, 389, 390, 391]. The corrections to the amplitude from tidal effects have been particularly neglected, only being treated in two related papers that we have found, viz., Chau [343] and Clark [342]. In fact, Chau and Clark do not consider the amplitude itself, just the binary's luminosity. The luminosity (and, indeed, the phase evolution) is also considered by Vines, Flanagan, and Hinderer (VFH) [368], who compute the corrections to the mass quadrupole, mass octupole, and current quadrupole, including 1PN corrections to the mass quadrupole, using the formalism developed in Vines and Flanagan (VF) [392]. However, they do not consider the waveform's amplitude (and the finite size contributions from higher-order multipoles combine together in nonobvious ways in the amplitude). Moreover, VFH consider an irrotational binary, while we consider a corotating one. Taniguchi and Shibata [393] consider finite size contributions to the energy and angular momentum loss of a corotating binary, but specialize to the equal-mass case, so the mass octupole and current quadrupole contributions vanish identically.

Chau and Clark both consider the effects of a linear tidal deformation of one member of the system on the lowest-order (Newtonian mass quadrupole) contribution to the system's gravitational wave luminosity, describing the tidal deformation using the body's Love number. Chau's contribution was in calculating the correction in terms of the deformed member's unperturbed radius and second (electric) Love number (a.k.a. apsidal constant of motion), though his result is a factor of 2 too small, due to a dropped factor of 2 in the Love number expression for the star's quadrupole. Clark then placed upper bounds on the magnitude of the effect by using realistic values for the Love number and obtaining an upper bound on the ratio of the star's radius to the orbital separation, using the Roche model. Clark found that the contribution of finite size effects to the (mass quadrupole) luminosity is at most 0.4% for compact binaries in which one star is distorted.

[1] There is also some discussion relevant to LISA observations of eccentric white dwarf binaries in [120, 121], and a discussion of tidal resonances in circular white dwarf binaries, including their effects on the orbit, in [384]. Additionally, Mora and Will [367] discuss aspects of the Newtonian theory from a post-Newtonian viewpoint in their appendices.

Here we revisit Chau's derivation using modern notation, and extending it to the current quadrupole and mass octupole contributions, in addition to writing out the explicit effects on the amplitude of the waveform. We also include the contributions from (co)rotation. [For extended bodies, such as white dwarfs, rotational contributions are Newtonian effects, even though they are suppressed by factors of $1/c^2$ for truly compact objects—i.e., objects whose radii are a few times their Schwarzschild radius—like neutron stars and black holes, as is discussed in, e.g., [213].]

The use of the Love number expressions for the tidally induced multipoles is a limitation of this method, since they give the body's linear response to tidal fields, while we are primarily concerned here with estimating the effect for the systems in which one component has overflowed its Roche lobe or is close to doing so, since these are the systems for which the finite size effects will be the largest. One would thus prefer to use the Roche model, or better yet, a self-consistent numerical construction of the binary's mass distribution for a realistic equation of state, as in [394]. However, the Love number model allows for simple, intuitive expressions for the effects, and also places these estimates in the same line as other discussions of finite size effects in gravitational radiation present in the literature (e.g., [367, 368, 386]). [Some idea of the extent to which nonlinearities can affect the results can be obtained from the results in Sirotkin and Kim [395]. The effects of nonlinearities appear to be $\lesssim 30\%$, except for nearly equal-mass systems, where the largest contributions (to the higher multipoles) will be suppressed by symmetry.]

We follow the modern treatment of tidal Love numbers given in Binnington and Poisson [396] in our analysis. Their main concern is in a relativistic generalization of these results, which we shall not need (except to note that the relativistic corrections for white dwarfs are as small as one would expect, since white dwarfs are only weakly relativistic, with radii that are $\sim 10^3$ times their Schwarzschild radii). However, Binnington and Poisson give a very clear presentation of the problem, in notation eminently compatible with the standard post-Newtonian multipolar wave generation formalism. (There is complementary work on relativistic Love numbers in [397].)

We start with the Newtonian mass multipoles: From Sec. I B of Binnington and Poisson, the tidal contribution to the Newtonian mass 2^l-pole ($l \geq 2$) of a star of unperturbed radius R, and electric Love numbers k_l in an external gravitational potential $U_{\rm ext}$ is

$$I_L^{\rm tidal} = \frac{2}{(2l-1)!!} k_l \frac{R^{2l+1}}{G}\, \partial_L U_{\rm ext}|_{\text{center of star}} \,. \tag{F.1}$$

(L is a multi-index of length l, and we have restored the explicit appearance of Newton's constant, G.) Now, since $U_{\rm ext} = Gm_c/\|\vec{x}-\vec{b}\|$, where m_c is the mass of the star's companion, $\vec{b}$ is the vector from the star's center-of-mass to that of its companion (the magnitude of this vector—i.e., the distance between the stars' centers-of-mass—is denoted by b), and we have taken the center of the star to be at the origin, we have

$$\partial_L U_{\rm ext}|_{\text{center of star}} = G[(-1)^l m_c (2l-1)!!] \frac{b_{\langle L\rangle}}{b^{2l+1}} \tag{F.2}$$

[this can be obtained by, e.g., shifting the origin in Eq. (A 34) in [398]], where $b_L := b_{i_1} b_{i_2} \cdots b_{i_l}$, and angle brackets denote the symmetric trace-free (STF) projection (i.e., symmetrize and remove all traces in the indices enclosed in brackets; this is discussed in, e.g., Appendix A of [398]). We thus have

$$I_L^{\rm tidal} = 2(-1)^l k_l m_c \left(\frac{R}{b}\right)^{2l+1} b_{\langle L\rangle}. \tag{F.3}$$

The star also obtains a quadrupolar distortion due to rotation. This is given by [Eq. (B9e) in [367]]

$$I_{kl}^{\rm rot} = -\frac{2}{3}\frac{k_2 R^5}{G}\omega_{\langle kl\rangle} \tag{F.4}$$

in the same linear approximation as the tidal distortion. Here $\vec{\omega}$ is the star's angular velocity. If we take the star to be corotating, since this is generally expected to be the case for close white dwarf binaries [though see the discussion in [369, 384]; but note that there are white dwarfs in (wide) binaries with significantly shorter rotational periods than any of the orbital periods we consider—the fastest of these is HD 49798/RX J0648.0-4418, with a rotational period of 13.2 s [370]], then we have $\omega^2 = G(m_1 + m_2)/b^3$ from Kepler's third law [neglecting the finite size corrections to this; for these, see Eq. (B9d) in [367]]. This leads to $\|I_{kl}^{\rm rot}\|/\|I_{kl}^{\rm tidal}\| = (1/3)(1 + m_1/m_2)$, where $\|\cdot\|$ denotes the magnitude of its (tensor) argument (i.e., the coefficient that multiplies an STF tensor constructed from unit vectors), and we have considered the quadrupole moments of m_1. Note that this rotational quadrupole moment from corotation is *not* time-dependent (neglecting the orbit's gradual inspiral), while the tidal quadrupole moment is.

Now, these multipole moments are evaluated with the origin taken to be the distorted star's center-of-mass (COM). The displacement of the star's COM from the COM of the binary (which defines the origin of the coordinate system in which we evaluate the binary's multipoles) generates time-varying contributions to every binary mass multipole of order 2 and higher from the star's lower-order multipoles. (Indeed, this is how the individual stars' monopole moments generate time-varying mass multipole moments.) We shall show explicitly how the stars' tidally induced mass quadrupole moments generate time-varying contributions to the binary's mass octupole moment. (In fact, not only is the contribution to the binary's mass octupole moment from the stars' tidally induced mass quadrupoles much larger than the contribution from the stars' tidally-induced mass octupole moments, but it is even fractionally larger than the finite size correction to the binary's mass quadrupole from the same tidally-induced mass quadrupoles, due to a combinatorial factor.)

Let us first consider a general mass multipole of the binary. We start with the density distribution of one of the stars, ρ, with mass multipoles $I_L^{\rm COM}$ about its centre-of-mass. [Explicitly, we have $I_L^{\rm COM} := \int_{\mathbb{R}^3} \rho(\vec{x}') x'_{\langle L\rangle} d^3x'$ and $I_k^{\rm COM} = 0$, denoting coordinates with their origin at ρ's center-of-mass using primes—see, e.g., the lowest-order piece of Eq. (85) in Blanchet [19].] If we now consider the multipole moments of the same distribution about an origin with ρ's center-of-mass at $\vec{a}$, we have

$$I_L = \sum_{m=0}^{l} \binom{l}{m} \int_{\mathbb{R}^3} \rho(\vec{x}) a_{\langle M} x_{L-M\rangle} d^3x = \sum_{m=0}^{l} \binom{l}{m} a_{\langle M} I_{L-M\rangle}^{\rm COM}, \tag{F.5}$$

where $\binom{\cdot}{\cdot}$ denotes the binomial coefficient. [This expression for I_L agrees with the Newtonian part of Eq. (4.6) in VF [392] upon expressing the binomial coefficient in terms of factorials.]

If we now take the higher multipoles to come solely from tidal and rotational distortions, we can compute the time-dependent (on the orbital timescale) pieces of the mass quadrupole and octupole for the entire system using our previously obtained Love number expressions for the bodies' intrinsic mass multipole moments. (We only consider this time-dependent part, since it is all that contributes to the gravitational wave signal. We thus only have contributions from the rotational quadrupole in the total octupole and higher mass moments—we denote these rotational distortion contributions by a superscript "rot.") These multipole moments are thus

$$I_{kl} = \mu b_{\langle kl\rangle} I_{[2]}, \qquad I_{klp} = \mu \left(b_{\langle klp\rangle} I_{[3]} + b_{\langle k} e^{(z)}_{lp\rangle} b^2 I^{\rm rot}_{[3]} \right), \tag{F.6}$$

where

$$\begin{aligned} I_{[2]} &:= 1 + 2\left[\left(1 + \frac{m_2}{m_1}\right)(k_2)_1 \left(\frac{r_1}{b}\right)^5 + (1 \leftrightarrow 2) \right] \\ I_{[3]} &:= -\frac{\delta m}{m} + \left[6\frac{m_2}{m_1}(k_2)_1 \left(\frac{r_1}{b}\right)^5 - 2\left(1 + \frac{m_2}{m_1}\right)(k_3)_1 \left(\frac{r_1}{b}\right)^7 - (1 \leftrightarrow 2) \right] \\ I^{\rm rot}_{[3]} &:= -2\left(2 + \frac{m_1}{m_2} + \frac{m_2}{m_1}\right)(k_2)_1 \left(\frac{r_1}{b}\right)^5 - (1 \leftrightarrow 2). \end{aligned} \tag{F.7}$$

Here $e^{(z)}_k$ denotes the unit vector in the z-direction (which we take to be in the direction of the system's angular momentum), we denote the individual stars' Love numbers by subscripts outside of parentheses [e.g., $(k_2)_1$ denotes the $l = 2$ Love number of star 1], and "$\pm(1 \leftrightarrow 2)$" implies that we add [resp. subtract] the preceding parts of the expression (inside the brackets) to [resp. from] itself with the stars' indices swapped. For instance, $(m_2/m_1)\,(k_2)_1\,(r_1)^5 - (1 \leftrightarrow 2) = (m_2/m_1)\,(k_2)_1\,(r_1)^5 - (m_1/m_2)\,(k_2)_2\,(r_2)^5$. Additionally, we have used Kepler's third law—here we can neglect the finite size corrections to it, since they would lead to a second-order perturbation to the multipole moment. We thus see that Chau dropped a factor of 2 in his expression for the change to the quadrupole moment [Eq. (8) in [343]].

We can check these expressions for the contributions from the tidal distortions (i.e., neglecting the "rot" terms) against those given in Eqs. (3.4) and (3.5) of VFH [368], and find exact agreement. [We only consider the Newtonian contributions to the electric quadrupole in VFH's Eq. (3.4), since all our computations are purely Newtonian.] VFH's expressions are specialized to the case where only m_2 has a tidal distortion, so to compare with our expressions, we take $(k_A)_1 = 0$, or, equivalently, only consider the $(1 \leftrightarrow 2)$ portions. We also need to write VFH's ω in terms of the system's mass and separation, which we do using their Eq. (2.9).

The values for these Love numbers for (Newtonian) polytropic models are given in Table II of Brooker and Olle [399]. The density distributions of $n = 3/2$ and $n = 3$ polytropes bracket the density distributions of realistic white dwarfs, with $n = 3/2$ a good approximation for the large, low mass stars we are most interested in—see Fig. 4 in Chandrasekhar [400]. For $n = 3/2$, we have $k_2 \simeq 0.143$ and $k_3 \simeq 0.0528$, while for $n = 3$, we have $k_2 \simeq 0.0144$ and $k_3 \simeq 0.00370$. [Recent computations for a modern, detailed white-dwarf model in Valsecchi *et al.* [121] find that k_2 for low-mass ($\leq 0.3\,\mathrm{M}_\odot$) white dwarfs depends upon the star's age, but asymptotes to ~ 0.13 for stars around 10 Gyr old.]

We now turn to the finite size corrections to the Newtonian current multipoles, focusing on the current quadrupole: These corrections are much more complicated than those for the mass multipoles, and are more surprising, since we shall see that there exist time-dependent finite size corrections to the current multipoles even for a binary consisting of spherical stars. However, upon reflection, this is just a consequence of the well-known appearance of spin in the Newtonian current quadrupole, as in Eq. (3.6b) in Blanchet, Buonnano, and Faye [215], combined with our assumption of corotation. (Note that Blanchet *et al.* take the spin to be a post-Newtonian effect, since they only consider truly compact objects, whose radii are a few times their Schwarzschild radii, though the contribution is Newtonian for less compact objects; there is no factor of $1/c^2$ from the Schwarzschild radius in this case.)

Since the star is static in the corotating frame, in our case, its velocity field in the inertial frame (with the origin at the system's centre-of-mass) is then given by $\vec{v} = \vec{\omega} \times \vec{x}$, where $\vec{\omega}$ is the angular velocity of the binary. Now, the Newtonian current multipoles are given by

$$J_L := \int_{\mathbb{R}^3} \rho(\vec{x}) \epsilon_{ab\langle i_l} x_{L-1\rangle a} v_b d^3x. \tag{F.8}$$

[See, e.g., the lowest-order piece of Eq. (85) in Blanchet [19]; we have left off the STF projection on $x_{(L-1)a}$ that Blanchet gives, since it is already enforced by the Levi-Civita symbol.] We want to write this in terms of the binary's centre-of-mass (Newtonian) mass multipoles, $I_L^{\rm COM}$. To do so, we first note that $\epsilon_{abi_l} x_a v_b \to \vec{x} \times \vec{v} = \vec{\omega}\|\vec{x}\|^2 - \vec{x}(\vec{\omega} \cdot \vec{x})$. Thus, if we take ρ's centre-of-mass to be located at $\vec{a}$ (with $\vec{\omega} \cdot \vec{a} = 0$, for simplicity, since such translations in the plane of the orbit are the physically interesting case) and hence make the shift $\vec{x} \to \vec{x} + \vec{a}$ in the above integral, we obtain an integrand of (leaving off the ρ, for simplicity)

$$(\|\vec{x}\|^2 + 2\vec{a} \cdot \vec{x} + \|\vec{a}\|^2) \sum_{m=0}^{l-1} \binom{l-1}{m} \omega_{\langle i_l} a_M x_{L-M-1\rangle} - (\vec{\omega} \cdot \vec{x}) \sum_{m=0}^{l} \binom{l}{m} a_{\langle M} x_{L-M\rangle}. \tag{F.9}$$

We want all the appearances of x_P to be STF, so we use the identity (valid for an arbitrary C_M)

$$x_{k\langle L} C_{M\rangle} = \hat{x}_{k\langle L} C_{M\rangle} + \frac{l}{2l+1} \|\vec{x}\|^2 \delta_{k\langle i_l} x_{L-1} C_{M\rangle}. \tag{F.10}$$

Here $\hat{x}_{kL} \equiv x_{\langle kL\rangle}$. This expression can be obtained by applying the identity in Eq. (A 21a) from [398] to make an STF decomposition of x_{kL} and then noting that only the two terms shown are left after applying the STF projection over the L and M indices. We thus see that we need to consider the multipole moments of $\rho(\vec{x}')\|\vec{x}'\|^2$, in addition to those of $\rho(\vec{x}')$, so we define the radially weighted COM (Newtonian) mass multipoles

$$I_L^{(n)} := \int_{\mathbb{R}^3} \|\vec{x}'\|^n \rho(\vec{x}') x'_{\langle L\rangle} d^3x'. \tag{F.11}$$

(However, note that we only need these for $n \in \{0, 2\}$, and that for $n = 0$ they reduce to the standard Newtonian COM mass multipoles. Also note that $I^{(2)}$ is $3/2$ times the principal moment

of inertia of a spherical star.) We thus obtain

$$J_L = \sum_{m=0}^{l-1} \binom{l-1}{m} \Bigg[\omega_{\langle i_l} a_M I^{(2)}_{L-M-1\rangle} + 2\omega_{\langle i_l} a_M I^{(0)}_{L-M-1\rangle k} a_k + \frac{2(l-m-1)}{2l-2m-1} \omega_{\langle i_l} a_{M+1} I^{(2)}_{L-M-2\rangle} + \|\vec{a}\|^2 \omega_{\langle i_l} a_M I^{(0)}_{L-M-1\rangle} \Bigg] - \sum_{m=0}^{l} \binom{l}{m} \Bigg[a_{\langle M} I^{(0)}_{L-M\rangle k} \omega_k + \frac{l-m}{2l-2m+1} a_{\langle M} I^{(2)}_{L-M-1} \omega_{i_l\rangle} \Bigg]. \tag{F.12}$$

Specializing this to the quadrupole case (and noting that $I^{(0)}_k = 0$, since the $I^{(n)}_L$ are computed in the COM frame), we obtain

$$J_{kl} = \omega_{\langle k} a_{l\rangle} (\|\vec{a}\|^2 I^{(0)} + I^{(2)}) + \frac{3}{5} \omega_{\langle k} I^{(2)}_{l\rangle} + 2\omega_{\langle k} I^{(0)}_{lp\rangle} a_p - 2a_{\langle k} I^{(0)}_{lp\rangle} \omega_p - I^{(0)}_{klp} \omega_p. \tag{F.13}$$

If we specialize to a linear tidal distortion, then we have $I^{(2)}_k = 0$, by symmetry, though none of the other contributions vanish, even if we assume that $\vec{\omega} \cdot \vec{a} = 0$.

We now want to give the final expression for a binary, but before doing so, it is convenient to define a dimensionless quantity that encodes the effects of a spherical star's density distribution on $I^{(2)}$, viz.,

$$l^{(2)} := \frac{4\pi}{I^{(0)} R^2} \int_0^R \rho(r) r^4 dr, \tag{F.14}$$

so $I^{(2)} = l^{(2)} I^{(0)} R^2$. (Here R is the star's radius.) This means that the star's (dimensionless) radius of gyration is $\sqrt{(2/3) l^{(2)}} R$. [N.B.: Here, in keeping with the astronomical literature, we are using the term "radius of gyration" for the dimensionless quantity I_*/MR^2, where I_* is the star's principal moment of inertia—equal to $(2/3) I^{(2)}$ in the spherically symmetric case—and M is the star's mass; see, e.g., [401, 402, 394].] We have $l^{(2)} = 3/5 = 0.6$ for a uniform density star, $l^{(2)} \simeq 0.307$ for an $n = 3/2$ polytrope, and $l^{(2)} \simeq 0.113$ for an $n = 3$ polytrope. The values of $l^{(2)}$ for realistic white dwarf models (using the Salpeter [403] equation of state) as well as polytropic stars are given in Tables 1 and 3 in Andronov and Yavorskij [404]. [Andronov and Yavorskij's α is equal to $(2/3) l^{(2)}$ for spherically symmetric stars.] One finds that the value of $l^{(2)}$ for an $n = 3/2$ polytrope agrees with that from the Salpeter equation of state to better than $\sim 5\%$ for masses between ~ 0.05 and $\sim 0.5\,\mathrm{M}_\odot$. Even and Tohline [394] give radii of gyration for the Chandrasekhar [400] equation of state in their Table 2.

N.B.: The $I^{(n)}$ also enter into the post-Newtonian equations of motion of spherical bodies with finite size. Nordvedt [405] first showed that the moment of inertia (our $I^{(2)}$) does not affect the post-Newtonian N-body equations of motion for spherical bodies in general relativity at $O([v/c]^2)$, even though this quantity does indeed enter at this order in scalar-tensor gravity. Kopeikin and Vlasov [406] then showed that $I^{(4)}$ and higher moments enter into the $O([v/c]^2)$ equations of motion even in general relativity; see their Sec. 11.4. (Kopeikin and Vlasov give an impressionistic overview in [407].)

The final Love number expression for a corotating binary (thus with $\vec{\omega} \cdot \vec{b} = 0$) is therefore

$$J_{kl} = \mu b^2 \omega_{\langle k} b_{l\rangle} \left\{ -\frac{\delta m}{m} + \left[(l^{(2)})_1 \left(\frac{r_1}{b}\right)^2 + \frac{8}{3} \frac{m_2}{m_1} (k_2)_1 \left(\frac{r_1}{b}\right)^5 - \frac{4}{5} \frac{m_2}{m_1} (k_3)_1 \left(\frac{r_1}{b}\right)^7 - (1 \leftrightarrow 2) \right] \right\}. \tag{F.15}$$

Here we have used the identities (valid for $\vec{\omega}\cdot\vec{a}=0$) $\omega_{\langle k}a_{lp\rangle}a_p = (4/15)a^2\omega_{\langle k}a_{l\rangle}$ and $a_{\langle klp\rangle}\omega_p = -(2/5)a^2\omega_{\langle k}a_{l\rangle}$, both of which can be obtained by direct calculation, using the definition of the STF projection. We have also neglected the effects of the star's tidal and rotational distortion in expressing $I^{(2)}$ in terms of $l^{(2)}$.

We can check Eq. (F.13) by computing the finite size contributions to the system's current quadrupole using the formalism given in VF [392]; this also provides some intuition about the origins of the various terms appearing in our expression. If we use Eqs. (4.5a), (4.5b), and (B3) in VF, we obtain (in our notation)

$$J_{kl} = I^{(0)}\|\vec{a}\|^2 a_{\langle k}\omega_{l\rangle} + \frac{3}{2}S_{\langle k}a_{l\rangle} + \epsilon_{sp\langle k}I^{(0)}_{l\rangle s}\dot{a}_p + \frac{1}{2}\epsilon_{sp\langle k}\dot{I}^{(0)}_{l\rangle p}a_s + S_{kl}, \tag{F.16}$$

where overdots denote time derivatives and the S_L are the body's current multipole moments, defined (using the same expression as for J_L, except now using COM coordinates) by

$$S_L := \int_{\mathbb{R}^3}\rho(\vec{x}')\epsilon_{ab\langle i_l}x'_{L-1\rangle a}v_b d^3x', \tag{F.17}$$

where ρ is the body's density distribution, with the origin of coordinates taken to be the body's center-of-mass. In our case, where we have $\vec{v}=\vec{\omega}\times\vec{x}'$, this means that

$$\begin{aligned} S_k &= \int_{\mathbb{R}^3}\rho(\vec{x}')\left[\omega_k\|\vec{x}'\|^2 - x'_k(\vec{\omega}\cdot\vec{x}')\right]d^3x' \\ &= \int_{\mathbb{R}^3}\rho(\vec{x}')\left[\frac{2}{3}\omega_k\|\vec{x}'\|^2 - x'_{\langle kp\rangle}\omega_p\right]d^3x' \\ &= \frac{2}{3}\omega_k I^{(2)} - I^{(0)}_{kp}\omega_p \end{aligned} \tag{F.18}$$

and

$$\begin{aligned} S_{kl} &= \int_{\mathbb{R}^3}\rho(\vec{x}')[\omega_{\langle k}x_{l\rangle}\|\vec{x}'\|^2 - x'_{\langle kl\rangle}(\vec{\omega}\cdot\vec{x}')]d^3x' \\ &= \int_{\mathbb{R}^3}\rho(\vec{x}')\left[\frac{3}{5}\omega_{\langle k}x'_{l\rangle}\|\vec{x}'\|^2 - x'_{\langle klp\rangle}\omega_p\right]d^3x' \\ &= \frac{3}{5}\omega_{\langle k}I^{(2)}_{l\rangle} - I^{(0)}_{klp}\omega_p. \end{aligned} \tag{F.19}$$

[We thus see that the $I^{(2)}$ contribution comes from the body's orbit-induced (co)rotation, as would be expected, but that the body's angular momentum also contains a contribution from the body's intrinsic mass quadrupole moment. Additionally, the $I^{(2)}_k$ and $I^{(0)}_{klp}$ contributions come from the body's intrinsic current quadrupole moment. We can also check that the contribution from S_k in Eq. (F.16) agrees with that given in Eq. (3.6b) of [215], recalling that their definition of the spin vector includes a factor of c.]

Thus, the VF expression for J_{kl} [Eq. (F.16)] agrees with our expression [Eq. (F.13)] provided that

$$2\omega_{\langle k}I^{(0)}_{lp\rangle}a_p - 2a_{\langle k}I^{(0)}_{lp\rangle}\omega_p = \epsilon_{sp\langle k}I^{(0)}_{l\rangle s}\dot{a}_p + \frac{1}{2}\epsilon_{sp\langle k}\dot{I}^{(0)}_{l\rangle p}a_s - \frac{3}{2}\omega_p I^{(0)}_{p\langle k}a_{l\rangle}. \tag{F.20}$$

This is indeed the case for the two situations of interest, viz., a tidal quadrupole, with $I^{(0)}_{kl} = Ka_{\langle kl\rangle}$, and a rotationally induced quadrupole, with $I^{(0)}_{kl} = K_{\rm rot}\omega_{\langle kl\rangle}$, where K and $K_{\rm rot}$ are some constants. In the first case, both sides give $2K\|\vec{a}\|^2 a_{\langle k}\omega_{l\rangle}$, and in the second, both give $-2K_{\rm rot}\|\vec{\omega}\|^2\omega_{\langle k}a_{l\rangle}$. [Here we have assumed that $\vec{\omega}\cdot\vec{a} = 0$, so $\vec{\omega}\times\dot{\vec{a}} = -\|\vec{\omega}\|^2\vec{a}$. We have also noted that, e.g., $\omega_k a_{\langle kl\rangle} = -(1/3)\|\vec{a}\|^2\omega_l$.]

N.B.: Our Eq. (F.15) does not reduce the result in Eq. (3.6) of VFH [368] when specialized to the case they considered, where m_2 is the only deformable body and only its $l = 2$ Love number is nonzero. This is to be expected, since VFH assumed an irrotational binary (so that $S_k = 0$, in their formalism), while we assumed a corotating binary, which leads to a contribution from the induced quadrupole to S_k [as seen in Eq. (F.18)], in addition to contributions to the induced quadrupole itself from tidal flattening.

Additionally, while each star would have an intrinsic current quadrupole induced by its companion's so-called magnetic tidal field (see the discussion in [396, 397]), this is a purely relativistic effect, and thus should not appear in our purely Newtonian calculation. Moreover, the effect is quite small in our situation. (The $l = 2$ magnetic Love number is $\sim 10^{-4}$ for a compactness of $\sim 3\times10^{-3}$, which is slightly more compact than a cold maximum mass white dwarf—see Table VI in [396]. Moreover, the companion's magnetic tidal fields are suppressed by a factor of v/c compared with its electric tidal fields—see, e.g., the expressions in Appendix B and the discussion in [180]—and $v/c \lesssim 0.04$ for the binaries we consider.)

Writing out the explicit corrections to the amplitude of the radiation at the three frequencies, we have

$$
\begin{aligned}
h_+^{\rm finite,\Phi} &= \frac{2G^2m_1m_2\omega}{c^5r}\sin\theta\left[\frac{2}{3}(l^{(2)})_1\left(\frac{r_1}{b}\right)^2 + C_2\,(k_2)_1\left(\frac{r_1}{b}\right)^5 + C_3\,(k_3)_1\left(\frac{r_1}{b}\right)^7 - (1\leftrightarrow 2)\right],\\
h_\times^{\rm finite,\Phi} &= \frac{G^2m_1m_2\omega}{c^5r}\sin 2\theta\left[\frac{2}{3}(l^{(2)})_1\left(\frac{r_1}{b}\right)^2 - \left(\frac{2}{9}+\frac{1}{9}\frac{m_1}{m_2}-\frac{13}{6}\frac{m_2}{m_1}\right)(k_2)_1\left(\frac{r_1}{b}\right)^5\right.\\
&\qquad\left. + \left(\frac{1}{6}-\frac{11}{30}\frac{m_2}{m_1}\right)(k_3)_1\left(\frac{r_1}{b}\right)^7 - (1\leftrightarrow 2)\right],\\
h_{+,\times}^{\rm finite,2\Phi} &= 2\left[\left(1+\frac{m_2}{m_1}\right)(k_2)_1\left(\frac{r_1}{b}\right)^5 + (1\leftrightarrow 2)\right]h^{2\Phi}_{+,\times}\\
h_{+,\times}^{\rm finite,3\Phi} &= \left[6\frac{m_2}{m_1}(k_2)_1\left(\frac{r_1}{b}\right)^5 - 2\left(1+\frac{m_2}{m_1}\right)(k_3)_1\left(\frac{r_1}{b}\right)^7 - (1\leftrightarrow 2)\right]h^{3\Phi}_{+,\times},
\end{aligned}
\tag{F.21}
$$

where

$$
\begin{aligned}
C_2 &:= -\left(\frac{1}{3}-\cos^2\theta\right)\left(\frac{2}{3}+\frac{1}{3}\frac{m_1}{m_2}+\frac{13}{12}\frac{m_2}{m_1}\right)+\frac{16}{9}\frac{m_2}{m_1},\\
C_3 &:= \frac{1}{4}\left(\frac{1}{3}-\cos^2\theta\right)\left(1+\frac{m_2}{m_1}\right)-\frac{8}{15}\frac{m_2}{m_1},
\end{aligned}
\tag{F.22}
$$

and the $h^{n\Phi}_{+,\times}$ are the point mass amplitudes at $n \in \{2,3\}$ times the orbital frequency, given in Eq. (6.2).

Bibliography

[1] T. Hardy, In a Museum, from Moments of Vision and Miscellaneous Verses, in *The Complete Poetical Works of Thomas Hardy*, edited by S. Hynes Vol. 2, Oxford University Press, Oxford, 1984.

[2] B. P. Abbott *et al.* (LIGO Scientific Collaboration), Rep. Prog. Phys. **72**, 076901 (2009), arXiv:0711.3041 [gr-qc].

[3] T. Accadia *et al.*, Classical Quantum Gravity **28**, 114002 (2011).

[4] L. Cadonati (for the LIGO Scientific Collaboration and Virgo Collaboration), J. Phys. Conf. Ser. **222**, 012030 (2010).

[5] B. F. Schutz, Classical Quantum Gravity **28**, 125023 (2011), arXiv:1102.5421 [astro-ph.IM].

[6] S. Nissanke, J. L. Sievers, N. Dalal, and D. E. Holz, arXiv:1105.3184 [astro-ph.CO].

[7] F. A. Jenet, A. Lommen, S. L. Larson, and L. Wen, Astrophys. J. **606**, 799 (2004), astro-ph/0310276.

[8] G. Hobbs *et al.*, Classical Quantum Gravity **27**, 084013 (2010), arXiv:0911.5206 [astro-ph.SR].

[9] M. Punturo *et al.*, Classical Quantum Gravity **27**, 194002 (2010).

[10] LISA: Laser Interferometer Space Antenna: A Cornerstone Mission for the observation of gravitational waves: System and Technology Study Report, ESA-SCI(2000)11, `http://www.srl.caltech.edu/lisa/documents/sts_1.05.pdf`.

[11] W.-T. Ni, Int. J. Mod. Phys. D **17**, 921 (2008), arXiv:0712.2492 [astro-ph].

[12] S. Kawamura *et al.*, Classical Quantum Gravity **28**, 094011 (2011).

[13] A. Einstein, Sitzungsber. Preuss. Akad. Wiss. Berlin (Math. Phys.), 688 (1916).

[14] D. Kennefick, *Travelling at the speed of thought: Einstein and the quest for gravitational waves* (Princeton University Press, Princeton, 2007).

[15] D. R. Lorimer, Living Rev. Relativity **11**, 8 (2008), `http://www.livingreviews.org/lrr-2008-8`.

[16] K. A. Postnov and L. R. Yungelson, Living Rev. Relativity **9**, 6 (2006), `http://www.livingreviews.org/lrr-2006-6`.

[17] A. Bonaldi and S. Ricciardi, Mon. Not. R. Astron. Soc. **414**, 615 (2011), arXiv:1101.4876 [astro-ph.CO].

[18] J. Frauendiener, Living Rev. Relativity **7**, 1 (2004), http://www.livingreviews.org/lrr-2004-1.

[19] L. Blanchet, Living Rev. Relativity **9**, 4 (2006), http://www.livingreviews.org/lrr-2006-4.

[20] L. Blanchet, G. Faye, B. R. Iyer, and S. Sinha, Classical Quantum Gravity **25**, 165003 (2008), arXiv:0802.1249 [gr-qc].

[21] R. Fujita, arXiv:1104.5615 [gr-qc].

[22] C. Cutler *et al.*, Phys. Rev. Lett. **70**, 2984 (1993), astro-ph/9208005.

[23] A. Einstein, Sitzungsber. Preuss. Akad. Wiss. Berlin (Math. Phys.), 154 (1918).

[24] K. S. Thorne, Rev. Mod. Phys. **52**, 299 (1980).

[25] E. Pazos, D. Brizuela, J. M. Martín-Garcia, and M. Tiglio, Phys. Rev. D **82**, 104028 (2010), arXiv:1009.4665.

[26] K. D. Kokkotas and B. Schmidt, Living Rev. Relativity **2**, 2 (1999), http://www.livingreviews.org/lrr-1999-2.

[27] M. Dafermos and I. Rodnianski, arXiv:1010.5137 [gr-qc].

[28] J. L. Friedman and N. Stergioulas, Bull. Astr. Soc. India **39**, 21 (2011).

[29] J. Thornburg, GW Notes **5**, 3 (2011), arXiv:1102.2857 [gr-qc].

[30] I. MacDonald, S. Nissanke, and H. P. Pfeiffer, Classical Quantum Gravity **28**, 134002 (2011), arXiv:1102.5128 [gr-qc].

[31] S. G. Hahn and R. W. Lindquist, Ann. Phys. (N.Y.) **29**, 304 (1964).

[32] L. S. Finn, Phys. Rev. D **79**, 022002 (2009), arXiv:0810.4529 [gr-qc].

[33] M. Pitkin, S. Reid, S. Rowan, and J. Hough, Living Rev. Relativity **14**, 5 (2011), http://www.livingreviews.org/lrr-2011-5.

[34] T. Bulik, K. Belczynski, and A. Prestwich, Astrophys. J. **730**, 140 (2011), arXiv:0803.3516 [astro-ph].

[35] J. M. Comerford *et al.*, Astrophys. J. **698**, 956 (2009), arXiv:0810.3235 [astro-ph].

[36] M. Eracleous, T. A. Boroson, J. P. Halpern, and J. Liu, arXiv:1106.2952 [astro-ph.CO].

[37] D. Merritt and M. Milosavljević, Living Rev. Relativity **8**, 8 (2005), http://www.livingreviews.org/lrr-2005-8.

[38] F. Mahmood Khan, A. Just, and D. Merritt, Astrophys. J. **732**, 89 (2011), arXiv:1103.0272 [astro-ph.CO].

[39] P. C. Peters, Phys. Rev. **136**, 1224 (1964).

[40] F. Pretorius, Phys. Rev. Lett. **95**, 121101 (2005), gr-qc/0507014.

[41] M. Campanelli, C. O. Lousto, P. Marronetti, and Y. Zlochower, Phys. Rev. Lett. **96**, 111101 (2006), gr-qc/0511048.

[42] J. G. Baker, J. Centrella, D.-I. Choi, M. Koppitz, and J. van Meter, Phys. Rev. Lett. **96**, 111102 (2006), gr-qc/0511103.

[43] I. Hinder, Classical Quantum Gravity **27**, 114004 (2010), arXiv:1001.5161 [gr-qc].

[44] S. T. McWilliams, Classical Quantum Gravity **28**, 134001 (2011), arXiv:1012.2872 [gr-qc].

[45] G. Lovelace, M. A. Scheel, and B. Szilágyi, Phys. Rev. D **83**, 024010 (2011), arXiv:1010.2777 [gr-qc].

[46] M. Campanelli, C. Lousto, Y. Zlochower, and D. Merritt, Astrophys. J. Lett. **659**, 5 (2007), gr-qc/0701164.

[47] J. Healy *et al.*, Phys. Rev. Lett. **102**, 041101 (2009), arXiv:0807.3292 [gr-qc].

[48] `http://www.black-holes.org/SpEC.html`.

[49] S. R. Lau, G. Lovelace, and H. P. Pfeiffer, arXiv:1105.3922 [gr-qc].

[50] C. Reisswig, N. T. Bishop, D. Pollney, and B. Szilágyi, Phys. Rev. Lett. **103**, 221101 (2009), arXiv:0907.2637 [gr-qc].

[51] C. Reisswig, N. T. Bishop, D. Pollney, and B. Szilágyi, Classical Quantum Gravity **27**, 075014 (2010), arXiv:0912.1285 [gr-qc].

[52] M. C. Babiuc, B. Szilagyi, J. Winicour, and Y. Zlochower, arXiv:1011.4223 [gr-qc].

[53] L. Lindblom, B. J. Owen, and D. A. Brown, Phys. Rev. D **78**, 124020 (2008), arXiv:0809.3844 [gr-qc].

[54] L. Lindblom, J. G. Baker, and B. J. Owen, Phys. Rev. D **82**, 084020 (2010), arXiv:1008.1803 [gr-qc].

[55] L. Lindblom, Phys. Rev. D **80**, 064019 (2009), arXiv:0907.0457 [gr-qc].

[56] T. Damour, A. Nagar, and M. Trias, Phys. Rev. D **83**, 024006 (2011), arXiv:1009.5998 [gr-qc].

[57] M. Hannam, S. Husa, F. Ohme, and P. Ajith, Phys. Rev. D **82**, 124052 (2010), arXiv:1008.2961 [gr-qc].

[58] M. Boyle, arXiv:1103.5088 [gr-qc].

[59] M. Boyle *et al.*, Phys. Rev. D **76**, 124038 (2007), arXiv:0710.0158 [gr-qc].

[60] M. A. Scheel *et al.*, Phys. Rev. D **79**, 024003 (2009), arXiv:0810.1767 [gr-qc].

[61] D. Brizuela and G. Schäfer, Phys. Rev. D **81**, 084014 (2010), arXiv:1002.4552 [gr-qc].

[62] K. Alvi, Phys. Rev. D **61**, 124013 (2000), gr-qc/9912113.

[63] N. Yunes, W. Tichy, B. J. Owen, and B. Brügmann, Phys. Rev. D **74**, 104011 (2006), gr-qc/0503011 (Paper I).

[64] N. Yunes and W. Tichy, Phys. Rev. D **74**, 064013 (2006), gr-qc/0601046 (Paper II).

[65] B. J. Kelly, W. Tichy, Y. Zlochower, M. Campanelli, and B. F. Whiting, Classical Quantum Gravity **27**, 114005 (2010), arXiv:0912.5311 [gr-qc].

[66] B. C. Mundim, B. J. Kelly, Y. Zlochower, H. Nakano, and M. Campanelli, Classical Quantum Gravity **28**, 134003 (2011), arXiv:1012.0886 [gr-qc].

[67] B. Brügmann, W. Tichy, and N. Jansen, Phys. Rev. Lett. **92**, 211101 (2004), gr-qc/0312112.

[68] B. Brügmann *et al.*, Phys. Rev. D **77**, 024027 (2008), gr-qc/0610128.

[69] G. Lovelace, Classical Quantum Gravity **26**, 114002 (2009), arXiv:0812.3132 [gr-qc].

[70] M. Hannam, S. Husa, F. Ohme, D. Müller, and B. Brügmann, Phys. Rev. D **82**, 124008 (2010), arXiv:1007.4789 [gr-qc].

[71] N. Bishop, D. Pollney, and C. Reisswig, arXiv:1101.5492 [gr-qc].

[72] B. J. Kelly, W. Tichy, M. Campanelli, and B. F. Whiting, Phys. Rev. D **76**, 024008 (2007), arXiv:0704.0628 [gr-qc].

[73] G. Lovelace, R. Owen, H. P. Pfeiffer, and T. Chu, Phys. Rev. D **78**, 084017 (2008), arXiv:0805.4192 [gr-qc].

[74] B. Abbott *et al.* (LIGO Scientific Collaboration), Phys. Rev. D **76**, 082001 (2007), gr-qc/0605028.

[75] B. Abbott *et al.* (LIGO Scientific Collaboration), Astrophys. J. Lett. **683**, L45 (2008), **706**, L203(E) (2009), arXiv:0805.4758 [astro-ph].

[76] J. Abadie *et al.* (LIGO Scientific Collaboration), Astrophys. J. **722**, 1504 (2010), arXiv:1006.2535 [gr-qc].

[77] B. P. Abbott *et al.* (LIGO Scientific Collaboration and Virgo Collaboration), Astrophys. J. **713**, 671 (2010).

[78] J. Abadie *et al.* (LIGO Scientific Collaboration and Virgo Collaboration), arXiv:1104.2712 [astro-ph.HE].

[79] B. Abbott *et al.* (LIGO Scientific Collaboration), Phys. Rev. D **79**, 022001 (2009), 0804.1747 [gr-qc].

[80] B. P. Abbott *et al.* (LIGO Scientific Collaboration), Phys. Rev. D **80**, 042003 (2009), arXiv:0905.1705 [gr-qc].

[81] B. Abbott *et al.* (LIGO Scientific Collaboration), Phys. Rev. Lett. **101**, 211102 (2008), arXiv:0808.2050 [astro-ph].

[82] B. P. Abbott *et al.* (LIGO Scientific Collaboration), Astrophys. J. Lett. **701**, L68 (2009), arXiv:0905.0005 [astro-ph.HE].

[83] J. Abadie *et al.* (LIGO Scientific Collaboration and Virgo Collaboration), Astrophys. J. Lett. **734**, L35 (2011), arXiv:1011.4079 [astro-ph.HE].

[84] M. Ruderman, Nature (London) **223**, 597 (1969).

[85] G. Baym and D. Pines, Ann. Phys. (N.Y.) **66**, 816 (1971).

[86] N. Chamel and P. Haensel, Living Rev. Relativity **11**, 10 (2008), http://www.livingreviews.org/lrr-2008-10.

[87] B. J. Owen, Phys. Rev. Lett. **95**, 211101 (2005), astro-ph/0503399.

[88] B. Haskell, N. Andersson, D. I. Jones, and L. Samuelsson, Phys. Rev. Lett. **99**, 231101 (2007), arXiv:0708.2984 [gr-qc].

[89] L.-M. Lin, Phys. Rev. D **76**, 081502(R) (2007), arXiv:0708.2965 [astro-ph].

[90] B. Knippel and A. Sedrakian, Phys. Rev. D **79**, 083007 (2009), arXiv:0901.4637 [astro-ph.SR].

[91] N. K. Glendenning, Nucl. Phys. B (Proc. Suppl.) **24**, 110 (1991).

[92] N. K. Glendenning, Phys. Rev. D **46**, 1274 (1992).

[93] D. G. Ravenhall, C. J. Pethick, and J. R. Wilson, Phys. Rev. Lett. **50**, 2066 (1983).

[94] M. Nayyar, PhD thesis, The Pennsylvania State University, 2007, http://www.etda.libraries.psu.edu/theses/approved/WorldWideIndex/ETD-1949/index.html.

[95] P. B. Demorest, T. Pennucci, S. M. Ransom, M. S. E. Roberts, and J. W. T. Hessels, Nature (London) **467**, 1081 (2010), arXiv:1010.5788 [astro-ph.HE].

[96] H. Sotani, arXiv:1106.2621 [astro-ph.HE].

[97] M. Gearheart, W. G. Newton, J. Hooker, and B.-A. Li, arXiv:1106.4875 [astro-ph.SR].

[98] G. Ushomirsky, C. Cutler, and L. Bildsten, Mon. Not. R. Astron. Soc. **319**, 902 (2000), astro-ph/0001136 (UCB).

[99] B. Haskell, D. I. Jones, and N. Andersson, Mon. Not. R. Astron. Soc. **373**, 1423 (2006), astro-ph/0609438 (HJA).

[100] T. Hinderer, Astrophys. J. **677**, 1216 (2008), **697**, 1216(E) (2009), arXiv:0711.2420 [astro-ph].

[101] O. Emersleben, Math. Nachr. **4**, 468 (1951).

[102] D. Borwein, J. M. Borwein, and K. F. Taylor, J. Math. Phys. **26**, 2999 (1985).

[103] E. S. Campbell, J. Phys. Chem. Solids **24**, 197 (1963).

[104] E. Zeidler, *Quantum Field Theory I: Basics in Mathematics and Physics* (Springer, Berlin, 2006).

[105] K. Becker, M. Becker, and J. H. Schwartz, *String Theory and M-Theory: A Modern Introduction* (Cambridge University Press, 2006).

[106] G. H. Hardy, *Divergent Series*, corr. ed. (Oxford University Press, Oxford, 1963).

[107] S. W. Hawking, Commun. Math. Phys. **55**, 133 (1977).

[108] R. Bellman, *A Brief Introduction to Theta Functions* (Holt, Rinehart and Winston, New York, 1961).

[109] J. H. Conway and N. J. A. Sloane, *Sphere Packings, Lattices and Groups*, 3rd ed. (Springer-Verlag, New York, 1999).

[110] B. Simon, J. Math. Phys. **12**, 140 (1971).

[111] S. D. Miller and W. Schmid, in *Noncommutative Harmonic Analysis: In honor of Jacques Carmona*, edited by P. Delorme and M. Vergne, p. 419, Birkhäuser, Boston, 2004, math/0304187 [math.NT].

[112] A. Stroeer and A. Vecchio, Classical Quantum Gravity **23**, S809 (2006), astro-ph/0605227.

[113] G. Nelemans, LISA verification sources, `http://www.astro.ru.nl/~nelemans/dokuwiki/doku.php?id=verification_binaries:intro`.

[114] J. Crowder and N. J. Cornish, Phys. Rev. D **75**, 043008 (2007), astro-ph/0611546.

[115] A. J. Ruiter, K. Belczynski, M. Benacquista, S. Larson, and G. Williams, Astrophys. J. **717**, 1006 (2010), 0705.3272 [astro-ph].

[116] S. Yu and C. S. Jeffrey, Astron. Astrophys. **521**, A85 (2010), arXiv:1007.4267 [astro-ph.SR].

[117] J. Liu, Z. Han, F. Zhang, and Y. Zhang, Astrophys. J. **719**, 1546 (2010).

[118] B. F. Schutz, Nature (London) **323**, 310 (1986).

[119] G. H. A. Roelofs *et al.*, Astrophys. J. Lett. **711**, L138 (2010), arXiv:1003.0658 [astro-ph.SR].

[120] B. Willems, A. Vecchio, and V. Kalogera, Phys. Rev. Lett. **100**, 041102 (2008), arXiv:0706.3700 [astro-ph].

[121] F. Valsecchi, W. M. Farr, B. Willems, C. J. Deloye, and V. Kalogera, arXiv:1105.4837 [astro-ph.SR].

[122] S. Chandrasekhar, *Relativistic Astrophysics*, Selected Papers Vol. 5 (University of Chicago Press, Chicago, 1990).

[123] F. Pretorius, in *Physics of Relativistic Objects in Compact Binaries: from Birth to Coalescence*, edited by M. Colpi, P. Casella, V. Gorini, U. Moschella, and A. Possenti, Springer, Berlin, 2009, arXiv:0710.1338 [gr-qc].

[124] E. Berti *et al.*, Phys. Rev. D **76**, 064034 (2007), gr-qc/0703053.

[125] J. G. Baker *et al.*, Phys. Rev. D **78**, 044046 (2008), arXiv:0805.1428 [gr-qc].

[126] J. A. González, U. Sperhake, and B. Brügmann, Phys. Rev. D **79**, 124006 (2009), arXiv:0811.3952 [gr-qc].

[127] S. Husa, J. A. González, M. Hannam, B. Brügmann, and U. Sperhake, Classical Quantum Gravity **25**, 105006 (2008), arXiv:0706.0740 [gr-qc].

[128] M. Hannam *et al.*, Phys. Rev. D **79**, 084025 (2009), arXiv:0901.2437 [gr-qc].

[129] B. Aylott *et al.*, Classical Quantum Gravity **26**, 165008 (2009), arXiv:0901.4399 [gr-qc].

[130] H. P. Pfeiffer *et al.*, Classical Quantum Gravity **24**, S59 (2007), gr-qc/0702106.

[131] S. Husa, M. Hannam, J. A. González, U. Sperhake, and B. Brügmann, Phys. Rev. D **77**, 044037 (2008), arXiv:0706.0904 [gr-qc].

[132] B. Walther, B. Brügmann, and D. Müller, Phys. Rev. D **79**, 124040 (2009), arXiv:0901.0993 [gr-qc].

[133] T. Bode, D. Shoemaker, F. Herrmann, and I. Hinder, Phys. Rev. D **77**, 044027 (2008), arXiv:0711.0669 [gr-qc].

[134] J. A. González, U. Sperhake, B. Brügmann, M. Hannam, and S. Husa, Phys. Rev. Lett. **98**, 091101 (2007), gr-qc/0610154.

[135] G. Lovelace *et al.*, Phys. Rev. D **82**, 064031 (2010), arXiv:0907.0869 [gr-qc].

[136] T. Chu, H. P. Pfeiffer, and M. A. Scheel, Phys. Rev. D **80**, 124051 (2009), arXiv:0909.1313 [gr-qc].

[137] G. B. Cook, Living Rev. Relativity **3** (2000), `http://www.livingreviews.org/lrr-2000-5`.

[138] E. Gourgoulhon, J. Phys. Conf. Ser. **91**, 012001 (2007), arXiv:0704.0149 [gr-qc].

[139] S. Brandt and B. Brügmann, Phys. Rev. Lett. **78**, 3606 (1997), gr-qc/9703066.

[140] P. Marronetti *et al.*, Classical Quantum Gravity **24**, S43 (2007), gr-qc/0701123.

[141] P. Marronetti, W. Tichy, B. Brügmann, J. González, and U. Sperhake, Phys. Rev. D **77**, 064010 (2008), arXiv:0709.2160 [gr-qc].

[142] W. Tichy and P. Marronetti, Phys. Rev. D **76**, 061502(R) (2007), gr-qc/0703075.

[143] W. Tichy and P. Marronetti, Phys. Rev. D **78**, 081501(R) (2008), arXiv:0807.2985 [gr-qc].

[144] W. Tichy, B. Brügmann, and P. Laguna, Phys. Rev. D **68**, 064008 (2003), gr-qc/0306020.

[145] W. Tichy and B. Brügmann, Phys. Rev. D **69**, 024006 (2004), gr-qc/0307027.

[146] M. A. Scheel *et al.*, Phys. Rev. D **74**, 104006 (2006), gr-qc/0607056.

[147] D. Shoemaker *et al.*, Classical Quantum Gravity **20**, 3729 (2003), gr-qc/0301111.

[148] G. B. Cook and H. P. Pfeiffer, Phys. Rev. D **70**, 104016 (2004), gr-qc/0407078.

[149] A. Ashtekar and B. Krishnan, Living Rev. Relativity **7** (2004), `http://www.livingreviews.org/lrr-2004-10`.

[150] D. Brown *et al.*, Phys. Rev. D **76**, 081503(R) (2007), arXiv:0707.3101 [gr-qc].

[151] N. Yunes, Classical Quantum Gravity **24**, 4313 (2007), gr-qc/0611128.

[152] See EPAPS Document No. E-PRVDAQ-80-080922 for the MAPLE scripts and C codes that generate the data. For more information on EPAPS, see `http://www.aip.org/pubservs/epaps.html`.

[153] L. E. Simone, S. W. Leonard, E. Poisson, and C. M. Will, Classical Quantum Gravity **14**, 237 (1997), gr-qc/9610058.

[154] A. Garat and R. H. Price, Phys. Rev. D **61**, 124011 (2000), gr-qc/0002013.

[155] J. A. Valiente Kroon, Classical Quantum Gravity **21**, 3237 (2004), gr-qc/0402033.

[156] S. Nissanke, Phys. Rev. D **73**, 124002 (2006), gr-qc/0509128.

[157] L. Blanchet, Phys. Rev. D **68**, 084002 (2003), gr-qc/0304080.

[158] W. Tichy, B. Brügmann, M. Campanelli, and P. Diener, Phys. Rev. D **67**, 064008 (2003), gr-qc/0207011.

[159] R. A. Matzner, M. F. Huq, and D. Shoemaker, Phys. Rev. D **59**, 024015 (1998), gr-qc/9805023.

[160] P. Marronetti and R. A. Matzner, Phys. Rev. Lett. **85**, 5500 (2000), gr-qc/0009044.

[161] P. Marronetti *et al.*, Phys. Rev. D **62**, 024017 (2000), gr-qc/0001077.

[162] U. Sperhake, Phys. Rev. D **76**, 104015 (2007), gr-qc/0606079.

[163] M. Hannam, S. Husa, B. Brügmann, J. A. González, and U. Sperhake, Classical Quantum Gravity **24**, S15 (2007), gr-qc/0612001.

[164] H. P. Pfeiffer, G. B. Cook, and S. A. Teukolsky, Phys. Rev. D **66**, 024047 (2002), gr-qc/0203085.

[165] H.-J. Yo, J. N. Cook, S. L. Shapiro, and T. W. Baumgarte, Phys. Rev. D **70**, 084033 (2004), gr-qc/0406020.

[166] L. Blanchet, G. Faye, and B. Ponsot, Phys. Rev. D **58**, 124002 (1998), gr-qc/9804079 (BFP).

[167] H. P. Pfeiffer, L. E. Kidder, M. A. Scheel, and S. A. Teukolsky, Comput. Phys. Commun. **152**, 253 (2003), gr-qc/0202096.

[168] M. Holst *et al.*, Phys. Rev. D **70**, 084017 (2004), gr-qc/0407011.

[169] T. Bode *et al.*, Phys. Rev. D **80**, 024008 (2009), arXiv:0902.1127 [gr-qc].

[170] N. Jansen and B. Brügmann (unpublished).

[171] E. Poisson and I. Vlasov, Phys. Rev. D **81**, 024029 (2010), arXiv:0910.4311 [gr-qc].

[172] G. B. Cook and M. A. Scheel, Phys. Rev. D **56**, 4775 (1997).

[173] S. Detweiler, Classical Quantum Gravity **22**, S681 (2005), gr-qc/0501004.

[174] E. Poisson, Phys. Rev. Lett. **94**, 161103 (2005), gr-qc/0501032.

[175] K. S. Thorne and J. B. Hartle, Phys. Rev. D **31**, 1815 (1985).

[176] X.-H. Zhang, Phys. Rev. D **34**, 991 (1986).

[177] M. E. Pati and C. M. Will, Phys. Rev. D **62**, 124015 (2000), gr-qc/0007087.

[178] M. E. Pati and C. M. Will, Phys. Rev. D **65**, 104008 (2002), gr-qc/0201001.

[179] C. M. Will and A. G. Wiseman, Phys. Rev. D **54**, 4813 (1996).

[180] S. Taylor and E. Poisson, Phys. Rev. D **78**, 084016 (2008), arXiv:0806.3052 [gr-qc].

[181] P. Musgrave, D. Pollney, and K. Lake, GRTensorII software, 1996, `http://grtensor.phy.queensu.ca/`.

[182] C. M. Bender and S. A. Orszag, *Advanced Mathematical Methods for Scientists and Engineers* (McGraw-Hill, New York, 1978).

[183] O. Poujade and L. Blanchet, Phys. Rev. D **65**, 124020 (2002), gr-qc/0112057.

[184] S. Detweiler (private communication).

[185] R. Rieth, in *Mathematics of Gravitation. Part II: Gravitational Wave Detection*, edited by A. Królak, , Banach Center Publications Vol. 41, pp. 71–74, Polish Academy of Sciences, Institute of Mathematics, Warsaw, 1997, nearly identical to gr-qc/9603043.

[186] T. Damour, P. Jaranowski, and G. Schäfer, Phys. Rev. D **62**, 084011 (2000), gr-qc/0005034.

[187] J. A. Isenberg, Int. J. Mod. Phys. D **17**, 265 (2008), gr-qc/0702113.

[188] J. R. Wilson, G. J. Mathews, and P. Marronetti, Phys. Rev. D **54**, 1317 (1996), gr-qc/9601017.

[189] H. Stephani, D. Kramer, M. MacCallum, C. Hoenselaers, and E. Herlt, *Exact solutions of Einstein's field equations*, 2nd ed. (Cambridge University Press, Cambridge, 2003).

[190] J. A. Schouten, *Ricci-Calculus: An Introduction to Tensor Analysis and its Geometrical Applications*, 2nd ed. (Springer, Berlin, 1954).

[191] L. Blanchet (private communication).

[192] G. Schäfer, Ann. Phys. (N. Y.) **161**, 81 (1985).

[193] L. Blanchet, Phys. Rev. D **47**, 4392 (1993).

[194] J. B. Hartle, K. S. Thorne, and R. H. Price, in *Black Holes: The Membrane Paradigm*, edited by K. S. Thorne, R. H. Price, and D. A. Macdonald, Yale University Press, New Haven, 1986.

[195] N. Straumann, *General relativity: with applications to astrophysics*, rev. ed. (Springer, Berlin, 2004).

[196] L. Blanchet and T. Damour, Ann. Inst. Henri Poincaré Phys. Théor. **50**, 377 (1989).

[197] S. Weinberg, *Gravitation and Cosmology: Principles and Applications of the General Theory of Relativity* (Wiley, New York, 1972).

[198] T. Damour, B. R. Iyer, and B. S. Sathyaprakash, Phys. Rev. D **63**, 044023 (2001), gr-qc/0010009.

[199] L. Blanchet and B. R. Iyer, Classical Quantum Gravity **20**, 755 (2003), gr-qc/0209089.

[200] T. Damour, Int. J. Mod. Phys. A **23**, 1130 (2008), arXiv:0802.4047 [gr-qc].

[201] J. D. Jackson, *Classical Electrodynamics*, 3rd ed. (Wiley, New York, 1999).

[202] S. M. Kopeikin and G. Schäfer, Phys. Rev. D **60**, 124002 (1999), gr-qc/9902030.

[203] K. S. Thorne and S. J. Kovács, Astrophys. J. **200**, 245 (1975).

[204] J. Pullin (private communication).

[205] I. Vega, P. Diener, W. Tichy, and S. Detweiler, Phys. Rev. D **80**, 084021 (2009), arXiv:0908.2138 [gr-qc].

[206] E. Schnetter (private communication).

[207] P. Ajith *et al.*, Classical Quantum Gravity **24**, S689 (2007), arXiv:0704.3764 [gr-qc].

[208] W. Tichy, Classical Quantum Gravity **26**, 175018 (2009), arXiv:0908.0620 [gr-qc].

[209] F. Pretorius (unpublished).

[210] M. Ansorg, B. Brügmann, and W. Tichy, Phys. Rev. D **70**, 064011 (2004), gr-qc/0404056.

[211] K. G. Arun, L. Blanchet, B. R. Iyer, and S. Sinha, Phys. Rev. D **80**, 124018 (2009), arXiv:0908.3854 [gr-qc].

[212] H. Tagoshi, A. Ohashi, and B. J. Owen, Phys. Rev. D **63**, 044006 (2001), gr-qc/0010014.

[213] G. Faye, L. Blanchet, and A. Buonanno, Phys. Rev. D **74**, 104033 (2006), **81**, 089901(E) (2010), gr-qc/0605139.

[214] C. M. Will, Phys. Rev. D **71**, 084027 (2005), gr-qc/0502039.

[215] L. Blanchet, A. Buonanno, and G. Faye, Phys. Rev. D **74**, 104034 (2006), **75**, 049903(E) (2007), **81**, 089901(E) (2010), gr-qc/0605140.

[216] N. Yunes and J. A. González, Phys. Rev. D **73**, 024010 (2006), gr-qc/0510076.

[217] J. C. Collins and M. J. Perry, Phys. Rev. Lett. **34**, 1353 (1975).

[218] N. Itoh, Prog. Theor. Phys. **44**, 291 (1970).

[219] A. Bodmer, Phys. Rev. D **4**, 1601 (1971).

[220] M. Alford, M. Braby, M. Paris, and S. Reddy, Astrophys. J. **629**, 969 (2005), nucl-th/0411016.

[221] S. Weissenborn, I. Sagert, G. Pagliara, M. Hempel, and J. Schaffner-Bielich, arXiv:1102.2869 [astro-ph.HE].

[222] N. K. Glendenning, Phys. Rep. **342**, 393 (2001).

[223] N. K. Glendenning, *Compact Stars: Nuclear Physics, Particle Physics, and General Relativity*, 2nd ed. (Springer, New York, 2000).

[224] H. Heiselberg, C. J. Pethick, and E. F. Staubo, Phys. Rev. Lett. **70**, 1355 (1993).

[225] A. Corsi and B. J. Owen, Phys. Rev. D **83**, 104014 (2011), arXiv:1102.3421 [gr-qc].

[226] K. Fuchs, Proc. R. Soc. A **153**, 622 (1936).

[227] C. J. Pethick and A. Y. Potekhin, Phys. Lett. B **427**, 7 (1998), astro-ph/9803154.

[228] T. Norsen and S. Reddy, Phys. Rev. C **63**, 065804 (2001), nucl-th/0010075.

[229] D. N. Voskresensky, M. Yasuhira, and T. Tatsumi, Phys. Lett. B **541**, 93 (2002), nucl-th/0109009.

[230] D. N. Voskresensky, M. Yasuhira, and T. Tatsumi, Nucl. Phys. A **723**, 291 (2003), nucl-th/0208067.

[231] T. Endo, Phys. Rev. C **83**, 068801 (2011), arXiv:1105.2445 [astro-ph.SR].

[232] P. P. Ewald, Ann. Phys. (Leipzig) **369**, 253 (1921).

[233] R. E. Johnson and S. Ranganathan, Phys. Rev. E **75**, 056706 (2007).

[234] D. A. Baiko, arXiv:1104.0173 [astro-ph.SR] [Mon. Not. R. Astron. Soc. (to be published)].

[235] G. Baym, C. Pethick, and P. Sutherland, Astrophys. J. **170**, 299 (1971).

[236] J. W. Negele and D. Vautherin, Nucl. Phys. A **207**, 298 (1973).

[237] J. M. Lattimer and M. Prakash, Astrophys. J. **550**, 426 (2001), astro-ph/0002232.

[238] A. Kurkela, P. Romatschke, A. Vuorinen, and B. Wu, arXiv:1006.4062 [astro-ph.HE].

[239] `http://theory.physics.helsinki.fi/~aekurkel/neutron/`.

[240] G. A. Lalazissis, J. König, and P. Ring, Phys. Rev. C **55**, 540 (1997), nucl-th/9607039.

[241] B. D. Lackey, M. Nayyar, and B. J. Owen, Phys. Rev. D **73**, 024021 (2006), astro-ph/0507312.

[242] J. Piekarewicz, J. Phys. G **37**, 064038 (2010), arXiv:0912.5103 [nucl-th].

[243] B.-A. Li *et al.*, arXiv:1103.4652 [nucl-th].

[244] A. W. Steiner, M. Prakash, J. M. Lattimer, and P. J. Ellis, Phys. Rep. **411**, 325 (2005), nucl-th/0410066.

[245] A. Chodos, R. L. Jaffe, K. Johnson, C. B. Thorn, and V. F. Weisskopf, Phys. Rev. D **9**, 3471 (1974).

[246] E. Farhi and R. L. Jaffe, Phys. Rev. D **30**, 2379 (1984).

[247] A. Kurkela, P. Romatschke, and A. Vuorinen, Phys. Rev. D **81**, 105021 (2010), arXiv:0912.1856 [hep-ph].

[248] M. B. Christiansen and N. K. Glendenning, Phys. Rev. C **56**, 2858 (1997), astro-ph/9706056.

[249] K. Nakamura *et al.* (Particle Data Group), J. Phys. G **37**, 075021 (2010).

[250] H. Sonoda, G. Watanabe, K. Sato, K. Yasuoka, and T. Ebisuzaki, Phys. Rev. C **77**, 035806 (2008), **81**, 049902(E) (2010), arXiv:0712.0052 [nucl-th].

[251] G. Watanabe *et al.*, Phys. Rev. Lett. **103**, 121101 (2009), arXiv:0904.0512 [nucl-th].

[252] C. J. Horowitz, M. A. Pérez-García, D. K. Berry, and J. Piekarewicz, Phys. Rev. C **72**, 035801 (2005), nucl-th/0508044.

[253] C. J. Horowitz and D. K. Berry, Phys. Rev. C **78**, 035806 (2008), arXiv:0807.2603 [astro-ph].

[254] B. Paladini and J. C. Sexton, Phys. Lett. B **448**, 76 (1999), hep-lat/9805021.

[255] D. C. Wallace, Phys. Rev. **162**, 776 (1967).

[256] T. Strohmayer, H. M. van Horn, S. Ogata, H. Iyetomi, and S. Ichimaru, Astrophys. J. **375**, 679 (1991).

[257] W. Voigt, *Lehrbuch der Kristallphysik* (Teubner, Leipzig, 1928).

[258] R. Hill, Proc. Phys. Soc. A **65**, 349 (1952).

[259] Z. Hashin and S. Shtrikman, J. Mech. Phys. Solids **10**, 343 (1962).

[260] J. P. Watt, G. F. Davies, and R. J. O'Connell, Rev. Geophys. Space Phys. **14**, 541 (1976).

[261] J. P. Watt, J. Appl. Phys. **50**, 6290 (1979).

[262] S. Ogata and S. Ichimaru, Phys. Rev. A **42**, 4867 (1990).

[263] J. J. Zach, Phys. Rev. D **65**, 123002 (2002), astro-ph/0204314.

[264] B. R. A. Nijboer and F. W. de Wette, Physica (Utrecht) **23**, 309 (1957).

[265] C. M. Fortuin, Physica (Utrecht) **86A**, 574 (1977).

[266] E. M. Stein and G. Weiss, *Introduction to Fourier Analysis on Euclidean Spaces* (Princeton University Press, Princeton, 1971).

[267] T. Endo, T. Maruyama, S. Chiba, and T. Tatsumi, Prog. Theor. Phys. **115**, 337 (2006), hep-ph/0510279.

[268] D. B. Blaschke, D. Gómez Dumm, A. G. Grunfeld, T. Klähn, and N. N. Scoccola, Phys. Rev. C **75**, 065804 (2007), nucl-th/0703088.

[269] T. Maruyama, S. Chiba, H.-J. Schulze, and T. Tatsumi, Phys. Rev. D **76**, 123015 (2007), arXiv:0708.3277 [nucl-th].

[270] M. Pitkin, arXiv:1103.5867 [astro-ph.HE] [Mon. Not. R. Astron. Soc. (to be published)].

[271] C. J. Horowitz and K. Kadau, Phys. Rev. Lett. **102**, 191102 (2009), arXiv:0904.1986 [astro-ph.SR].

[272] A. I. Chugunov and C. J. Horowitz, Mon. Not. R. Astron. Soc. Lett. **407**, L54 (2010), arXiv:1006.2279 [astro-ph.SR].

[273] C. J. Horowitz, Phys. Rev. D **81**, 103001 (2010), arXiv:0912.1491 [astro-ph.SR].

[274] B. Carter and H. Quintana, Proc. R. Soc. A **331**, 57 (1972).

[275] M. Karlovini and L. Samuelsson, Classical Quantum Gravity **20**, 3613 (2003), **22**, 771(E) (2005), gr-qc/0211026.

[276] B. L. Schumaker and K. S. Thorne, Mon. Not. R. Astron. Soc. **203**, 457 (1983).

[277] K. S. Thorne and A. Campolattaro, Astrophys. J. **149**, 591 (1967), **152**, 673(E) (1968).

[278] T. Regge and J. A. Wheeler, Phys. Rev. **108**, 1063 (1957).

[279] J. R. Ipser, Astrophys. J. **166** (1971).

[280] L. Lindblom, G. Mendell, and B. J. Owen, Phys. Rev. D **60**, 064006 (1999), gr-qc/9902052.

[281] C. Cutler, G. Ushomirsky, and B. Link, Astrophys. J. **588**, 975 (2003), astro-ph/0210175.

[282] G. B. Arfken and H. J. Weber, *Mathematical Methods for Physicists*, 6th ed. (Elsevier, Boston, 2005).

[283] R. M. Wald, *General Relativity* (University of Chicago Press, Chicago, 1984).

[284] S. L. Detweiler and J. R. Ipser, Astrophys. J. **185**, 685 (1973).

[285] B. F. Schutz, Jr., Astrophys. J. Suppl. Ser. **24**, 343 (1972).

[286] L. S. Finn, Mon. Not. R. Astron. Soc. **245**, 82 (1990).

[287] F. Douchin and P. Haensel, Astron. Astrophys. **380**, 151 (2001), astro-ph/0111092.

[288] P. Haensel and A. Y. Potekhin, Astron. Astrophys. **428**, 191 (2004), astro-ph/0408324.

[289] P. Haensel, A. Y. Potekhin, and D. G. Yakovlev, *Neutron Stars 1: Equation of State and Structure* (Springer, New York, 2007).

[290] `http://www.ioffe.ru/astro/NSG/NSEOS/`.

[291] T. Binnington and E. Poisson, Phys. Rev. D **80**, 084018 (2009), arXiv:0906.1366 [gr-qc].

[292] T. Damour and A. Nagar, Phys. Rev. D **80**, 084035 (2009), arXiv:0906.0096 [gr-qc].

[293] J. M. Lattimer and M. Prakash, arXiv:1012.3208 [astro-ph.SR].

[294] P. Haensel, in *Physics of Neutron Star Interiors*, edited by D. Blaschke, A. Sedrakian, and N. K. Glendenning, , Lecture Notes in Physics Vol. 578, p. 127, Berlin, 2001, Springer.

[295] K. Hurley *et al.*, Nature (London) **434**, 1098 (2005), astro-ph/0502329.

[296] D. M. Palmer *et al.*, Nature (London) **434**, 1107 (2005), astro-ph/0503030.

[297] G. Svirski, E. Nakar, and E. O. Ofek, arXiv:1103.0006 [astro-ph.HE] [Mon. Not. R. Astron. Soc. (to be published)].

[298] T. Hinderer, B. D. Lackey, R. N. Lang, and J. S. Read, Phys. Rev. D **81**, 123016 (2010), arXiv:0911.3535 [astro-ph.HE].

[299] S. Postnikov, M. Prakash, and J. M. Lattimer, Phys. Rev. D **82**, 024016 (2010), arXiv:1004.5098 [astro-ph.SR].

[300] K. Ioka and M. Sasaki, Astrophys. J. **600**, 296 (2004), astro-ph/0305352.

[301] R. Ciolfi, V. Ferrari, and L. Gualtieri, Mon. Not. R. Astron. Soc. **406**, 2540 (2010), arXiv:1003.2148 [astro-ph.SR].

[302] C. J. Horowitz and J. Hughto, arXiv:0812.2650 [astro-ph].

[303] P. Painlevé, *Analyse des travaux scientifiques* (Gauthier-Villars, Paris, 1900), this quote is often attributed to Jacques Hadamard in the form of, "Le plus court chemin entre deux vérités dans le domaine réel passe par le domaine complexe" or even as, "The shortest path between two truths in the real domain passes through the complex domain," or something similar. These appear to be paraphrases of Hadamard's (English!) original, which was in turn referring back (without citation) to the Painlevé quote given. The provenance of the quote was investigated by Palle Jorgensen—see `http://www.cs.uiowa.edu/~jorgen/hadamardquotesource.html`; A. I. Shtern identified Painlevé as the original author.

[304] R. Contino and A. Gambassi, J. Math. Phys. **44**, 570 (2003), hep-th/0112161.

[305] A. Sklar, in *Report of the Institute in the Theory of Numbers*, edited by D. C. B. Marsh, p. 104, American Mathematical Society, Boulder, CO, 1959.

[306] W. L. Ferrar, Compos. Math. **4**, 394 (1937).

[307] H. Cohen, *Number Theory, Volume II: Analytic and Modern Tools* (Springer, New York, 2007).

[308] M. Baake, D. Frettlöh, and U. Grimm, J. Geom. Phys. **57**, 1331 (2007), math/0610408 [math.SP].

[309] H. Iwaniec and E. Kowalski, *Analytic Number Theory* (American Mathematical Society, Providence, RI, 2004).

[310] M. N. Huxley, *Area, Lattice Points, and Exponential Sums* (Oxford University Press, New York, 1996).

[311] E. T. Whittaker and G. N. Watson, *A Course of Modern Analysis* (Cambridge University Press, Cambridge, 1944).

[312] `http://functions.wolfram.com`.

[313] J. B. Conway, *A Course in Functional Analysis*, 2nd ed. (Springer, New York, 1990).

[314] S. Lang, *Real Analysis*, 2nd ed. (Addison-Wesley, Reading, MA, 1983).

[315] J. Roe (private communication).

[316] A. Uribe, in *First Summer School in Analysis and Mathematical Physics, Cuernavaca, Mexico*, edited by S. Pérez-Esteva and C. Villegas-Blas, p. 61, American Mathematical Society, 2000.

[317] C. Ryavec, Aequ. Math. **21**, 246 (1980).

[318] A. Córdoba, C. R. Acad. Sci. Paris Sér. I Math. **306**, 373 (1988).

[319] A. Córdoba, Lett. Math. Phys. **17**, 191 (1989).

[320] G. Nelemans, L. R. Yungelson, and S. F. Portegies Zwart, Astron. Astrophys. **375**, 890 (2001), astro-ph/0105221.

[321] J.-E. Solheim, Publ. Astron. Soc. Pac. **122**, 1133 (2010).

[322] T. R. Marsh, Classical Quantum Gravity **28**, 094019 (2011), arXiv:1101.4970 [astro-ph.SR].

[323] G. H. A. Roelofs, G. Nelemans, and P. J. Groot, Mon. Not. R. Astron. Soc. **382**, 685 (2007), arXiv:0709.2951 [astro-ph].

[324] A. Stroeer, A. Vecchio, and G. Nelemans, Astrophys. J. Lett. **633**, L33 (2005), astro-ph/0509632.

[325] R. F. Webbink, in *International Conference on Binaries: In celebration of Ron Webbink's 65th Birthday*, edited by V. Kalogera & M. van der Sluys, p. 217, 2010, arXiv:1011.6317 [astro-ph.SR].

[326] A. M. Sintes and A. Vecchio, in *Gravitational Waves: Third Edoardo Amaldi Conference*, edited by S. Meshkov, p. 403, 2000, gr-qc/0005059.

[327] R. W. Hellings and T. A. Moore, Classical Quantum Gravity **20**, 181 (2003), gr-qc/0207102.

[328] M. Trias and A. M. Sintes, Classical Quantum Gravity **25**, 184032 (2008), arXiv:0804.0492 [gr-qc].

[329] E. K. Porter and N. J. Cornish, Phys. Rev. D **78**, 064005 (2008), arXiv:0804.0332 [gr-qc].

[330] B. S. Sathyaprakash and B. F. Schutz, Living Rev. Relativity **12** (2009), `http://www.livingreviews.org/lrr-2009-2`.

[331] L. Lindegren, in *Proc. IAU Symp. 261, Relativity in Fundamental Astronomy: Dynamics, Reference Frames, and Data Analysis*, edited by S. A. Klioner, P. K. Seidelmann, M. H. Soffel, p. 296, Cambridge University Press, 2010.

[332] G. Nelemans, Classical Quantum Gravity **20**, 81 (2003).

[333] S. L. Morris and S. A. Naftilan, Astrophys. J. **419**, 344 (1993).

[334] M. Kilic *et al.*, Mon. Not. R. Astron. Soc. Lett. **413**, L101 (2011), arXiv:1103.2354 [astro-ph.GA].

[335] W. R. Brown *et al.*, arXiv:1107.2389 [astro-ph.GA] [Astrophys. J. Lett. (to be published)].

[336] L. S. Finn, Phys. Rev. D **46**, 5236 (1992), gr-qc/9209010.

[337] C. Cutler and É. É. Flanagan, Phys. Rev. D **49**, 2658 (1994), gr-qc/9402014.

[338] M. Kilic, W. R. Brown, C. Allende Prieto, S. J. Kenyon, and J. A. Panei, Astrophys. J. **716**, 122 (2010), arXiv:0911.1781 [astro-ph.SR].

[339] L. Blanchet, G. Faye, B. R. Iyer, and S. Sinha, Classical Quantum Gravity **25**, 165003 (2008), arXiv:0802.1249 [gr-qc].

[340] B. Willems *et al.*, Astrophys. J. Lett. **665**, L59 (2007), arXiv:0705.4287 [astro-ph].

[341] R. K. Kopparapu and J. E. Tohline, Astrophys. J. **655**, 1025 (2007), astro-ph/0610555.

[342] J. P. A. Clark, Astrophys. Lett. **18**, 73 (1977).

[343] W. Y. Chau, Astrophys. Lett. **17**, 119 (1976).

[344] A. Vecchio and E. D. L. Wickham, Phys. Rev. D **70**, 082002 (2004), gr-qc/0406039.

[345] L. J. Rubbo, N. J. Cornish, and O. Poujade, Phys. Rev. D **69**, 082003 (2004), gr-qc/0311069.

[346] N. J. Cornish, arXiv:1007.4820 [gr-qc].

[347] LISA International Science Team, Laser Interferometer Space Antenna (LISA) Measurement Requirements Flowdown Guide, 2009, 2nd issue, `http://lisa.gsfc.nasa.gov/Documentation/LISA-MSE-TN-0001_v2.0.pdf`.

[348] LISA International Science Team, LISA Science Requirements Document, 2007, v4.1, `http://lisa.gsfc.nasa.gov/Documentation/LISA-ScRD_v4.1a.pdf`.

[349] T. E. Strohmayer, Astrophys. J. **627**, 920 (2005), astro-ph/0504150.

[350] R. K. Kopparapu, Astrophys. J. **697**, 2089 (2009), arXiv:0809.1890 [astro-ph].

[351] J. Liu, Mon. Not. R. Astron. Soc. **400**, 1850 (2009).

[352] M. Benacquista and K. Holley-Bockelmann, Astrophys. J. **645**, 589 (2006), astro-ph/0504135.

[353] G. Nelemans, L. R. Yungelson, and S. F. Portegies Zwart, Mon. Not. R. Astron. Soc. **349**, 181 (2004), astro-ph/0312193.

[354] `http://nedwww.ipac.caltech.edu/forms/calculator.html`.

[355] D. J. Schlegel, D. P. Finkbeiner, and M. Davis, Astrophys. J. **500**, 525 (1998), astro-ph/9710327.

[356] G. H. A. Roelofs *et al.*, Astrophys. J. **666**, 1174 (2007), arXiv:0705.3855 [astro-ph].

[357] B. M. S. Hansen, Astrophys. J. **520**, 680 (1999), astro-ph/9903025.

[358] A. Cooray, A. J. Farmer, and N. Seto, Astrophys. J. Lett. **601**, L47 (2004), astro-ph/0310889.

[359] I. Iben, Jr., A. V. Tutukov, and A. V. Fedorova, Astrophys. J. **503**, 344 (1998).

[360] J. N. Bahcall and R. M. Soneira, Astrophys. J. Suppl. Ser. **44**, 73 (1980).

[361] Y. C. Joshi, Mon. Not. R. Astron. Soc. **362**, 1259 (2005), astro-ph/0507069.

[362] J. A. Cardelli, G. C. Clayton, and J. S. Mathis, Astrophys. J. **345**, 245 (1989).

[363] T. Muñoz Darias, J. Casares, and I. G. Martínez-Pais, Astrophys. J. **635**, 502 (2005), astro-ph/0508547.

[364] M. Kilic (private communication).

[365] E. Mason *et al.,* arXiv:1003.1986 [astro-ph.GA].

[366] C. Cutler, Phys. Rev. D **57**, 7089 (1998), gr-qc/9703068.

[367] T. Mora and C. M. Will, Phys. Rev. D **69**, 104021 (2004), gr-qc/0312082.

[368] J. Vines, É. É. Flanagan, and T. Hinderer, Phys. Rev. D **83**, 084051 (2011), arXiv:1101.1673 [gr-qc].

[369] B. Willems, C. J. Deloye, and V. Kalogera, Astrophys. J. **713**, 239 (2010), 0904.1953 [astro-ph.SR].

[370] S. Mereghetti *et al.,* arXiv:1105.6227 [astro-ph.HE].

[371] D. Levitan *et al.,* arXiv:1107.1209 [astro-ph.SR] [Astrophys. J. (to be published)].

[372] W. R. Brown, M. Kilic, C. A. Prieto, and S. J. Kenyon, Astrophys. J. **723**, 1072 (2010), arXiv:1011.3050 [astro-ph.GA].

[373] M. Kilic *et al.,* Astrophys. J. **727**, 3 (2011), arXiv:1011.4073 [astro-ph.GA].

[374] T. Barclay *et al.,* Mon. Not. R. Astron. Soc. **413**, 2696 (2011), arXiv:1101.2445 [astro-ph.GA].

[375] R. Napiwotzki *et al.,* Astron. Nachr. **322**, 411 (2001), astro-ph/0203147.

[376] M. Vallisneri, Phys. Rev. D **77**, 042001 (2008), arXiv:gr-qc/0703086.

[377] K. Yagi and T. Tanaka, Prog. Theor. Phys. **123**, 1069 (2010), arXiv:0908.3283 [gr-qc].

[378] E. Poisson, Phys. Rev. D **70**, 084044 (2004), gr-qc/0407050.

[379] L. E. Kidder, C. M. Will, and A. G. Wiseman, Phys. Rev. D **47**, 3281 (1993).

[380] P. S. Ho, Phys. Rev. **169**, 523 (1968).

[381] M. L. Glasser and I. J. Zucker, in *Theoretical Chemistry: Advances and Perspectives*, edited by H. Eyring and D. Henderson Vol. 5, pp. 67–139, Academic Press, New York, 1980.

[382] Z. Kopal, *Dynamics of Close Binary Systems* (D. Reidel Publishing Company, Dordrecht, 1978).

[383] P. Eggleton, *Evolutionary Processes in Binary and Multiple Stars* (Cambridge University Press, 2001).

[384] J. Fuller and D. Lai, Mon. Not. R. Astron. Soc. **412**, 1331 (2011), arXiv:1009.3316 [astro-ph.HE].

[385] V. Ferrari, L. Gaultieri, and F. Pannarale, Phys. Rev. D **81**, 064026 (2010), arXiv:0912.3692 [gr-qc].

[386] É. É. Flanagan and T. Hinderer, Phys. Rev. D **77**, 021502(R) (2008), arXiv:0709.1915 [astro-ph].

[387] J. S. Read *et al.*, Phys. Rev. D **79**, 124033 (2009), arXiv:0901.3258 [gr-qc].

[388] F. Pannarale, L. Rezzolla, F. Ohme, and J. S. Read, arXiv:1103.3526 [astro-ph.HE].

[389] M. Turner, Astrophys. J. **216**, 914 (1977).

[390] C. M. Will, Astrophys. J. **274**, 858 (1983).

[391] L. Bildsten and C. Cutler, Astrophys. J. **400**, 175 (1992).

[392] J. Vines and É. É. Flanagan, arXiv:1009.4919 [gr-qc].

[393] K. Taniguchi and M. Shibata, Phys. Rev. D **58**, 084012 (1998), gr-qc/9807005.

[394] W. Even and J. E. Tohline, Astrophys. J. Suppl. Ser. **184**, 248 (2009), arXiv:0908.2116 [astro-ph.SR].

[395] F. V. Sirotkin and W.-T. Kim, Astrophys. J. **698**, 715 (2009), arXiv:0904.2939 [astro-ph.SR].

[396] T. Binnington and E. Poisson, Phys. Rev. D **80**, 084018 (2009), arXiv:0906.1366 [gr-qc].

[397] T. Damour and A. Nagar, Phys. Rev. D **80**, 084035 (2009), arXiv:0906.0096 [gr-qc].

[398] L. Blanchet and T. Damour, Philos. Trans. R. Soc. London, Ser. A **320**, 379 (1986).

[399] R. A. Brooker and T. W. Olle, Mon. Not. R. Astron. Soc. **115**, 101 (1955).

[400] S. Chandrasekhar, Mon. Not. R. Astron. Soc. **95**, 207 (1935).

[401] G. Nelemans, L. R. Yungelson, S. F. Portegies Zwart, and F. Verbunt, Astron. Astrophys. **365**, 491 (2001), astro-ph/0010457.

[402] R. K. Kopparapu, PhD thesis, Louisiana State University, 2006, http://etd.lsu.edu/docs/available/etd-11162006-152427/.

[403] E. E. Salpeter, Astrophys. J. **134**, 669 (1961).

[404] L. L. Andronov and Y. B. Yavorskij, Contr. Astron. Obs. Skalnate Pleso **20**, 155 (1990).

[405] K. Nordtvedt, Phys. Rev. D **49**, 5165 (1994).

[406] S. Kopeikin and I. Vlasov, Phys. Rep. **400**, 209 (2004), gr-qc/0403068.

[407] S. Kopeikin and I. Vlasov, in *Proc. 11th Marcel Grossmann Meeting*, edited by H. Kleinert, R. T. Jantzen, R. Ruffini, p. 2475, Singapore, 2006, World Scientific, gr-qc/0612017.

Vita

Nathan Kieran Johnson-McDaniel was born May 28th, 1981 in Athens, Georgia. Ze attended the University of Georgia as an undergraduate, obtaining a B.S. in Physics and Astronomy and a B.MUS. in Music Performance (violin), both *summa cum laude*. Nathan decided to go on in physics for graduate work, and attended The Pennsylvania State University, receiving the University Graduate Fellowship and Braddock/Roberts Fellowship zir first year, in addition to joining Benjamin Owen's group. Nathan will be joining Bernd Brügmann's group at the University of Jena as a postdoc after graduation.